Direct Imaging and Subsequent Modeling of the Cement Microstructure and Integrity of Cement/Casing and Cement/Formation Interfaces

by

Xinxiang Yang

A thesis submitted in partial fulfillment of the requirements for the degree of

Doctor of Philosophy

in

Petroleum Engineering

Department of Civil and Environmental Engineering
University of Alberta

Abstract

As a key component of the wellbore barrier system, cement provides zonal isolation and structural support during the entire life of a well. However, even when the cement is properly placed in the well, the zonal isolation may be lost over time. Failure to establish and maintain an effective barrier can result in negative environmental and economic impacts such as leakage of formation fluids into the environment or loss of productions and costly remediation operations. The microstructure of the wellbore cement body and the various possible interfaces (e.g. cement-casing and cement-rock) have a large influence on controlling the long-term integrity of the well.

This study presents ~~a~~ systematic workflows for preparing, characterizing and analyzing the downscaled samples simulating cement body and various interface conditions (e.g., cement-casing, cement-rock), which represent various potential leakage pathways in a well at the microscale. Formation rocks, steel pipes and various cement blends were utilized to prepare the downscaled samples. Microscope, micro computed tomography (micro-CT), traditional and environmental scanning electron microscopy (SEM/ESEM) were employed to characterize the prepared samples at a resolution from 0.01 µm to 16.87 µm. Digital image processing technique and CT-based CFD modelling were conducted to examine and analyze the 2D and 3D microstructures and their impact on permeability.

At the micron scale (2.64 µm), non-uniform porosity distribution in cement sample was observed, which caused the permeability disparities at different locations. A characteristic correlation between effective porosity and permeability was used to estimate the permeability of the cement sample. A comparative study on the porosity and permeability of early-age well cement and

formation rocks reveals that the cement porosity and permeability data are mainly comparable to those of a tight sandstone. Comparisons also show that the early-age well cement has a narrower permeability range than formation rocks. The trend of cement linear fitting curve suggests that if the hydration process of neat early-age well cement sample continues, poroperm characteristics will approach those of shale.

Analysis on the stress-induced cement fractures generated by uniaxial compression demonstrates that the fractures in cement matrix created by the monotonic compressive stress (up to the limit of uniaxial compressive strength, UCS), are not likely to form continuous leakage pathways. This is because the 2D fractures in cement matrix as shown by SEM images are in limited dimensions while the 3D fractures in cement matrix observed from CT-based 3D models have poor connectivity, generally indicating that leakage pathways which have significant permeability would not form as a result of compressing the cement samples up to their UCS limits. Inclusion of a fiber additive is expected to enhance cement integrity by limiting the fracture propagation.

Any significant change in the relative humidity (RH) of the environment during the cement preparation, curing and testing processes significantly affects the size of the gap at the cement-casing interface in test samples. Analyses of the ESEM images have shown that the 2D non-uniform gap size between the cement and the casing is inversely proportional to the change in the relative humidity (RH) of the environment. As long as the RH of the environment does not change significantly, the cement is expected to undergo a limited shrinkage and the gap between the cement and the casing may not induce any significant leakage pathway as the gap is only locally distributed at the cement polished surface without showing any significant connectivity along the wellbore axis.

Analyses on the cement-rock CT images revealed that the cement-rock interface zone had higher porosity than its neighboring zones. CT-based flow simulation study implies that the cement-rock interface is more likely to provide the leakage pathway when intact caprock exists. The size of the gaps observed at the cement-rock interface through ESEM images was significantly reduced by optimizing the cement chemistry. The effect of the expansion agent on gap size change, however, varied depending on the rock properties such as rock density and porosity. The reduction rate of the gap size due to addition of expansion agent was found to be improved with the low-density rocks.

Porosity and gap (between casing and cement) size analysis on the casing-cement-casing samples show that the inner cement-casing interface has a better bonding than the outer cement-casing interface. The density gradient caused the non-uniform porosity distribution in the vertical direction. Analysis on the rock-cement-casing samples indicates that cement porosity close to the cement-casing interface is lower than the cement porosity close to the cement-rock interface and this result is independent of rock type. Gaps were observed at the cement-rock interface in the rock-cement-casing samples. Besides, the gap size found at the cement-rock interface is significantly larger than those observed at the cement-casing interface.

Preface

This thesis is an original work by Xinxiang Yang. The research was carried out under the supervision of Dr. Ergun Kuru and Dr. Murray Gingras at the University of Alberta. The data collection, data analysis and composition of research papers have all been completed by Xinxiang Yang. Several sections of the current thesis either have been published or are pending publication.

Chapter 4 was published in Construction and Building Materials journal as "Yang, X., Kuru, E., Gingras, M., & Iremonger, S. (2019). CT-CFD integrated investigation into porosity and permeability of neat early-age well cement at downhole condition. *Construction and Building Materials*, *205*, 73-86. https://doi.org/10.1016/j.conbuildmat.2019.02.004". Data collection, analysis, and manuscript writing have all been accomplished by Xinxiang Yang.

Chapter 5 has been published and presented before. This chapter was initially presented as "Yang, X., Kuru, E., Gingras, M., Iremonger, S., Taylor, J., & Lin, Z. (2019, November). Quantifying 2D and 3D Fracture Leakage Pathways Observed in Wellbore Cement after Uniaxial Compressive Loading" In SPE Thermal Well Integrity and Design Symposium, 19-21 November, Banff, Alberta, Canada. https://doi.org/10.2118/198683-MS". Additionally, it was published in SPE Journal as "Yang, X., Kuru, E., Gingras, M., Iremonger, S., Taylor, J., Lin, Z., & Chase, P. (2020). Quantifying the Impact of 2D and 3D Fractures on Permeability in Wellbore Cement after Uniaxial Compressive Loading. *SPE Journal*. https://doi.org/10.2118/198683-PA". Data collection, analysis, manuscript writing have all been completed by Xinxiang Yang.

Chapter 6 of the thesis was accepted by *SPE Journal* for publication as "Yang, X., Kuru, E., Gingras, M., Iremonger, S., Chase, P., & Lin, Z. Characterization of the Microstructure of the Cement-Casing Interface Using ESEM and Micro CT Scan Techniques". Data collection, analysis, and writing of the research paper were accomplished by Xinxiang Yang.

Chapter 7 of the thesis has been submitted to *SPE Journal* for possible publication as: "Yang, X., Kuru, E., Gingras, M., Iremonger, S., Biddle, S., & Lin, Z. Characterization of the Microstructure of the Cement-Rock Interface Using ESEM and Micro CT Scan". Data collection, analysis, and writing of the research paper were done by Xinxiang Yang.

Acknowledgements

I would like to express my sincere gratitude to my supervisor Dr. Ergun Kuru and co-supervisor Dr. Murray Gingras for their support, inspiration and priceless supervision. I received prolonged constructive and positive feedbacks from Dr. Kuru. The way of thinking and the attitude towards research that I learned from Dr. Kuru will be my lifelong fortune. Dr. Gingras offered me excellent resources for my research. His patience, encouragement and invaluable suggestions guided me to complete my research. It is a great honor and pleasure for me to be a PhD student under their supervisions.

I sincerely thank Dr. Simon Iremonger for his professional guidance on my cement study and persistent demand for excellence throughout this work. Dr. Iremonger provided me lots of valuable suggestions and comments in industrial perspective and these helped me narrowed the gap between academic research and industry needs, which is vital to my future career. I am also grateful for the committee members serving in my PhD final exam: Dr. Tayfun Babadagli, Dr. Nobuo Maeda, Dr. Zhehui (Charlie) Jin and Dr. Simon Iremonger. My special thanks go to Dr. Daoyong (Tony) Yang for accepting to be the external examiner in my defense exam.

This study has been conducted as part of the collaborative research project supported by Natural Sciences and Engineering Research Council of Canada and Sanjel Energy Services (NSERC EGP 507672-16 Kuru, NSERC CRDPJ 531509-18 Kuru). I would like to thank the financial support to this work from China Scholarship Council (CSC) (No. 201608370084).

I would like to acknowledge the technical help that I received from Todd Kinnee, Lixing Lin, Georgeta Istratescu and John Czuroski. I also want to thank my friends and my colleagues Yingkun Fu, Chuan Lu, Xin Xu, Zichao (Rinbo) Lin, Shuyu Zhang and Chenyang Feng for their help to my both research and life.

I would like to express my deep appreciation to my parents, my wife for their love and support. They are the driving force and sunshine of my life. I also want to thank my daughter Julia for born on time, which offered me enough time to complete and optimize this thesis.

Table of Contents

List of Tables

List of Figures

Chapter 1 Introduction

1.1 Overview

Following drilling operations, oil and gas wells are completed by running nested steel casing pipes in the borehole and cementing the annular space between different casing strings and/or between the last casing string and the surrounding ground/formation (see Figure 1-1a). Wellbore cement is the most important barrier. Good well cementing provides structural support and zonal isolation throughout the life of a well, from well construction, through hydrocarbon production, to post-abandonment. Failure to establish and maintain an effective barrier can result in negative environmental and economic impacts such as leakage of formation fluids into the environment or loss of productions and costly remediation operations.

However, even when cement is properly placed in the well, zonal isolation may be lost over time. Leakage may occur from oil and gas wells due to the failure of the wellbore barrier system. Celia et al. (2005) summarized the possible causes of the leakage, as shown in Figure 1-1b. The leakage can be treated under two categories: surface casing vent flow (SCVF) and gas migration (GM). Surface casing vent flow is the gas leaking from the annular space between the production casing and the surface casing, corresponding to the cases II, III and IV in Figure 1-1. Gas migration is the gas leaking into the formations or soil outside of the surface casing, corresponding to the cases I, V and VI in Figure 1-1. Bonett & Pafitis (1996) explained the detailed major contributing parameters for gas migration, as shown in Figure 1-2.

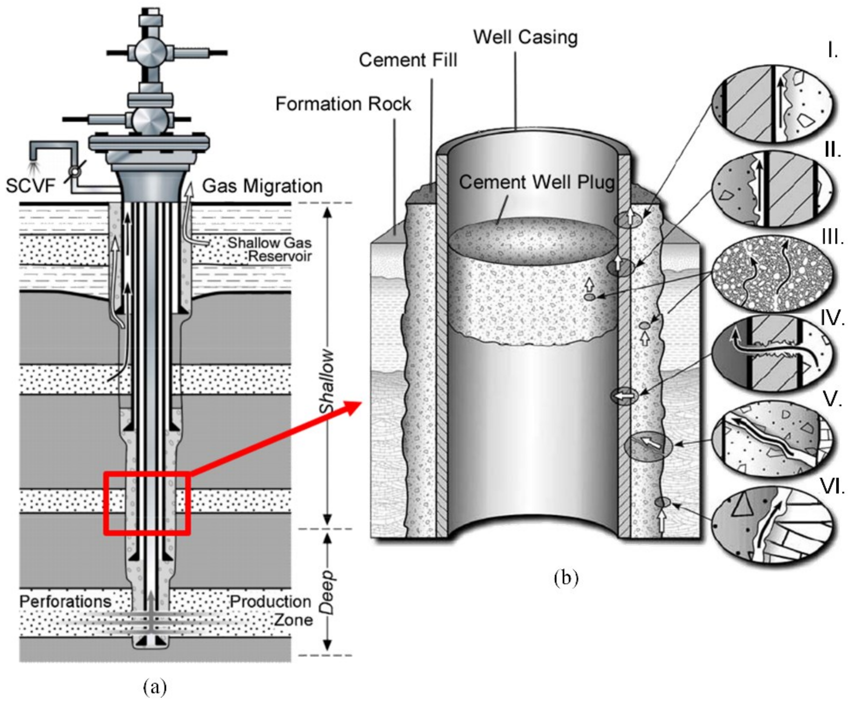

Figure 1-1 Potential leakage pathways in the well.

Between cement and casing (I and II), through the cement (III), through the casing (IV), through fractures (V), and between cement and formation (VI). Modified from (Bachu, 2017; Celia et al., 2005).

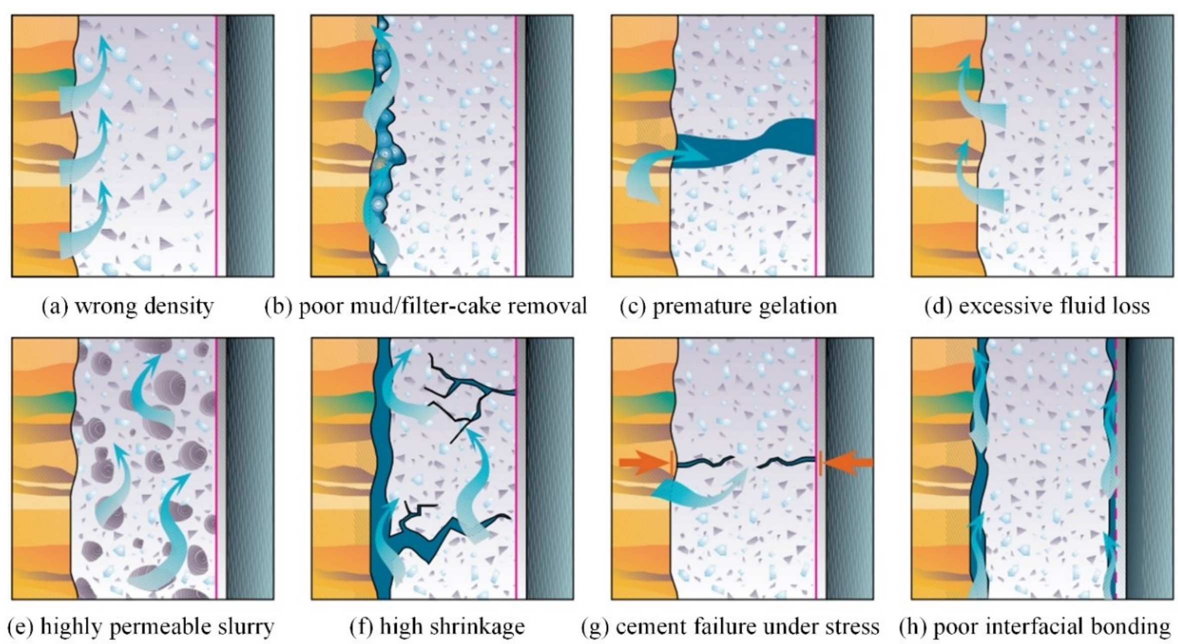

Figure 1-2 Main reasons caused the gas migration(modified from Bonett & Pafitis (1996)).

The negative impact of gas leakage on field production can range anywhere from blowout, which may cause the death of the field personnel, destruction of the oil field facility and the long-term cessation of the production, to residual gas pressure of just a few psi at the wellhead (Bonett & Pafitis, 1996). Besides, conducting frequent remedial cementing jobs to reduce the gas leakage levels to meet the safety policies and regulations, could be very time consuming and costly (Bol et al.1991).

As a main component of natural gas, methane traps more than 70 times more heat over a 20-year period than the equivalent amount of carbon dioxide(Government of Canada, 2019). Methane is also the second most common greenhouse gas (GHG) in Canada, responsible for about 15% of the total GHG emissions. The oil and gas sector is the largest industrial polluter of methane emissions in Canada, releasing 44% of the country's total methane emissions(Government of Canada, 2018a). As the main oil and gas producer in Canada, Alberta has the largest number of oil and gas wells in the country (~75%) by far. Fugitive emissions from oil and gas wells are a major contributor to uncontrolled methane release. The latest report from the Alberta Energy Regulator (Alberta Energy Regulator, 2018) showed that Alberta has an increasing trend of leaking wells, as shown in Figure 1-3.

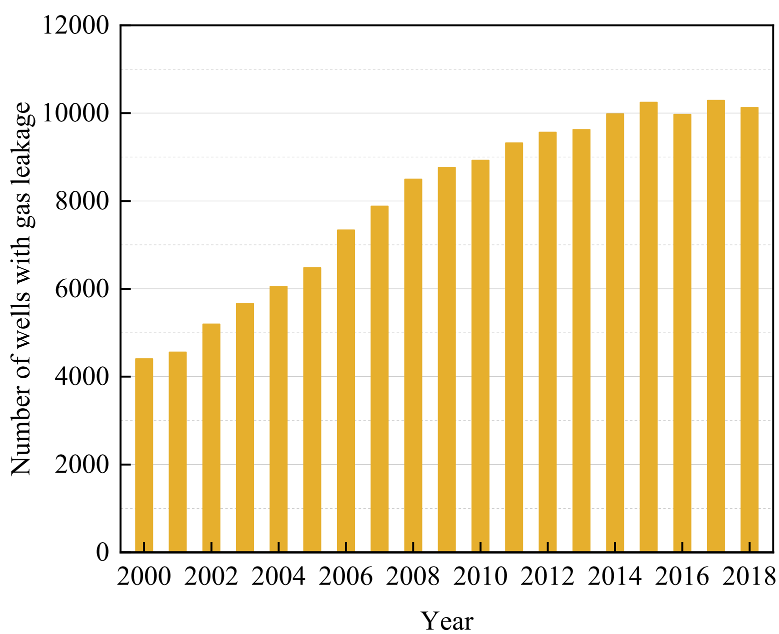

Figure 1-3 The increasing trend of leaking wells in Alberta since 2000 (Alberta Energy Regulator, 2019).

An improved understanding of the drivers behind fluid leakage (i.e. stresses creating fractures along the cement/casing, cement/borehole interfaces and within the cement body), based on the results from the experimental investigation and numerical simulation studies were investigated in this study and such efforts result in a better understanding of the factors influencing the gas leakage from oil and gas wells, which will be useful for fulfilling Canada's plan to reduce its greenhouse gas emissions to 30% below 2005 levels by the year 2030 (Government of Canada, 2018).

1.2 Statement of the problem

A major contributing factor to the growth in leakage is the increased mechanical stresses to which modern wells are being subjected. Multi-stage hydraulic fracturing treatments, for example, subject the wells to high cyclic stress loads, which arise from the high-pressure swings used in each fracturing stage. Depending on the formation, it is quite common for wells to be stimulated up to 50 stages. Such cyclic loads are well known to debond the cement from the casing and the general trend is for methane emission rates to increase post-fracturing treatment significantly. The rates of post-fracturing leakage will likely be further exacerbated by new refracturing technology in which existing wells are re-stimulated years after their initial stimulation. This subjects the wells to even more cyclic stresses on top of any damage from the first round of stimulation. The impact of refracturing on gas leakage is not understood, but it is highly likely that it will not have positive impacts on well integrity and gas leakage. Debonding can also be caused by thermal stresses due to thermal cycling induced by injection of a relatively cold or hot fluid down the well (Lavrov & Cerasi, 2013).

Experimental observations of cement bonding to a wall made of steel or sandstone suggested that debonding maybe associated with the microstructural changes that take place in the near-wall zone, also known as the interfacial transition zone (ITZ), which is developed along the cement/casing and cement/rock interfaces (Scrivener et al., 2004). A recent experimental study (Torsæter et al., 2015a) has shown that fracturing and debonding of cement in the ITZ can occur and that the exact failure mode depends on the curvature of the interface. Samples with a convex interface between cement and steel pipe (cement surrounding a casing) displayed radial fractures oriented normal to the interface. Samples with a concave interface (cement plug inside a rock/steel hollow cylinder) displayed discontinuities (fractures) running within the ITZ, along the interface. The discontinuity developing along a concave interface between cement and porous rock was found to be more irregular than the one developing along a concave cement-steel interface.

Despite the importance of the microstructure of the near-wall zone, there are only a few studies that have investigated the cement-casing interface at the micron scale. Torsæter et al., (2015) studied the microstructure of the cement-casing interface by using micro-CT and scanning electronic microscope (SEM). They found gaps (also called as microannuli) at the cement-casing interface. The gaps at the cement-casing interface were indicated as one of the most significant leakage pathways (Carey et al. 2010). Experimental tests shown the gas permeability of cemented casing section with gaps could reach to 600 mD (Rushch et al., 2004). Torsæter et al., (2015) suggested that these gaps were likely to be caused by the cement shrinkage. The cement shrinkage can be divided into two major categories: a chemical shrinkage, which results from autogenous chemical reactions taking place in the cement matrix, and a drying shrinkage, which is sensitive to the RH change (Gajewicz et al. 2016). Although the cement shrinkage was suspected to be the main reason for the discontinuities shown in SEM images, no experimental evidence has been reported to confirm this assumption. Furthermore, which shrinkage type is mainly responsible for the discontinuities in SEM images is still unclear.

Besides, the effect of the sample preparation (e.g., polishing for SEM characterization) on the bonding characterization remains unclear. Lavrov et al., (2017) characterized the particle size distribution in the ITZ using micro-CT with synchrotron radiation, which significantly increased the resolution of the CT image. However, the cement was placed in a glass tube rather than a steel casing. This may affect microstructure in the ITZ because casing has different electrical properties than glass, and the electric field affects the particle size distribution near the wall (Lavrov et al., 2018). Moreover, the debonding, which normally occurs at the cement-casing interface (Lavrov., 2016), may not be captured at the interface between the cement and the glass tube. In short, very little is currently known about the microstructure of the cement-casing interface in relation to the debonding phenomena.

The cement-rock interface is also a major component of the wellbore barrier system. Leakage may result from the poor bonding between cement and rock interface. Rock properties at the cement-rock interface vary greatly as a well is normally drilled through several different formations. Therefore, as far as the interface properties are considered, the cement-rock interface seems more prone to have leakage than the cement-casing interface. A notable example has been observed in a well after 30 years of CO_2-flooding operation, where textural studies on the cores revealed that the due to the carbonation, the cement-rock interface was degraded much more than the cement-casing interface and there was a high porosity zone at the cement-rock interface (Carey et al. 2007).

Many previous cement-rock interface studies have been related to the carbon capture and storage (CCS) wells, where the main focus was to understand the influence of chemical reaction at the cement-rock interface (Carey et al., 2007; Agbasimalo and Radonjic, 2012; Jung et al., 2013; Newell and Carey, 2013; Jung et al., 2014; Labus and Wertz, 2017). It was noteworthy to point out that the geometry of cement-rock interface of the samples used in these studies had either a flat surface or some other irregular shapes but did not have a realistic circular shape.

Researchers from SINTEF have investigated the effect of mud properties (Opedal et al., 2014; Opedal et al., 2014), cement defect (Kjøller et al., 2016), interface geometry (Torsæter., 2015) and cement stiffness (Lavrov, 2018) on cement-rock interface integrity. In the majority of these studies, micro-CT scanning technique was used to non-destructively characterize the cement-rock interface. Due to the large sample sizes used in these studies, the resolution of micro-CT was limited to 24-200 m. Considering the multiscale nature of the cement and pore size of the rock, scanning electron microscope was used together with micro-CT as SEM can characterize the cement microstructure at nanoscale. However, traditional SEM characterization can cause cement shrinkage and thus degrade the quality of characterization results (Kjellsen and Jennings, 1996).

So far, very little attention has been paid to the role of formation rock properties on the cement-rock interface integrity. One good recent work by Opedal et al., (2014) had a short discussion of rock types on cement-rock interface integrity where they qualitatively concluded that the different rock formations exhibited different interactions with the cement. But they did not offer much discussion about what actual mechanisms were behind their conclusion. To answer this question, more in-depth quantitative studies are needed. The cement used in their study was neat Portland cement which has been commonly employed in previous cement-rock studies such as Agbasimalo and Radonjic (2012); Opedal et al., (2014); Labus and Wertz, (2017). However, the neat Portland cement without additives is normally not stable and therefore has not been used in real wellbores. A cement blend that is used in real wellbores should be considered in the cement-rock interface study as it is more relevant to the industrial practice.

Permeability is considered to be an important indicator to evaluate the durability of cement, and it is influenced by the microstructure of cement. The microstructures used in previous research are normally created by computer programs, and therefore they might not be able to represent the real microstructures of cement properly. Micro-computed tomography or "micro-CT" has been widely used for cement research due to its non-destructive characteristic. Moreover, it is possibly the only way to obtain realistic 3D geometry efficiently. The statistical and morphological analyses using micro-CT provides a new view of the cement microstructure because it gives a realistic 3D geometry. Stress-induced cracks also affect the permeability of cement. The influence of these cracks on the mechanical properties has been well studied. However, only very few recent research efforts (Carey et al., 2014; Kabilan et al., 2016) focused on how the stress-induced cracks contribute to the cement paste permeability. Because of the multiscale characteristic of cement microstructures, it is impossible to capture all the stress-induced cracks by just using micro-CT (Gallucci et al., 2007; Kabilan et al., 2016). Therefore, SEM was adopted to characterize the features beyond the resolution of the micro-CT.

Some special cement blends and additives are used to mitigate or remediate the leakage pathways. However, the effectiveness of these special blends and additives needs more quantitative analysis to prove. CT-based numerical simulation provides a way to estimate the cement permeability based on its realistic microstructures. The element-based finite volume method was proven to have a high efficiency to handle the flow simulations with complex geometry (Marcondes et al., 2013a; 2013b) and has been widely used in realistic porous media simulations (Song et al., 2017; Wang et al., 2016). It is also worth noting that at the micron scale, the microstructure of cement may still behave as a heterogeneous material (Bossa et al., 2015; Viejo et al., 2016). The local permeability may change at different positions. In order to obtain the representative permeability value of cement, representative volume elements (RVEs) need to be built. The RVE is the smallest volume over which a measurement or simulation can be carried out to produce a result that is representative of the macroscopic property (Yio et al., 2017). Although the RVE has been commonly used in micromechanics to analyze and predict the mechanical behavior of cement (Das et al., 2016; Viejo et al., 2016), the application of the RVE to flow study (at micron scale) has not been covered before.

To summarize, very little quantitative information is known about the microstructure of the various potential leakage pathways along the oil and gas wells. Such data are the key to understand and mitigate the leakage pathways. Additionally, the most suitable characterization and analysis methods for studying the potential leakage pathways at the micron scale are still unclear. CFD modeling of the fluid flow through the potential leakage pathway based on the realistic geometries reconstructed from CT images are limited.

1.3 Objectives of the study

The primary objective of this research is to conduct comprehensive experimental and numerical studies of the microstructure of potential leakage pathways in oil and gas wells. As shown in Figure 1-4, six different wellbore cement scenarios (derived from Figure 1-1) were analyzed. In-depth analyses were performed to quantify cement microstructure failure and debonding behavior and to determine how these failures affect the fluid movement through the cement microstructures and various interfaces encountered in the cemented oil and gas wells.

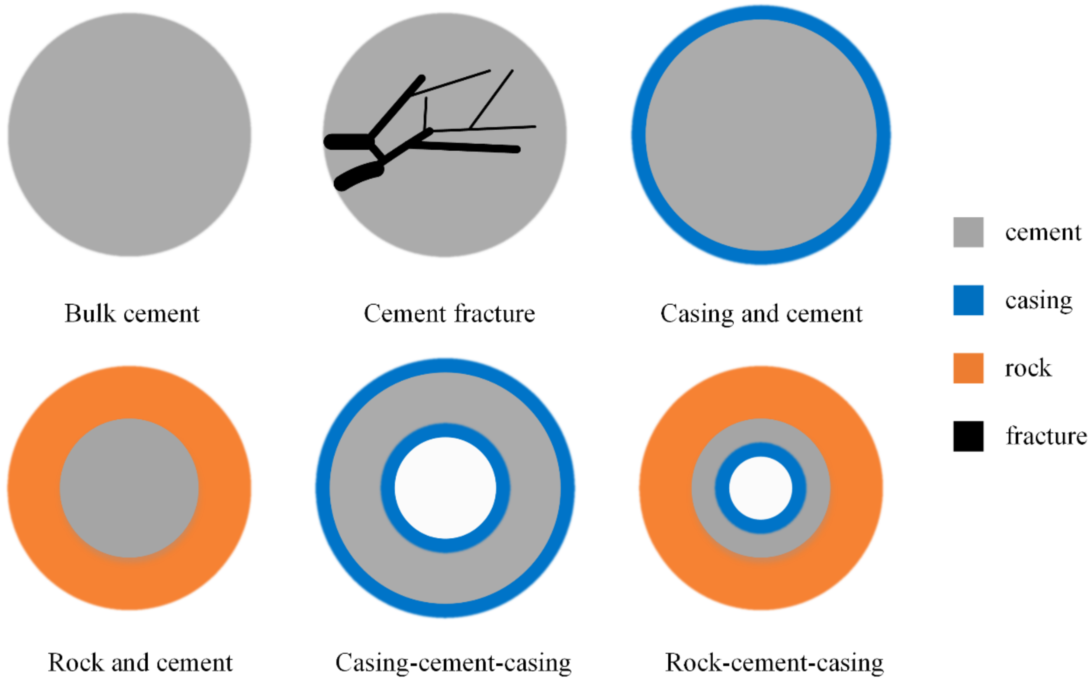

Figure 1-4 Six types of downscaled samples prepared for studying wellbore cement microstructure.

More specifically, this study has the following objectives:

- Obtain the most suitable method for preparing bulk cement and cement interface samples (i.e., cemented casing samples and cemented rock samples).
- Optimize the microstructure characterization method to minimize the artificial effects such as polishing, or storage on microstructure analysis.
- Suggest the resolution required to characterize the potential leakage pathways.
- Determine the impact of stress on fluid flow pathways in cement body using micro-CT, SEM and other analytical techniques.
- Investigate the effect of using specific additives on the bulk cement microstuctural properties (i.e. porosity and permeability).
- Characterize microstructure of the cement/casing and the cement/rock interfaces for cement bond quality assessment.

- Investigate the effect of cement drying shrinkage on the integrity of cement-casing interface.
- Determine the influence of rock type on the integrity of cement-rock interface.
- Investigate the effect of using specific additives on the integrity of cement-casing, cement-rock interface.
- Evaluate the leakage through potential pathways via CT-based CFD fluid flow simulation.
- Quantify the radial and axial porosity distribution in cement sheath between two casings and between rock and casing.

1.4 Contributions of the research

The main contributions of this research can be summarized as follows:

- Established a series of methods for preparing the cement samples and interface samples for micro scale study.
- Optimized the CT scan parameters for cement, rock and casing CT scan. The contrast and quality of the CT images were improved.
- Clarified the resolution required to sufficiently characterize the potential leakage pathways at micron scale.
- Developed a digital cement method that can be used to obtain the morphological data of cement based on cement CT images. Pore size distribution and porosity can be calculated via the digital cement method.
- Established a 3D simulation model that can represent the multiscale nature of the cement microstructure. This 3D simulation model can be utilized for evaluating the cement permeability.
- Quantified the impact of 2D and 3D fractures on permeability in wellbore cement after uniaxial compressive loading.
- Investigated the influence of fiber additive on limiting the fracture propagation in cement.

- Established a method for processing the cement-casing and cement-rock samples for surface characterization use.
- Quantified and visualized the gap at cement-casing interface and cement-rock interface under high resolution (0.05 µm ESEM, 11.92 µm micro-CT).
- Evaluated the influence of expansion agent on minimizing the gap at cement-casing interface or cement-rock interface.
- Investigated the impact of cement drying shrinkage on the development of gap at the cement-casing and cement-rock interface.
- Investigated the role of rock type on the integrity of cement-rock interface. Various rock types were analyzed.

All these achievements can be summarized under two categories: 1) A unique methodology for studying the microstructure of the cement and related cement interfaces was developed, as they are the potential leakage pathways. This unique methodology includes specified sample preparation, sample characterization and sample analysis including CT-based numerical simulation. 2) Quantified and visualized microstructure of the cement body and related interfaces in the wellbore was provided. Not only does this kind of data rarely exist in petroleum literature, but also it will facilitate understand and mitigate the potential leakage pathways in petroleum wells.

1.5 Structure of the thesis

This PhD thesis is composed of the following 10 chapters: Chapter 1 provides a general introduction and is intended to offer a brief overview of the investigated subject, followed by the statement of the problem, objectives of the study and the contributions of the research.

Chapter 2 starts with a comprehensive review of the available literature focused on the major leakage pathways. The literature on microstructure characterization techniques and CT-based CFD simulation was also reviewed as they are the main methodology utilized in this work. Studies of the impact of various additives on the cemented wellbore integrity were also reviewed.

Chapter 3 describes the detailed methodology of this work. Details of the sample preparation, characterization were fully explained. The digital cement method and CT-based CFD modeling, which were widely used in this study for analyzing and evaluating the cement integrity, were also presented in this chapter**.**

Chapters 4 to 9 conducted a comprehensive study on six wellbore cement scenarios presented in Figure 1-4. As shown in below Figure 1-5, these six scenarios correspond to the research topic of chapters 7 to 9.

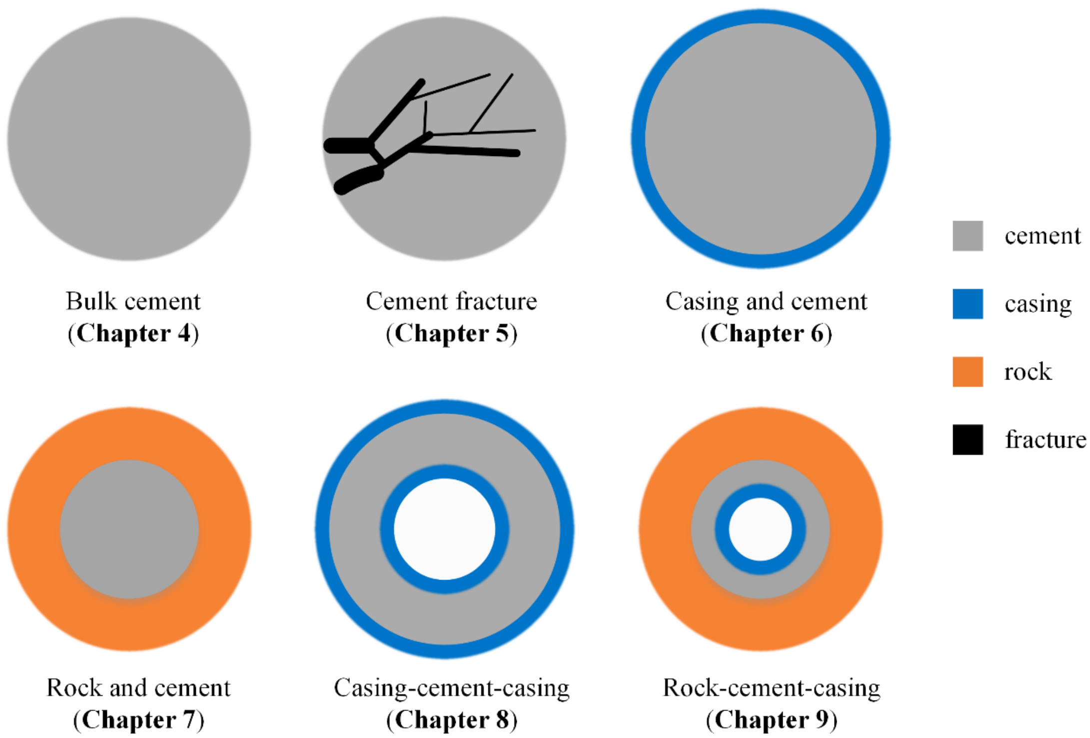

Figure 1-5 Research topics for chapters 7 to 9.

Chapter 4 proposed a new experimental/numerical approach, which combines CT characterization and CFD modeling to investigate the permeability of neat early-age well cement sample. This approach provides a quantitative means to estimate the porosity and permeability of representative volume elements selected from cement sample.

Chapter 5 investigated the effect of stress-induced 2D and 3D fractures on permeability in wellbore cement after uniaxial compressive loading. SEM and micro-CT techniques were utilized to quantify the 2D and 3D geometrical parameters of cement fractures in mature thermal thixotropic cement samples that were subjected to pre- and post-peak compressive stress. A novel simulation method was also proposed to quantify the impact of the stress-induced realistic 3D fractures on the cement permeability.

Chapter 6 studied the effects of the environmental conditions (i.e., relative humidity of the storage and testing conditions), cement drying shrinkage and the expansion agent on the integrity of the bonding at the cement-casing interface at micron scale by using ESEM and micro-CT (μ-CT) scanning techniques

Chapter 7 explored the effect of formation rock types on the cement-rock integrity, and how to improve the cement-rock integrity by applying suitable cement blends. A novel method was also proposed allowing to characterize the cement-rock interface at around 0.05 μm resolution with minimal cement shrinkage by using the ESEM. Potential leakage pathways in the cement-rock samples was also discussed via CT-based flow simulations.

Chapters 8 and 9 focused on the microstructure of the cement sheath between two casings and the cement sheath between cement and formation rocks, respectively. Scaled-down casing-cement-casing samples and rock-cement-casing samples were prepared. Radial and axial porosity distributions in cement were calculated based on the CT images. Gaps observed at the cement-casing or cement-rock interface were analyzed.

Chapter 10 provides key conclusions of this study and recommendations for future research.

Chapter 2 Literature Review and Background

This chapter first provides a comprehensive review of available literature related to the major leakage pathways, which were investigated in this study. They are leakage through cement matrix (including cement fractures), leakage through cement-casing interface and leakage through cement-rock interface. The literature on microstructure characterization techniques and CT-based CFD simulation was also reviewed as they are the main methodology employed in this work. Studies of the impact of various additives on the cemented wellbore integrity were also reviewed.

2.1 Potential leakage pathways through petroleum wells

As a key component of the wellbore barrier system, cement provides zonal isolation and structural support during the entire life of a well. However, even when cement is properly placed in the well, zonal isolation may be lost over time. Leakage may occur from the oil and gas wells due to the failure of the wellbore barrier system. Viswanathan et al. (2008) summarized the possible causes, which could lead to failure of the wellbore barrier system, as shown in Figure 2-1.

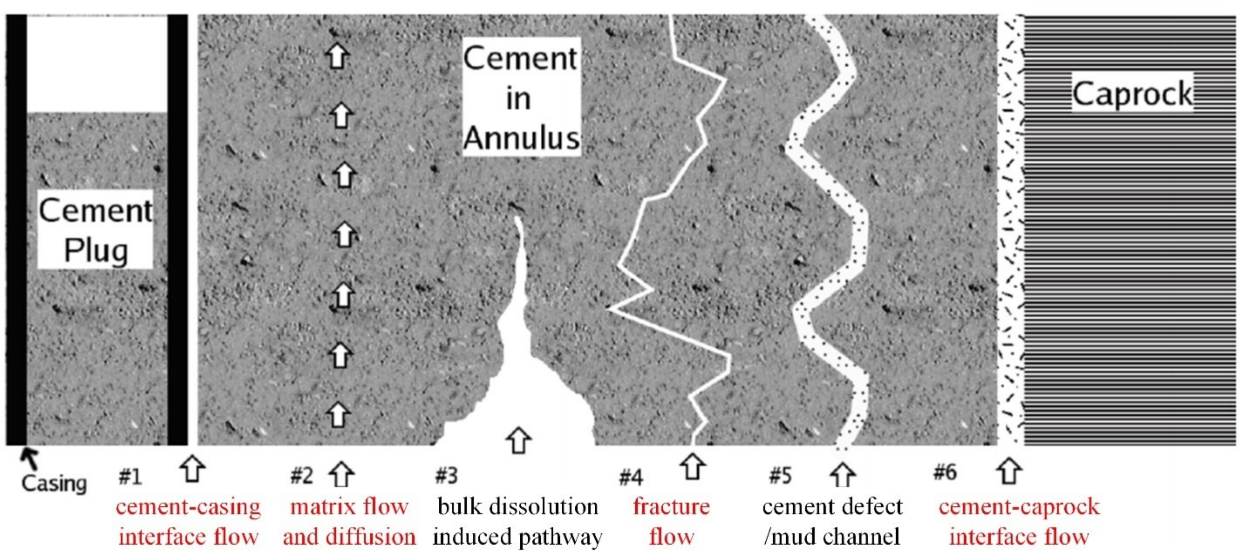

Figure 2-1 Potential leakage pathways investigated in this study.

Modified from (Viswanathan et al., 2008a).

According to Figure 2-1, a majority of the leakage pathways are through the cement matrix or the cement interfaces (marked in red). A more detailed account of leakage pathways through cement is given in the following section.

2.1.1 Leakage through cement matrix

Permeability is a measure of the ability of a material to allow fluids to flow through it. Permeability can be used as an important indicator to assess fluid transport in the cement (Baroghel-Bouny et al., 2009; Basheer et al., 2001; Luping and Nilsson, 1992). The permeability of the cement is strongly affected by the microstructure (Luping and Nilsson, 1992; Tiab and Donaldson, 2015). A considerable number of studies have been conducted to understand the link between the permeability and the microstructure of the cement using experimental, analytical, and numerical techniques.

One common experimental technique to study the microstructure of the cement is the Mercury intrusion porosimetry (MIP) (Alford and Rahman, 1981; Bágel' and Živica, 1997; Holly et al., 1993; Liu and Winslow, 1995). The drying process required before conducting MIP can damage and alter the pore microstructure (Holly et al., 1993), therefore, the accuracy of mercury intrusion porosimetry is limited. High intrusion pressures can also change the pore microstructure of small pores (Beaudoin, 1979). Modifications and other techniques have also been used to test the cement permeability such as the Helium pycnometric method (Beaudoin, 1979), non-contact impedance measurement (Tang et al., 2014), beam bending method (Valenza and Thomas, 2012) and constant water flow method (i.e. Darcy tests) (Phung et al., 2013).

Modern wells are subjected to complex external forces during their lifetime, such as thermally induced stresses in steam-assisted gravity drainage (SAGD) wells or cyclic stress due to multistage fracturing (Fjar et al., 2008). These external loads have the potential to create stress-induced fractures and deformations, which may result in interconnected flow paths leading to increased permeability and potential gas leakage (Bonett and Pafitis, 1996; Skorpa and Vrålstad, 2018). An example of this is the hydraulic fracturing treatment for horizontal wells. Wellbore cementing is a significant process prior to the perforation. Stress-induced fractures would be generated after perforation and then fluid leakage would happen. The interactions among created fractures, other formation discontinuities and wellbore cement would give rise to the alteration of cement integrity and its corresponding permeability (Tang et al., 2019; Zhang et al., 2019). Despite the importance of controlling the long-term well integrity, far too little attention has been paid to the nature of stress-induced fractures and their contribution to cement permeability. The importance of having quantitative information for stress-induced fractures is not just limited to the control of methane leakage in production or abandoned wells, but also to the control of CO_2 leakage in CCS wells.

Quantitative data of the stress-induced fractures allow a better understanding of the interrelation between the fractures and the resultant permeability. Considering the multiscale nature of the cement pore structure, the dimensions of stress-induced fractures also range from nanometer to millimeter scales (Barnes and Bensted, 2002). Therefore, no one imaging method can capture the entirety of the complex fracture geometries expected in wellbore cements. SEM and micro-CT techniques have been widely used to observe fractures in cement paste (Attiogbe and Darwin, 1987; Panduro et al., 2017; Gallucci et al., 2007; Hlobil et al., 2016; Jung et al., 2013; Kabilan et al., 2016; Kutchko et al., 2009; Shadravan et al., 2015; Stutzman, 2012; Torsæter et al., 2015b).

2.1.2 Leakage through cement-casing interface

The question of which type of pathways leaked the most methane is still unclear but a few recent research indicated that the failure of the cement interfaces in a well, either cement-casing interface, or the cement-formation interface, is the most common reason caused the loss of zonal isolation (Baumgarte et al., 1999; Bourgoyne et al., 2000). It also reveals that the cement interfaces seem more prone to have leakage than the cement matrix. This section reviewed the studies on the cement-casing interface.

In recent years, more attention has been paid to studying the cement-casing interface of the CCS wells. A majority of these studies have concentrated on the influence of CO_2–cement chemical reaction on the integrity of the cement-casing interface (Bachu and Bennion, 2009; Carey et al., 2010; Jung et al., 2013). Nonetheless, the leakage does not only occur in CCS wells. Many questions, such as the reasons behind the weak bonding among the production or abandonment wells still remain unanswered. The cement microstructure has a considerable influence on cement transport and mechanical properties (Bentz et al., 1999). Experiment results suggested the cement-casing bonding quality is probably related to the microstructural changes that occur in the near-wall zone, also known as the interfacial transition zone (ITZ) (Scrivener et al., 2004), which is develops along with the cement interfaces such as cement-casing interface.

Despite of the importance of the microstructure of the near-wall zone, there are only a few studies that have investigated the cement-casing interface at the micron scale. Torsæter et al. (2015) studied the microstructure of the cement-casing interface by using micro-CT and SEM. They found gaps or microannuli at the cement-casing interface. The gaps at the cement-casing interface were pointed out as one of the key leakage pathways (Carey et al., 2010). Permeability is considered to be an important indicator to evaluate the durability of the wellbore barrier element. Experimental studies have shown that the gas permeability of the cemented casing section with gaps could reach to 600 mD but the gap dimensions were not mentioned in these studies (Rusch et al., 2004). Bachu and Bennion (2009) indicated that the presence of an annular gap and/or cracks in an order of 10–300 μm in aperture leads to a significant increase in effective permeability in a range of 0.1–1 mD.

Apart from the larger gaps, smaller gaps that do not change short-term permeability may still bring long-term risk, which is critical in abandonment applications. Smaller gaps act as the starting points for a chemical attack by corrosive fluids or gases, which rises the risk of the gap growing into one that impacts wellbore permeability and integrity. This process is likely to be slow but considering the timescale of abandonment wells, so the impact of the small gaps on well integrity should not be neglected. Torsæter et al. (2015) suggested that the gaps shown in SEM images were likely to be caused by the cement shrinkage. The cement shrinkage can be divided into two major categories: a chemical shrinkage, which results from autogenous chemical reactions taking place in the cement matrix, and a drying shrinkage, which is sensitive to the RH change (Gajewicz et al., 2016a). In Torsæters' research, although the cement shrinkage was suspected to be the main reason for the discontinuities shown in SEM images, no experimental evidence has been reported to confirm this assumption. Furthermore, which shrinkage type is mainly responsible for the discontinuities in SEM images is still unclear.

In addition, the influence of the sample preparation on the bonding characterization remains unclear. Lavrov et al. (2017) investigated the particle size distribution in the ITZ using micro-CT with synchrotron radiation, which significantly increased the resolution of the CT image. However, the cement was placed in a glass tube rather than a steel casing. This may affect microstructure in the ITZ because casing has different electrical properties than glass, and the electric field affects the particle size distribution near the wall (Lavrov, 2018). Besides, the debonding, which normally occurs at the cement-casing interface (Lavrov et al., 2016), may not be captured at the interface between the cement and the glass tube. In short, very little is currently known about the microstructure of the cement-casing interface in relation to debonding phenomena (gaps at the interface).

2.1.3 Leakage through cement-rock interface

Compared to the casing properties, rock properties at the cement-rock interface vary greatly as a well is normally drilled through several different formations. Therefore, as far as the interface properties are considered, the cement-rock interface seems more prone to have leakage than the cement-casing interface. A notable example has been observed in a well after 30 years of CO_2-flooding operation, where textural studies on the cores revealed that the cement-rock interface degraded much more than the cement-casing interface and there was a high porosity zone at the cement-rock interface (Carey et al. 2007).

Many previous cement-rock interface studies have been related to the CCS wells, where the main focus was to understand the influence of chemical reaction at the cement-rock interface (Carey et al., 2007; Agbasimalo and Radonjic, 2012; Jung et al., 2013; Newell and Carey, 2013; Jung et al., 2014; Labus and Wertz, 2017). It was noteworthy to point out that the cross-sectional geometry of the cement-rock interface of the samples used in these studies had either a flat surface or some other irregular shapes but did not have a realistic circular shape.

SINTEF did lots of work regarding the effect of drilling fluid properties (Opedal et al., 2014), cement defect (Kjøller et al., 2016), interface geometry (Torsæter et al., 2015) and cement stiffness (Lavrov, 2018) on cement-rock interface integrity. In the majority of these studies, micro-CT scanning technique was used to non-destructively characterize the cement-rock interface. Due to the large sample sizes used in these studies, the resolution of micro-CT was limited to 24-200 μm. Considering the multiscale nature of the cement and pore size of the rock, scanning electron microscope was used together with micro-CT as SEM can characterize the cement microstructure at the nanoscale. However, traditional SEM characterization can cause cement shrinkage and thus degrade the quality of characterization results.

So far, very little attention has been paid to the role of formation rock properties on the cement-rock interface integrity. One very good recent work by Opedal et al., (2014) had a short discussion of rock types on the cement-rock interface integrity where they qualitatively concluded that the different rock formations exhibited different interactions with the cement. But they did not offer much discussion about what actual mechanisms were behind their conclusions. To answer this question, more in-depth quantitative studies are needed. The cement used in their study was neat Portland cement, which has been commonly employed in previous cement-rock studies such as Agbasimalo and Radonjic, (2012); Opedal et al., (2014); Labus and Wertz, (2017). However, the neat Portland cement without additives is normally not stable and therefore has not been used in real wellbores. Cement blends that have been applied in real wellbores should be considered in the cement-rock interface study as it is more relevant to the industrial practice.

2.2 Microstructure characterization techniques for cement, rock and interfaces

Micro-CT scanner and SEM are two common tools for materials microstructure characterization. There is a considerable amount of literature involved in using these two techniques. In the following sections, a detailed review of the applications of these two techniques on the wellbore cement microstructure characterization was presented.

2.2.1 Micro-computed tomography (μ-CT)

Micro computed tomography or "micro-CT" has been widely used for cement research due to its non-destructive characteristic. Moreover, it is possibly the only way to obtain 3D material internal structure information efficiently. The micro-CT was initially used as a standalone characterization tool to investigate the internal structure of the cement such as the cement particle shapes (Bentz, 2006; Garboczi and Bullard, 2004; Helfen et al., 2005) and the pore network (Bossa et al., 2015; Gallucci et al., 2007; Promentilla et al., 2009). The statistical and morphological analyses using the computed tomography provides a new view of the cement microstructure because it gives a realistic 3D geometry.

Kjøller et al. (2016) looked into the self-healing procedure of a composite cement-rock specimen subjected to a water-alternating-gas (WAG) flooding scheme by using the computed tomography combined with the electron microscopy. Comparison of SEM and EDX (energy dispersive X-ray spectroscopy) data before/after flooding shows that, with an increasing number of WAG cycles, the porosity of the cement plug decreased. Kjøller et al., (2016) also proposed an integrated method to evaluate the permeability of cement-caprock systems by combining the computed tomography with finite element modeling. The imperfect bonding and defect zones in the cement was characterized and meshed successfully; thus, the FEM simulation can be performed to quantify the leakage through defect cement.

De Andrade et al. (2014) investigated the influence of casing centralization on cement sheath integrity during thermal cycling by CT scanning and found that the thermal cycling caused considerable enlargement of cracks and voids initially present in the cement sheath, and this enlargement was significantly more severe when the casing was not centralized. Then, based on previous research, De Andrade et al. (2015) improved the experimental equipment and took the pressure into further consideration. Based on the 3D models reconstructed from the CT images, he indicated that bonding between cement-to-casing and cement-to-rock have especially been enhanced by the hydrostatic pressure. Skorpa and Vrålstad, (2018) imported microannuli of degraded cement sheaths, captured by the micro-CT, into a CFD software that calculates and visualizes the pressure-driven fluid flow, and results show a non-linear relationship between the mass flow and the pressure drop, indicating that Darcy's law might not be sufficient to describe the effective permeability of the degraded cement sheath.

Torsæter et al. (2015) investigated the effect of different geometry (concave vs. convex) of the interface on the development and structure of the ITZ, and on fracture development in it. SEM and CT scan were conducted to visualize the impact of the ITZ on well cement integrity. It was found that fracturing and debonding of cement in the ITZ can occur and that the exact failure mode depends on the curvature of the interface. Opedal et al. (2014) characterized the cement-formation interfaces of specimens with various rock formation types and drilling fluid types by using micro-CT. The result pointed out that both rock type and mud type affect the development of porosity at the cement-formation interface, but no conclusive trends could be drawn on the actual processes giving rise to the porosity variations.

2.2.2 Traditional and environmental scanning electron microscopy (SEM/ESEM)

The resolution of the CT scan is significantly influenced by the sample size. Because of the multiscale characteristics of the cement microstructure, some small pores and fractures can not be captured by the micro-CT since their size is beyond the resolution of micro-CT. Although small gaps may have a limited impact on the short-term permeability, they may function as the starting point of chemical attack and thus jeopardize the long-term wellbore integrity. In order to capture these small gaps and have a closer look at the cement-casing interface, a higher resolution characterization tool is thus needed.

The SEM technique has been used for analyzing 2D fractures in the cement paste by Attiogbe and Darwin (1987), Ammouche et al., (2000), Wong et al., (2012) and other researchers. The geometrical fracture parameters (i.e., length, width, and shape factor) are usually measured at a certain magnification. However, the results of the fracture measurements can significantly vary depending on the magnification used during the observations, mainly because of the heterogeneous and multiscale characteristics of the cement paste microstructure.

Previous research (Bisschop and van Mier, 2002; Neubauer et al., 1997) has indicated that the traditional SEM coating and characterization can cause cement drying shrinkage because both processes take place in a high vacuum chamber whose RH is pretty low. To minimize the cement drying shrinkage, an ESEM would probably be a more appropriate technique to use as the ESEM is able to image the hydrated cement interface samples at the controlled RH conditions (Kjellsen and Jennings, 1996; Neubauer et al., 1997).

2.3 CT-based CFD simulation to evaluate potential leakage pathway

2.3.1 Digital cement method

Since the digital cement was a relatively new methodology, and there is only a small number of published research work using the digital cement technique. Yang et al. (2019) called the 3D models reconstructed from cement CT images as digital cement models. They proposed that "digital" not only means that the cement microstructure can be presented and analyzed numerically using a computer but also suggested that the porous media parameters like pore volume, surface area, porosity, permeability, etc. can be easily calculated from the digital cement models.

Yang et al. (2020) quantified the impact of 2D and 3D fractures on permeability in wellbore cement after uniaxial compressive loading using the digital cement method. By using the digital cement method, geometrical parameters such as fracture length, fracture width, and shape factor of 3D fractures in a cement matrix were quantified.

Vrålstad and Skorpa, (2020) developed an experimental methodology that uses X-ray computed tomography to obtain 3D visualizations of cracks and microannuli in annular cement sheaths. They have demonstrated the value of using such digital cement methods to study well cement and also shown that the digital cement method provided an improved understanding of cement sheath integrity. For example, it was seen that radial cracks did not form in symmetrical patterns and that microannuli did not have uniform geometries. Such experimental findings can potentially be used as a benchmark to validate and improve cement integrity simulation tools.

2.3.2 Permeability estimation using CT-based simulation

The determination of the cement permeability through experiments is time-consuming and not cost-effective (Faiz, 2014). For analytical methods, the governing equation that controls the fluid flow is non-linear and difficult to solve. Assumptions and simplification can be applied to make analytical problems easier to solve, even though the simplification introduces errors. In most cases, however, even the simplified equations cannot be solved analytically (Ferziger and Perić, 2002). To overcome these challenges, there is a need to develop a new method to make the prediction of cement permeability easier and more efficient. Once the power of computers had been recognized, interest in numerical approaches increased dramatically.

Only a few recent research efforts combined numerical approach with the CT-based 3D geometry. Kjøller et al. (2016) evaluated the permeability of defect cement zones by combining micro-CT imaging and numerical modeling. Kabilan et al. (2016) combined micro-CT imaging with CFD modeling to study the effect of geochemical and geomechanical processes on fracture permeability in composite Portland cement-basalt caprock core samples. The geometry used in both research is cement with defect zones or fractures. Apparently, the flow in such a geometry is dominated by the defect zones rather than the capillary pores. Moreover, due to the large dimensions of the cement sample they prepared, the precision of the CT scan was limited to 10-25 µm. However, the bulk of the capillary pores cannot be characterized at this resolution. No information is available on the fluid flow in the neat cement samples considering the realistic 3D geometry without defect zones or stress-induced fractures. Higher precision of the CT scan, which can capture more details of the capillary pores is also needed.

The element-based finite volume method was proven to have high efficiency to handle the flow simulations with complex geometry (Marcondes et al., 2013a, 2013b) and has been widely used in realistic porous media simulations (Dixit and Ghosh, 2018; Song et al., 2017; Wang and Dai, 2017). It is also worth noting that at the micron scale, the microstructure of the cement may still behave as heterogeneous material (Bossa et al., 2015; Viejo et al., 2016). The local permeability may change at different positions. In order to obtain the representative permeability value of the cement, representative volume elements (RVEs) need to be built. The RVE is the smallest volume over which a measurement or simulation can be carried out to produce a result that is representative of the macroscopic property (Yio et al., 2017). Although a RVE has been commonly used in micromechanics to analyze and predict the mechanical behavior of the cement (Das et al., 2016; Viejo et al., 2016), its application to flow study (at this scale) has not been covered before.

2.4 Impact of additives on cement integrity

Bonett and Pafitis (1996) explained the multi-mechanisms for gas migration and also pointed out that compared to other treatments, which normally have some limitations, special blends and additives showed effective in resisting gas migration. Iremonger et al. (2015) identified a fiber additive that can improve the cement tensile strength under SAGD conditions. Cheung and Myrick (1983) summarized 84 cement jobs performed in Texas, Oklahoma, New Mexico and Louisiana. Their results showed that the "impermeable cement" system has been extremely successful in controlling gas flow problems.

Murtaza et al. (2013) tested the performance of certain class G cement formulations and reported that with the use of silica flour, the porosity and permeability of the cement are decreased. Coker et al. (1992) demonstrated that the lightweight lead cements plays an important role in preventing shallow gas migration in offshore wells. The high fineness amorphous silica was used as a key ingredient in the cement design. Zeng et al. (2012) developed the salt-tolerant latex L additive, which exhibited good anti-migration performance. Cowan and Eoff (1993) discussed the use of surface-active agents (surfactants) to modify the properties of Portland cements for well cementing operations. They concluded that the surfactants can improve the interfacial bonding between cement and casing. Abbas et al. (2013) reported that hydroxypropylmethylcellulose (HPMC) polymer could be effectively used as a gas migration preventer at high temperature in field applications.

Chapter 3 Experimental Programs

3.1 Cement sample preparation

3.1.1 Hardened cement paste

The materials and procedures used for mixing, molding and curing for preparation of hardened cement paste samples are explained in the following sections.

3.1.1.1 Cement material

Various cement blends have been used in this study. Two examples are shown in Figure 3-1. Neat Class G cement is widely used throughout the entire work to expedite the repeatability and the validation of the experimental results and to serve as a baseline for performance. Special cement blends such as the one used in thermal wells (i.e., thermal cement blends) and in abandonment operations (i.e., abandonment blends) were also investigated.

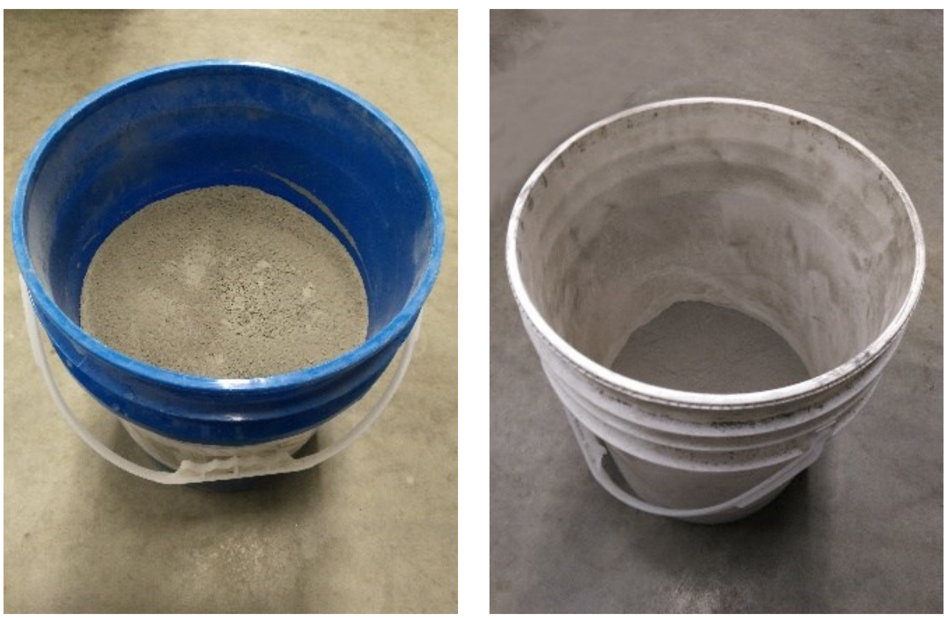

(a) Class G cement　　　(b) Thermal cement

Figure 3-1 Neat Class G blend and thermal blend.

3.1.1.2 Cement mixing procedure

Mixing is the first step for cement sample preparation. Tap water was used at a water-cement (w/c) ratio of 0.45. According to the API 10A (American Petroleum Institute, 2002), the mixer should be turned on and maintained at 4000 rpm while the cement sample is added at a uniform rate in no more than 15 seconds. After all of the cement was added to the mix water, we put a lid on the mixing container and continued mixing using 12000 rpm for 35 seconds, followed by 30 minutes mixing at 150 rpm.

A combination of two mixers was used for cement mixing. At the beginning, a handheld high rpm mixer (shown in Figure 3-2a), which can work at 12000 rpm was used after all of the cement has been added to the water. Then, a low rpm mixer (shown in Figure 3-2b) was adjusted to 150 rpm to mix the slurry for 30 minutes.

(a) handheld high rpm mixer

(b) low rpm mixer

Figure 3-2 Two mixers used for cement mixing.

The mixing speed and the time should be strictly controlled to minimize the intrusion of air, especially for the high rpm mixing.

3.1.1.3 Preparation of cement mold and cement curing procedure

The mixed cement slurry was then injected into the cement molds. High-temperature PTFE (Teflon) pipe was selected to make the molds. Reasons for selection of PTFE material are given below:

- Compared to metal materials, PTFE pipe has a lower density and thus makes it easy for X-ray to penetrate. Besides, metal materials normally have a higher density than cement. Most of the microstructure data will be lost if we use a metal mold. Moreover, because of the bonding between metal and cement, it is difficult to take the cement out of the metal molds. The PTFE pipe has a lower density than the cement. In addition, some specially made PTFE pipes have a super-smooth interior surface. Using this specially made PTFE pipe, the molds can be easily separated from the cement.
- After finishing the molding process, the cement samples together with the molds were inserted into a pressure cell and then cured under elevated pressure and temperature. The curing pressure and temperature were about 1500 psi and 50 °C, respectively. The curing condition required that the molds should be able to withstand such pressure and temperature. The high-temperature PTFE pipe has a temperature range of -450 °F (-267 °C) to 550 °F (287 °C) and can withstand a pressure of 3500 psi.

Apart from the PTFE pipe, Teflon film, which has a slippery surface that prevents sticking and allows objects to slide across it easily, was used to seal the mold. Depending on the size of the mold, no-hap curved-head cable ties, and some plastic containers were also used to seal the mold.

Figure 3-3 High-temperature PTFE (Teflon) pipe, Teflon film, no-gap cable ties.

Two different size molds were used. Reasons for selecting these two size molds are listed below:

- All cement samples are placed into the micro-CT scanner to determine the 3D cement microstructure. The mold is placed into the CT scanner together with the cement samples in place. However, every micro-CT scanner has its limitation with the object size. This restriction called maximum object size. For the micro-CT scanner used in this research (SkyScan 1172, see more details in Section 3.2.1), the maximum object size was 27 mm in diameter. In this way, so the diameter of the mold could not exceed 27 mm.
- If the cement contains some large particles, such as fibers, according to ASTM C 31, the sample size must be three times bigger than that of the maximum aggregate size. If we call the fibers aggregate and use the 3mm fiber, then the minimum sample size is 9 mm. For a better result, five times is more preferred so that the minimum sample size will be 15mm. Thus, from the above reason, the diameter of the mold should be between 15 mm and 27 mm.
- The mold size should be as small as possible if there are no fibers in the cement. This is because the precision of the CT scan is limited to the sample size. The smaller sample will get images with higher accuracy.

According to the standard pipe information chart, 3/4 in and 1/8 in size pipes were used to make the molds. By using the cutting machine, 3/4 in size pipe was cut into small pieces of 20 mm length, and 1/8 in size pipe was cut into small pieces of 5 mm length. The two different size molds are shown in Figure 3-4.

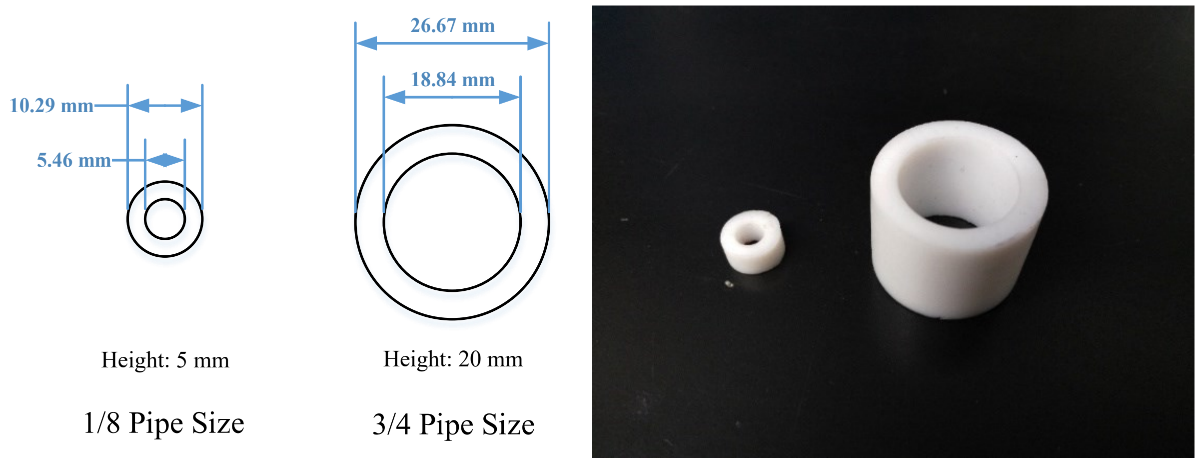

Figure 3-4 1/8 inch pipe size mold and 3/4 inch pipe size mold.

The first step of molding is to seal the one end of the mold. For 3/4 inch pipe size mold, the bottom of the mold was wrapped with a piece of plastic film and then placed into the bigger plastic container. The reason for using the bigger plastic container is to obtain a smooth top surface of the cement samples. The cement will shrink during the curing process, and this makes the top surface uneven. If using the bigger plastic container, it is recommended to pour a little bit more slurry than the pipe mold can hold.

Then, the cement slurry is injected into the mold. Depending on the mold size, different tools can be used for injecting the slurry such as syringe, injector or even pastry bag with nozzles. The cement slurry should be well mixed again by hand before injecting them into the mold. Also, it is better to shake the syringe or injector before the injection. Before sealing the other end of the molds, a small tamping rod was used to tamp the slurry to remove the bubbles inside the slurry as much as possible. The last step of the molding is to use the cable tie to seal the other end of the mold.

In order to accelerate the cement curing, in this study, most of the samples were cured the cement samples at 50 °C and 1500 psi. The apparatus used for curing is shown in Figure 3-5.

Figure 3-5 Equipment used for curing cement samples.

A steel pressure cell (Figure 3-6) placed in an oven was used to hold the cement samples. A water pump was connected to this pressure cell to provide constant pressure. Pressure can be set at the water pump, and the temperature was controlled by the oven.

To keep the cement samples in stable position, the pressure cell was placed vertically, and all the cement samples were also placed vertically. The layout of the cement samples in the pressure cell is shown in schematic drawing (Figure 3-6). The maximum number of 3/4 inch pipe size samples was three, and the rest of the space was used by placing 4 samples of 1/8 inch diameter.

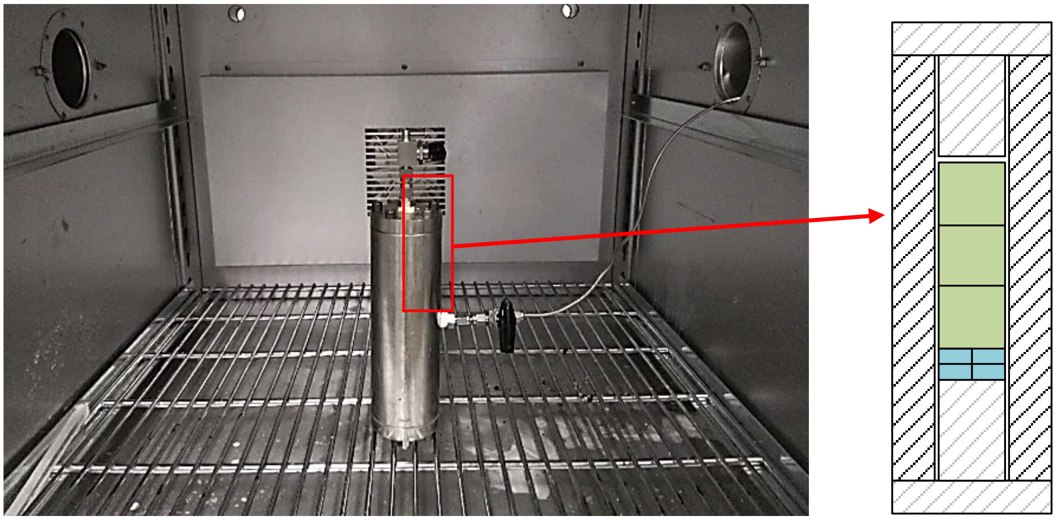

Figure 3-6 Positions of the pressure cell inside the oven and cement samples inside the pressure cell.

The following procedure was used for curing the cement samples: i-) Open the both top valve and middle valve of the pressure cell; ii-) Start injecting water into the pressure cell through the middle valve at a low pump pressure; iii-) When the water leaks from the top valve (which means no air in the cell), close the top valve and gradually increase the pump pressure to 1500 psi; iv-) Keep the cell pressure at 1500 psi and record the pressure change every 24 hours; v-) Turn on the oven and initially set the temperature at 50 °C; vi-) Attach a thermometer inside the pressure cell to check the temperature and make sure the temperature inside the oven is set to 50 °C; and vii-) Gradually increase the temperature if it is lower than 50 °C.

The duration of the cement curing is seven days. There was no water added during the curing process, and the cement cured only with the initial water content. Cement samples should be well sealed and stored after they are taken out of the oven. The cement samples can be wrapped by a plastic film or stored in a sealed plastic bag (Figure 3-7) to prevent the water loss of cement and isolate the cement samples from the contacting with air.

Figure 3-7 Samples stored in sealed plastic bags.

3.1.2 Cement-casing interface samples

The preparation of cement interface samples is very similar to the hardened cement samples. The key in the preparation of cement interface samples is to collect suitable casing or rock materials and process them into suitable dimensions.

When selecting the appropriate metal tubes to simulate the casing, the surface roughness of selected material should be similar to one of the commonly used casings, such as J55, K55 and N80, suggested by the API Casing Steel Grades. In this study, the 304 stainless steel pipe (9 mm OD, 8.6 mm ID) was used as the casing material. The 304 stainless steel is used as raw material to make casing and tubing according to the dimensions required by API 5 CT. Because of the dimensions of the casings employed in this study had to be small enough so that they can be scanned by the micro-CT, the actual field grade casings (e.g. N-80, P110, etc.) therefore were didn't used. Once obtaining the suitable material, the next step is to process them into suitable dimensions. Since the prepared cement-casing samples will be scanned at a high resolution, only a few millimeters of the pipe was need. To avoid the damage and deformation of the 304 pipe, it is better to cut them using wire cut technique. As shown in Figure 3-8, the 304 pipe was cut into short sections of 4 mm length.

Figure 3-8 Short sections of the 304 stainless steel pipe.

The procedure for preparation of cement slurry has been explained in Section 3.1.1. The cement slurry was injected into the casing and then sealed using no-gap cable ties and Teflon film as shown in Figure 3-9. After curing, the cement-casing samples should have a flat bottom surface. The top surface will shrink a little bit and, therefore, will not be even.

Figure 3-9 Cement-casing sample after curing and after removing the sealing materials.

The samples shown in Figure 3-9 can be directly scanned by micro-CT. However, its surface is not smooth enough for SEM scan. Therefore, the individual cement-casing samples were further polished and processed into thin composite sections. Figure 3-10 summarizes the entire process. The individual cement-casing samples were placed in a container. Epoxy was injected into the container after vacuuming the container. Once the epoxy is solidified, remove the container and polish the thin composite section to a shorter thickness. Figure 3-9e shows the processed composite.

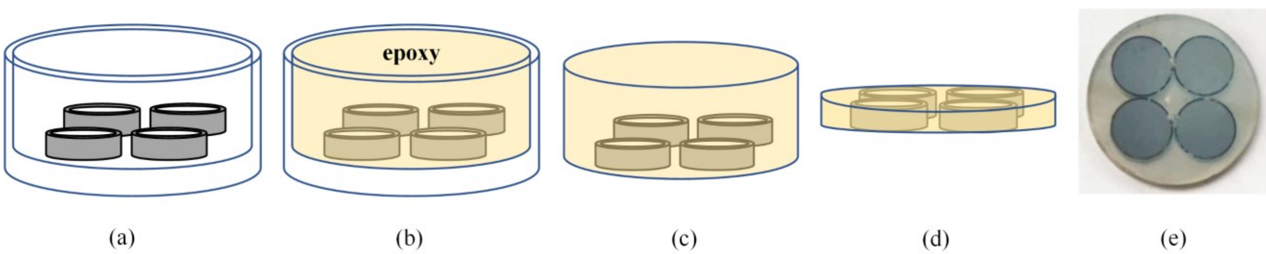

Figure 3-10 Schematic diagram of the preparation of cement-casing interface samples.

3.1.3 Cement-rock interface samples

The preparation of cement-rock interface samples follows a similar process to prepare cement-casing samples. The rocks were collected from the AER Core Research Center in Calgary. Partial sections were cut from the rock cores (Figure 3-11).

(a) (b)

Figure 3-11 Formation rock cores and partial sections.

Rock samples from six different Alberta formations were collected. The lithology of the collected rock samples was further confirmed by photomicrographs. Core analysis results such as porosity and permeability of the rock cores are also available from AccuMap software. Table 3-1 summarized the details of the collected rocks.

Table 3-1 Details of the collected rocks.

Rock	Well ID	Lithology	Depth /m	Porosity /%	Permeability /mD
PEKISKO	02/16-03-044-10W5/0	limestone	2868.41 - 2868.45	0.9	0.01
BANFF	02/16-03-044-10W5/0	dolostone	2951.14 - 2951.32	7.2	1.73
NOTIKEWIN	00/02-22-063-06W6/0	siltstone	2596.43 - 2596.62	4.0	0.07
DOIG	00/05-25-063-04W6/0	sandstone	2882.31 - 2882.49	1.1	-
MONTNEY	00/04-04-062-03W6/0	siltstone	3277.18 - 3277.34	4.2	0.01
WILRICH	00/08-07-062-03W6/0	siltstone	2874.35 - 2874.51	3.5	-

The partial rock sections shown in Figure 3-11b were further processed into hollow rock cylinders by using a drill press and a polishing machine (Figure 3-12). The processed hollow rock cylinders have an outside diameter of 21 mm, an inside diameter (hole size) of 9 mm. To save the usage of rock samples, the hollow rock cylinders were cut into halves. Therefore, the height of the hollow rock cylinders is about 10 mm. Examples of the prepared hollow rock cores are shown in Figure 3-13.

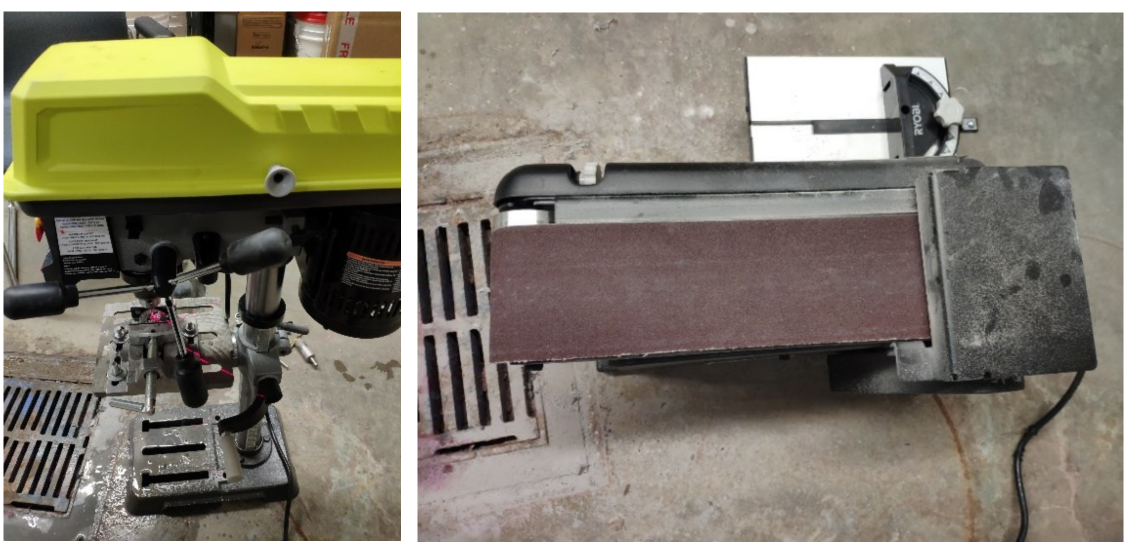

Figure 3-12 Drill press and a polishing machine used for rock sample preparation.

Figure 3-13 Examples of the hollow rock core samples.

To prepare the cement-rock interface samples, cement slurry was injected into the hollow rock cylinders. The sealing method of the cement-rock samples is different from the one used in cement-casing sample preparation. Instead of using Teflon film, the electrical tape was used to seal both the top and bottom surface of the cement-rock samples (Figure 3-14). After curing, the cement-rock samples should be stored in a small plastic bag to prevent water loss.

Figure 3-14 Prepared cement-rock samples.

Samples shown in Figure 3-14 can be directly scanned by micro-CT after curing. However, for SEM characterization, the cement-rock samples need to be further processed. This process is very similar to the one shown in Figure 3-10. The main difference is that, as shown in Figure 3-15, the cement-rock sample is much bigger than the cement-casing samples and therefore there is only one cement-rock sample in the thin section.

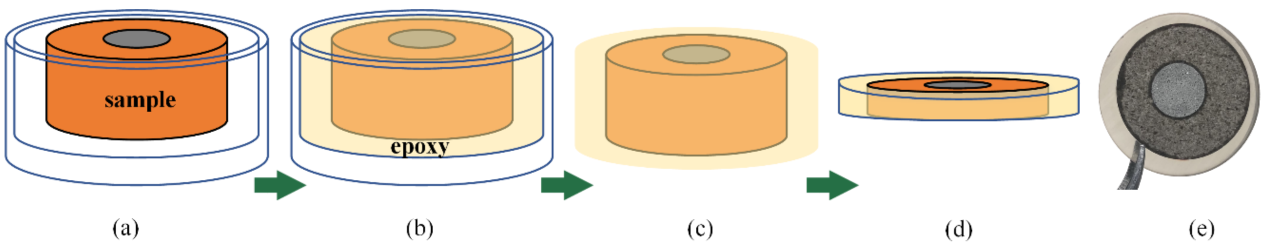

Figure 3-15 Schematic diagram of the preparation of cement-rock interface samples.

3.2 Microstructure characterization techniques for cement, rock and interfaces

Micro-CT and SEM were the two main techniques used for the cement microstructure characterization. Details of the implementation of these two techniques are described in the following sections.

3.2.1 Micro-CT scanner measurements

A SkyScan 1172 desktop X-ray micro-CT (shown in Figure 3-16) available at the Earth and Atmospheric Science Department, University of Alberta was used for the microstructure characterization throughout this work. Depending on the sample size, the resolution (pixel size) is isotropic and continuously varied from 0.9 μm to 35.0 μm. For a single run, X-ray shadow projection images were generated and then digitized into TIF images and stored in the computer. The cross-section images can be reconstructed from the projection images by using NRecon software (v1.7.4.2). Since the cross-section images are commonly used as the input for CT data processing software, therefore the term *CT images* refer to the cross-section images.

Figure 3-16 SkyScan 1172 desktop X-ray micro-CT scanner.

Cement, casing pipes, and rocks are treated as high-density materials (Bruker, 2008). In order to obtain high contrast images, high energy X-rays are thus needed. The adjustment of energy or voltage of the X-rays can be achieved by changing scan filters. The SkyScan 1172 offers three filter options: no filter, aluminum filter and copper plus aluminum filter. No filter option is rarely used in this study. The aluminum filter can be selected to scan light weight cement or bulk cement in smaller dimensions. For large cement samples and cemented casing or rock samples, copper plus aluminum filter should be selected for the CT scan. Flat field correction and alignment tests should be performed before the CT scan as these two operations would make sure that the CT images have high contrast and with less noise.

Long CT duration decreases the quality of cement CT images. Averaging frames and rotation degrees are the two main factors controlling the CT duration. Averaging frames allows improvement of the image quality by averaging the several images in every angular position. Increasing the number of frames will increase the quality but also makes the acquisition longer (Skyscan NV, 2011). Using 360 degrees rotation can reduce symmetrical artifacts from dense objects across the surrounded low absorption material. This will also almost double the scanning time. Figure 3-17 shows the difference between two CT images using different rotation degrees. The grain boundaries tend to be less clear from inside to the outside of the image obtained by using 360 rotation degrees. Images obtained by using 180 rotation degrees have relatively clear grain boundaries.

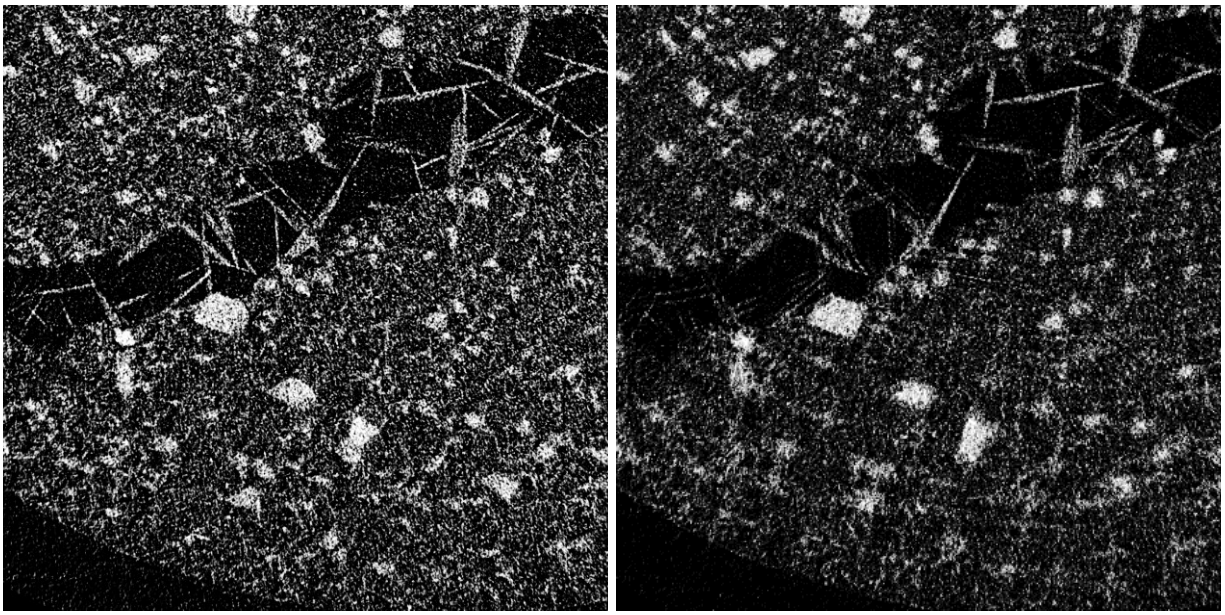

(a) 180 degrees (b) 360 degrees

Figure 3-17 CT Images of cement sample scanned by using 180 and 360 degrees of rotation.

A few reconstruction parameters have to be adjusted manually in a trial-and-error fashion to correct the beam hardening, ring artifacts, and provide alignment optimization (Skyscan NV, 2011). It requires quite some efforts to save the preview images, view them and then make a decision. A raw CT image without any correction is compared with the corrected image, as shown in Figure 3-18. After many different scan attempts, the optimum values for the scan and reconstruction parameters were found as shown in Table 3-2.

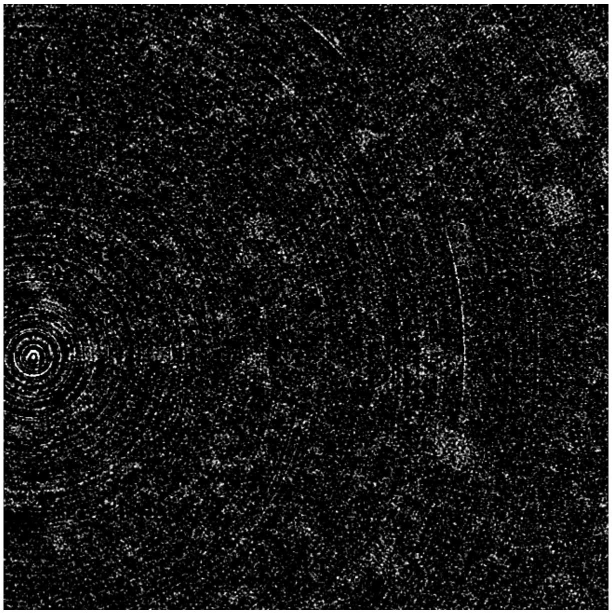

(a) Raw image

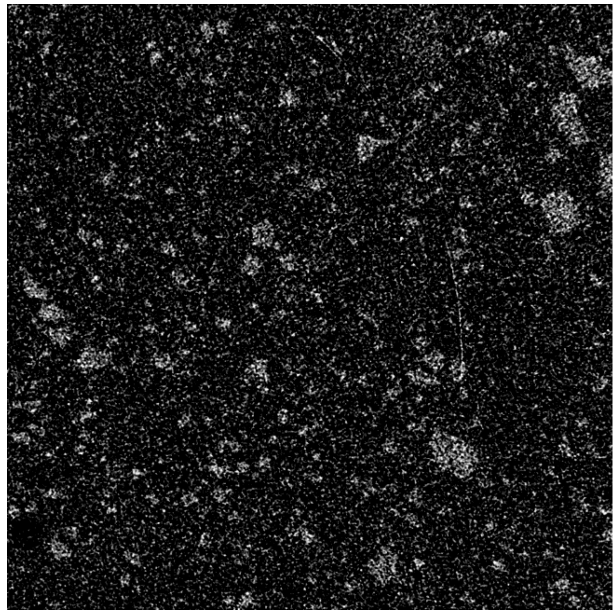

(b) Corrected image

Figure 3-18 Raw and corrected cross-section images of the cement microstructure.

Table 3-2 Optimized scan and reconstruction parameters for CT characterization.

Scan parameters	Value	Reconstruction parameters	Value
source voltage (kV) and current (uA)	100, 100	smoothing	0
scan filter	Al + Cu	ring artifact correction (%)	45
rotation step (degree)	0.3	beam hardening correction (%)	60
resolution (μm)	2.64	cross-section image depth (bits)	8
frame averaging	2	cross-section image height (pixels)	4000
random movement	1	cross-section image width (pixels)	4000
use 360 rotation	No	cross-section image format	BMP

Special attention should be paid when scanning cement interface samples. More specifically, for cement-casing samples, scanning the samples vertically can reduce the effect of beam hardening artifacts. For cement-rock samples, during the reconstruction process, the contrast of the cross section CT images should be improved as much as possible. This is because the CT images are generated based on the object density profile. If the density difference between cement and rock is small, then the contrast of the CT image will be pretty low, which makes it harder to differentiate the cement-rock interface.

3.2.2 SEM/ESEM measurements

Zeiss Sigma Field Emission SEM (shown in Figure 3-19) is available at the Earth and Atmospheric Science Department, University of Alberta. It can reach a resolution about 10 nm. This SEM is equipped with a secondary and backscattered electron detectors, and in-lens electron detector. Cement is a non-conductive material so the cement sample should be coated by carbon to make them conductive.

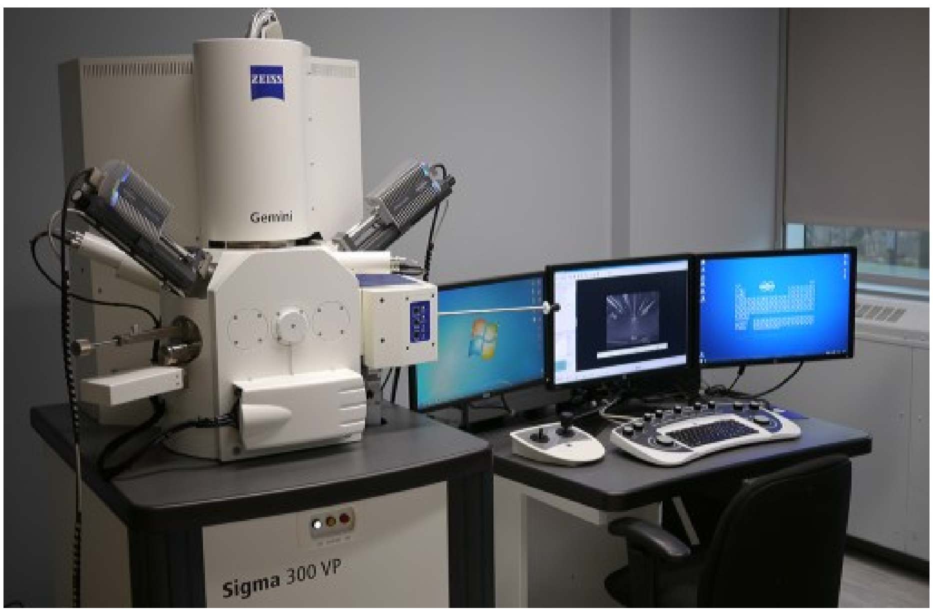

Figure 3-19 Zeiss Sigma Field Emission SEM.

Modified from (SEM Lab, 2020)

The resolution of micro-CT scan is limited by the sample size and the SEM can overcome this limitation. Figure 3-20 shows the detectable range of human's naked eye, micro-CT and SEM. Although the resolution offered by the CT scan is capable to capture the microstructural details, it is still of interesting to have a closer look at the features below 1 μm and, therefore, SEM was selected.

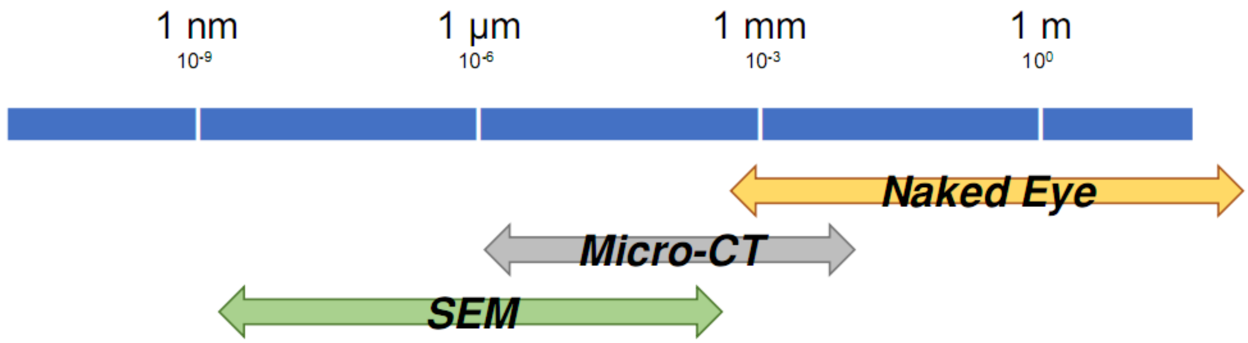

Figure 3-20 Characterization range of naked eye, micro-CT and SEM.

The SEM normally operates under high vacuum; however, most of the samples were prepared in this study need to maintain high relative humidity to prevent water loss. The high vacuum condition can significantly change the microstructure. Environmental SEM is able to characterize the samples under humid conditions. Zeiss EVO LS15 EP-SEM (as shown in Figure 3-21) located at the Earth and Atmospheric Science Department, University of Alberta is an environmental SEM.

Figure 3-21 Zeiss EVO LS15 EP-SEM (ESEM).

Modified from (SEM Lab, 2020)

The relative humidity can be adjusted by changing the pressure and temperature in the chamber. As shown in Figure 3-22, a lower temperature requires a narrower pressure range to achieve full relative humidity range (0%-100%). Therefore, when performing the ESEM scan, the temperature of the chamber is set at 10 °C. The target relative humidity can be achieved by changing the chamber pressure. High relative humidity will degrade the quality of the ESEM images because of the skirting effect. To obtain high-quality ESEM images, the maximum relative humidity should not exceed 95%.

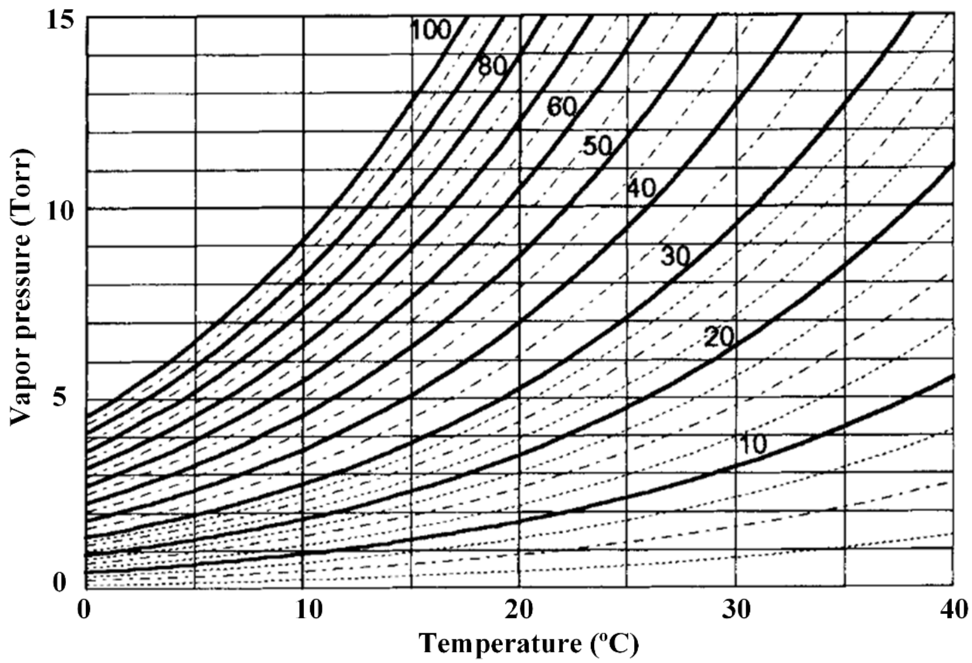

Figure 3-22 Relative humidity isobar chart (modified from Messier and Vitale, 1993).

3.3 Digital cement method

The CT images and SEM images were the main sources used for both qualitative and quantitative analyses. This section describes the method employed for the analysis work. Since all analyses were based on the cement digital images, this method was named as a digital cement method.

Figure 3-23 presents the flowchart of the digital cement method. The characterization techniques illustrated in Section 3.2 is the first step of the digital cement method. The raw CT or SEM images need to be further processed before they can be analyzed. After processing, the CT images can be immediately analyzed. Some 2D properties such as 2D length and width can be directly calculated. However, for 2D porosity calculation, threshold segmentation is needed to obtain the 2D binary images used for porosity calculation.

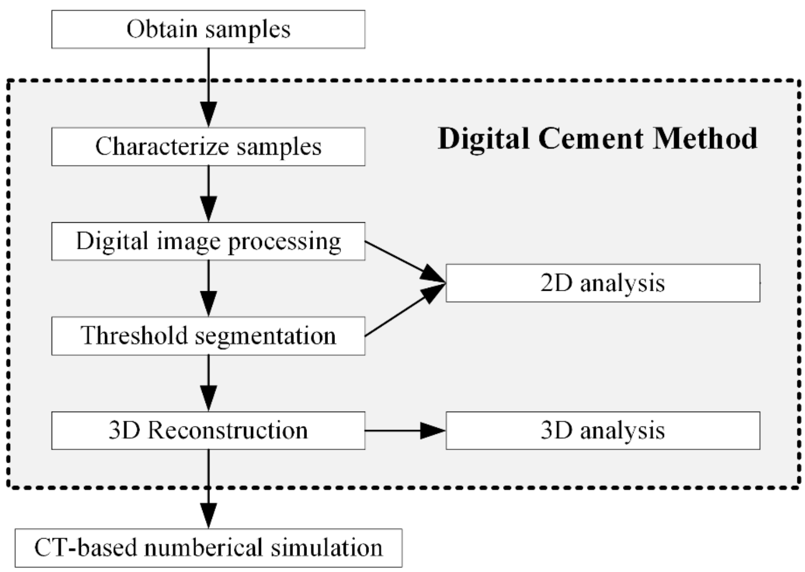

Figure 3-23 Flowchart of the digital cement method.

The 2D binary images are also the input for 3D reconstruction, which converts the 2D images into the 3D models, also called as digital cement models. The 3D analysis is performed based on the digital cement models. The digital cement model can also be used as the physical model for numerical simulation, which will be introduced in the next section.

3.3.1 Digital image processing

Several stepwise procedures need to be followed before analyzing the CT or SEM images. These procedures include (but not limited to) convert image format, crop image, and enhance image brightness and contrast. Simpleware, a commercial 3D data visualization and process software, was used to perform the image processing operations.

3.3.1.1 Convert image format

Digital images are stored in the computer in different format such as BMP, PNG, PDF or JPG, but not all of them are favorable for digital image analysis. This is because some image formats use data compression algorithm, which will save the storage space but may significantly decrease the image quality. BMP is normally used as an image format without data compression. Therefore, for both CT and SEM images, it is better to store them in BMP format.

Another important aspect of the image file is the image bit depth. Although the images are in BMP format, their bit depth might be different. The image bit depth determines how many colors that the image is able to store. Below Table 3-3 lists the common image bit depth and the total colors available.

Table 3-3 Number of colors available under different image bit depths

Image bit depth	Number of colors available
1	2
2	4
4	16
8	256
16	65536

In this work, CT and SEM images are stored in the computer as 8-bit bmp files, which contain 256 grayscale colors (see Figure 3-24). Changes in the gray value of images reflect the internal density changes of the objects. White color means the highest gray value and the object density, and indicates the cement matrix, while the black color means the lowest gray value and the object density and reveals the pore structure of the cement sample. The gray color is in between the white and the black. Because most pixels of the CT images are gray, the threshold segmentation is used to select an appropriate gray value and convert the CT images into binary images with only the black and the white colors.

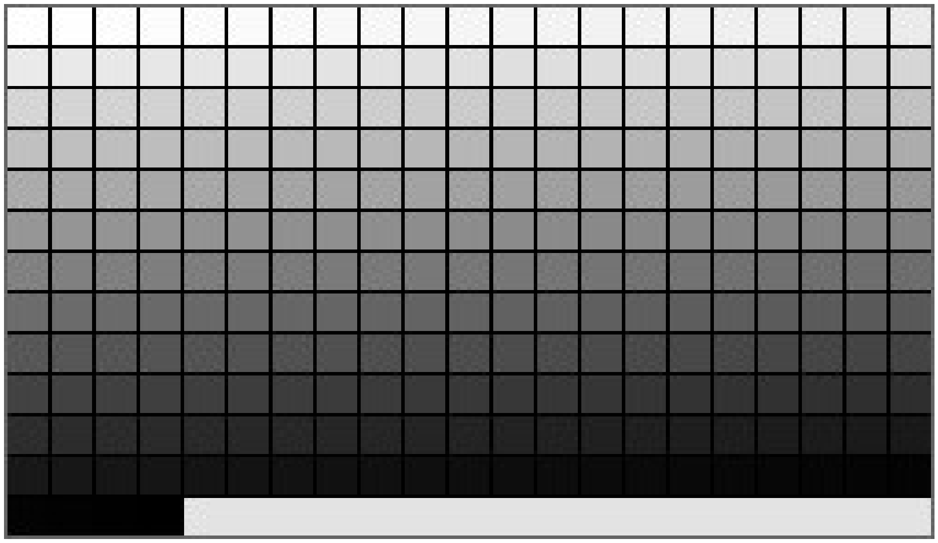

Figure 3-24 Grayscale color chart.

Apart from the 8-bit images, 1-bit images which are also known as binary images were frequently used throughout this work. The purpose of the threshold segmentation described in following section is actually to convert the 8-bit images into the 1-bit images.

3.3.1.2 Crop image

The principle for 2D porosity calculation is simply divided the pore area by the total image area. However, the region of interest might be the partial image. Therefore the crop process is needed. One example is shown in below Figure 3-25. In order to calculate the 2D porosity of the cement matrix, the background information (i.e., scales, background image) and the large cement fractures should be excluded. Partial image in white box was cropped and the 2D porosity should be performed on the cropped image.

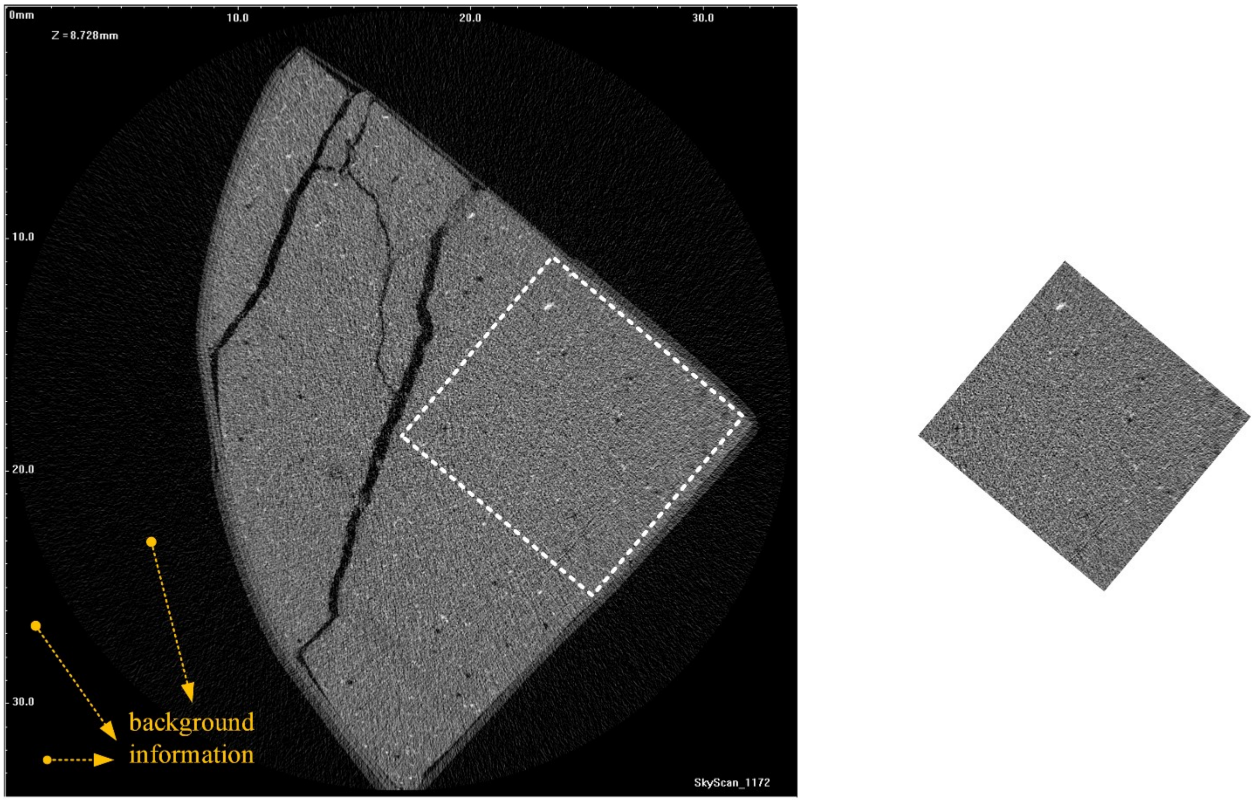

(a) original CT image (b) cropped CT image

Figure 3-25 Original and cropped CT images of a fractured cement sample.

3.3.1.3 Enhance the image brightness and contrast

The image brightness and contrast mainly depends on the material density and scan energy. For CT images, the image brightness and contrast can be adjusted while generating the cross-section CT images by the NRecon software (v1.7.4.2). For SEM images, the image brightness and contrast were configured during the scan.

Further adjustment on the image brightness and contrast can be achieved by various image processing software. Figure 3-26 shows a comparison of an original ESEM image with an enhanced ESEM image.

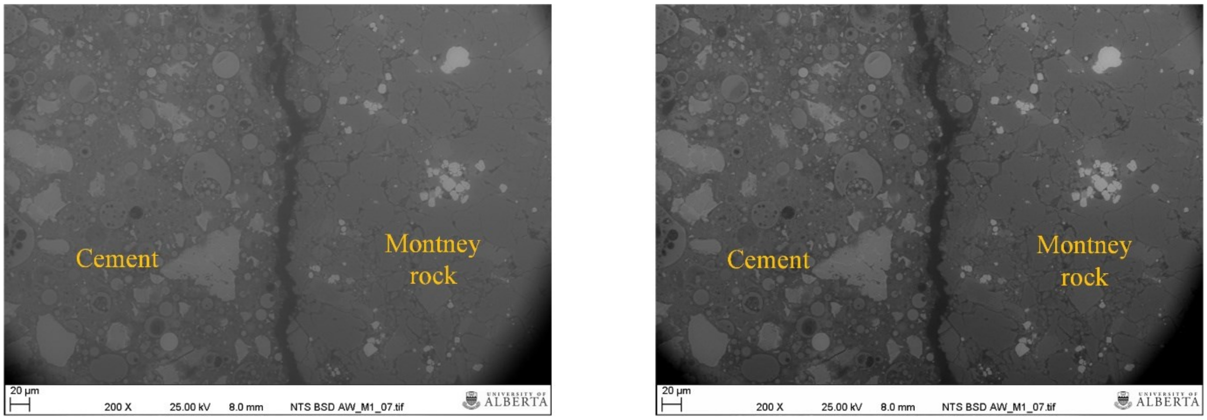

(a) original ESEM image (b) enhanced ESEM image

Figure 3-26 Original and enhanced ESEM images of a cement-rock sample.

3.3.2 Threshold segmentation and 2D porosity calculation

Gaussian deconvolution is an effective threshold segmentation method (Bossa et al., 2015; Němeček et al., 2011) and was employed in this work. Histogram of CT images is used to perform the Gaussian deconvolution. Histogram is a graph showing the number of pixels in a 2D or 3D object at each different intensity value found in that object. Since our CT images were 8 bit bmp files, the total possible intensity was also 256. In this case, the histogram graphically displayed 256 numbers showing the distribution of pixels amongst those grayscale values.

Based on the deconvolution theory (Bossa et al., 2015; Němeček et al., 2011; Sammartino et al., 2002; Vandamme and Ulm, 2009), cement image histogram can be deconvoluted by three Gauss curves, Gauss 1, Gauss 2 and Gauss 3 as shown in Figure 3-27. At a certain grayscale, the corresponding total number of voxel of three gauss curves is equal to the corresponding number of voxel of histogram and this can be written as shown in Eq. (3-1)

$$f_{histogram} = f_{Gauss\ 1} + f_{Gauss\ 2} + f_{Gauss\ 3} \tag{3-1}$$

Mineral identification by XRD and their respective calculated linear attenuation coefficient indicated that each of the gauss curves was attributed to one or multiple phases (pores and solid phases) of cement (Bossa et al., 2015). The threshold value defining the frontier between the pores and the cement material is set at the intersection between the Gauss curve associated to void and the Gauss curve associated to hydrated mineral C–S–H and portlandite. From Figure 3-27, the grayscale value of the green point is the threshold value.

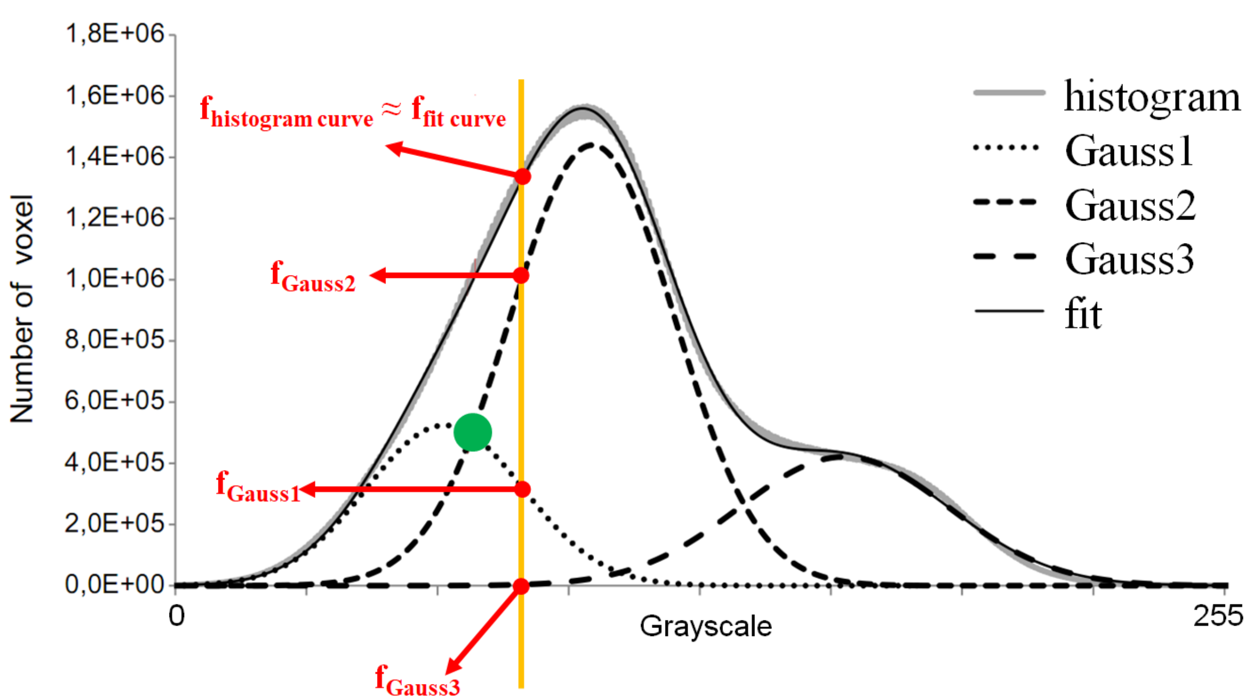

Figure 3-27 Threshold method using Gauss deconvolution.

(Modified from (Bossa et al., 2015))

The ratio between black color pixels and total pixels is the 2D porosity. As shown in Figure 3-28 different threshold leads to different 2D porosity.

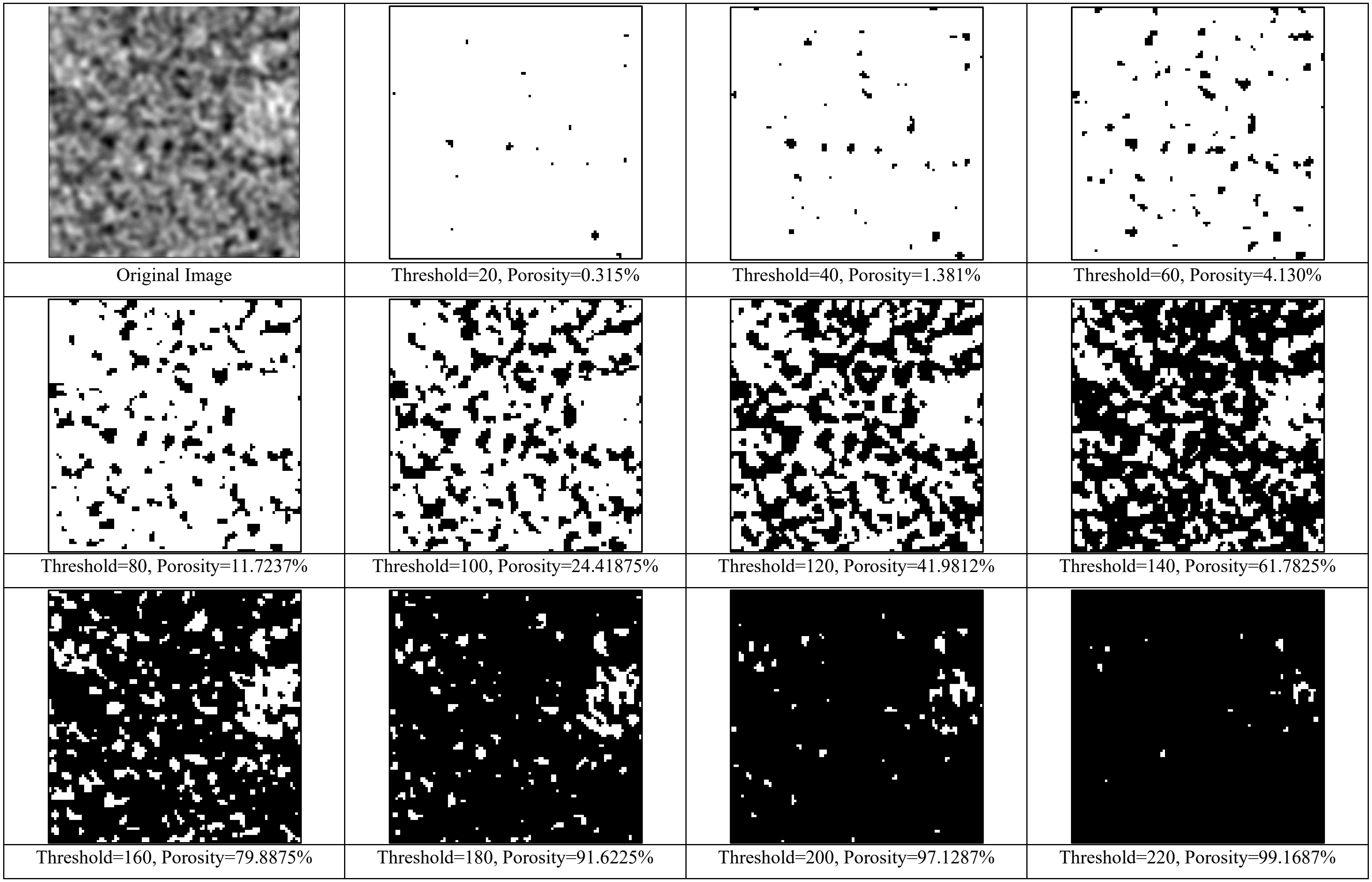

Figure 3-28 Porosity change due to different threshold value.

3.3.3 3D reconstruction and 3D porosity calculation

X-ray microcomputed tomography (micro-CT) enables the internal microstructures in cement to be visualized. More specifically, the visualization is achieved by the 3D reconstruction technique, which can transfer a series of 2D cross-section CT images into a 3D volume, and thus the 3D structure of the scanned object can be easily visualized and used for further analysis, like porosity calculation and CFD simulation.

3D Reconstruction is currently known as a mature technique, and several state-of-the-art software packages provide the 3D reconstruction function and make it easy to use. In this research, Simpleware ScanIP was used to reconstruct the 3D cement models from cross-section images. The 3D cement models generated using CT images were called as digital cement models. “Digital” not only means that the cement microstructure can be stored and shown in the computer but also indicates that the porous media parameters measured from experiments like pore volume, surface area, porosity, permeability, etc., can be easily calculated from the digital cement models.

One important advantage of digital cement models is that the connected pores can be easily tracked and the effective porosity can then be calculated. Flood fill, also called seed fill, is an algorithm that determines the area connected to a given node in a multi-dimensional dataset. Using this algorithm, connected pores will be marked in a different color and extracted from the digital cement models. In Figure 3-29, connected pores are shown in cyan color compared with all pores shown in red color.

For 3D porosity calculation, the 3D porosity is simply equal to the connected pores divided by the total volume of the digital cement model. Since the digital cement model is established based on a set of 2D cross-section CT images, the 3D porosity is approximately equal to the average value of the 2D porosities of the CT images.

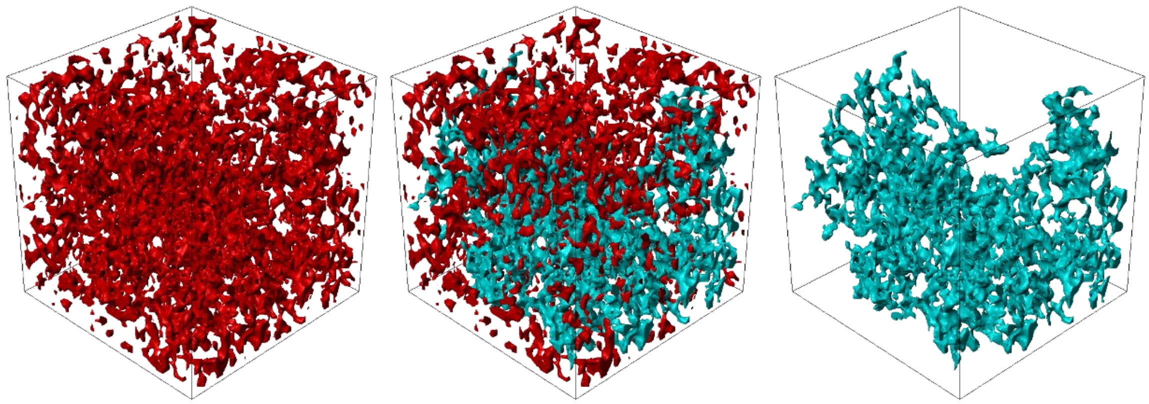

Figure 3-29 Connected pores tracked by the flood fill algorithm.

The volume rendering technique makes the digital cement model looks more real. According to the density difference, different compositions in the cement structure can be easily identified and visualized (Figure 3-30).

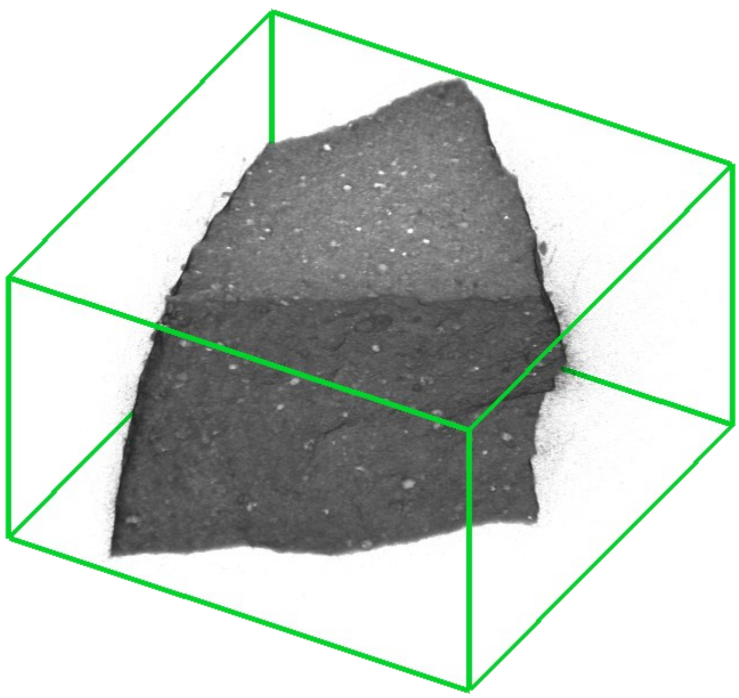

Figure 3-30 A thermal cement piece displayed using volume rendering.

3.3.4 Analyses of geometrical parameters

Table 3-4 summarizes the geometrical parameters that can be analyzed using the digital cement method. For 2D analysis, the analysis work can be either performed by commercial software such as Simpleware or open source software such as ImageJ. It is noteworthy to mention that for fracture tracking and measurement, ImageJ would be the best option. Figure 3-31 is a SEM image of a cement matrix with fractures. The fractures were labeled and measured using ImageJ.

Table 3-4 Geometrical parameters determined from 2D and 3D analysis.

2D analysis	3D analysis
area	surface area
2D length	3D length
2D width	3D width
2D porosity	3D porosity
	volume
	3D shape factor

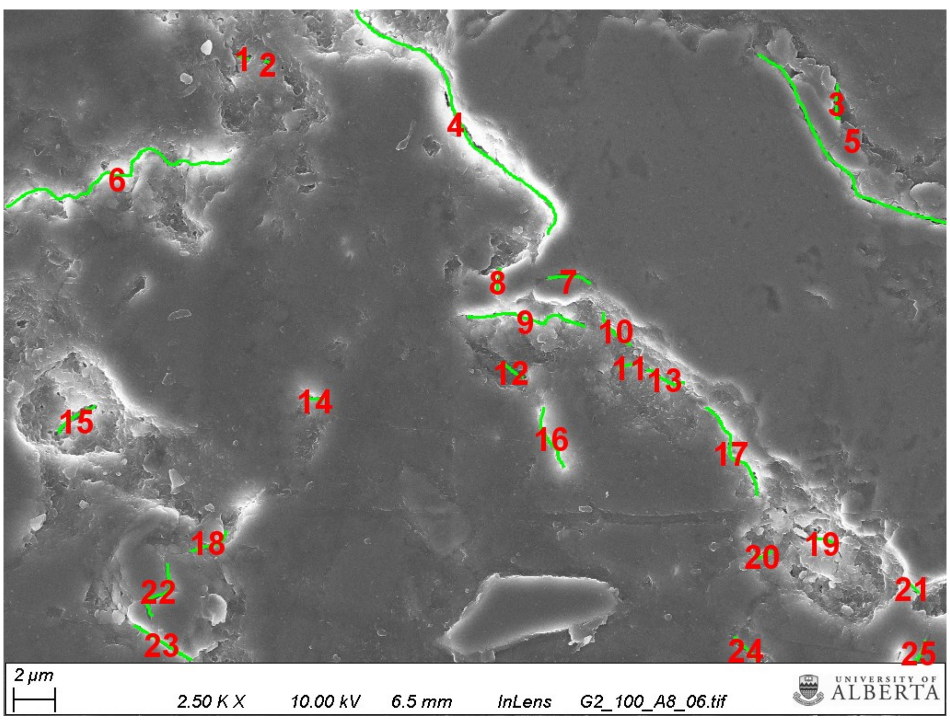

Figure 3-31 Cement fractures in SEM image were labelled by ImageJ.

For 3D analysis, many embedded functions are available in commercial software to calculate the geometrical parameters. The 3D objects are commonly in irregular shapes. Therefore, the 3D dimensions such as length and width are obtained by measuring the Feret diameters of the 3D object (see Figure 3-32). The Feret diameter is a measure of an object size along a specified direction. In general, it can be defined as the distance between the two parallel planes restricting the object perpendicular to that direction. The maximum Feret diameter was defined as the length of the 3D object whereas the minimum value was defined as the width of the 3D object. So, the length is the largest dimension and the width is the smallest dimension (Ruzyla, 1986).

Figure 3-32 Example of Feret diameter measurement.

The 3D shape factor is a dimensionless parameter that describes the shape of the 3D object. Its calculation can be varied and this thesis adopted the calculation shown in the Eq. (3-2).

$$3D\ shape\ factor = \frac{surface\ area^3}{36 \times \pi \times volume^2} \tag{3-2}$$

3.4 CT-based numerical simulation using ANSYS CFX

3.4.1 Principles of absolute permeability determination by using CFD simulation

Permeability is a measure of the ability of a porous material to allow fluids to flow through it. Absolute permeability is an intrinsic property of the material. It is a function of the material structure only. Once the material microstructure details were obtained and displayed in the computer by CT scan and 3D reconstruction technique, then the absolute permeability could be calculated by using the FEM simulation of the digital cement models. A flow chart summarizing the step by step permeability calculations is shown in Figure 3-33.

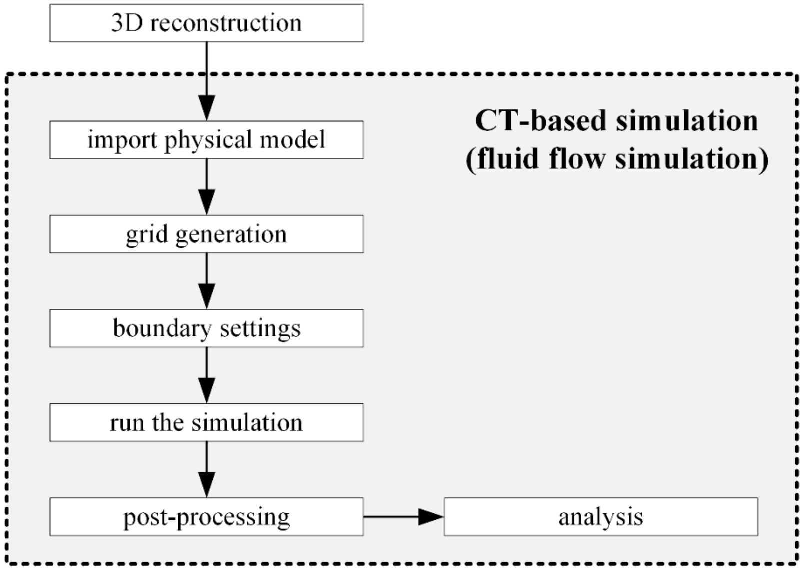

Figure 3-33 Flow chart of permeability calculation using a digital cement model and FEM analysis.

Absolute permeability is usually measured by the steady-state flow through the porous media method. This has been the industry standard for many years because it is a convenient technique and the equipment is easy to operate. Permeability can then be calculated by using the integrated form of Darcy's law for a compressible fluid, as shown by Eq. (3-3) (Yang et al., 2019):

$$k_a = \frac{2000 p_a \mu q_a L}{(p_1^2 - p_2^2) A} \tag{3-3}$$

k_a = Air permeability, mD

p_a = Atmospheric pressure, atm

p_1 = Upstream pressure, atm

p_2 = Outlet pressure, atm

L = Length, cm

μ = Air viscosity, cP

q_a = Gas flow rate at atmospheric pressure, cm^3/s

A = Cross-sectional area, cm^2

For absolute permeability calculation based on the numerical simulation, the method used was similar to the experimental measurement technique. One difference was that at first, the flow model was set as laminar flow. The program tries different flow rates until the flow regime is confirmed as laminar, and all material balance equations are satisfied. When the simulation is finished, the flow rate can be extracted from the post-processing step, and it will be used to calculate the permeability. From Eq (3-1), the permeability k can be calculated based on q_a.

3.4.2 Grid generation and simulation settings

As shown in Figure 3-34, the first step of the CT-based numerical simulation is to create the physical model. The digital cement model created by the 3D reconstruction is precisely the physical model of the cement sample. As the fluid flows through the pores, only the connected pore structure needs to be extracted from the cement. The rest of the work is to transfer the digital cement model (pores) to mesh file. Simpleware provides a function to achieve this transformation.

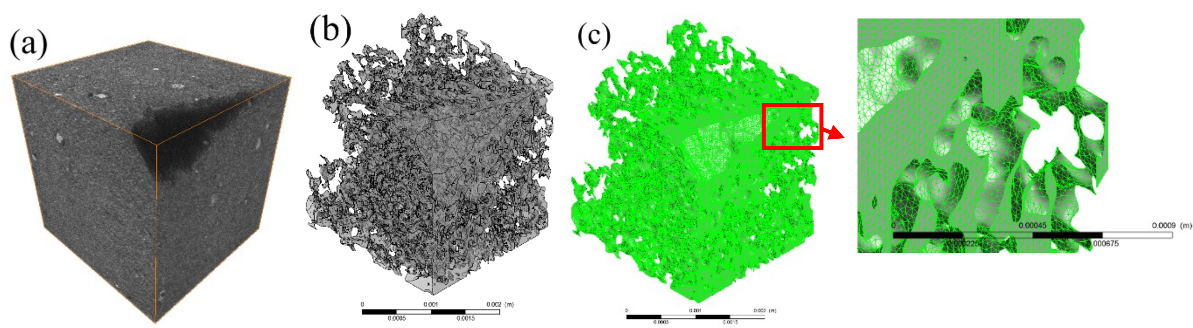

(a) 3D cement model using volume rendering (b) 3D pore structure (c) FEM mesh of pore structure

Figure 3-34 Transformation of the digital cement model (pores) to the FEM mesh.

As for the boundary conditions, the inlet pressure was set to be equal to the total injection pressure and the outlet pressure was set to be equal to the atmospheric pressure. The atmospheric pressure depends on the local elevation. The pressure gradient used in the simulation should be equal to the pressure gradient of the realistic condition.

Normally, a cubic section is extracted from the cement body and is used for permeability calculation. Due to the heterogeneity of the pore structure at the micron level, the location change of the small section may affect the permeability. Examples are shown in Figure 3-35. Nine subsections at a cubic cement sample were extracted. Connected pores were shown in green color. It is apparent that the connected pores varied a lot at different locations. The extreme case is at location 5 where no connected pores were observed and thus the effective porosity is equal to 0. Considering the porosity variation, the permeability should also vary at a different location. So how to calculate permeability in such a situation? A detailed solution technique was discussed in Chapter 4.

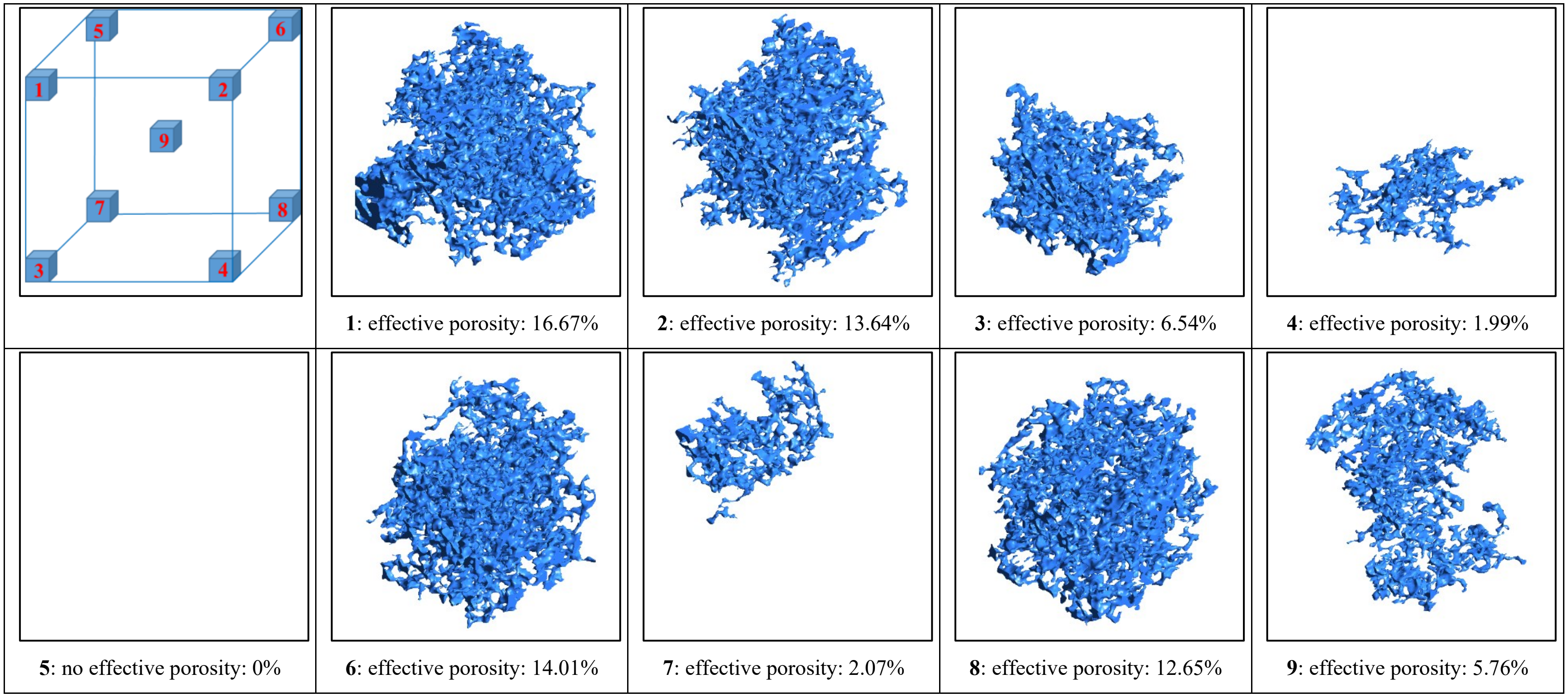

Figure 3-35 Connected pores of cement samples obtained from 9 different locations.

3.4.3 The dual-domain simulation model

In recent years, using the CT-based 3D simulation to investigate the mechanical and transport properties of cement paste became a topic of interest for many researchers (Das et al., 2016; Kabilan et al., 2016; Kjøller et al., 2016; Viejo et al., 2016). How to consider the multiscale characteristic of cement structures is l the key issue in these simulation works. Some researchers (Hlobil et al., 2016; Zhang et al., 2017) answered this question by building a multiscale model, which characterizes the cement paste at different levels individually when studying the mechanical properties of the cement paste. But this question remained for the cement transport simulation. A dual-domain transport simulation method, which considers the multiscale characteristic of cement structures is, therefore, proposed in this study.

Cui and Cahyadi (2001) presented a bicomposite model to predict the permeability of the cement paste. In their model, the cement paste consists of two phases. One phase is the relatively high-permeability phase, like capillary pores and the other one is a relatively low-permeability phase, such as C-S-H gel, CH, and unhydrated cement particles. The dual-domain model is developed based on the concept of the bicomposite model.

The microstructure of the cement paste is captured non-destructively using micro-CT and image analysis technique, instead of using mercury intrusion porosimetry (MIP), which was used by Cui and Cahyadi (2001). The microstructure of the cement paste consists of two parts: the easily identified pores and fractures, and the cement matrix, which is beyond the resolution of CT scan and thus cannot be captured (Figure 3-36a). Traditional simulation defines the pores and fractures as fluid domain and only focuses on the flow in this single domain. Therefore, this simulation method is called as single-domain simulation (Figure 3-36b). In the dual-domain simulation (Figure 3-36c), apart from the fluid domain, the cement matrix is defined as porous domain. The porous domain is designed to model features that can not be feasibly resolved or discretized because it would require an impossibly fine grid.

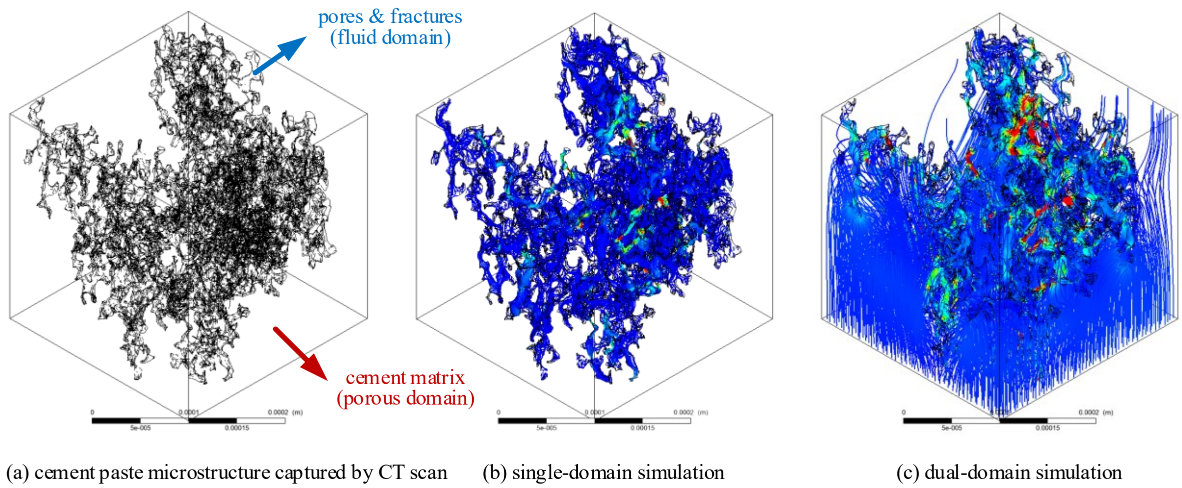

Figure 3-36 Schematic diagram shows the difference between single-domain simulation and dual-domain simulation.

Figure 3-37 compares the flow chart of the traditional single-domain simulation with the dual-domain simulation. The major difference is that the porosity and permeability of the porous domain should be estimated before running the simulation. For cement study, this requires the porosity and permeability of the cement matrix to be obtained. The porosity of the cement can be theoretically calculated or measured by using a simple drying method. For the permeability of the cement matrix, it can be tested by using a permeameter.

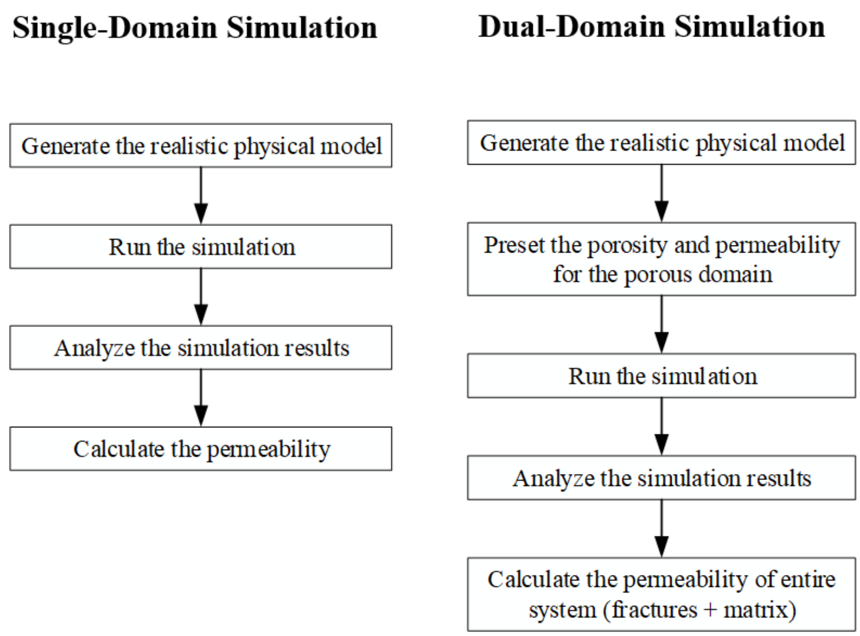

Figure 3-37 Flowcharts of single and dual--domain simulations, respectively.

3.4.4 Permeability test apparatus

Figure 3-38 shows the apparatus used for cement permeability measurement. It has an ISCO syringe pump used for fluid injection into the cement. A nitrogen gas tank was used to provide the confining pressure. The inlet fluid injection pressure was measured by using the pressure transducer. A specially designed core holder was able to hold a cylindrical cement sample, which has a diameter of one inch and a length of one inch to three inches.

When testing the cement permeability, the nitrogen tank was turned on first to provide the confining pressure, and then the inlet pressure was gradually increased to a desired value. The fluid injection pressure and the flow rate can be real-time monitored, and the pressure and flow rate can be recorded by the computer for further analysis. The cement permeability was calculated by using Darcy's law.

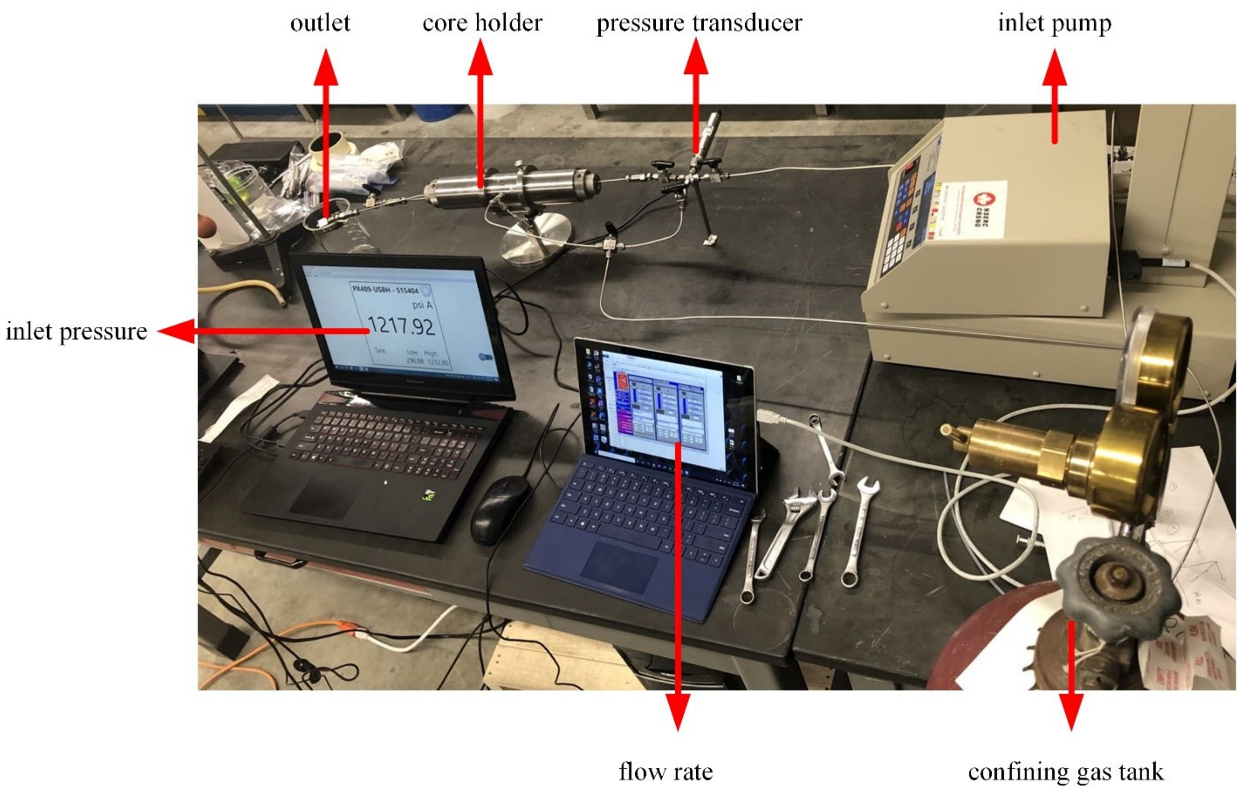

Figure 3-38 Permeameter used for cement permeability measurement.

Chapter 4 CT-CFD Integrated Investigation into Porosity and Permeability of Neat Early-age Well Cement at Downhole Condition*

4.1 Abstract

This study presents an experimental and numerical approach to investigate the permeability of neat early-age (7 days) well cement sample under downhole conditions (50 °C and 10 MPa). Realistic representative volume elements (RVEs) were first extracted from Class G cement sample. Porosity and permeability (poroperm) of the RVEs were then calculated through combining computed tomography (CT) with three-dimensional (3D) computational fluid dynamics (CFD) technique. In the end, poroperm data of well cement and formation rocks were compared. Results show that 1) at the micron scale (2.64 μm), non-uniform porosity distribution in cement sample was observed, which caused the permeability disparities at different locations. The minimum RVE size should be determined on a case-by-case basis. The characteristic linear curve-fitting line was generated to correlate the permeability with the effective porosity. 2) Average effective porosity values calculated from the representative element volumes were introduced into the correlation curve to determine the permeability of cement sample. From the simulation, the permeability of the neat early-age Class G cement sample at downhole condition was estimated to be 9.771×10^{-17} m^2. 3) Juxtaposed with poroperm experiment data of different formation rocks, the poroperm of neat early-age well cement are mainly distributed in the sandstone zone, which suggests that the permeability of neat early-age cement is close to permeability of tight sandstone formations. The linear relationship between poroperm of neat early-age well cement sample in semi-log plot indicates its permeability behavior will approach to that of shale if the hydration process of cement is continued.

*This chapter was published as "Yang, X., Kuru, E., Gingras, M., & Iremonger, S. (2019). CT-CFD integrated investigation into porosity and permeability of neat early-age well cement at downhole condition. Construction and Building Materials, 205, 73-86. https://doi.org/10.1016/j.conbuildmat.2019.02.004"

4.2 Introduction

Well cement is used to seal and stabilize the oil and gas wells. In the duration of the wells' lifetime, they are prone to have leakage any time after the commencement of production (Bonett and Pafitis, 1996). This leakage brings many problems to both field production and the environment (Bol et al., 1991; Visschedijk et al., 2018). It also put threats to the security of CO_2 Capture and Storage (CCS), which may store the CO_2 in the oil and gas reservoirs (Lavrov and Torsæter, 2016; Rimmelé et al., 2008; Saasen et al., 2011). Permeability is considered to be an important indicator to evaluate the durability of cement (Bouny et al., 2009; Basheer et al., 2001; Luping and Nilsson, 1992). It is known that the permeability of cement is strongly affected by the pore structure (Luping and Nilsson, 1992; Tiab and Donaldson, 2015). Many researchers have attempted to establish the relationship between permeability and pore-structure of the cement from experimental, analytical, and numerical perspective.

Mercury intrusion porosimetry (MIP) is one experimental technique commonly used to study the microstructure of cement (Bágel' and Živica, 1997; Justo-Reinoso et al., 2018; Liu and Winslow, 1995; Zajac et al., 2018). However, the accuracy of mercury intrusion porosimetry is limited. For example, the drying process required before conducting MIP can damage and alter the pore microstructure (Holly et al., 1993). The high pressures that are necessary for the intrusion of the smaller pores alters the pore microstructure (Beaudoin, 1979). Modifications and other techniques have also been used to test the cement permeability such as Helium pycnometric method (Beaudoin, 1979), non-contact impedance measurement (Tang et al., 2014), beam bending method (Valenza and Thomas, 2012) and constant water flow method (i.e. Darcy Tests) (Phung et al., 2013).

As for analytical research on cement permeability, Hughes (1985) reported the influence of average pore radius on permeability by using Poiseuille's formula. Tang and Nilsson (Luping and Nilsson, 1992) theoretically analyzed the quantitative relationship between permeability and pore size distribution by introducing the concept of long-range force. Based on the General Effective Media (GEM) theory, Cui and Cahyadi (2001) presented a model to predict the water permeability of ordinary Portland cement (OPC) paste from its pore structure. Atzeni et al. (2010) used geometric models to calculate fluid permeability coefficients of hardened cement pastes. After the publication of Katz and Thompson permeability theory (Katz and Thompson, 1986), some researchers have applied the Katz and Thompson permeability theory to predict the permeability of cementitious materials (Christensen et al., 1996; El-Dieb and Hooton, 1994; Zhou et al., 2017).

The determination of the cement permeability through experiments is time consuming and not cost effective (Faiz, 2014). For analytical methods, the governing equation that controls the fluid flow is non-linear and difficult to solve. Assumptions and simplification can be applied to make analytical problems easier to solve even though the simplification introduces errors. However, in most cases, even the simplified equations cannot be solved analytically (Ferziger and Perić, 2002). To overcome these challenges, there is a need to develop a new method to make the prediction of cement permeability easier and more efficient. Once the power of computers had been recognized, interest in numerical approaches increased dramatically.

Regarding numerical approaches on cement permeability, lattice Boltzmann (LB) and discrete element method (DEM) are two main methods of computational fluid dynamics (CFD) used to simulate the fluid flow through the cement. Zalzale and McDonald (2012) used the LB method to calculate the permeability of microstructures (generated by a software called μIC) as a function of water-to-cement ratio and degree of hydration of the paste. They also developed a 3D LB model to calculate the water and gas permeabilities of model cement pastes at different degrees of water saturation (Zalzale et al., 2013). Li et al. (2016a) investigated the liquid water and gas permeability of partially saturated cement paste by DEM approach. They named the dynamic DEM-based modeling approach as complete methodology to estimate the permeability of cement pastes by their pore structures (Li et al., 2016b). One of the main conclusions from these numerical studies (Li et al., 2016a, 2016b; Zalzale et al., 2013; Zalzale and McDonald, 2012) is that the permeability of a cement paste is not only dependent on the degree of saturation but also on three-dimensional (3D) microstructure of cement paste. However, the 3D microstructures used in (Li et al., 2016a, 2016b; Zalzale et al., 2013; Zalzale and McDonald, 2012) were virtual microstructures generated by computer-based models, which might not be able to properly represent the real microstructures of cement paste and so need further validation.

Micro computed tomography or "micro-CT" has been widely used for cement research due to its non-destructive characteristic. Moreover, it is possibly the only way to obtain 3D material internal information efficiently. The micro-CT was initially used as a standalone characterization tool to investigate the internal structure of cement such as cement particle shapes (Garboczi and Bullard, 2004; Nitka and Tejchman, 2018; Ueda et al., 2018) and pore network (Bossa et al., 2015; Brisard et al., 2018; Gallucci et al., 2007). The statistical and morphological analyses using computed tomography provides a new view of the cement microstructure because it gives a realistic 3D geometry. The realistic 3D geometry represents the real pore structure of cement, and it influences the permeability of the cement. Only a few recent research efforts combined numerical approach with the realistic 3D geometry. Kjøller et al. (Kjøller et al., 2016) evaluated the permeability of defect cement zones by combining micro-CT imaging and numerical modeling. Kabilan et al. (2016) combined micro-CT imaging with CFD modeling to study the effect of geochemical and geomechanical processes on fracture permeability in composite Portland cement-basalt caprock core samples. The geometry used in both researches are cement with defect zones or fractures. Apparently, the flow in such a geometry is dominated by the defect zones rather than the capillary pores. Moreover, due to the large dimensions of the cement sample they prepared, the precision of the CT scan was limited to 10-25 μm. However, the bulk of the capillary pores cannot be characterized at that resolution. No information is available on the fluid flow in neat cement samples considering the realistic 3D geometry without defect zones or stress-induced fractures. Higher precision of the CT scan, which can capture more details of the capillary pores is also needed.

Instead of using lattice Boltzmann or DEM approach, an element-based finite volume method was used in this research to simulate fluid flow through cement. The element-based finite volume method was proven to have high efficiency to handle the flow simulations with complex geometry (Marcondes et al., 2013a, 2013b) and has been widely used in realistic porous media simulations (Dixit and Ghosh, 2018; Song et al., 2017; Y. S. Wang and Dai, 2017). It is also worth noting that at the micron scale, the microstructure of cement may still behave as heterogeneous material (Bossa et al., 2015; Viejo et al., 2016). The local permeability may change at different positions.

In order to get the representative permeability value of cement, representative volume elements (RVEs) need be built. The RVE is the smallest volume over which a measurement or simulation can be carried out to produce a result that is representative of the macroscopic property (Yio et al., 2017). Although RVE has been commonly used in micromechanics to analyze and predict the mechanical behavior of cement (Das et al., 2016; Viejo et al., 2016), the application of RVE to flow study (at this scale) has not been covered before.

This paper aims to investigate the permeability of the neat early-age (7 days) well cement sample at the downhole conditions (50 °C and 10 MPa). An integrated approach combining the micro-CT and the element-based finite volume method was proposed. The proposed approach provides a quantitative means to estimate the porosity and permeability of neat early-age well cement sample taking into account the realistic microstructure. For the first time, the representative volume element method is used to assist the permeability calculation of cementitious material. Following this introduction and review of the state of the art, the integrated CT-CFD approach is fully described in the subsequent section. Porosity and permeability results are discussed in the next section with validation of the numerical approach. The study ends with a set of conclusions.

4.3 Methodology

4.3.1 Specimen preparation

Pure Class G cement powder was used to prepare the cement slurry. 0.45 water-cement (w/c) ratio was used in this study. High-temperature 1/8 in PTFE (Teflon) pipe was selected to make the molds. Reasons for selection of PTFE material are: 1) Every micro-CT scanner has its limitation with the object size. For the micro-CT scanner used in this research (SkyScan 1172), the maximum object size was 27 mm in diameter. So the diameter of the mold could not exceed 27 mm. In addition, the precision of the CT scan is limited to the sample size. The smaller sample will get images with higher accuracy; 2) Compared with metal materials, PTFE pipe has lower density and thus make it easy for X-ray to penetrate. Besides, some specially made PTFE pipes have a super-smooth interior so the molds can be easily separated from the cement; 3) The high-temperature PTFE pipe has a temperature range of -268 °C to 287 °C and can withstand 24 MPa pressure. The cement sample with the molds can be placed into the pressure cell together and then cured under elevated pressure and temperature.

As for the height of the cement sample, we found that the length affects the cement microstructure. For example, cement samples with 10 cm, 15 cm and 20 cm lengths compared to cement samples with 5 mm length, it was found that the cement samples with 5 mm length were prone to have bubbles inside. Optimization work has been done and decided to use cement sample with 15 mm length. Apart from the PTFE pipe, PTFE film (which has a slippery surface that prevents sticking and allows objects to slide across it easily) and no-hap curved-head cable ties were used to seal the mold. The complete mold used in this research is shown in Figure 4-1.

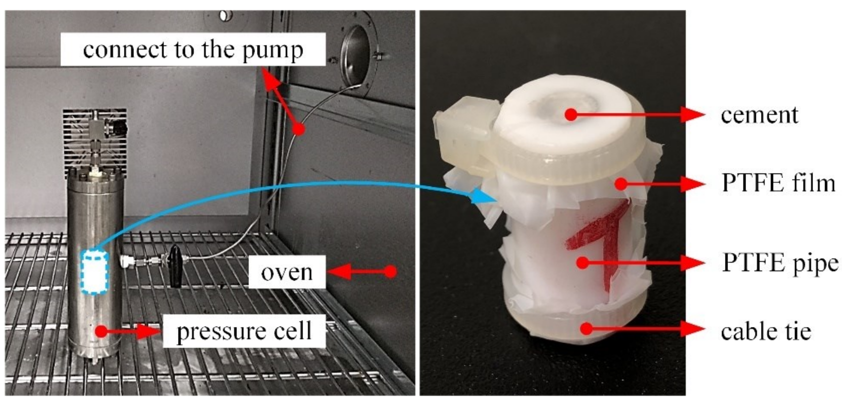

Figure 4-1 Illustration of the cement curing apparatus and the sample mold.

The cement slurry was mixed according to API standard 10A. Then, the cement slurry was injected into the mold by using the syringe. Before sealing the mold, a small tamping rod was used to tamp the slurry to remove the bubbles from the slurry as much as possible. In order to simulate the cement behavior under downhole conditions, we cured the cement samples at 50 °C and 10 MPa. The curing procedure is as follows: 1) A cement sample is placed inside a cylindrical cell, which is filled up with water and pressurized using a water pump; 2) The pressurized cylinder is then placed inside an oven for temperature control. A picture of the curing set-up is shown in Figure 4-1. Note that the water pump is located externally to the oven and not shown in Figure 4-1. To keep the cement samples in a stable position to get the smooth ends, the pressure cell and the cement samples inside were all placed vertically. The duration of the cement curing is 7 days. Cement samples should be well stored after they are taken out of the oven. The cement samples were wrapped by plastic film to prevent the water loss and isolate the cement samples from the contact with air.

4.3.2 CT characterization of specimens

Micro-computed X-ray tomography (CT) equipment available at the Earth and Atmospheric Science Department, University of Alberta was used for the cement microstructure characterization. The device is a SkyScan 1172 desktop X-ray micro-CT. X-ray shadow projection images were generated first during the scan process and then digitized as 4000 × 2090 pixel with 16-bit depth. Once the CT scan is finished, NRecon software is used to reconstruct cross-section images from X-ray shadow projection images according to the Feldkamp algorithm. Normally, the term CT images mean the cross-section images. The reconstructed cross-sections are in 4000 × 4000 pixel (floating point) format.

Cement is considered as a high-density material. High energy X-rays are needed to scan high-density materials. The adjustment of energy or voltage of the X-rays can be achieved by changing scan filters. Copper plus aluminum filter (Cu + Al) was selected for the cement CT scan. Because of the sample size, the highest resolution of 1/8 inch size samples was about 2.64 μm. To minimize the end effect, only the middle part of the specimen was scanned. Flat field correction and alignment tests were required before the CT scan. These two operations would make sure that the CT images have high contrast and with less noise.

Based on the scan experience, long CT duration decreases the quality of cement CT images. Averaging frames and rotation degree are the two main factors controlling the CT duration. Averaging frames allows improvement of the image quality by averaging the several images in every angular position. Increasing the number of frames will increase the quality but also makes the acquisition longer (Skyscan NV, 2011). Using 360 degrees rotation can reduce symmetrical artifacts from dense objects across the surrounded low absorption material. This will also almost double the scanning time. Figure 4-2 shows the difference of two CT images using different rotation degrees. The grain boundaries tend to be less clear from inside to the outside of the image obtained by using 360 rotation degrees. Images obtained by using 180 rotation degrees have relatively clear grain boundaries.

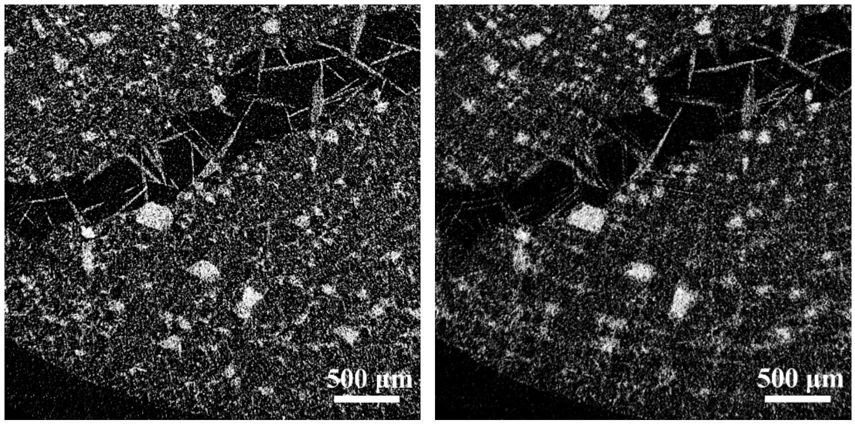

(a) 180 degrees (b) 360 degrees

Figure 4-2 CT Images of cement sample scanned by using 180 and 360 degrees of rotation.

A few reconstruction parameters have to be adjusted manually in a trial-and-error fashion to correct the beam hardening, ring artifacts, and provide alignment optimization (Skyscan NV, 2011). It requires quite some effort to save the preview images, view them and then make a decision. A raw CT image without any correction is compared with the corrected image as shown in Figure 4-3. After many different scan attempts, the optimum values for the scan and reconstruction parameters were found as shown in Table 4-1.

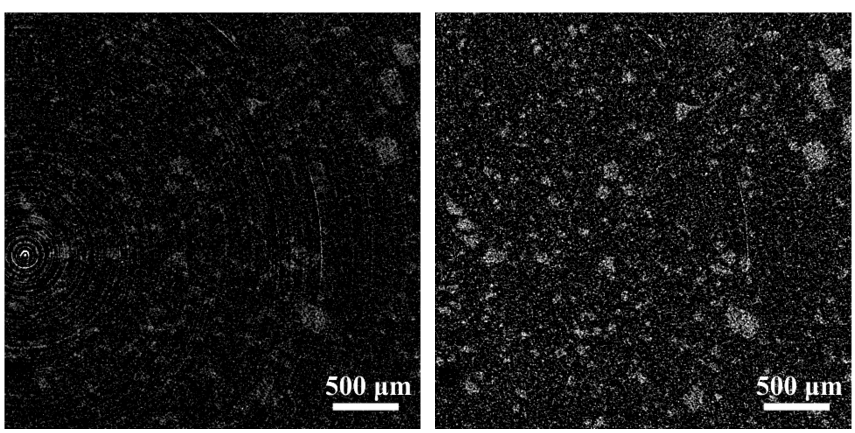

(a) Raw image (b) Corrected image

Figure 4-3 Raw and corrected cross-section images of the cement microstructure.

Table 4-1 Optimized scan and reconstruction parameters for CT characterization.

Scan parameters	Value
acquisition time (min)	50
X-ray beam form	cone beam
Total number of projections	486
source voltage (kV) and current (uA)	100, 100
scan filter	Al + Cu
rotation step (degree)	0.4
resolution (μm)	16.87
frame averaging	2
random movement	1
use 360 rotation	No

4.3.3 Image processing and porosity calculation

CT technique is based on the ability of X-ray to penetrate objects with a certain thickness to collect the attenuated post-penetration information of a specific section. In the CT images obtained from Section 4.3.2, changes in the gray value reflect the internal density changes of the objects. White color means the highest gray value and object density and indicates cement solid phase while black color means the lowest gray value and object density and reveals the void phase of the cement. Because most pixels of CT images are gray, threshold segmentation method is used to select an appropriate gray value and convert the CT images into binary images with only black and white colors.

Gaussian deconvolution is proved as an effective threshold segmentation method for identifying the different phases in CT images of cement (Bossa et al., 2015; Němeček et al., 2011). A histogram of CT images is used to perform the Gaussian deconvolution. The histogram shows the number of pixels in a 2D or 3D object at each different intensity value found in that object. For 8-bit grayscale CT images, there are 256 different possible intensities. Histogram graphically displays 256 numbers showing the distribution of pixels amongst those grayscale values.

From the deconvolution theory (Bossa et al., 2015; Němeček et al., 2011; Sammartino et al., 2002; Vandamme and Ulm, 2009), cement image histogram can be deconvoluted by three Gauss curves. Based on the mineral identification by XRD analysis and the respective calculation of each mineral's linear attenuation coefficient, each of the Gauss curves was realted to one or multiple phases of the cement (Bossa et al., 2015): The Gauss1 curve associated to void phase, the Gauss2 curve associated to the hydrated mineral C–S–H and Portlandite, and the Gauss3 curve was related to unhydrated cement particles. The threshold value defining the frontier between the pores and the cement material was set at the intersection between the Gauss1 curve and the Gauss2 curve. Histograms after Gaussian deconvolution are shown in Figure 4-4. A threshold value of 88 was applied to Class G cement. As can be seen from Figure 4-5, using the obtained threshold value, the CT images (Figure 4-5a) were converted into the binary images (Figure 4-5b) which were used as the input information for the 3D reconstruction process demonstrated below.

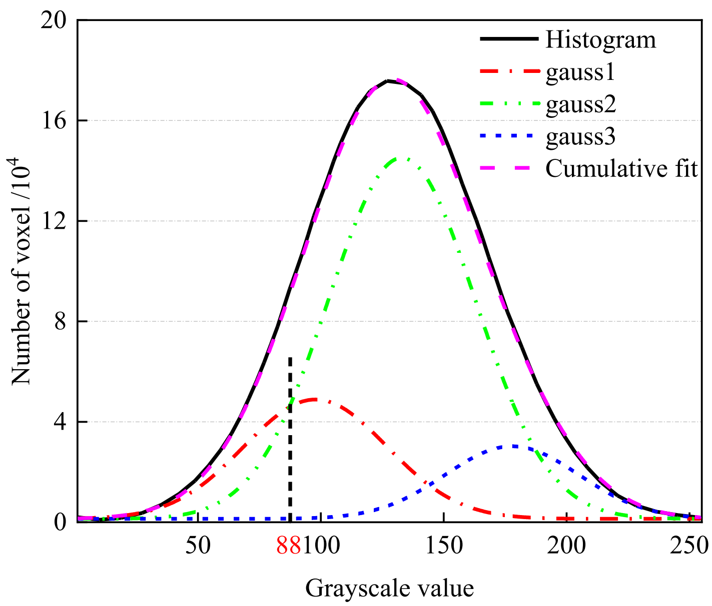

Figure 4-4 Deconvolution of histogram of Class G cement.

The 3D cement model (Figure 4-5c) was extracted from the binary images (Figure 4-5b) by using 3D reconstruction technique, which interpolates the data between binary images to form the volumetric 3D model. 3D Reconstruction is currently known as a mature technique, and several state-of-the-art software packages provide the 3D reconstruction function and make it easy to use. Here, ScanIP from Synopsys Inc. was used to reconstruct the 3D cement models from cross-section images.

The 3D cement model (Figure 4-5c) generated using CT images were also called as the digital cement model. “Digital” not only means that the cement microstructure can be stored and shown in the computer but also indicates that the porous media parameters like pore volume, surface area, porosity, permeability, etc. can be easily calculated from the digital cement models. For example, one of the most critical advantages of the digital cement models is that the connected pores can be easily tracked and the effective porosity can then be calculated. Connected pores link the two ends of a sample in the flow direction and serve as the effective flow channels in the cement. Flood fill, also called seed fill, is an algorithm that determines the area connected to a given node in a multi-dimensional dataset. Using this algorithm, connected pores (Figure 4-5d) can be extracted from the digital cement model (Figure 4-5c). Under this condition, the total porosity equals to the ratio between the red pore volume and the cube volume in Figure 4-5c, and the effective porosity equals to the ratio between the cyan pore volume and the cube volume in Figure 4-5d.

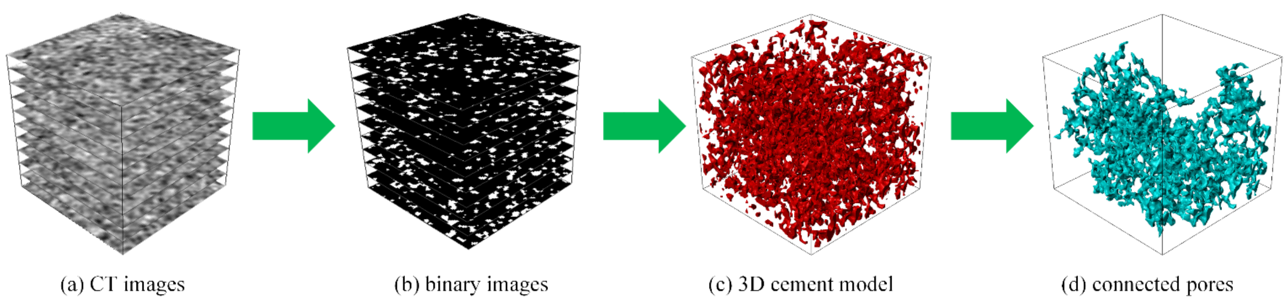

Figure 4-5 Extraction of 3D connected pores from the 2D CT images.

3D reconstruction technique makes the scanned object easily visualizable. The 3D geometry created by the 3D reconstruction technique can not only be used for morphological and statistical analysis (Bentz, 2006; Bossa et al., 2015; Gallucci et al., 2007; Garboczi, 1990; Helfen et al., 2005; Promentilla et al., 2009), but also to provide the realistic physical geometry, which plays a vital role in later CFD simulation.

4.3.4 Gas permeability calculation and governing equation

Permeability is a measure of the ability of a porous material to allow fluids to pass through it. Absolute permeability is an intrinsic property of the material. It is a function of the material structure only. The CT-based 3D model can be used as a basis for numerical assessment of absolute permeability.

Because of the convenience, absolute permeability is usually measured by the steady-state method and it has been the industry standard for many years (ASTM D4525-13e1, n.d.; Morton-Thompson and Woods, 1993a). The pressure differential between the two ends of the test core and flow rate is kept at steady state, resulting mass flux is used to calculate permeability using Darcy's law as shown below:

$$k_g = \frac{2p_a \mu q_g L}{(P_1^2 - P_2^2)A} \qquad \text{Eq. (4-1)}$$

$k_g =$ Gas permeability, m^2

$p_a =$ Atmospheric pressure, MPa

$P_1 =$ Upstream pressure, MPa

$P_2 =$ Outlet pressure, MPa

$L =$ Length, m

$\mu =$ Air viscosity, MPa·s

$q_g =$ Gas flow rate at atmospheric pressure, m^3/s

$A =$ Cross-sectional area, m^2

$$v_g = \frac{q_g}{A} = \frac{(P_1^2 - P_2^2)}{L} \times \frac{k_g}{2p_a \mu} \qquad \text{Eq. (4-2)}$$

To ensure that flow conditions satisfy Darcy's law, several gas flow rates have usually been used for measurements. In practice, gas permeability is calculated from the slope of the plot of the seepage velocity v_g versus $(P_1^2 - P_2^2)/L$, which results in a straight line passing through the origin (according to Eq. (4-2)) as long as the conditions for Darcy's flow are established (Morton-Thompson and Woods, 1993b).

For absolute permeability calculation based on the numerical simulation, the method used was similar to the experimental measurement technique. Because the simulation in this research focuses solely on the internal flow in the microstructure of cement, the most basic control equation is used for this simulation. Ignoring the change in air density in the flow process, the flow of gas in cement can be seen as an incompressible viscous flow which follows the three physical conservation laws (conservation of mass, momentum and energy). Therefore, the flow can be described by the Navier-Stokes equation (Ferziger and Perić, 2002), whose vector formula is given as follows:

$$\rho\left[\frac{\partial \boldsymbol{v}}{\partial t}+(\boldsymbol{v}\cdot\nabla)\boldsymbol{v}\right]=\rho\boldsymbol{f}-\nabla p+\mu\nabla^2\boldsymbol{v} \qquad \text{Eq. (4-3)}$$

Where the left side of Eq. (4-3) denotes the inertial force, $\rho\boldsymbol{f}$ on the right side is the body force, ∇p is the pressure force, and $\mu\nabla^2\boldsymbol{v}$ is the viscous force.

The simulation program tries different flow rates until the flow regime is confirmed as laminar, and all material balance equations are satisfied. When the simulation is finished, the flow rate is extracted, and it is used to calculate the permeability. Using Eq. (4-2), if we know q_g, we can then calculate the permeability k_g.

4.3.5 Representative volume element selection

The representative volume element (RVE) is the smallest volume over which a measurement or simulation can be carried out to produce a result that is representative of the macroscopic property (Yio et al., 2017). In order to get the representative permeability value of cement, RVEs of cement sample should be selected and built. The RVE size (or characteristic length) is an important parameter need to be considered while selecting RVE. Theoretically, the RVE must be large enough compared to the dimension of the heterogeneities yet small enough compared to the system analyzed (Gitman et al., 2007). Usually, a larger RVE tends to provide more representative or accurate result, but for CFD simulation, a larger RVE may have two or three times grid elements than a smaller one, which will significantly increase the calculation time. Compromise between an accurate estimation of the RVE size and the required CPU time is normally necessary (Pelissou et al., 2009).

Recent research (Yio et al., 2017) suggested that the minimum RVE size of cementitious materials should be larger than 100^3 μm^3. Based on a cubic shape, the physical length of the RVE should bigger than 100 μm. As the resolution of CT images in this research equals 2.64 μm, a side length of 100 pixel equals physical size 264 μm. This RVE size satisfies the minimum RVE size requirement recommended by (Yio et al., 2017). As demonstrated in the Section 4.3.2, to minimize the end effect, only the middle part (Figure 4-6b) of the cement sample (Figure 4-6a) was scanned. Then a main 3D volume (Figure 4-6c) was cropped from the middle part. At last, to avoid the random error, RVEs (Figure 4-6d) at 27 different locations were selected from the main 3D volume in this research.

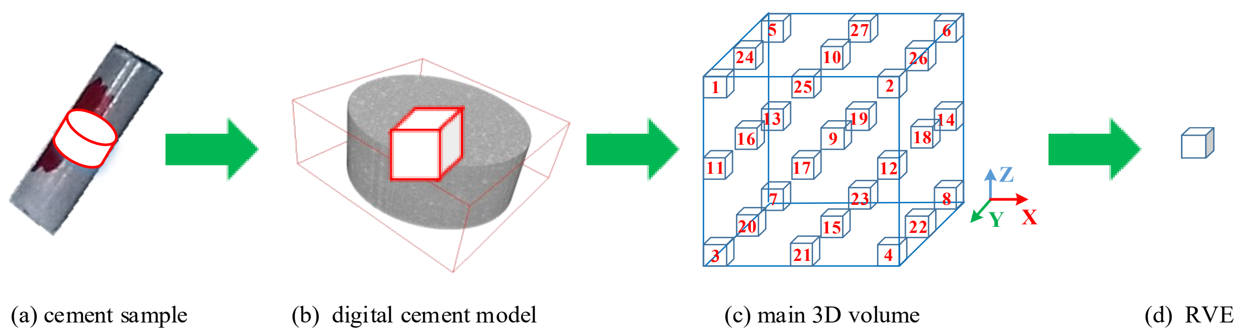

Figure 4-6 Selection of RVE from the cement sample.

4.3.6 Geometry and boundary conditions

The first step of any CFD simulation is to create the physical model and generate CFD grid. Digital cement model is precisely the physical model of the cement sample. As the fluid flow through the pores, only the connected pore structure needs to be extracted from the cement. The rest of the work is to transfer the digital cement model (pores) to CFD grid. ScanIP from Synopsys Inc. provides a function to achieve this transformation. Figure 4-7 shows the connected pores extracted from a RVE, which has the volume of 100 pixel^3. Part of the CFD grid is shown in the enlarged view. After the CFD grid is ready, boundary conditions can be applied to the physical model.

As shown in Figure 4-7, total pressure and static pressure were set as the inlet (pink) and outlet (cyan) boundary respectively (see Figure 4-7). The rest of the RVE were set as no-slip wall (grey) conditions. The outlet pressure normally equals to the atmospheric pressure. However, the atmospheric pressure depends on the local elevation. After took account of the local elevation (1045 m, Calgary, Canada). The outlet pressure was set at 0.088 MPa. Key parameters of the simulation are summarized in Table 4-2. The determination of inlet pressure values listed in Table 4-2 will be discussed in Section 4.4.1.

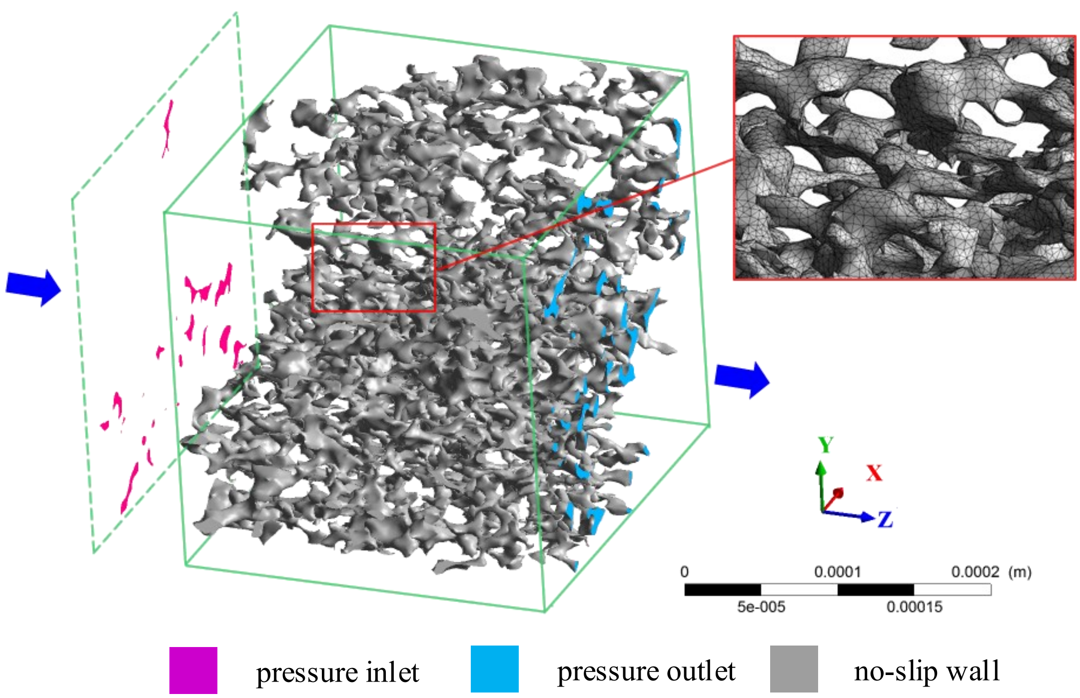

Figure 4-7 CFD grid and boundary conditions setting.

Table 4-2 Key parameters of the numerical simulation.

Parameter	Value

Simulation type	steady simulation
Fluid type	air at 25ºC
Fluid density	1.185 kg·m^{-3}
Fluid viscosity	1.831×10^{-11} MPa·s
Domain type	single fluid domain
Heat-transfer model	isothermal model (25 ºC)
Time scale	physic time scale (2 s)
Initial velocity	*U=0, V=0, W*=2 (m·s^{-1})
Boundary conditions	inlet pressure: 0.096, 0.103, 0.110, 0.118, 0.125 and 0.133 MPa outlet pressure: 0.088 MPa (local atmospheric pressure) no-slip wall

NOTE: *U, V* and *W* are the velocity values of fluid in the *X-, Y-* and *Z-* directions in Cartesian coordinate system.

4.4 Results and discussion

4.4.1 Determination of the inlet pressure values

The physical size of the RVE (246 μm^3) used in the simulation is much smaller than the cement core utilized experimentally (usually 1 inch in diameter). So the inlet pressure applied in the actual experiment was no longer suitable for the simulation. Considering the outlet pressure (equal to local atmospheric pressure, 0.088 MPa) and the confining pressure (~3 MPa), different inlet pressure values between 0.088 MPa and 3MPa were selected and the corresponding flow rates were determined by using the CFD simulation of flow through cement body. Curves of seepage velocity v_g versus $(P_1^2 - P_2^2)/L$ under different inlet pressure upper limit were plotted in Figure 4-8.

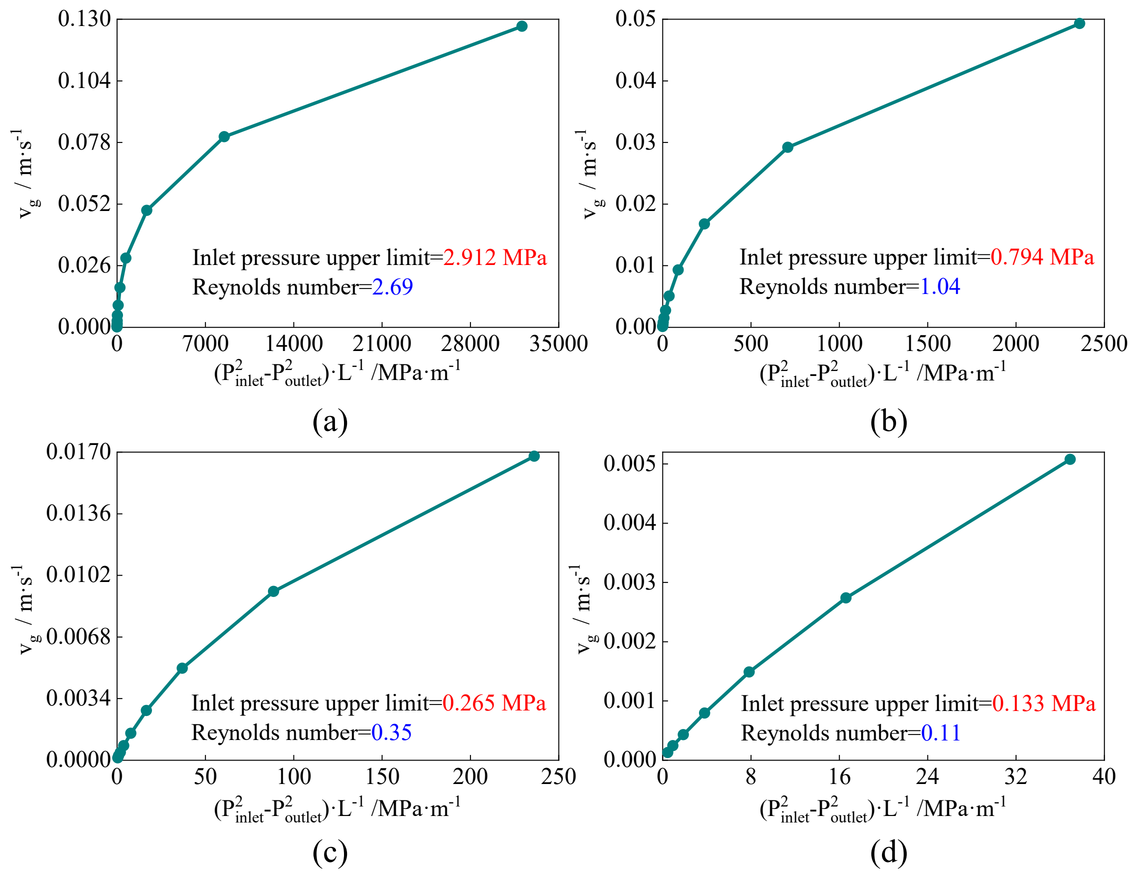

Figure 4-8 The curves of v_g versus (P_{inlet}^2-P_{outlet}^2)/L at the different inlet pressure upper limit.

As shown in Figure 4-8, higher inlet pressure caused the flow deviated from the linear relationship, and the non-Darcy effect became significant. The non-Darcy effect in the simulation is possibly due to the heterogenous cement structure at the micron level (Kaiser, 2006; Muljadi et al., 2016). The high tortuosity of CT-based cement model causes the convective acceleration and because of this the inertial effect becomes more important. Moreover, the heterogenous pore structure leads to the velocity fluctuations. Local velocity in narrow pores is increased and the flow pattern may become turbulent (J. Zhang et al., 2018; Y. Zhao et al., 2018). The existence of non-Darcy flow will influence the accuracy of the permeability calculation.

To minimize the non-Darcy effect in the flow, Reynolds number under different inlet pressure upper limit was calculated. Reynolds number is an important indicator to predict flow patterns. Although various methods for calculating Reynolds number have been proposed (Z. Zeng and

Grigg, 2006), the method proposed by Ergun (1952) is applied in this research since Ergun's method include porosity ϕ and intrinsic velocity u which can be extracted from the CT-based flow simulation:

$$Re = \frac{\rho D_p u}{\mu} \frac{1}{1-\phi} \qquad \text{Eq. (4-4)}$$

where ρ is the fluid density and D_p is the diameter of cement particles. Ergun observed a critical value of *Re*=3-10 for the occurrence of non-Darcy flow. Later, Scheidegger (2013) modified this range to 0.1-75.

Reynolds number shown in Figure 4-8 indicate that 0.133 MPa (Figure 4-8d, Re≈0.1) should be the appropriate upper limit for the inlet pressure. This inlet pressure value is similar to the value of 0.124 MPa proposed by Jikich et al. (2010). In order to avoid uncertainty and get a representative value, five different pressure values between outlet pressure and upper limit inlet pressure are also used as inlet pressure (see Table 4-2). So in total, six data points were obtained after the simulation performed at each RVE. A linear fitting was used to calculate the slope of the curve that connected all six data points. Then the final permeability value can be calculated from the slope.

4.4.2 Non-uniform distribution of porosity in cement sample

4.4.2.1 Discussion on minimum RVE size of cementitious material

As shown in Figure 4-6c, 27 RVEs in 100 pixel^3 size were extracted at different locations and connected pores were tracked by using flood fill algorithm (Figure 4-5). Based on the connected pores, gas permeability was calculated by applying the procedure introduced in Section 4.3.4. Figure 4-9 shows the total porosity, effective porosity and gas permeability change at different RVE location. Both total and effective porosity changed significantly with the model location and thus led permeability varied as high as three orders of magnitude.

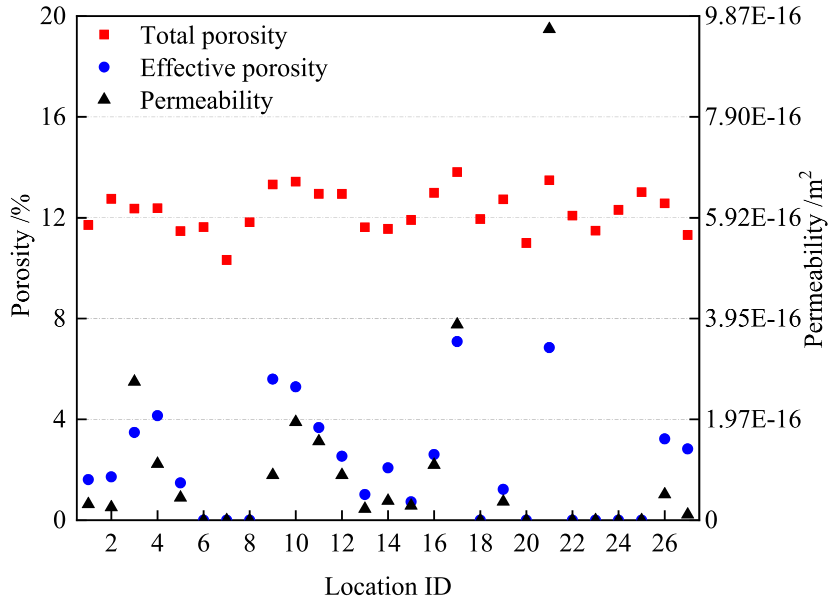

Figure 4-9 Porosity and permeability of cement sample obtained from 27 RVEs at different locations.

The variation in Figure 4-9 is because of the non-uniform porosity distribution in the cement sample. By plotting the total porosity at different locations in the main 3D volume (Figure 4-6c) and perform 3D data interpolation, we can obtain the 3D total porosity distribution, as shown in Figure 4-10. The non-uniform distribution of porosity can be easily identified from the Figure 4-10. As mentioned in Section 4.3.5, Yio et al. (2017) suggest that the minimum RVE size is 100 μm^3. This means the porosity of RVEs at different positions should remain constant when RVE size is bigger than 100 μm^3. However, according to Figure 4-10, the porosity still varied after RVE size approaches 100 μm^3.

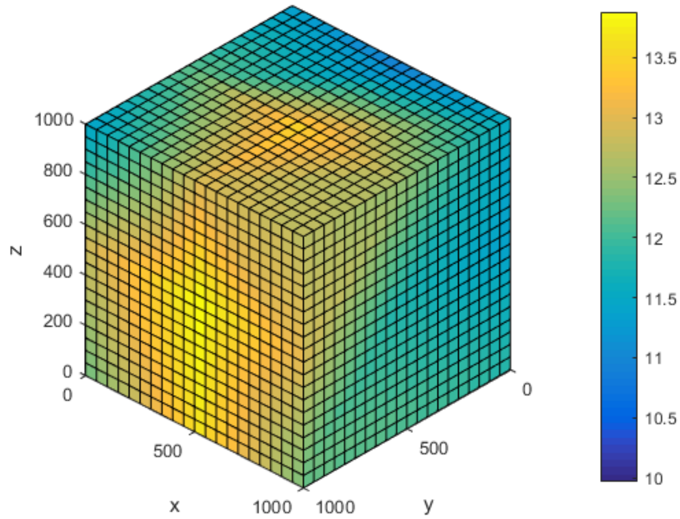

Figure 4-10 Total porosity distribution in the main 3D volume generated by performing 3D data interpolation.

So the suggested RVE size by Yio et al. (2017) is not applied to the early-age (7 days) cement. Although Yio et al. (2017) also cured the cement samples for 7 days, their pre-treatment for microscopic porosity analysis, however, required at least 90 days. Under this condition, the microstructure of cement samples will change significantly after 97 days because of the hydration process. The change of microstructure will affect the RVE size determination (Pelissou et al., 2009), therefore, the minimum RVE should be determined on a case-by-case basis.

In practice, the changes in porosity are far too small and they can only be captured at the micron scale. If we further increase the RVE size, the porosity of the RVE will gradually approach a constant value. To prove this, different RVEs with size changed from 100 pixel^3 to 1000 pixel^3 were cropped from the main 3D volume (Figure 4-6c) in two different methods: method A and B, as shown in Figure 4-11.

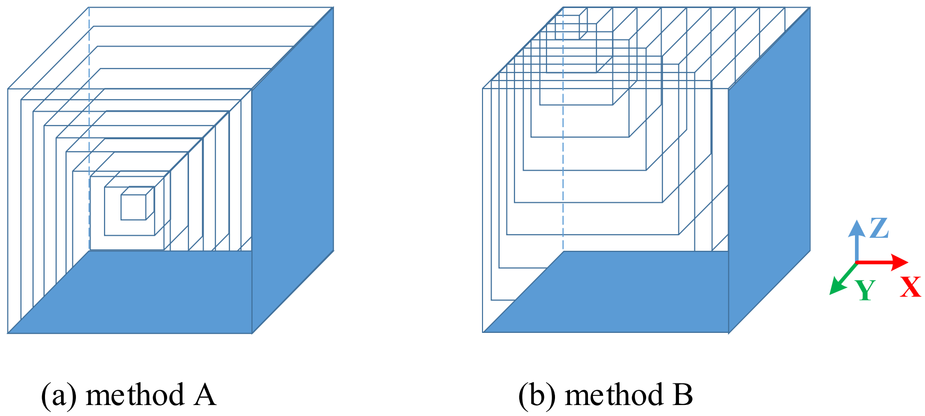

Figure 4-11 Cropping of different size RVEs from the main 3D volume in two different ways.

Figure 4-12 shows how the porosity changes with the changing RVE size. For RVEs of Class G cement sample with side length longer than 800 pixels, the total porosity values are almost the same. The total porosity of cement tends to reach a constant value after increasing the RVE to a certain side length.

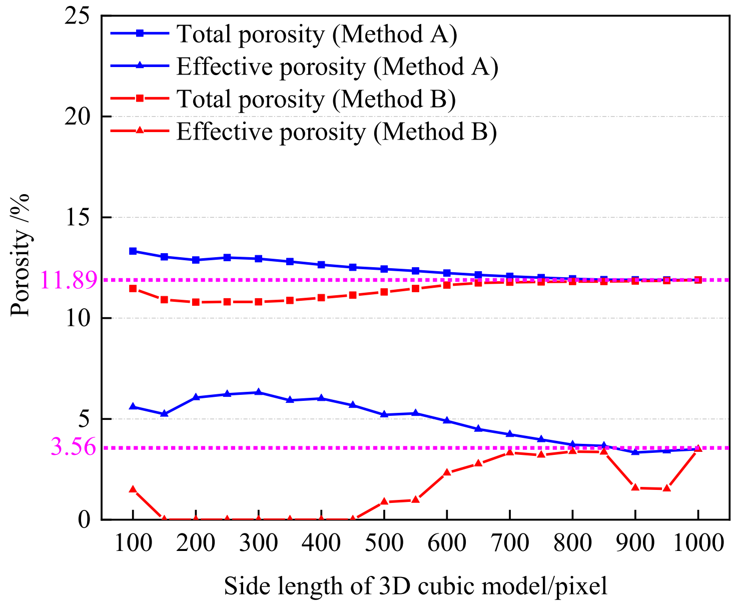

Figure 4-12 Porosity of the different size RVEs cropped from the main 3D volume in two ways.

The main difference between method A and method B is that they approach the constant value from two opposite directions. The reason is that although the total porosity distribution is non-uniform, the total porosity has a decreasing trend from sample's center to sample's edge. So when using method A (Figure 4-11a) to crop the cement, as the RVE size increases, a lot more low porosity areas are included in the RVE, so the porosity thus decreased. In contrast, if use method B (Figure 4-11b), as the RVE size increase, more and higher porosity areas are included in the RVE, so the porosity thus increased. In general, an average result of method A and method B will provide a constant value. Lake (1989) illustrated a similar result that the porosity varied before reaching constant values, as shown in Figure 4-13.

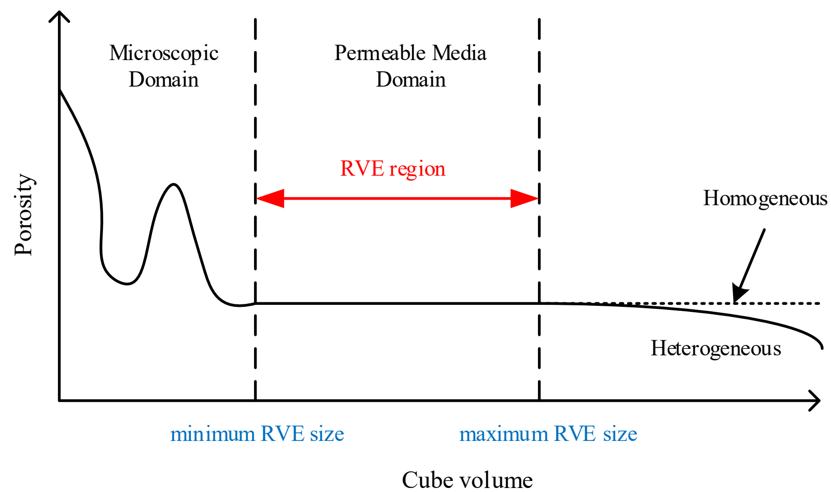

Figure 4-13 Ideal porosity change with cube volumes (modified from Lake (1989)).

4.4.2.2 Correlation between effective porosity and permeability

Due to the limitation of the computer processing power, the optimum size of RVE used in this research is 100 pixel^3. Because of the non-uniform porosity distribution in cement sample, however, the porosity of 100 pixel^3 size RVE cannot fully represent the real cement sample. Under this condition, determining a representative permeability value for a cement sample is not an easy task. In this section, a statistical method is proposed to calculate the permeability based on the 100 pixel^3 size RVEs.

The power law between poroperm is widely accepted by many researchers and linear fitting between poroperm in semi-log plots is commonly adopted (Dong et al., 2017; Ehrenberg et al., 2006; Ehrenberg et al., 2006; Jules et al., 2016; Nagatomo and Archer, 2015). Using the data presented in Figure 4-9, the linear fitting was used to correlate the permeability (k) and the effective porosity (ϕ) in Figure 4-14. The R^2 value of the linear fitting was increased from 0.64782 (red fitting line) to 0.75039 (green fitting line) by eliminating the outlier data point shown in Figure 4-14. The permeability of Class G cement shows a moderately strong (R^2=0.75) correlation with effective porosity. Therefore, here we use the red fitting line to calculate the permeability of the Class G cement sample. The equation of the fitting line is:

$$\log_{10} k = 0.20241\phi - 16.72782 \qquad \text{Eq. (4-5)}$$

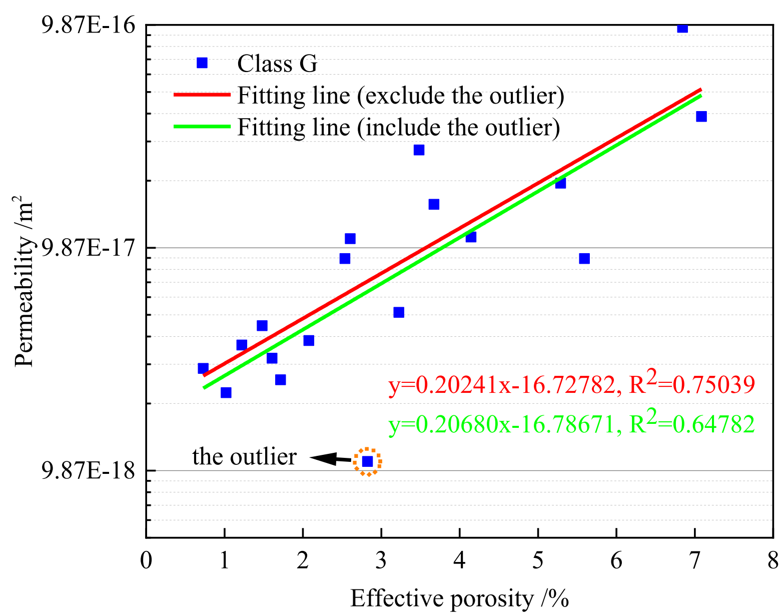

Figure 4-14 Curve fitting of the permeability versus effective porosity data of Class G cement.

If the porosity of the cement is known, then the permeability of the cement can be easily calculated based on Eq. (4-5). According to statistics theory, larger sample size should hypothetically lead to more accurate or representative results. According to Figure 4-12, the porosity approaches a constant value, which can represent the porous medium. We can assume that the porosity of RVE with 800 pixel^3 volume can represent the real Class G cement sample, and the corresponding effective porosity value in Figure 4-12 was determined as 3.56%. By substituting above effective porosity value in Eq. (4-5), the permeability of the early-age Class G cement at downhole condition was estimated to be 9.771×10^{-17} m^2.

4.4.3 Porosity and permeability validation

4.4.3.1 Validation of porosity

So far, all porosity values discussed above were obtained by processing of CT images. However, because of the existence of artifacts like rings or beam hardening, it is better to verify the calculated porosity using another method. The drying method is a convenient way to get the approximate value of the cement porosity. The weights of the cement sample were measured immediately after the curing process finished. Then the sample was marked, placed on a tray and placed into an oven. The oven temperature was set at 60 °C and weights of the cement sample was recorded as a function of time. The test was finished when the weight reaches a certain value and remained relatively constant.

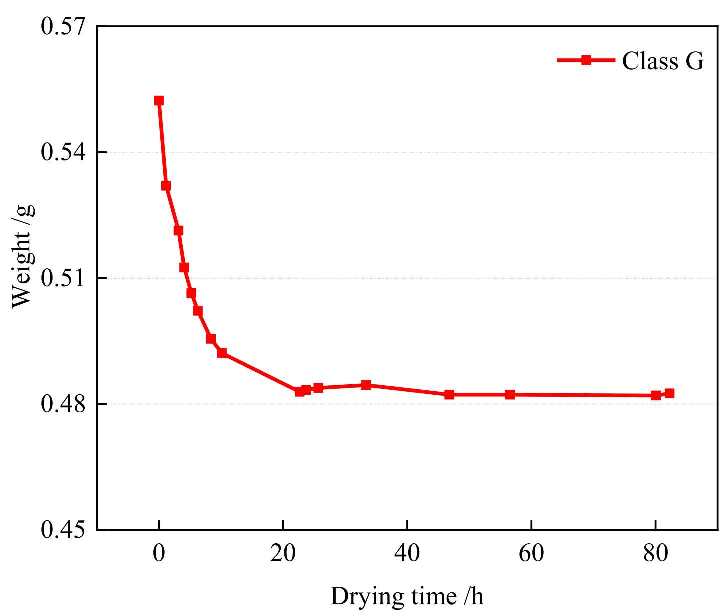

Figure 4-15 Weight changes of the cement sample while drying.

Figure 4-15 shows the weight change of Class G cement sample as a function of time. The weights decreased rapidly during the first ten hours and then decreased slowly to a specific value and remained almost constant at the end. The difference in the initial and the final weight was calculated. As the weight difference, in this case, was due to the water loss, the difference gave us the water weight. Using the water density, the weight loss can be converted into water volume, which was assumed to be equal to pore volume. The total (bulk) volume of the cement sample was calculated using their dimensions and the geometrical shape. So the porosity was then calculated as the ratio of the pore volume to the bulk volume. Calculation details are shown in Table 4-3.

Table 4-3 Porosity calculations.

Cement type	Volume of lost water	Total volume of sample	Total porosity from drying method	Modified total porosity from drying method (Gallé, 2001)	Total porosity from image processing of CT images
Class G	69.80 mm^3	375.38 mm^3	18.59%	14.59%	11.89%

The porosity obtained from the drying method is the total porosity and the values are greater than porosity values obtained from CT images. One major reason for this is the drying effect. The oven-drying treatment altered the pore structure of cement sample increasing inter-connecting pores and thus created additional total porosity. From Gallé's research (Gallé, 2001), about 4% of porosity is overestimated by using oven-drying treatment. As shown in Table 4-3, after considering the drying, 4% porosity modification was applied to porosity values of Class G cement.

After the modification, there is still about 3% difference of the porosity values between modified total porosity and the ones obtained from image processing. A 2% porosity difference is commonly observed between CT image processing and conventional porosity testing method like helium porosimetry (Taud et al., 2005) or density analysis (Anderson et al., 2003). This porosity difference may come from the gel pores because around 80% of water in gel pores and interlayers will be removed after 3-day oven drying (60 °C) (Gajewicz et al., 2016b). The gel pores, however, cannot be captured by the micro-CT as their size are under the resolution of 2.64 μm. Hence the porosity calculated based on CT images is lower than the one obtained by the drying method. Moreover, in this research, the 3D model obtained using CT technique was further optimized to generate the smooth CFD grid. Although a smooth CFD grid will improve the convergence of the CFD calculations (Ferziger and Perić, 2002), the smoothing operation indeed further increased the porosity difference (Iassonov et al., 2009).

4.4.3.2 Validation of permeability

Figure 4-16 shows the pore size distribution of the main 3D volume (Figure 4-6c) inside the cement sample. Based on the 3D cement model, the average pore size is about 7.37 μm and the smallest pore size that the micro-CT can detect is 3.21 μm. This distribution is also in line with the earlier observation by Diamond and Leeman (1994). Limited to the resolution of micro-CT, the gel pores cannot be captured by the micro-CT. The impact of gel pores on cement permeability has been intensively discussed. It is generally accepted the gel pores is part of low permeability phase in the cement (Cui and Cahyadi, 2001). Hearn et al. (1994) indicated that they are the capillary pores, which constitute the effective porosity (contributing to the permeability) of cement paste instead of gel pores. Ye (2005) and Haecker et al. (2005) pointed out that the fluid transport in cement is controlled by the capillary pores especially when capillary pores were connected. In summary, the gel pores contributed little to the cement permeability.

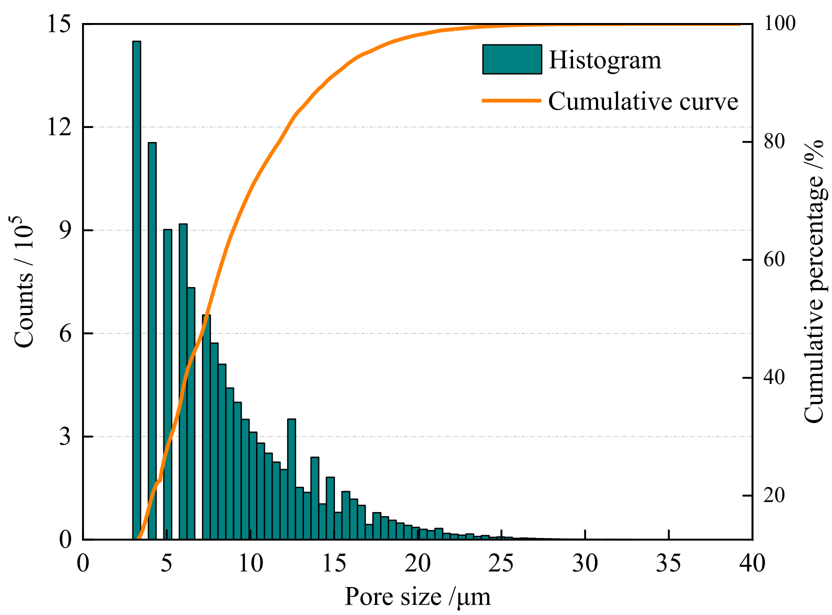

Figure 4-16 Pore size distribution of the main 3D volume.

Table 4-4 Permeability results of Class G cement from other published research.

	Simulation data	Ozyurtkan et al. (2013)	Le-Minous et al. (2017)
Cement type	Class G	Class G	Class G
Curing duration	7 days	7 days	7 days
Curing temperature	50 °C	25 °C	66 °C
Curing pressure	10 MPa	ambient (~0.101 MPa)	21 MPa
Permeability	9.771×10^{-17} m^2	2.369×10^{-16} m^2	8.882×10^{-18} m^2

Table 4-4 shows the permeability calculated from the simulation in Section 4.4.2 and permeability data from published experiment tests. In author's opinion, the variation of permeability mainly due to the different curing conditions. Experiments by Pang (Enein et al., 2018; El-Gamal et al., 2018; Pang, 2011; Wang et al., 2017) indicated that the higher curing temperature and pressure would accelerate the hydration process of Class G cement. As the permeability was found to decrease with an increase in the degree of hydration (Banthia and Mindess, 1989), the permeability thus has an inverse relationship with the increasing curing temperature and pressure.

The curing temperature and pressure used in this research are higher than Ozyurtkan et al. (Ozyurtkan et al., 2013) used, so the permeability is comparably lower. On the contrary, Le-Minous et al. (Le-Minous et al., 2017) obtained even lower permeability by using much higher curing temperature and pressure.

4.4.5 Porosity-permeability relationship of neat early-age well cement sample

Discussed above, Figure 4-14 shows the porosity and permeability (poroperm) relationship of the well cement. In the real field applications, most of the injected cement is surrounded by formation rocks. Knowledge of the poroperm relationship of both well cement and the surrounding rock is essential before questions concerning the gas migration, the cement failure, and the imperfect bonding can be answered (Bonett and Pafitis, 1996). Poroperm characteristics of various rocks has been well-studied by researchers (Aguilera, 2014; Bloch et al., 2002; Cai et al., 2014; Dong et al., 2017; S. N. Ehrenberg et al., 2006; Ehrenberg et al., 2006; Dizaji and Bonab, 2009; Givens et al., 1990; Jules et al., 2016; Kibodeaux, 2014; Mbia et al., 2014; Nagatomo and Archer, 2015). In order to provide further insight into the poroperm characteristics of well cement, we have used some of these published data to make an analogy between well cement and formation rocks. As shown in Figure 4-17, poroperm data of five types of common formation rocks: sandstone, limestone, dolostone, mudstone and shale (Aguilera, 2014; Bloch et al., 2002; Cai et al., 2014; Dong et al., 2017; S. N. Ehrenberg et al., 2006; Ehrenberg et al., 2006; Dizaji and Bonab, 2009; Givens et al., 1990; Jules et al., 2016; Kibodeaux, 2014; Mbia et al., 2014; Nagatomo and Archer, 2015) are collected and compared with the poroperm data of Class G cement obtained from our CFD simulation study.

Data presented in Figure 4-17 indicate that there are four distinct regions dominated by certain rock types (i.e. sandstone, limestone/dolostone, mudstone and shale). For early-age cement cured under downhole conditions, the poroperm data primarily resides within the sandstone region suggesting that the early-age cement exhibits porosity-permeability characteristics similar to low permeability tight sandstone (Lake, 2006). The Class G cement permeability varies from 9.87×10^{-18} m^2 (10^{-2} mD) to 9.87×10^{-16} m^2 (10^{0} mD). At cement (total) porosity ranges from 10% to 14%, the modeled cement permeabilities are higher than the shale and lower than the limestone or the dolostone.

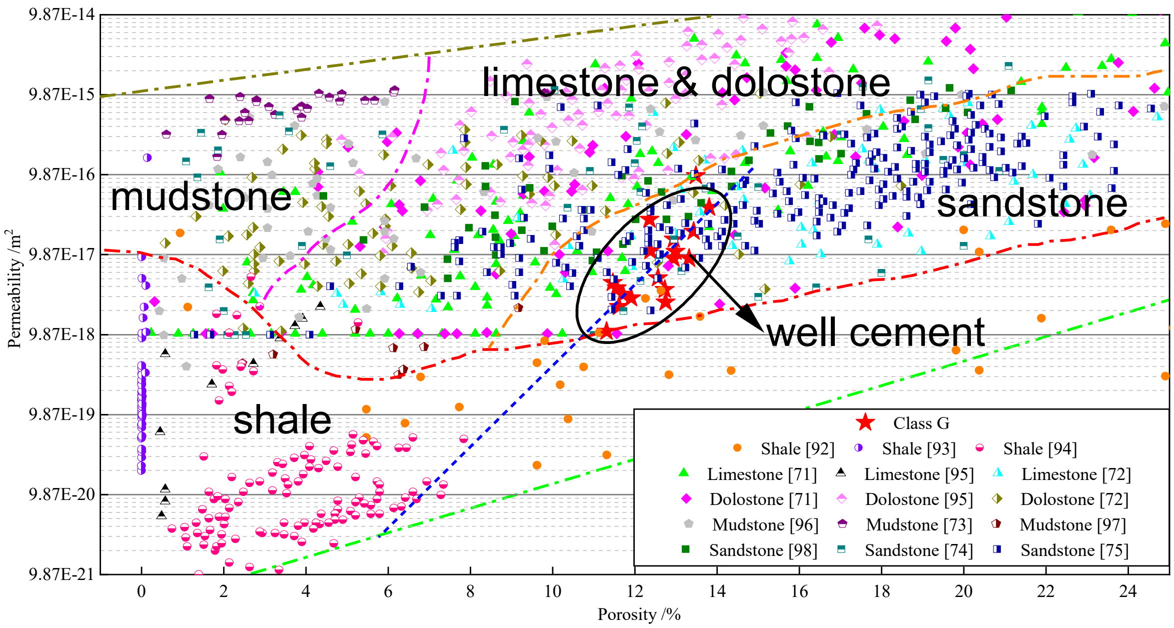

Figure 4-17 Comparison of cement poroperm data with poroperm data of various formation rocks.

The blue dash line in Figure 4-17 is the linear fitting curve of the poroperm data of cement. Because both the porosity and the permeability will decrease as a result of continuing hydration of the cement (Banthia and Mindess, 1989), the blue dash line in Figure 4-17 will eventually extend to the left-bottom corner and intersect the shale zone. This is consistent with the findings that with sufficient hydration time, the mature cement will increasingly behave like a shale, the lowest permeability flow media shown in Figure 4-18 (Fjaer et al., 2016; Loizzo et al., 2017; Powers, 1954; Williams et al., 2009).

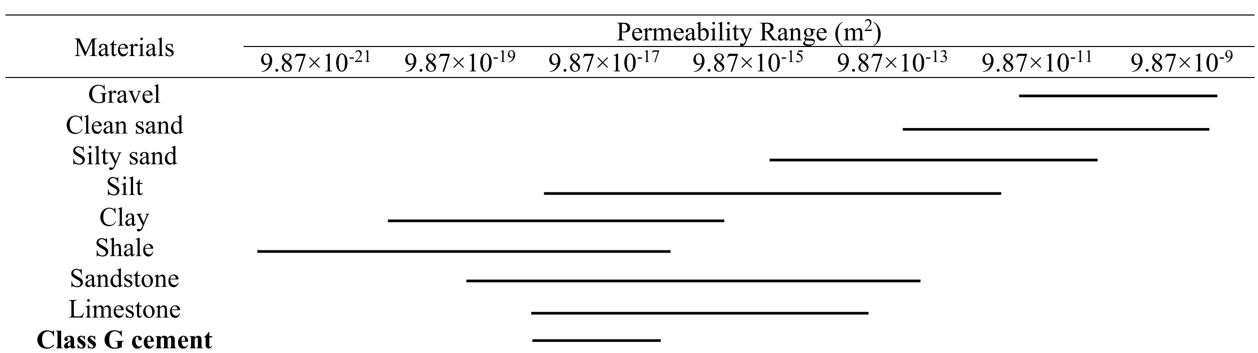

Figure 4-18 Permeability range of well cement and common rock types (modified from Brace (1980), and Wang and Narasimhan (1985)).

The data presented in Figure 4-17 also show that the permeability range of various rocks overlapped with each other. Similar results have also been reported by Brace (Brace, 1980) and Wang and Narasimhan (Wang and Narasimhan, 1985) (Figure 4-17). By comparing the permeability range of early-age well cement to the ones shown Figure 4-18, we can see that the cement permeability range also overlapped with shale, sandstone and limestone. However, the permeability range of neat early-age well cement samples is much narrower than formation rocks like shale, sandstone or limestone. The Class G cement is made from limestone and clay, and one interesting finding from Figure 4-18 is the permeability range of early-age Class G cement stays in the overlapping range between limestone and clay.

4.5 Conclusions

In this study, a new experimental/numerical approach is proposed which combines CT characterization and CFD modeling to investigate the permeability of neat early-age well cement sample. This approach provides a quantitative means to estimate porosity and permeability of representative volume elements selected from cement sample. The main findings are:

1) For the CT scans performed on cement samples, quicker scan times and good seals can improve the quality of the CT images. Based on the computed tomography and 3D reconstruction technique, the realistic microstructure of the cement can be visualized and then modeled for fluid flow simulation. As the physical model in the simulation is much smaller than that used during the experimental measurement of cement permeability. The inlet pressure in the simulation should be adjusted accordingly to make sure that the flow is laminar and stable.

2) At micron scale (2.64 μm), the non-uniform porosity distribution of cement samples makes the porosity and permeability vary at different RVE locations. The minimum RVE should be determined on a case-by-case basis. Analysis of RVE size effect shows that the porosity probably decreased from cement sample’s center to the cement sample’s edge. The characteristic effective porosity versus permeability correlation curve was generated to calculate the permeability of the

cement sample. The permeability of the early-age Class G cement at downhole condition was estimated to be 9.771×10^{-17} m^2.

3) Comparative study of the porosity and permeability of early-age well cement and formation rocks indicates the cement poroperm data are mainly comparable to tight sandstone. Comparisons also show that the early-age well cement has a narrower permeability range than formation rocks. The trend of cement linear fitting curve suggests that if the hydration process of neat early-age well cement sample continues, poroperm characteristics will approach those of shale.

Future work will involve an experimental test of the permeability of cement cured under the same downhole condition. A major focus will be on the use of more powerful tools which can overcome the limit of handling large RVEs. Practically, the cement poroperm correlations should be used only for qualitative purposes. To obtain a more accurate correlation between the poroperm, a large number of data points should be collected with considering various physical factors such as irreducible fluid saturation, grain size distribution, grain shape, lithology, and mineralogy, etc.

Chapter 5 Quantifying the Impact of 2D and 3D Fractures on Permeability in Wellbore Cement after Uniaxial Compressive Loading*

5.1 Summary

Stress-induced fractures in wellbore cement can form high-risk pathways for methane or carbon dioxide leakage yet little to no quantitative information on the impact of these fractures has been reported. To investigate this, scanning electron microscopy (SEM) and micro computed tomography (micro-CT) techniques were utilized to quantify the 2D and 3D geometrical parameters of cement fractures in mature thermal thixotropic cement samples that were subjected to pre- and post-peak compressive stress. A novel simulation method was also proposed to quantify the impact of the stress-induced realistic 3D fractures on the cement permeability.

Results show that: i-) For pre-peak samples, 90% of the 2D fractures have length and width smaller than 100 μm and 5 μm, respectively. Although higher compressive stress reshaped the 3D fractures and increased the fracture length and width, no well-propagated fractures were observed; ii-) For post-peak samples, distinctly visible (> 0.1 mm) well-propagated fractures were generated but failed to penetrate the entire sample, therefore the effect of stress-induced fractures (up to 1.0% strain) on cement sample's permeability is limited; and iii-) CT-based 3D visualization and simulation both show that inclusion of a correctly engineered fiber additive is able to blunt the fracture propagation in cement samples.

We conclude that the fractures in cement matrix created by the monotonic compressive stress (up to the limit of uniaxial compressive strength, UCS), are not likely to form continuous leakage pathways. This is because the 2D fractures in cement matrix as shown by SEM images are in

* This chapter was published as "Yang, X., Kuru, E., Gingras, M., Iremonger, S., Taylor, J., Lin, Z., & Chase, P. (2020). Quantifying the Impact of 2D and 3D Fractures on Permeability in Wellbore Cement after Uniaxial Compressive Loading. SPE Journal. https://doi.org/10.2118/198683-PA"

limited dimensions while the 3D fractures in cement matrix observed from CT-based 3D models have poor connectivity, generally indicating that leakage pathways of significant permeability would not form as a result of compressing the cement samples up to their UCS limit. Inclusion of a fiber additive is expected to enhance cement integrity by limiting the fracture propagation.

5.2 Introduction

As the main component of natural gas, methane has a global warming potential more than 70 times greater than carbon dioxide (CO_2) over a 20-year period (Government of Canada, 2019). Upstream oil and gas industry facilities are Canada's largest industrial emitters of methane, releasing 44% of the country's total methane emissions (Government of Canada, 2019). Alberta is the main oil and gas producer in Canada and by far has the largest number of oil and gas wells in the country (~75%). Fugitive emissions from oil and gas wells are a major contributor to uncontrolled methane release. The latest report from the Alberta Energy Regulator (Alberta Energy Regulator, 2018) showed that Alberta has an increasing trend of leaking wells, as shown in Figure 5-1.

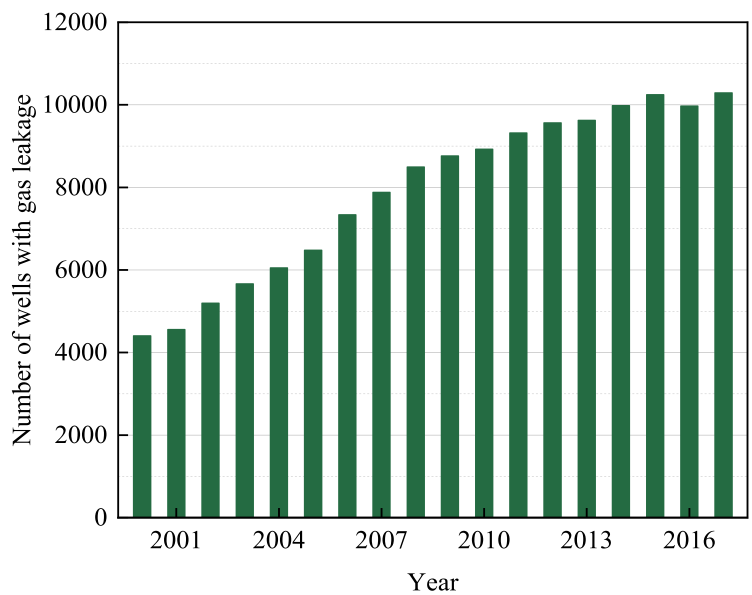

Figure 5-1 The increasing trend of leaking wells in Alberta since 2000 (Alberta Energy Regulator, 2018).

Understanding and mitigating leakage pathways is essential to minimize the impact of leaking wells on the environment. Various blends of Portland cement are generally used to provide well integrity by sealing wellbores from hydrocarbon bearing formations. Good wellbore cementing is expected to provide structural support and zonal isolation throughout the life of a well, from well construction, through hydrocarbon production, to post-abandonment. Modern wells are subjected to complex external forces during their lifetime, such as thermally induced stresses in steam-assisted gravity drainage (SAGD) wells or cyclic load due to multistage fracturing (Fjar et al., 2008). These external loads have the potential to create stress-induced fractures and deformations, which may result in interconnected flow paths leading to increased permeability and potential gas leakage (Bonett and Pafitis, 1996; Skorpa and Vrålstad, 2018). An example of this is the hydraulic fracturing treatment for horizontal wells. Wellbore cementing is a significant process before the perforation. Stress-induced fractures would be generated after perforation and then fluid leakage would happen. The interactions among created fractures, other formation discontinuities and wellbore cement would give rise to the alteration of cement integrity and its corresponding permeability (J. Tang et al., 2019; F. Zhang et al., 2019).

In spite of their importance for controlling the long-term integrity of the well, very little quantitative information is known about the nature of stress-induced fractures and their contribution to cement permeability. The importance of having quantitative information for stress-induced fractures is not just limited to the control of methane leakage in production or abandoned wells, but also to the control of CO_2 leakage in CO_2 Capture and Storage (CCS) wells. Most of the previous research in this case has focused on the influence of CO_2–cement chemical reaction on wellbore cement integrity (Carey and Lichtner, 2011; Garnier et al., 2010; Yalcinkaya et al., 2011). Self-healing is one of the outcomes of the CO_2–cement chemical reaction, which can significantly affect the wellbore cement integrity. Recent studies indicated that the self-healing of wellbore cement depends on the fracture width (Abdoulghafour et al., 2013; Carroll et al., 2017).

Quantitative characterization of the stress-induced fractures would facilitate an understanding of the interrelation between the fractures and the resultant permeability. Because the cement pore sizes show a wide range of variability, the dimensions of the fractures also range from nanometer to millimeter scales (Barnes and Bensted, 2002). Thus, no one imaging method can capture the entirety of the complex fracture geometries expected in wellbore cements. Scanning electron microscopy (SEM) and X-ray computed microtomography (micro-CT) techniques have been widely used to observe fractures in cement paste (Attiogbe and Darwin, 1987; Panduro et al., 2017; Gallucci et al., 2007; Hlobil et al., 2016; Jung et al., 2013; Kabilan et al., 2016; Kutchko et al., 2009; Shadravan et al., 2015; Stutzman, 2012; Torsæter et al., 2015b). For the first time in the literature, we report quantified geometrical parameters of 3D fractures in a cement matrix using micro-CT techniques and also determine the importance of SEM imaging and magnification on the 2D characterization of the fracture width and length.

Once quantitative information about fracture geometry is determined, the next focus is establishing a relationship between stress-induced fractures and permeability. Information about the connectivity of the captured fractures would be highly affected by the resolution of the characterization equipment (Gallucci et al., 2007; Kabilan et al., 2016). Hence, any fractures beyond the resolution of the characterization equipment will be not captured. To overcome this limitation, a novel numerical simulation, the dual-domain model, was proposed. The new model not only considers the realistic microstructures of the cement matrix but also the geometrical features such as fractures, pores, flaws or grain boundaries beyond the resolution of the testing methods.

The present study is aimed at improving the understanding of the influence of the compressive stress on the cement permeability, which is the primary factor pertaining to potential gas leakage. The experimental procedures on quantitatively characterizing stress-induced fractures and the novel dual-domain simulation method are described first. The effect of the compressive stress on the cement permeability and a possible solution for improving the cement integrity are discussed next by considering the 2D and 3D quantitative results of stress-induced fractures.

5.3 Materials and methods

5.3.1 Specimen preparation.

Samples were prepared using Class G cement mixed with 40% silica flour (by weight of cement). The blend also contained a typical additive package used in oil and gas well applications, which include expansion, accelerator, fluid loss, free water control, dispersant and anti-foam agents. Notably, all these additives were minor components (<2% each) relative to that of the bulk. The water/cement ratio of the samples was 0.48. The cement slurry was transferred to a 50.8 mm (diameter) × 101.6 mm (height) plastic cylindrical mold and then was placed into the curing chamber. Samples were cured overnight at 15 MPa under ambient temperature conditions (~22 °C). Subsequently, the temperature was ramped to 50 °C for an additional 6 days to accelerate curing. Finally, the samples were cooled to room temperature overnight (8 days total). Images of the curing chamber as well as other experiment apparatus used in this research can be found in Figure 5A-1 in Appendix A.

5.3.2 Uniaxial compression tests

After curing, cylindrical samples were machined using a diamond surface grinder to produce samples with two flat, parallel surfaces (± 0.1 mm tolerance) free of surface defects. Dimensions of the ground samples were about 100.0 mm in length and 50.0 mm in diameter. Uniaxial compression tests were conducted using a GCTS RTX-1000 testing system. Axial and radial strains were measured using a combination of linear variable displacement transducers (LVDT). The sensitivity of the LVDT was ± 0.1 μm.

A 0.05% strain/minute deformation rate was maintained during the test. The strain-controlled mode was employed to avoid uncontrolled failure while reaching the maximum compressive strength. The test duration was 12–20 minutes and the stress and strain data was collected throughout the test.

5.3.3 2D fracture characterization by the SEM technique.

Thin sections of the cement samples (Figure 5-2a) were prepared at the thin section lab of the University of Alberta. One limitation of SEM technique is that the cement internal structure can be affected during SEM sample preparation. This limitation has been thoroughly discussed and a practicable method proven to induce minimum damage was used to prepare cement thin sections for SEM examination (Bisschop and van Mier, 2002; H. Zhao and Darwin, 1992). Thin slices were removed with a circular saw from the cement pieces along the longitudinal direction using ethanol as lubricant. For thin sections, the mounting faces were flattened first. Then, epoxy impregnation was applied after the samples were dried. Finally, excess sample material was trimmed off and the sample was lapped to its final thickness of 900 μm.

Since cement is a non-conductive material, the cement thin sections were coated with carbon to make them conductive. SEM images were then obtained using Zeiss Sigma Field Emission SEM equipment. Figure 5-2 illustrates the process of the 2D fracture characterization. To ensure an accurate representation of the sample, consistency and veracity of the measurement results, the following guidelines were strictly adhered to.

For each thin section (Figure 5-2a), SEM images were captured under six different magnifications (39, 156, 625, 1250, 2500, 10000×) and at eight different locations to minimize the impact of local defects and acquire more representative data (Figures 5-2b and c). A total of 384 SEM images were obtained and analyzed. At each selected location, the SEM images were captured starting at lower magnification and moving to higher without changing the center of the focus (example images can be found in Figure 5A-2). Pores were also included in the fracture measurements as there is no clear standard technique to differentiate the pores from the fractures, especially when their dimensions are similar, such as with crack-like pores (Kendall et al., 1983) and shrinkage cracks (Grassl et al., 2010).

Fractures were measured manually using ImageJ (Schneider et al., 2012), a well-known open-source image analysis software. To determine the dimensions of the fractures, free-hand lines were drawn on the observed fractures in the SEM images (Figure 5-2d). After setting the scale according to magnification of each SEM image, the length of each fractures could be calculated automatically (Figure 5-2e). While the inherent measurement error in SEM is approximately 3%, the actual error value depends on the resolution of the measurements. The resolution range of SEM measurements varied from 2.86 μm to 0.01 μm. Since SEM images were obtained under various magnifications, the error of the lowest useful magnification (156×) of 0.02 μm was used to represent the error of all SEM images.

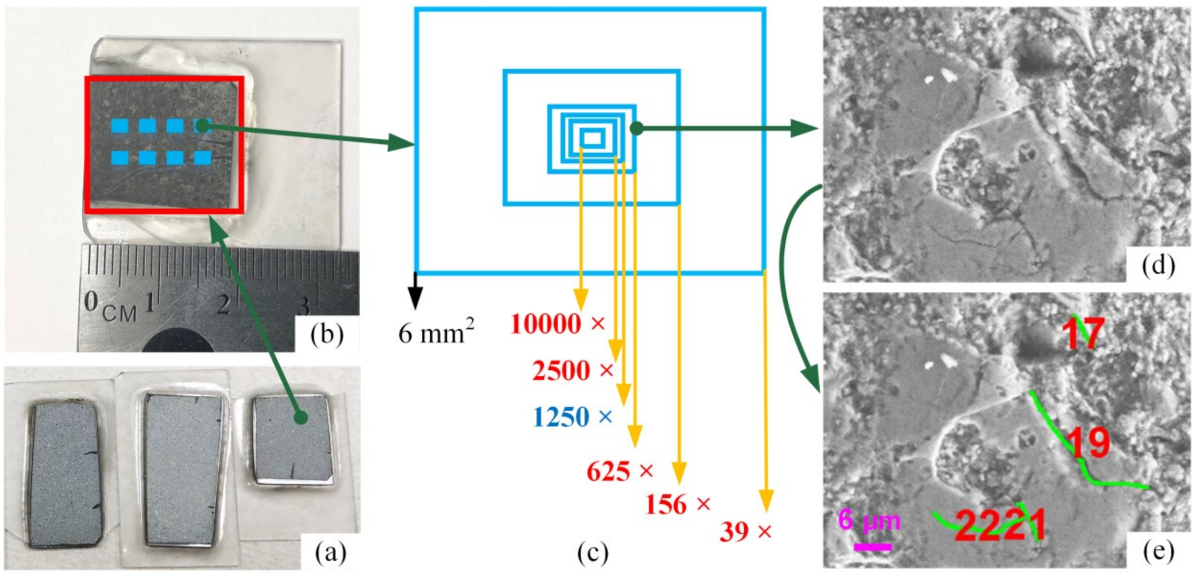

Figure 5-2 Illustration of the 2D fracture characterization process.

(a) cement thin sections. (b) scanned areas (blue) in each cement thin section. (c) scale of SEM images under different magnifications. (d) SEM image obtained under 625× magnification. (e) 2D fratures were labeled and numbered.

5.3.4 3D fracture characterization by micro-CT scan technique

Pre-peak cement samples were prepared by quartering the cylinders from the uniaxial compressions tests using a diamond saw and scanned using a SkyScan 1172 micro-CT scanner. The cylindrical samples were machined using a diamond surface grinder to produce samples with two flat, parallel surfaces for uniaxial compression test. To minimize the effect of the machining of cement end surfaces on the cement microstructure analyses, we only scanned the middle section of the cement samples. High energy X-rays are needed for the scan as cement samples were considered as high-density material. The adjustment of energy of the X-rays can be achieved by changing scan filters. A copper plus aluminum filter (Cu + Al) was selected for the CT scan to improve the contrast of CT images and also to reduce the beam hardening artifact. Flat field correction and alignment tests were performed before the CT scan. These two operations would make sure that the CT images have high contrast with less noise. Detailed scan parameters used for CT characterization are summarized in Table 5-3.

X-ray shadow projection images were generated first during the scan process. Once the CT scan was finished, NRecon software was used to reconstruct cross-sectional images from X-ray shadow projection images according to the Feldkamp algorithm (Bruker, 2013). A few reconstruction parameters have to be adjusted manually in a trial-and-error fashion to correct the beam hardening, ring artifacts, and provide alignment optimization.

Table 5-1 The scan parameters used for CT characterization.

Scan parameters	Value
Acquisition time (min)	50
X-ray beam form	cone beam
Total number of projections	486
Total number of cross-sectional images	987
Source voltage (kV) and current (uA)	100, 100
Scan filter	Al + Cu
Rotation step (degree)	0.4
Resolution (μm)	16.87

After reconstruction, volume data sets of 33.74 × 33.74 × 17.14 mm^3 with a resolution of 16.87 μm were obtained. The CT data was then imported into Simpleware^{TM}, a commercial 3D visualization and analysis software, for image segmentation. Gaussian deconvolution, which was proven as an effective threshold segmentation method for identifying the different phases in CT images of cement (Bossa et al., 2015; Němeček et al., 2011), was used to extract the 3D cement fractures from the gray-scale CT images. Prior to segmentation, Gaussian filter and gradient anisotropic diffusion filter (Pang et al., 2017) were applied to smooth the noise in CT images. 3D geometrical parameters of each individual 3D fracture were calculated to determine how the cement microstructure changed due to the uniaxial compressive loading. These 3D geometrical parameters collected were the fracture length and, the fracture width as well as the 3D shape factor (Devarrewaere et al., 2015).

5.3.5 The dual-domain model

CT-based 3D simulation techniques have recently been used to investigate the mechanical and transport properties of cement paste (Das et al., 2016; Kabilan et al., 2016; Kjøller, Torsæter, et al., 2016; Yang et al., 2019). Handling and cognizance of the multiscale characteristic of the cement structures are critical to the accuracy of the CT-based 3D simulation. A multiscale model which characterizes the cement paste at different levels individually has been built to study the mechanical properties of the cement paste (Hlobil et al., 2016; Hongzhi Zhang et al., 2017). However, there still remains a challenge to simulate bulk cement transport properties. Considering the more realistic multiscale characteristic of the cement microstructures, a dual-domain transport simulation method is, therefore, used in this study.

Cui and Cahyadi (2001) (Cui and Cahyadi, 2001) presented a bicomposite model to predict the permeability of the cement paste. In their model, cement paste consists of two phases. One phase is the relatively high-permeability phase, like capillary pores, and the other is a relatively low-permeability phase, such as unhydrated cement particles as well as crystalline and amorphous hydration products. The dual-domain model proposed here is conceptually similar to bicomposite model. However, there are some major differences between these two models on how they are used to predict the permeability of materials with multi-scale characteristics. The bicomposite model is an analytical model, which is utilized to calculate the cement permeability based on the mercury intrusion porosimetry measurements. However, the dual-domain model used in this study is a numerical model based on finite volume method, which calculates the cement permeability based on the CT-based cement microstructures.

The simulated flow in the dual-domain model can be described by the Navier-Stokes equation, whose vector formula is given as follows:

$$\rho\left[\frac{\partial \boldsymbol{v}}{\partial t} + (\boldsymbol{v}\cdot\nabla)\boldsymbol{v}\right] = \rho\boldsymbol{f} - \nabla p + \mu\nabla^2\boldsymbol{v} \qquad \text{Eq. (5-1)}$$

where the left side of Eq. (5-1) is the inertial term, $\rho\boldsymbol{f}$ on the right side is the body force term, ∇p is the pressure gradient, and $\mu\nabla^2\boldsymbol{v}$ is the viscous term (Ferziger and Perić, 2002). The simulated flow through cement body was assumed to be steady state, fluid is incompressible, and the gravity effect is negligible. Under these assumptions, inertial and body forces can be neglected. Hence the Navier-Stokes equation in Eq. (5-1) can be simplified into Darcy equation Eq. (5-2):

$$q = -\frac{k}{\mu}(\nabla p) \qquad \text{Eq. (5-2)}$$

Based on the model presented in Eq. (5-2), the pressure differential ∇p drives the flow and, therefore, controls the flow velocity. In our analyses, the steady state flux q and its corresponding ∇p were first extracted from the simulation results. As the flow rate q, the fluid viscosity μ and pressure ∇p are known, the permeability k could then be calculated.

The first advantage of the dual-domain model is that it can represent the multiscale nature of the cement microstructure. Figure 5-3 shows the difference in fluid flow results between the dual-domain simulation used here and a traditional single-domain simulation (Kabilan et al., 2016; Kjøller, Torsæter, et al., 2016). Because of the multiscale characteristic of the cement microstructure, some small pores and fractures can not be captured by micro-CT investigations since their size is beyond the resolution of the technique. Therefore, these small pores and fractures are normally ignored in the single-domain simulation (Figure 5-3b). These structures are named as the porous domain in the dual domain simulation (Figure 5-3c). The porous domain is conveniently used to model the smaller cement characteristic features such as pores, flaws or grain boundaries that can not be practically resolved or discretized because they would require an impossibly fine grid.

The second advantage of the dual-domain model is that the model can be used to quantify the flow impact of seemingly-isolated fractures on the entire sample. We use the term ‘seemingly-isolated fracture’ to refer to the fractures that are isolated at the resolution of the micro-CT scanner used in our analyses. In reality, the seemingly-isolated fractures will be permeable if they are connected to a permeable media (i.e. porous domain). Simulation results discussed in later sections show that the seemingly-isolated fractures still affect the cement permeability. The fracture geometry of a cement paste (Figure 5-3a) is captured non-destructively by using the CT image analysis technique. The fracture geometry is treated as a relatively high-permeability phase and set as a fluid domain when running the simulation.

Finally, the dual-domain model can be utilized for mechanical property simulation. As the primary interest of this study is identification of potential leakage pathways, the dual-domain model application is limited to fluid transport simulation. The limitation of the dual-domain model is that the simulation requires the porosity and permeability of the porous domain (cement matrix), which need to be experimentally measured before performing the numerical simulation. Detailed dual-domain simulation parameters are summarized in Table 5A-1. For the application of CT-based 3D simulation of the fluid transportation in a cement matrix, full details of the developed methodology and implementation have been previously reported (Yang et al., 2019).

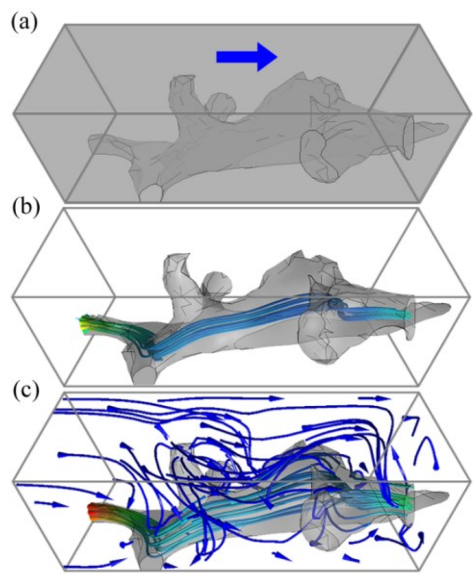

Figure 5-3 Comparison of the single-domain simulation and the dual-domain simulation.

(a) fracture geometry. (b) result of fluid flow using single-domain simulation. (c) result of fluid flow using dual-domain simulation.

5.4 Results and discussions

5.4.1 Compression testing and micro-CT/SEM imaging.

Uniaxial compression tests were performed to determine the stress-strain behavior of the cement samples, which is depicted in Figure 5-4. Sample A, a control sample, was not exposed to any compressive load, representing the cement structure under unstressed conditions. Samples B and

C were loaded to a uniaxial compressive stress of 11.12 MPa and 15.86 MPa, respectively. For Sample C, the (peak) strain was recorded as 0.66% under the stress equivalent to uniaxial compressive strength (UCS=15.86 MPa). Samples B and C were categorized as pre-peak samples in this study. Two samples were compressed beyond the peak strain level of 0.66%. These two samples, Samples D and E, were compressed up to 0.82% and 1.02% strain levels, respectively, and were categorized as post-peak samples. Note that all cement samples were loaded using the same axial strain rate. For the post-peak samples, the recorded compressive stress was reduced from the peak levels to 15.56 and 10.47 MPa for Samples D and E, respectively.

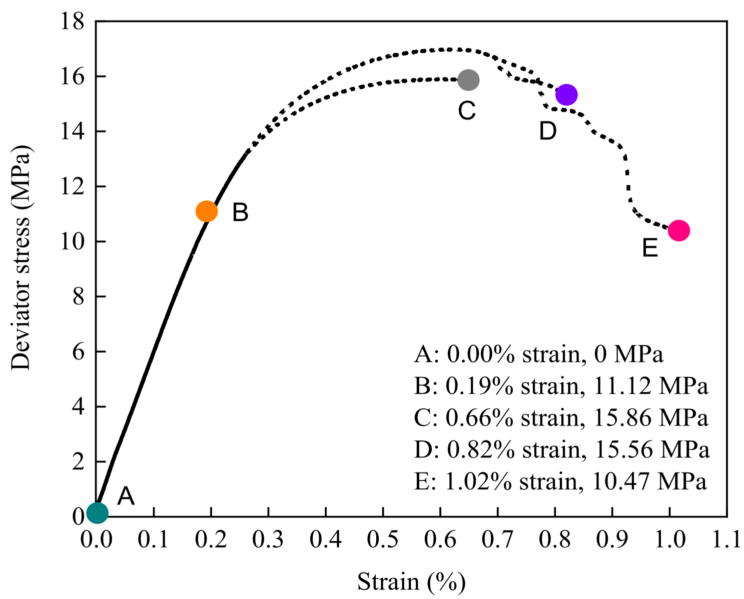

Figure 5-4 Stress-strain curves of the five samples obtained by the uniaxial compression test.

After uniaxial compressive loading, the samples were initially characterized using micro-CT, which is currently the only mature method allowing for non-destructive investigation of the interior 3D microstructure cement paste. Figure 5-5 illustrates the process of the 3D fracture characterization. The resolution of the micro-CT technique was limited by sample size, which must be small enough to acquire high resolution CT images. However, larger samples, as shown in Figure 5-5a, tend to give more representative results by minimizing size effects (Su et al., 2015). In addition, larger samples are easier to prepare and test. Here, a compromise was made with the pre-peak samples: prepare larger samples for uniaxial compression testing and subsequently cut them into smaller pieces for the CT scan tests (Figure 5-5b).

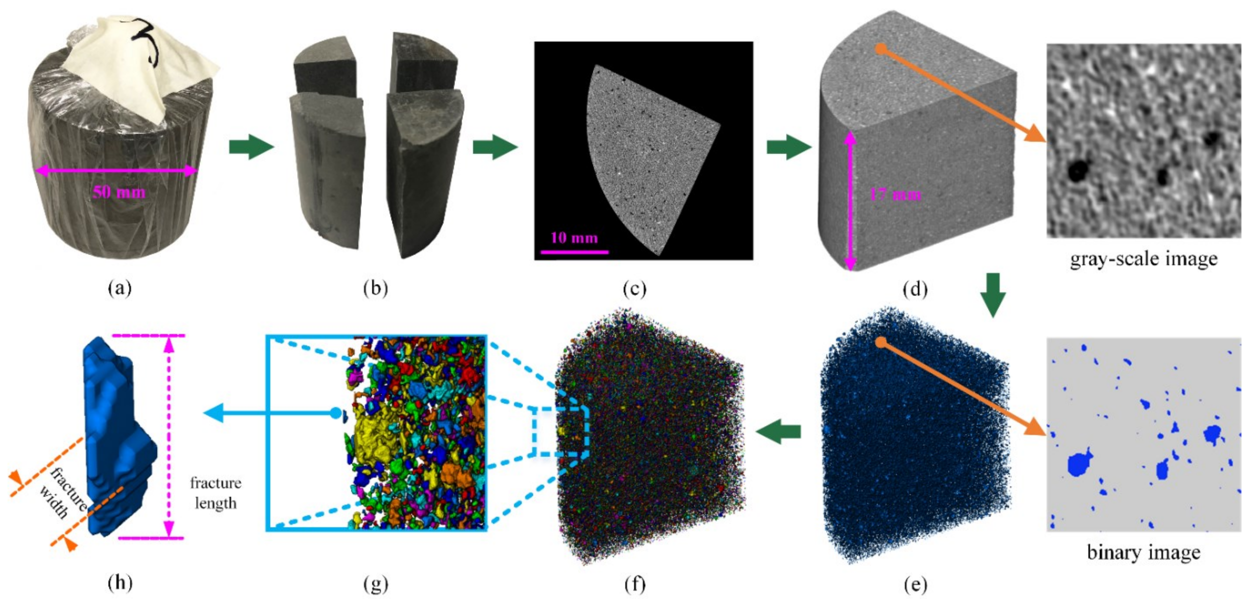

Figure 5-5 Illustration of the 3D fracture characterization process.

(a) cement sample. (b) cement pieces after sawing. (c) a cross-section CT image of a cement piece. (d) reconstructed 3D model of a cement piece. (e) extracted cement pores and fractures. (f) colored pores and fractures for identification purpose. (g) an enlarged view of (f). (h) fracture length and width measurement on an individual fracture.

SEM was commonly used together with micro-CT to characterize materials which have multiscale microstructures such as coal, rock and cement (Ramandi et al., 2016, 2017; Vrålstad et al., 2016). This is because the resolution of the micro-CT is significantly influenced by the sample size. In this case, the SEM was used to capture the smaller cement characteristic features such as pores, flaws or grain boundaries beyond the resolution of the micro-CT. SEM technique has previously been used for analyzing 2D fractures in cement paste by Attiogbe and Darwin (1987), Ammouche et al., (2000), Wong et al., (2012) and other researchers. The fracture geometrical parameters (i.e. length, width, and shape factor) are usually measured at a certain magnification. However, results of the fracture measurements can substantially vary depending on the magnification used during the observations, mainly because of the heterogeneous and multiscale characteristics of the cement paste microstructure. Taking these factors into account, it was found that the preferred magnification for SEM analysis was 156× to 625×, see Appendix B, which covers a wide range of structure dimension from 11 nm to 3 mm. A full discussion on impact of magnification range is presented in the supplementary information. SEM images obtained at 1250× magnification allow for comparison to previous studies on fracture density, the length of the fractures per unit area (Attiogbe and Darwin, 1987).

5.4.2 2D and 3D fracture data in pre-peak stress samples.

To quantify the relationship between fracture data and pre-peak stress, compatible measures which can be applied to both 2D and 3D fracture data needed to be identified. This is due to the differences in magnification levels used to obtain the SEM and micro-CT data. Here, the fracture length and width distribution at different pre-peak stress levels were analyzed as both of these parameters could be calculated from the 2D and 3D analyses.

Figure 5-6 depicts the length and width distribution for the 2D and 3D fracture data. Using this, the D50, a statistical measure where 50% of the measured data is smaller than this value, was extracted and D50 values are summarized in Table 5-2. For 2D fractures, the maximum observed fracture length was longer than 200 μm, however, more than 90% of the fracture lengths were shorter than 50 μm. As such, the histograms and the cumulative curve plots, shown in Figures 5-6a and b, respectively, were only focused on the fracture length distribution ranging between 0 and 50 μm. The 2D fracture width, shown in Figures 5-6c and d, also exhibited a wide distribution range but more than 90% of the fractures were smaller than 5 μm and thus, the width distribution analyzed was 0 to 5 μm.

Table 5-2 Summary of geometrical parameters of 2D and 3D fractures in uniaxially compressed (pre-peak) cement samples.

Sample	Stress (MPa)	Percentage of Uniaxial Compressive Strength	3D Shape Factor	2D Fracture (μm)		3D Fracture (μm)	
				Length	Width	Length	Width
Sample A	0	0	1.05	1.74	0.220	75.65	44.14
Sample B	11.12	70	1.12	2.48	0.345	77.07	44.67
Sample C	15.86	100	1.13	3.05	0.275	80.78	46.17

As shown in Figure 5-6 and Table 5-2, D50 values of the length and width generally increased with increasing compressive stress for both 2D and 3D fractures, indicating that the average size of the fractures increased with the increasing compressive stress. In other words, higher compressive loads caused fracture propagation or simply created more fractures, which is in line with the results from a previous study (Spooner et al., 1976).

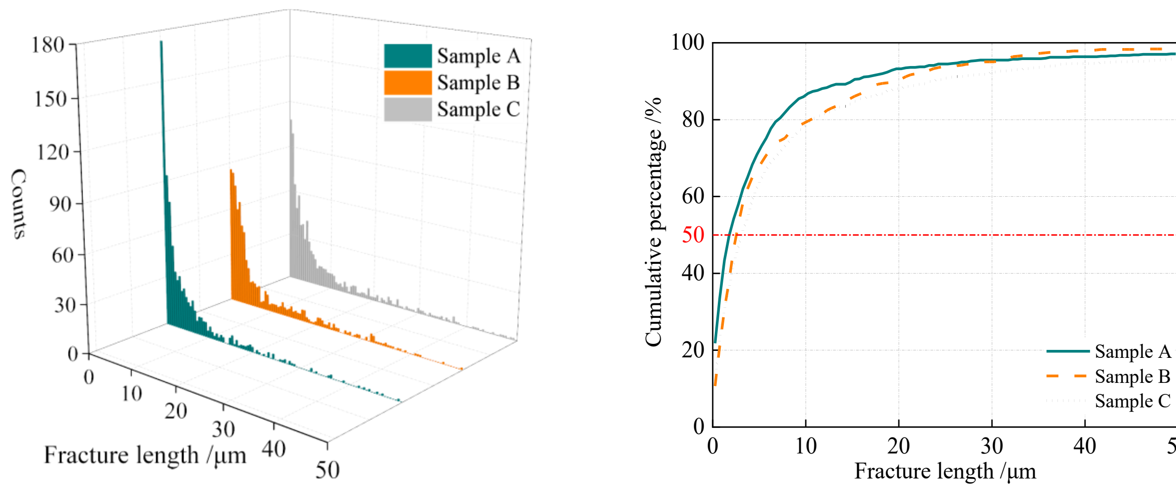

2D fracture length (a) Histograms (b) Cumulative curves

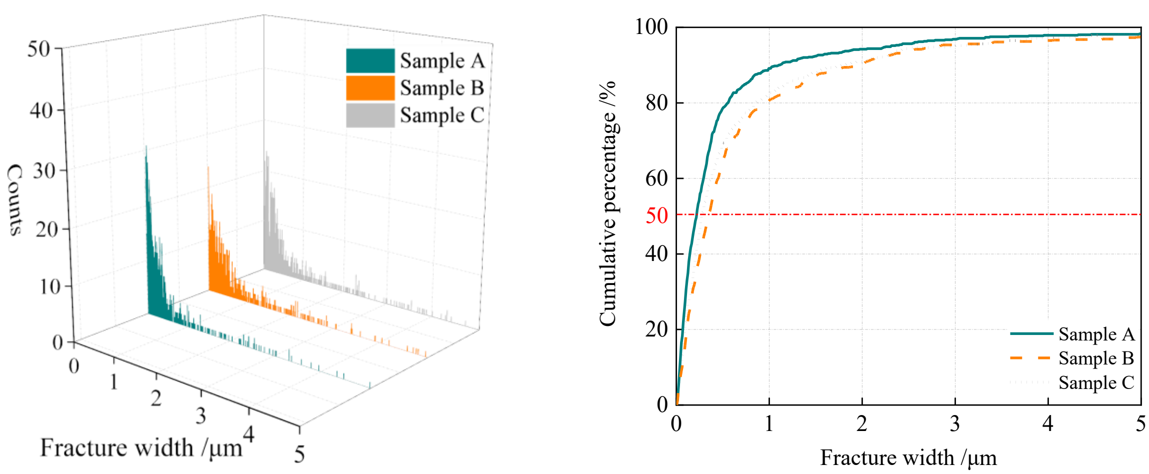

2D fracture width (c) Histograms (d) Cumulative curves

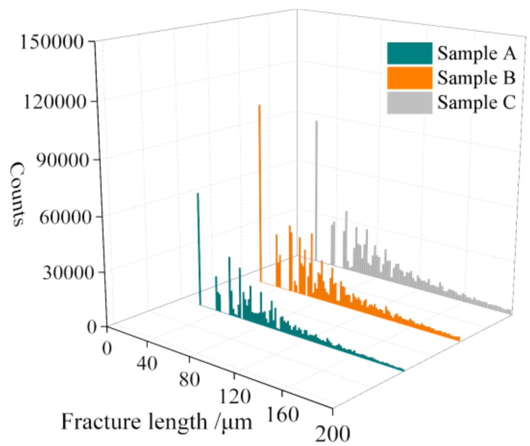

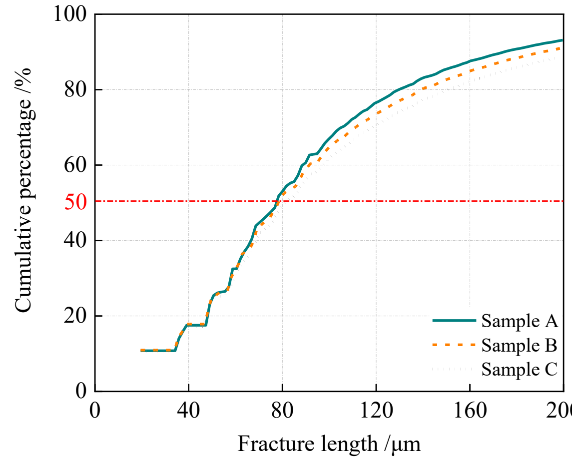

3D fracture length (e) Histograms (f) Cumulative curves

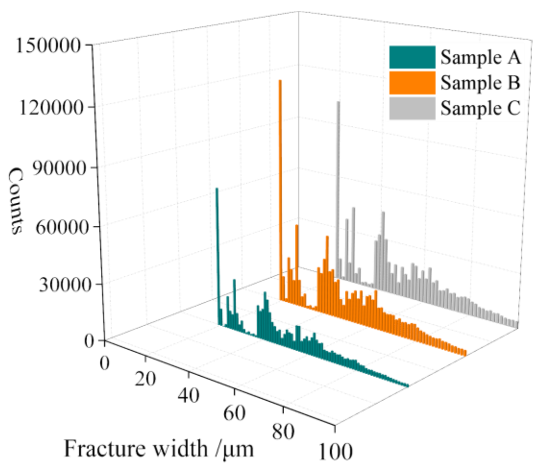

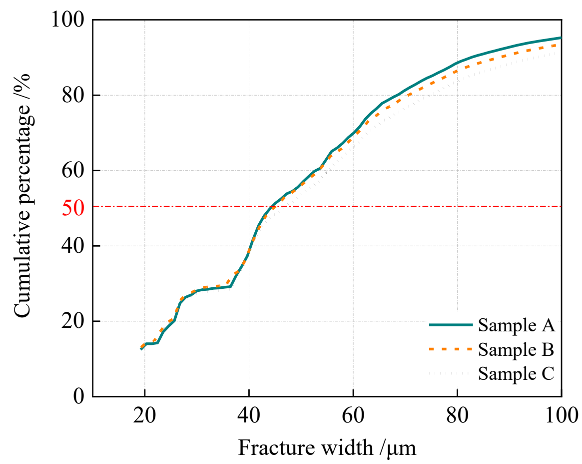

3D fracture width (g) Histograms (h) Cumulative curves

Figure 5-6 Fracture length and width measurement results based on the 2D and the 3D analyses of pre-peak cement samples.

One unanticipated finding was that the D50 of width in Sample B obtained from 2D fracture data was higher than that of Sample C. While there are few published research results directly showing how the 2D surface fracture geometry of cement changes with increasing compressive stress, related research aided in indirectly explaining this finding. Saito and Ishimori. (1995) observed that the permeability of cementitious material decreased with the increasing compressive stress. Generally, both the fracture length and the width are expected to affect the permeability (Hoseini et al., 2009). The results from this study and others (Lim et al., 2000) show that fracture length generally increases with the increasing compressive stress. However, the change in fracture width is not a monotonic function of the increasing compressive stress. Here, the fracture width first increased with increasing compressive stress from 0 to 11.12 MPa and it then decreased when the compressive stress further increased from 11.12 MPa to 15.16 MPa. Therefore, the permeability decrease with the increasing compressive stress reported by Saito and Ishimori. (1995) could potentially be caused by the change of the fracture width rather than the change of the fracture length.

5.4.3 3D geometrical parameters vs. pre-peak stress.

The 3D geometrical parameters vs. compressive stress data are shown in Figures 6e to 6h and also summarized in Table 5-2. Due to the relatively low resolution of the micro-CT scan, the first half of the cumulative curves are not as smooth as the 2D scans. The lowest resolution used for obtaining SEM images was 2.70 μm, which was still higher than the resolution of the micro-CT (16.87 μm). Therefore, the observed 3D fractures from CT-scans mainly consisted of large capillaries and air voids, which are substantially larger than the fine fractures observed in 2D SEM images. As a result, the D50 of 2D and 3D fractures are significantly different. While compressing the cement sample, the large capillaries and air voids (acting as inherent flaws) may promote fracture propagation. In order to characterize the fracture geometry, the 3D shape factor is also used, which is equal to $1/\text{sphericity}^3$. The sphericity of an entity is defined as the ratio of an area of an entity to the area of a sphere, which has the same volume as the entity. Hence, the shape factor is equal to 1 for a perfect sphere. As shown in Table 5-2, the shape factor of 3D fractures also increased with the increasing compressive stress.

The increases in the 3D fracture length, width and the shape factor reveal that the applied compressive stress caused fracture propagation and reshaped the fractures. However, up to maximum compressive stress, no well-propagated fractures were found in pre-peak samples. Figure 5-7a and b show the cutting faces of Sample C and indicate that no visibly detectable fractures (>0.1 mm) can be observed from the cutting faces. Figures 7c to f show the CT images and 3D models of the cut sections of Sample B and C. On the micron scale, no well-propagated fractures were found in the pre-peak samples. In total, these findings suggest that the impact of pre-peak stress on cement integrity is quite limited.

It has been reported that the size, shape and distribution of the flaws initially present in the cement matrix and the magnitude of the applied load have significant effects on fracture propagation (Fossen, 2010; Lawn and Evans, 1977). Based on the analysis presented here, only limited fracture propagation was observed, even the cement sample was compressed to the uniaxial compressive strength. As suggested by an earlier study (ACI Committee 224, 2001), the cement paste is a nonlinearly deforming material, which can sustain a substantial amount of damage within the paste. A previous experimental study (L. Martin et al., 1991) demonstrated that damage in cement paste could be locally distributed without forming a continuous failure. In some special cases, the failure did not manifest itself until the pore structure was completely destroyed (Xie et al., 2008). Even though our experimental conditions are disparate from realistic wellbore conditions, recent research using triaxial tests also indicated that the impact of compressive loading on the bulk was very limited as the formation of well-propagated fractures was not observed (J. William Carey et al., 2014). After reaching the yielding stress, the wellbore cement samples either generated some small fractures followed by continuous deformation or simply plastically deformed. An abrupt stress drop normally indicates failure of a material. However, a recent experimental study (Sakai et al., 2016) has shown that under confining pressure conditions, an abrupt change in stress does not necessarily cause the formation of macroscopic fractures.

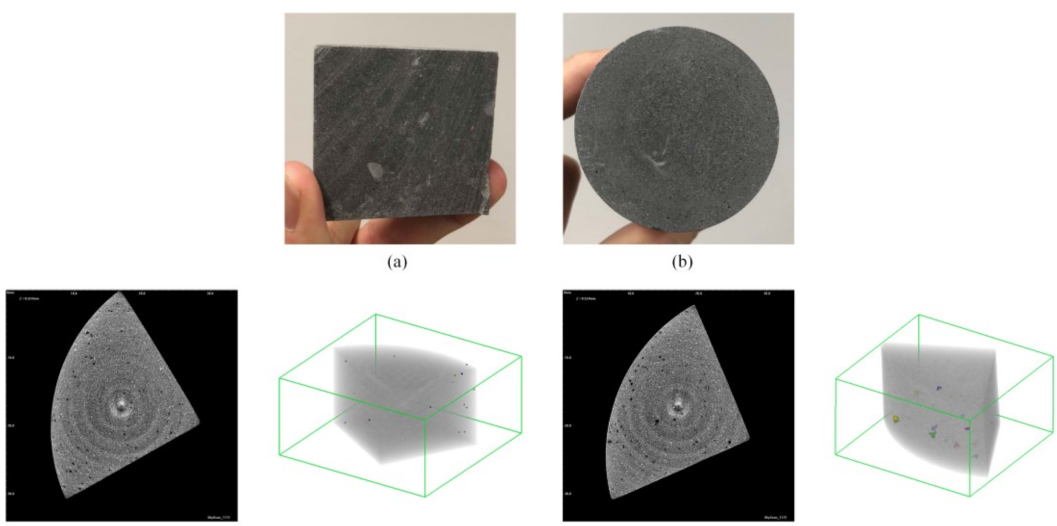
(a) (b)
(c) (d) (e) (f)

Figure 5-7 Cutting faces, CT images and 3D fractures of the pre-peak samples.

(a) Vertical cutting face, Sample C; (b) horizontal cutting face, Sample C; (c) CT image, cut section of Sample B; (d) 3D model, cut section of Sample B. (e) CT image, cut section of Sample C; (f) 3D model, cut section of Sample

5.4.4 Effect of post-peak stress on cement permeability.

Further compression above the maximum compressive strain resulted in visual observation of well-propagated fractures (>0.1 mm). Due to the presence of the large defects and to maintain the integrity of the remaining sample, CT scans was conducted for the full-size post-peak samples. Figures 5-8a and b show reconstructed 3D fractures. The largest observed fracture based on maximum fracture volume in Sample D had dimensions of 42.92 by 10.35 mm, whereas the largest fracture in Sample E was 71.12 by 40.26 mm. Both post-peak cement samples exhibit similar failure modes. In the horizontal plane, the fractures were propagated along the tangential direction in close proximity to the samples' lateral surface. In the vertical direction, the fractures failed to penetrate the entire cylinder and therefore still categorized as seemingly-isolated fractures.

The resolution of the micro-CT images used to reconstruct the 3D fractures is 17.20 μm and therefore, the observed seemingly-isolated fractures may be connected by other smaller cement characteristic features such as pores, flaws or grain boundaries. Therefore, the dual-domain simulation model was utilized to evaluate the impact of these large seemingly-isolated fractures on the cement permeability. The 3D models shown in Figs 8a and 8b can not only be used for 3D visualization, but also to provide the realistic physical geometry, which plays a vital role in computational fluid dynamics simulation. Based on these 3D models, we established the dual-domain model containing the realistic stressed-induced fractures (fluid domain). The experimentally measured permeability of the control sample, Sample A, is 0.1 mD and is set as the permeability of the cement matrix (porous domain). Both the upstream and downstream portions of the domain were extended to avoid creating unrealistic streamlines. The direction of the simulated flow is parallel to the compressive loading direction (from the top to the bottom in Figure 5-8). Sample dimensions, D50 of the observed fracture lengths, and permeability values obtained after the simulation are summarized in Table 5-3. Visualization of the simulation results, including the streamlines in each model, are shown in Figure 5-8.

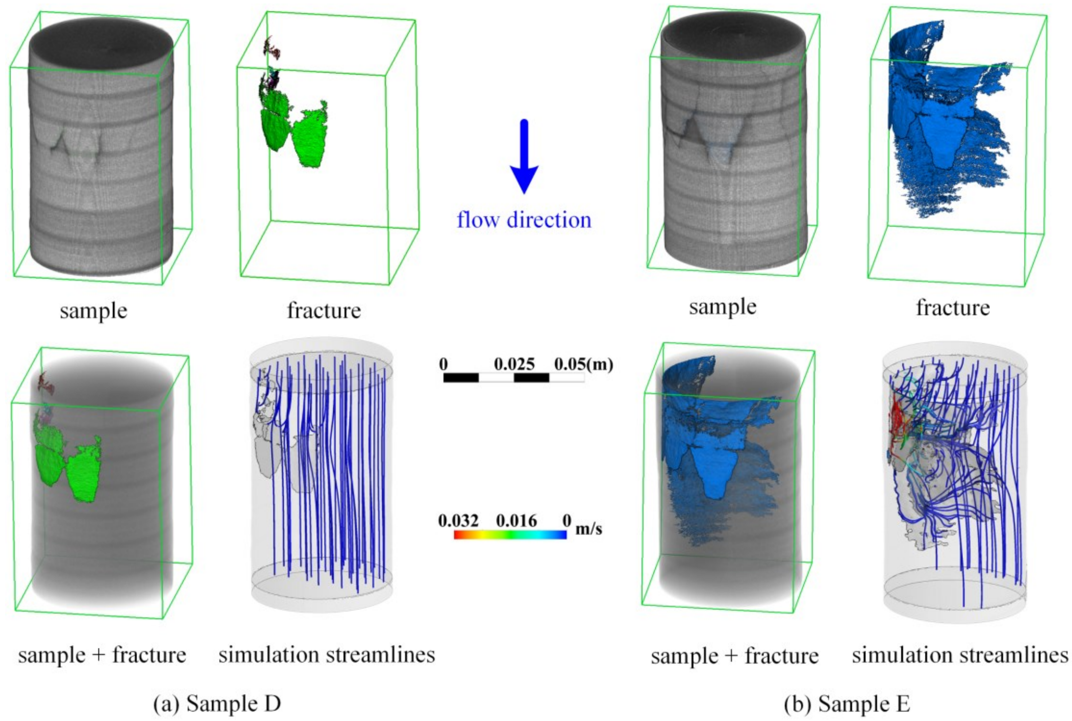

Figure 5-8 3D reconstruction results and simulation streamline of the post-peak samples.

Each cylinder sample were divided into seven segmentations and scanned individually. The dark rings in the cylinder lateral surface are artifacts generated during assembly of the segmentations into to a full-size cylinder. The color map represents velocities of the streamlines.

Due to the existence of the seemingly-isolated fractures, the direction of some streamlines in Sample D and E was altered. The heterogenous cement fractures leads to the heterogenous velocity field (Muljadi et al., 2016). As can be seen from Figure 5-8, there are some high velocity regions which were formed while the heterogenous 3D flow geometry giving rapid flow into large fracture spaces (J. Zhang et al., 2018).

Table 5-3 Permeability and fracture dimensions of the uniaxially compressed (pre and post-peak) cement samples.

Sample	Poisson's Ratio	Young's Modulus (GPa)	Strain (%)	Stress (MPa)	D50 of Fracture Length (mm)	Permeability of the Scanned Section (mD)
Sample A	-	-	0	0	0.07	0.10
Sample B	0.20	6.90	0.19	11.12	0.07	0.10
Sample C	0.20	6.37	0.66	15.86	0.08	0.10
Sample D	0.16	5.52	0.82	15.56	0.22	0.11
Sample E	0.14	5.54	1.02	10.47	0.21	0.21

For the purpose of gas migration, the larger visible fractures would contribute the most to the permeability rather than the cement matrix. However, since these fractures in Samples D and E are seemingly isolated, the permeability only increased by 0.01 mD and 0.1 mD, respectively. Thus, the effect of post-peak stress on the cement permeability seems to be limited under the strain conditions investigated. Table 5A-2 presents the most common casing/wellbore dimensions used in the field and the corresponding cement sheath thicknesses. It is notable that D50 values of 3D fracture lengths (Table 5-3) are significantly smaller than the cement sheath thicknesses reported in Table 5A-2. For example, Sample D has the largest D50 of 3D fracture length (0.22 mm), which is much smaller than the minimum cement sheath thickness of 22.22 mm in production section, shown in Table 5A-2. Results from this comparison further supports the conclusion that fractures formed within uniaxially compressed cement samples are very likely to be confined within the cement body (i.e. isolated fractures) and may not lead to significant leakage pathways.

These results can be explained by the Katz-Thompson permeability theory (Katz and Thompson, 1986) which describes the fluid permeability as a function critical pore diameter (which is related to the microstructure of materials). This is different from Darcy's law, which calculates the permeability based on the measured pressure gradient and the flow rate. The critical pore diameter is the smallest pore size of the effectively connected pores. The critical pore diameters for cement matrix have been reported to be less than 5 micron (Christensen et al., 1996). Since the resolution of the CT scanner used in this study (16.87 μm) is not high enough to capture the critical pore diameter of wellbore cement (< 5 μm), no through-going fractures were observed in the post-peak samples. Therefore, in this case the main contribution to the cement permeability comes from the cement matrix (porous domain). As a result, the seemingly-isolated fractures have limited effect on the permeability change unless they are able to penetrate the entire sample.

5.4.5 Improvement to cement performance via addition of fibers.

Previous results (Iremonger et al., 2015) have shown that fiber additives can significantly improve the ultimate failure strength of the samples under tensile load without sacrificing any other performance parameters. A recent study (Iremonger et al., 2017) also pointed out that fibers can limit crack propagation and dissipate the energy through a fiber pull out mechanism. Two fiber containing samples were prepared under identical conditions and incorporate 0.25% fibers by weight of the blend. After curing, the two fiber containing samples, F1 and F2, were compressed to the same strain level as the post-peak samples D and E, respectively. The stress and strain curves are shown in Figure 5-9 and 3D reconstruction and simulation results are shown in Figure 5-10.

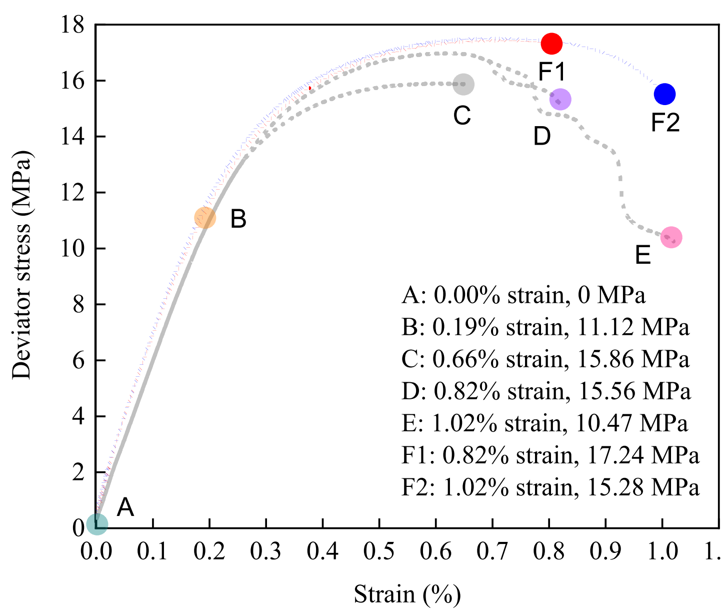

Figure 5-9 Stress-strain curve of the fiber containing samples obtained by the uniaxial compression test.

As detailed in Figure 5-9, the stress decrease was slower and less overt at higher strain compared to the post-peak samples, which decreased rapidly after reaching the maximum compressive stress.

This indicates that the fiber containing samples are more ductile than the unmodified post-peak samples. As shown in Figure 5-10, fewer fractures are observed in fiber containing samples under the same strain conditions. The largest fracture in Sample F1 is 0.76 by 0.22 mm, whereas the largest fracture in Sample F2 is 5.85 by 1.69 mm. In addition, the observed fracture propagation in Samples F1 and F2 is very limited, in line with the findings reported by Iremonger et al. (2017) indicating that fiber additives reduce crack propagation.

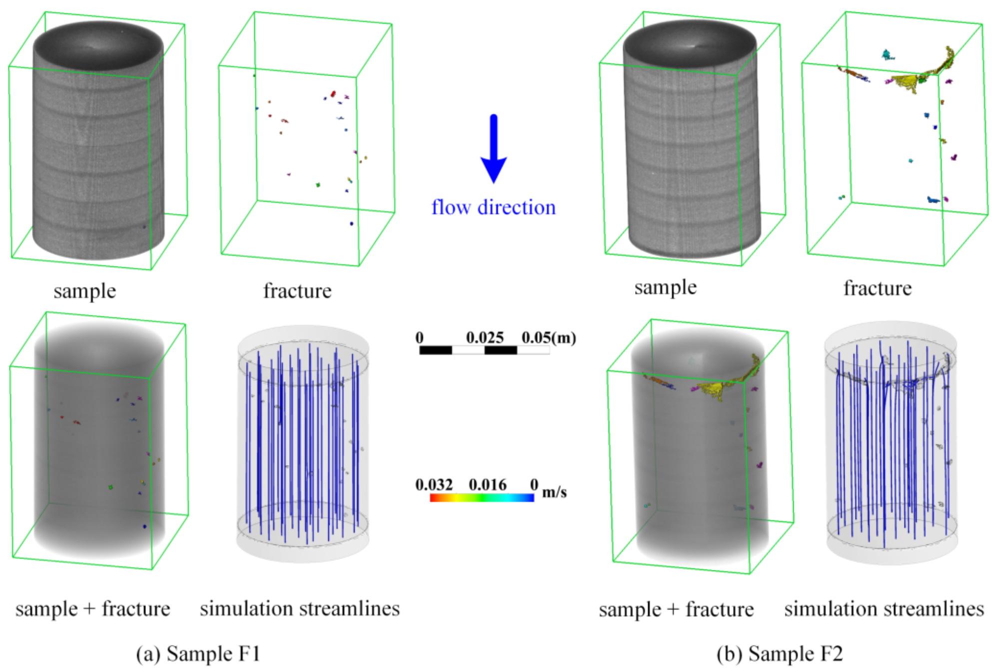

Figure 5-10 3D reconstruction results and simulation streamline of the fiber containing samples.

The dual-domain models were also established based on the full-size 3D models and the simulation streamlines are shown in Figure 5-10. Fracture dimensions and permeability values obtained after the simulation are summarized in Table 5-4. Remarkably, the permeability of fiber containing Sample F2 was 0.1 mD lower than Sample E, which was contained no fiber, under the same strain. The simulation results support those of Iremonger et al. (2017) in that a fiber additive is expected to enhance the cement integrity by mitigating the leakage pathways through limiting fracture size and propagation.

Table 5-4 Permeability and fracture dimensions of the fiber containing samples.

Sample	Poisson's Ratio	Young's Modulus (GPa)	Strain (%)	Stress (MPa)	D50 of Fracture Length (mm)	Permeability of the Scanned Section (mD)
Sample F1	0.20	5.78	0.82	17.24	0.06	0.11
Sample F2	0.17	5.83	1.02	15.28	0.06	0.11

5.5 Conclusions

The presented study demonstrates that the monotonic compressive stress (up to 1.0% strain) is unlikely to create significant leakage pathways in wellbore cement. Under pre-peak stress loading conditions, most of the observed 2D fractures are smaller than 5 μm, which can be self-healed through calcium carbonate precipitation (Abdoulghafour et al., 2013; Carroll et al., 2017; Jung et al., 2014). In addition, no well-propagated fractures were observed even though higher pre-peak stress reshaped the 3D fractures and increased the fracture length and width. Based on these findings, the fractures generated by the pre-peak stress does not increase the permeability of the cement and thus, is not a contributing factor to the formation of leakage pathways.

Once the compressive stress exceeds the uniaxial compressive strength, the higher strain will lead to considerable fracture propagation. However, these larger well-propagated fractures observed in the post-peak cements failed to penetrate the entire sample and therefore, still have have poor overall connectivity. In the dual-domain simulations, the calculated permeabilities were similar, again indicating poor communication between the large fractures and, thus, their contribution to bulk cement permeability is also found to be very limited. Addition of a fiber additive to post-peak stress cements was found to mitigate the number and size of the stress-induced fractures, giving a more robust structure through blunting of fracture propagation under these conditions. In addition, the permeability of the highest strained fiber containing sample was reduced compared to the non-fiber cement and is comparable to the values of the lower strain samples.

The proposed 2D and 3D fracture analysis methods give insight into a potential process to quantitatively characterize the stress-induced fractures in bulk cement. Currently, we are expanding this work to image and model the interface regions. Future studies will investigate fracture development or micro-annulus formation in cement paste under more realistic conditions (i.e. triaxial condition) and will consider, for example, the effects of cyclic loading on the cement microstructure and the quality of the wellbore cement/steel or cement/formation interfaces. Such efforts are likely to result in a better understanding of the factors influencing the gas leakage from oil and gas wells, which will be useful for fulfilling Canada's plan to reduce its greenhouse gas emissions to 30% below 2005 levels by the year 2030 (Government of Canada, 2018).

5.6 Appendix A-Supplementary figures and table

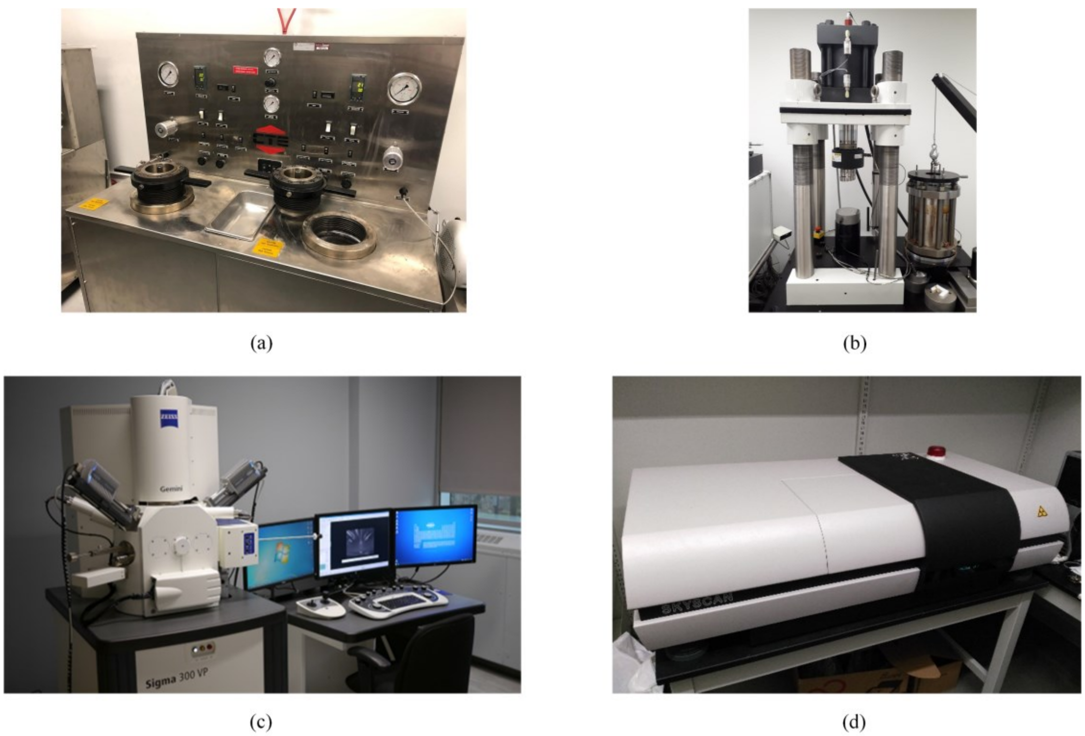

Figure 5A-1 Experimental set-up used for curing, uniaxial compressive stress testing and characterization of cement samples.

(a) Ametek-Chandler 7375 pressure curing chamber. (b) GCTS RTX-1000 triaxial testing system. (c) Zeiss Sigma 300 VP-FESEM used for 2D cement fracture characterization (d) Bruker Skyscan 1172 CT scanner used for 3D cement fracture characterization.

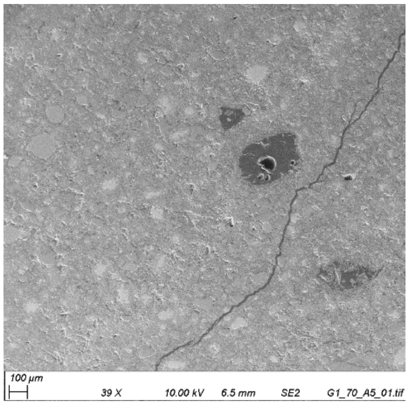

39×

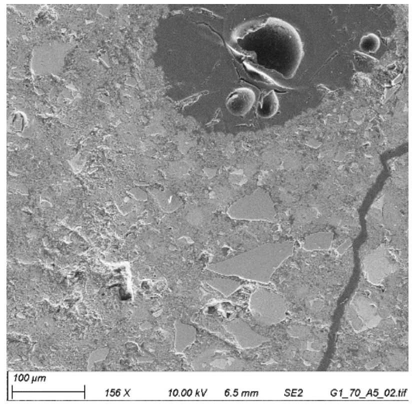

156×

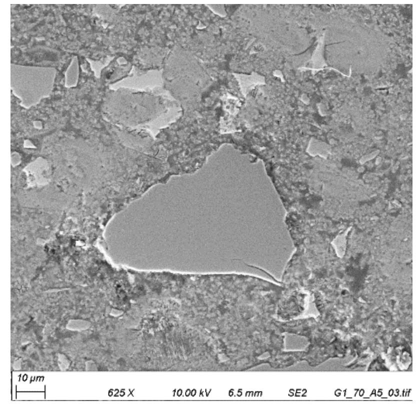

625×

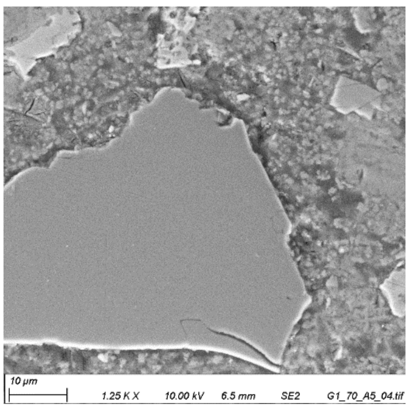

1250×

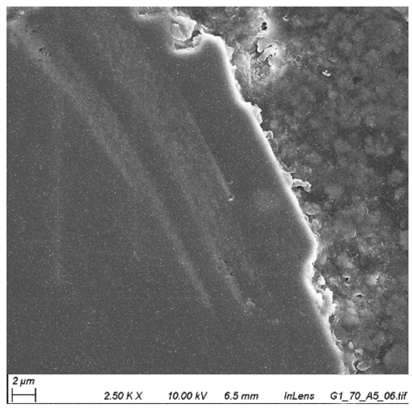

2500×

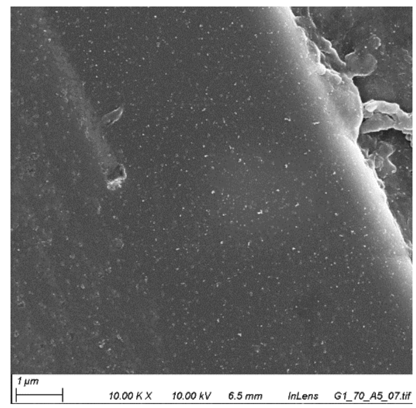

10000×

Figure 5A-2 Examples of SEM images captured at different magnifications.

SEM images were captured from the lower magnification to the higher magnification without change the center of the focus. This cement thin section was extracted from the Sample B.

Table 5A-1 Key parameters of the dual-domain simulation.

Parameter	Value
Simulation Type	Steady Simulation
Simulation Precision	Double Precision
Fluid Type	Air at 25ºC
Fluid Density	1.185 $kg \cdot m^{-3}$
Fluid Viscosity	1.831×10^{-11} MPa·s
Domain Type	Fluid Domain and Porous Domain
Porous Domain Permeability	9.869×10^{-17} m^2 (0.1 mD)
Heat-transfer Model	Isothermal Model (25 ºC)
Time Scale	Automatic Time Scale
Initial Velocity	$U=0$, $V=0$, $W=0.01$ ($m \cdot s^{-1}$)
Inlet Boundary	Total Pressure: 0.096, 0.103, 0.110, 0.118, 0.125 and 0.133 MPa
Outlet Boundary	Static Pressure: 0.088 MPa (Local Atmospheric Pressure)
Wall Boundary	No-slip Wall
Interface Model	Conservative Interface Flux

Note: U, V and W are the velocity values of fluid in the X, Y and Z directions in the Cartesian coordinate system.

Table 5A-2 Common well geometries and the associated cement sheath thickness values.

Components		Realistic Well		Cement Thickness	
		inches	millimeter	inches	millimeter
Surface Section	Bit size	16.00	406.40	1.31	33.33
	Casing OD	13.37	339.72		
Intermediate Section	Bit size	12.25	311.15	1.31	33.33
	Casing OD	9.62	244.47		
Production Section	Bit size	8.75	222.25	0.875	22.22
	Casing OD	7.00	177.80		

5.7 Appendix B-Discussion on SEM magnification vs. 2D fracture density

Due to the multiscale characteristic of the cement fractures, we need to select a certain scale before investigating the quantitative relationship between the fractures and pre-peak stress. Figure 5B-1 shows that the 2D fracture densities at different locations (Figure 5-2b) all increased with increasing SEM magnifications. This is a normally expected trend, which can be explained by a simple derivation given as follows:

We assume that M is the total length of fractures in an area whose size is N. So according to the definition, the initial fracture density F_1 is,

$$F_1 = \frac{M}{N} \qquad \text{Eq. (5A-1)}$$

If we increase the magnification to x, the new fracture density F_x will be,

$$F_x = \frac{M/x}{N/x^2} = \frac{M}{N} \cdot \frac{x^2}{x} = \frac{M}{N} x \qquad \text{Eq. (5A-2)}$$

Eq. (5A-2) not only indicates that the fracture density increases with the magnification but also implies that the fracture density is related to the magnification. Therefore, it is critical to determine the optimal magnification before investigating the quantitative relationship between induced fractures and pre-peak stress levels.

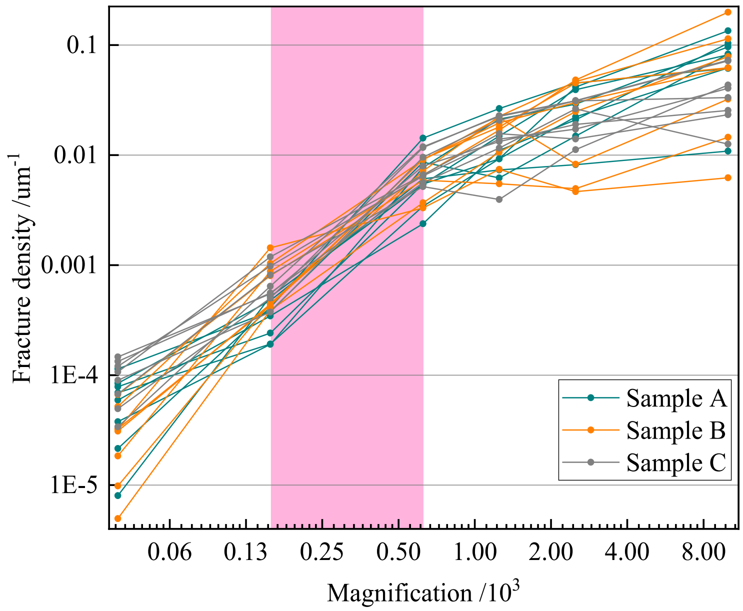

Figure 5B-1 2D fracture density versus SEM magnification measured from different cement samples.

As shown in Figure 5B-1, the fracture density fluctuated under both low and high magnifications. The significant variation under high magnifications is due to the greater heterogeneity of the cement structure at the fine-scale. Under high magnification, such as 10000× (as we used in the measurements), the resolution of a SEM image is 11 nm and the physical area of the SEM image is about 87.5 μm^2, which is smaller than the average cement particle size of 177 μm^2 (assuming particles are in a circular shape with an average diameter of 15 μm) (Bentz et al., 1999; Taylor, 1997).

Although there are no standards that stipulate the minimum required SEM image size for cement structure analysis, ASTM C 31 (ASTM, 2003) states that to prepare a representative concrete sample, the sample size must be at least 3 times bigger than the maximum grain size. We can make an analogy and apply this criterion to calculate the minimum required SEM image size. The maximum particle size of Portland cement is approximately 100 μm (Bentz et al., 1999; Taylor, 1997), so the minimum SEM image size should be around 23562 μm^2 (circular-shaped cement particle) or 30000 μm^2 (square-shaped cement particle), corresponding to a magnification of 608× or 539×, respectively. These values all reside in the pink area, which is in the magnification range from 156× to 625×, as labeled in Figure 5B-1. In addition, curves in the pink area also show less fluctuations than those observed in other regions.

Under a comparatively low magnification of 39×, the resolution of the SEM image is 2.70 μm. Most of the measured 'fractures' observed in the SEM image within this magnification range are actually large air voids, which usually have a circular shape (Figure 5B-2a). In some cases, we also captured the large artificial fractures, which were generated while preparing the cement thin sections (Figure 5B-2a). In a previous study, researchers used Wood's metal to preserve the stress-induced fractures and, therefore, allow easier differentiation between the stress-induced fractures and the artificial fractures (Nemati et al., 1998). However, the injection of the Wood's metal is a pressure-driven process and, therefore, causes some new artificial fractures to form (Klaver et al., 2015). As such, apart from some significantly large artificial fractures as shown in Figure 5B-2a, most of the fractures observed in this study are stress-induced.

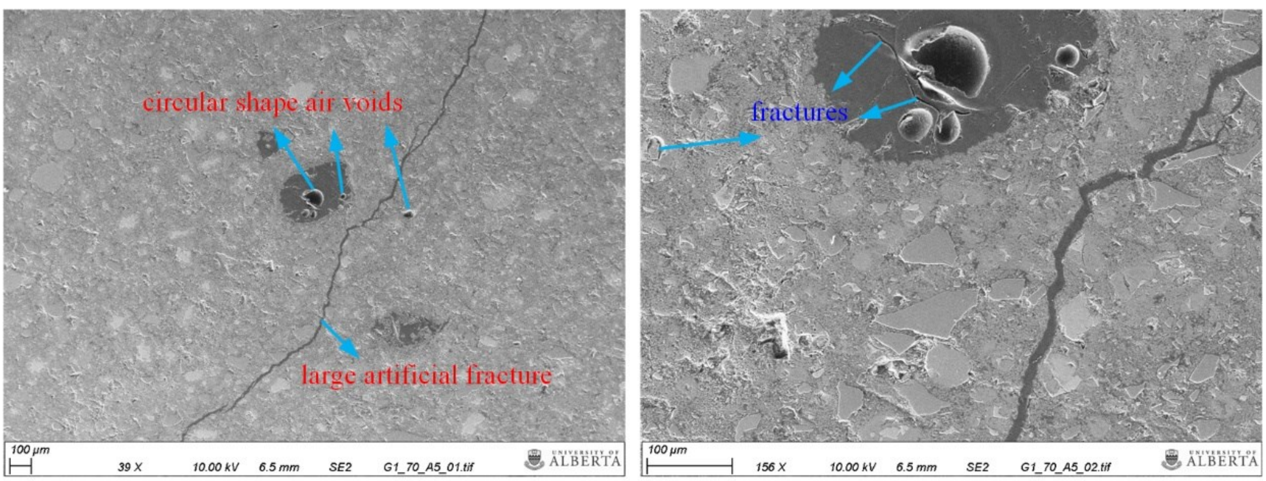

(a) (b)

Figure 5B-2 SEM images of cement thin sections show various features under different magnifications.

(a) circular shape air voids and large artificial fracture in low magnification SEM image. (b) stress-induced fractures start to emerge when magnification was increased to 156×.

Under low magnifications, the fracture density mainly depends on the number of large air voids and the existence of the large artificial fractures, rather than the real stress-induced fractures, which are exceedingly difficult to capture. According to our observation, after increasing the magnification to 156×, the stress-induced fractures start to emerge, as shown in Figure 5B-2b. Based on the analyses presented above, we have concluded that the optimal magnifications for quantitative cement fracture analysis should be between 156× and 625×.

Figure 5B-3 shows the 2D fracture density of the Samples A, B and C analyzed by SEM at different magnifications. Under both 156× and 625× magnifications, we have observed that the fracture density values increased with the increasing compressive stress levels. Attiogbe and Darwin (Attiogbe and Darwin, 1987) obtained a similar trend when they performed measurement using 1250× magnifications. This similar trend at higher magnification was likely due to a larger number measured of samples, which compensated for loss of representativeness under such high magnifications.

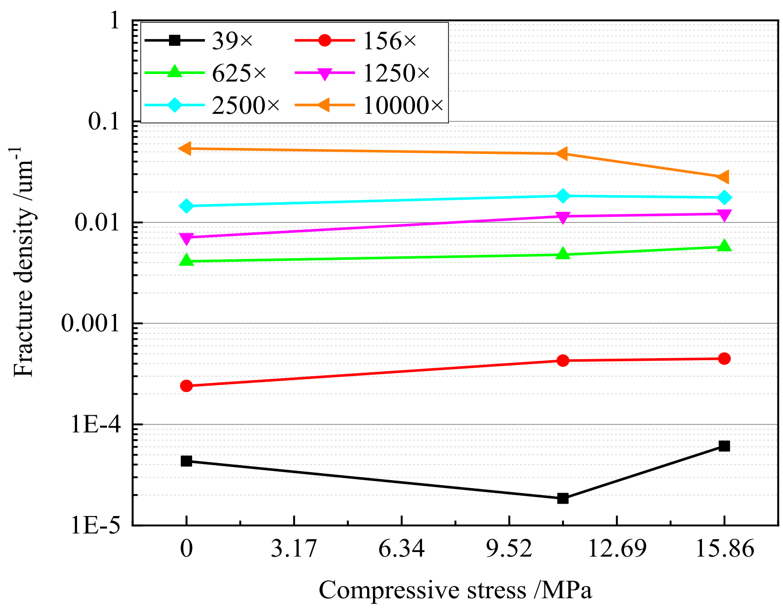

Figure 5B-3 Pre-peak stress level versus fracture density at different magnifications.

Chapter 6 Characterization of the Microstructure of the Cement-casing Interface Using ESEM and Micro CT scan Techniques*

6.1 Summary

Integrity of the cement-casing interface is an essential element of establishing an effective barrier system in cased and cemented wellbores. Failure to establish and maintain an effective barrier can result in negative environmental and economic impacts such as leakage of formation fluids into the environment or loss of production and costly remediation.

The main focus of this paper is defined as the characterization of the cement-casing interface microstructure, which is critical for better understanding of the requirements for establishing effective zonal isolation and the long-term integrity of cemented wellbore sections of active wells as well as the integrity of the abandoned wells.

Primary objectives of this study were; firstly, to confirm the most suitable methods for preparing cement-casing samples and characterize the microstructure of the cement-casing interface (i.e. quantify the size of the microchannel due to possible debonding (gap) at the cement-casing interface and its progression along the wellbore axis); understand how different test methods can impact the microstructure and once we have a firm baseline, analyze the impact of different cement compositions on the performance. More specifically, we have investigated effects of the cement composition and preparation, environmental conditions (i.e. relative humidity of the storage and testing conditions), cement shrinkage and the expansion additive on the integrity of the cement-casing interface at micron scale by using environmental scanning electron microscope (ESEM, 0.05 μm resolution) and micro-CT (μ-CT, 11.92 μm resolution) scanning techniques. Cemented casing samples were prepared by using Class-G and special abandonment cement blends with and without expansion additives and stainless-steel pipes.

---

* This chapter was accepted by SPE Journal as "Yang, X., Kuru, E., Gingras, M., Iremonger, S., Chase, P., & Lin, Z. Characterization of the Microstructure of the Cement-Casing Interface Using ESEM and Micro CT Scan Techniques."

Results showed that any significant change in the relative humidity (RH) of the environment during the cement preparation, curing and testing process significantly affects the size of the gap at the cement-casing interface in test samples. Analyses of the ESEM images have shown that the 2D non-uniform gap size between the cement and the casing is inversely proportional to the change in the relative humidity (RH) of the environment.

Results suggested that cement slurries set and cured under downhole conditions with relatively constant RH may not undergo significant shrinkage and yield only minimal debonding effect.

The 3D gap model reconstructed from the micro-CT images confirmed that the gap between cement and casing mostly occurred at the cement polished surface and the gap didn't show any significant connectivity below the cement polished surface indicating that common sample preparation methods can significantly impact the near surface interface. Cement blends prepared with expansion additives have shown smaller gap size. The use of expansion additives enhances the cement-casing interface integrity by effectively reducing the gap size at the cement-casing interface.

We conclude that as long as the RH of the environment does not change significantly, the cement is expected to undergo a limited shrinkage and the gap between the cement and the casing may not induce any significant leakage pathway as the gap is only locally distributed at the cement polished surface without showing any significant connectivity along the wellbore axis.

6.2 Introduction

As a key component of the wellbore barrier system, cement is supposed to provide the zonal isolation and structural support during the entire life of a well. However, even when cement is properly placed in the well, zonal isolation may be lost over time. Leakage may occur from the oil and gas wells due to the failure of wellbore barrier system. Celia et al. (2005) summarized the possible causes, which could lead to failure of wellbore barrier system. The most common cases are failure of the cement interfaces in the well, either cement-casing interface, or the cement-formation interface (Bourgoyne et al., 2000). This paper focuses on the cement-casing interface.

Cement/casing bond quality has been commonly used to assess the gas leakage potential through the cement-casing interfaces (Carter and Evans, 1964; Kremieniewski, 2019; Scott and Brace, 1966). In recent years, with the development of Carbon Capture and Storage CCS) technique, more attentions have been paid to studying the permeability of the cement-casing interface. Most of these studies have focused on the influence of CO_2–cement chemical reaction on the integrity of the cement-casing interface (Bachu and Bennion, 2009; Carey et al., 2010; Jung et al., 2013). However, the leakage does not only occur in CCS wells. Many questions such as the reasons behind the poor bonding among the production or abandonment wells still remain unanswered. The cement microstructure has a large influence on cement transport and mechanical properties (Bentz et al., 1999). Experimental observations suggested that the bonding quality may be associated with the microstructural changes that takes place in the near-wall zone, also known as the interfacial transition zone (ITZ) (Scrivener et al., 2004), which develops along the cement interfaces such as cement-casing interface.

Despite the importance of the microstructure of the near wall zone, there are only a few studies that have investigated the cement-casing interface at micron scale. Torsæter et al. (2015) studied the microstructure of the cement-casing interface by using micro-CT and scanning electronic microscope (SEM). They found gaps (also called as microannuli) at the cement-casing interface. The gaps at the cement-casing interface was indicated as one of the most significant leakage pathways (Carey et al., 2010). Permeability is considered to be an important indicator to evaluate the durability of wellbore barrier element. Experimental tests shown the gas permeability of cemented casing section with gaps could reach to 600 mD but the gap dimensions were not mentioned (Rusch et al., 2004). Bachu and Bennion (2009) indicated that the presence of an annular gap and/or cracks in the order of 10–300 μm in aperture leads to a significant increase in effective permeability in the range of 0.1–1 mD.

While larger gaps are the main focus of research, as they provide an immediate communication channels, smaller gaps which don't change short-term permeability may still create elevated long-term risk which is critical in abandonment applications. Smaller channels may initiate pathways for chemical attack by corrosive fluids or gases which increases the risk of the gap growing into one that impacts wellbore permeability and integrity. This is likely to be a slow process but realistic issues on the timescales of abandoned wells. Torsæter et al. (2015) suggested that the gaps shown in SEM images were likely to be caused by the cement shrinkage. The cement shrinkage can be divided into two major categories: a chemical shrinkage (Backe et al., 1998; Justnes et al., 1995), which results from autogenous chemical reactions taking place in the cement matrix, and a drying shrinkage, which is sensitive to the RH change (Gajewicz et al., 2016). Although the cement shrinkage was suspected to be the main reason for the discontinuities shown in SEM images, no experimental evidence has been reported to confirm this assumption. Furthermore, which shrinkage type is mainly responsible for the discontinuities in SEM images is still unclear.

Besides, the effect of the sample preparation (e.g. polishing for SEM characterization) on the bonding characterization remains unclear. Lavrov et al. (2017) characterized the particle size distribution in the ITZ using micro-CT with synchrotron radiation, which significantly increased the resolution of the CT image. However, the cement was placed in a glass tube rather than a steel casing. This may affect microstructure in the ITZ because casing has different electrical properties than glass, and the electric field affects the particle size distribution near the wall (Alexandre Lavrov, 2018). Moreover, the debonding, which normally occurs at the cement-casing interface (Lavrov et al., 2016), may not be captured at the interface between the cement and the glass tube. In short, very little is currently known about the microstructure of the cement-casing interface in relation to debonding phenomena.

The main objectives of the study were: 1) characterize the cement-casing interface using 2D and 3D characterization methods at micron scale, so that we can have a better understanding on what resolution we need for cement-casing interface study. Different fundamental sample preparation and characterization methods are critically examined, and the effect of polishing and storage conditions, which have yet to be addressed in cement interface studies, are also discussed. 2) factors that can affect cement-casing interface bonding. Effects of the sample preparation, the cement shrinkage, and the expansion additives on the degree of debonding at the cement-casing interface are investigated by using detailed image analysis test results. Following this introduction, various sample preparation and characterization approaches are fully described in the subsequent section. Factors influencing bonding quality at the cement-casing interface are discussed in the next section. The study ends with a set of conclusions.

6.3 Methods

6.3.1 Materials and sample preparation

Analytical techniques (i.e. SEM and micro CT scan) used for the cement-casing sample characterizations require an extremely small sample size, which prohibited us from using casings of common grades (e.g. J-55, N-80, etc.). Cement-casing interface samples were prepared by filling cement slurry into the short sections of 304 stainless steel pipe, which has an outside diameter of 9 mm, a wall thickness of 0.2 mm and a height of 4 mm (Figure 6-1). We have used the neat Class G cement to expedite the repeatability and the validation of the experimental results and to serve as a baseline for performance. We used a prefix 'G_' to represent the Class G cement for naming the samples. A water-cement (w/c) ratio of 0.45 was used giving a slurry density of 1901 kg/m^3.

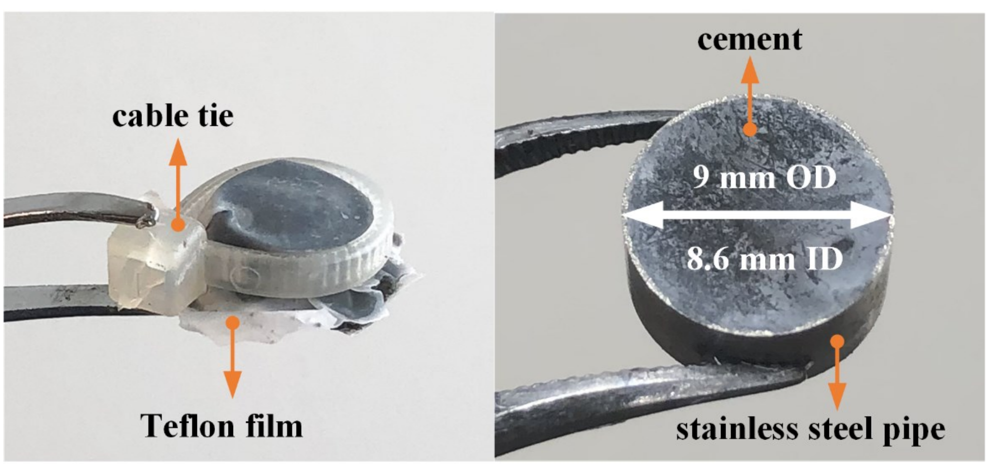

(a) (b)

Figure 6-1 Illustration of the cement-casing interface sample.

The cement slurry was mixed according to API standard 10A and the slurry was then injected into the pipes. A small tamping rod was used to remove the bubbles from the slurry. Both ends of the pipes were sealed by the Teflon plastic films and no-gap curved-head cable ties. The samples were conditioned at ambient temperature (~21 °C) and cured in a steel pressure cell at 50 °C and 1500 psi for 7 days. Once the samples were taken out of the steel pressure cell, they were immediately wrapped in PTFE film to prevent the water loss and isolate the cement interface samples from contacting the air.

One disadvantage of the above sample preparation method was the uneven cement surface, which made it difficult to observe the cement-casing interface after curing. The usual procedure to overcome this limitation is to polish the sample's bottom surface (Torsæter et al., 2015b). Detailed polishing procedures are described in Section 6.3.2.

We have also proposed another method to observe the cement-casing interface without polishing the cement surface. This method was described in Figure 6-2 and the prepared samples were called as polish-free samples. Instead of using soft Teflon films, here we placed solid Teflon sheets at the bottom of the sample. Steel pipes were glued on the Teflon sheet by using a special spray adhesive. Both the Teflon sheet and the spray adhesive can withstand the curing temperature of 50 °C. After curing, a fast-acting adhesive remover was utilized to separate the cement-casing interface of the sample from the Teflon sheet. The slippery surface of the Teflon sheet also helped facilitate the separation. The top surface of the sample was sealed by the PTFE film.

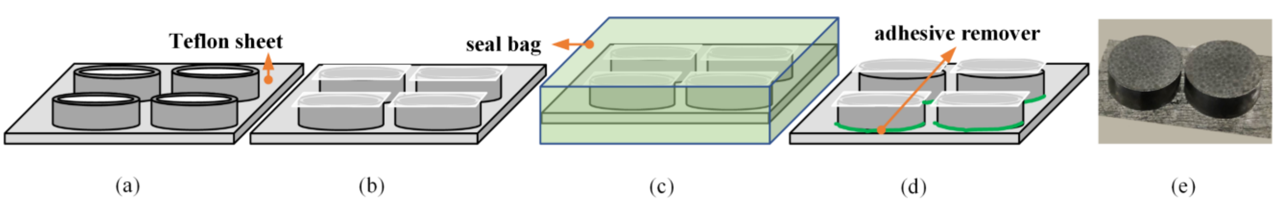

Figure 6-2 Procedure for the preparation of polish-free cement-casing interface samples.

(a) glue one end of the steel pipe using spray adhesive. (b) seal the other end using Teflon film and tape. (c) place all samples in a vacuum bag during curing. (d) use adhesive remover to detach the samples. (e) is the final sample.

6.3.2 Sandpaper polishing and the diamond paste polishing

When studying the surface features of the cement interface samples, polishing is normally a mandatory process to get a smooth surface. Sandpaper is one of the most common polishing tools and many researchers (Jankovic and van Mier, 2002; Kawashima and Shah, 2011) have utilized sandpapers to polish the cement surface. Abrasive particles are glued to one face of the sandpaper and their size are in a range from ~10 µm to ~1000 µm. This range causes some uncertainties about the effect of polishing on cement-casing interface as our interest is to study the interface at a micron scale (1-10 µm). The methods described in the following section are used to qualitatively estimate the effect.

While polishing the cement-casing interface samples, following guidelines were strictly adhered to:

- Sandpapers were treated as one-time use materials. Only the fresh surface of the sandpaper can be used to polish the cement surface. This is essential to minimize the amount of cement debris on the cement surface.
- Polishing was performed in a certain one-way direction. The direction was labeled in the cement sample.
- Once the cement deposits on the casing surface were fully cleaned, polishing was stopped.

Ultra-fine sandpapers (2000 grit) is the finest sandpaper readily available. It has an average abrasive particle size of 10.3 µm. This is still relatively coarser compared to the 15 µm average grain size of the cement particles (Taylor, 1997). Further fine polishing requires special equipment, which was not available in the course of this work.

In optical mineralogy and petrography, thin sections are prepared for detailed ultra-structural studies and then analyzed using the light microscope or the SEM. Cement thin sections are useful for understanding the microstructure of the cement (Stutzman, 2012). The cement-casing samples prepared for this study could then be transformed into thin sections. The thin section lab at the University of Alberta has a sequence of successively finer polishing pastes composed of fine diamond particles ranging from 10 μm down to 0.25 μm. Figure 6-3 shows how the thin section lab prepared the samples. Steps shown in Figures 6-3a to 3c, describe a standard process, which is commonly called epoxy impregnation.

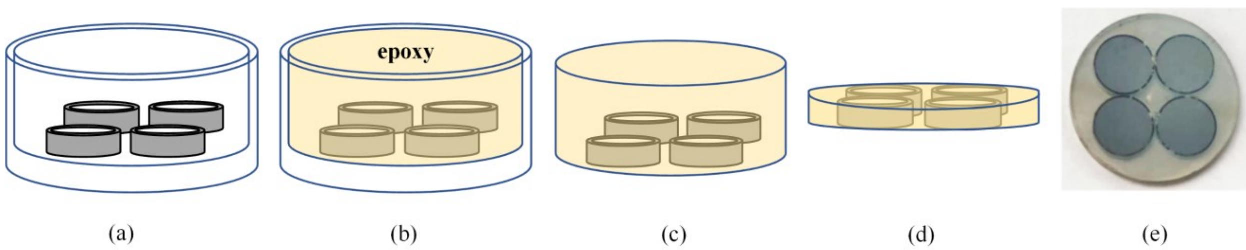

Figure 6-3 Procedure for the preparation and polishing of the composite thin sections.

(a) place the individual samples in a container. (b) vacuum the container and then inject epoxy. (c) remove the container once the epoxy solidified. (d) polish the composite thin section to certain thickness. (e) is the final sample.

As shown in Figure 6-3e, one composite sample contains four individual interface samples. Using the diamond paste polishing, five sets of composite samples, named as Sample G_A, G_B, G_C, G_D and G_E, were prepared in the same way at the same time. Only one surface (bottom side) of each sample was polished and this surface was simply called as a polished surface to differentiate it from the other surface (top side), which is not polished. The samples were then stored for one week under different relative humidity conditions as described in the next section.

6.3.3 Sample storage conditions and the relative humidity measurement

The volume of a cement sample is sensitive to the relative humidity (RH) of the environment. If the RH of the surrounding environment is less than 100%, the cement sample will contract, which is known as cement drying shrinkage. Since the RH may vary depending on the storage conditions, we have investigated effects of four different storage conditions on the cement drying shrinkage. As shown in Figure 6-4, the first storage method is an unsealed method where the samples were stored under ambient room condition (21 °C and 33% RH). In the rest three methods, the samples were all stored in a sealed bag. An ambient seal method is simply to store the samples in a sealed bag. In the water seal method, the samples were stored by immersing in water. Finally, in the humid seal method, samples were wrapped in a wet paper towel.

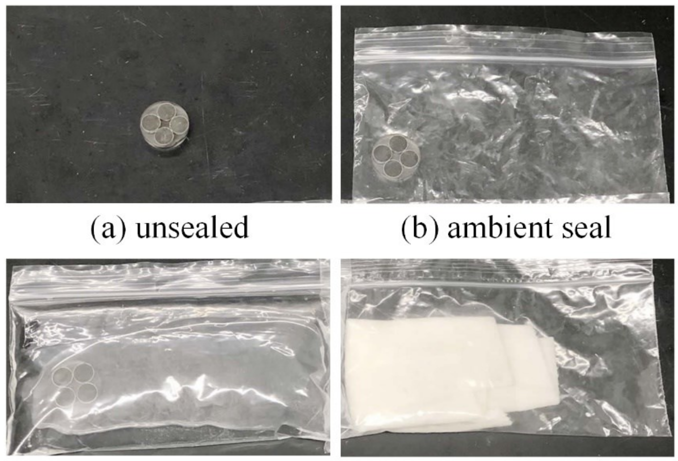

(a) unsealed (b) ambient seal

(c) water seal (d) humid seal

Figure 6-4 Different cement storage conditions.

RH in above mentioned methods were measured by using a humidity meter which measures RH from 10% to 95%, with 0.1% resolution and ±2% accuracy. For the water seal case (Figure 6-4c), the relative humidity of the air (above water) in the sealed bag was measured. The RH of each storage method was estimated by averaging three measurements. RH was measured every day for 7 days. Samples G_A, G_B, G_C and G_D were stored in unsealed, ambient seal, water seal and humid seal conditions, respectively. The Sample G_E was also stored in water seal condition.

6.3.4 3D Cement-casing interface characterization by using micro-CT scan technique

Computed tomography is currently the only mature method, which can non-destructively investigate 3D microstructure of the materials. All prepared cement samples were first characterized by a SkyScan 1172 micro-CT scanner located at the Department of Earth and Atmospheric Science, University of Alberta. Considering the high densities of both cement and the casing, copper plus aluminum filter (Cu + Al) was selected to improve the quality of CT images. Placement of the samples also affects the resolution of the CT scan. Samples placed horizontally while scanning allowed a resolution of 2.81 μm (see Figure 6-5a). However, the beam-hardening effect of the casing and the ring artifact impair the characterization of the cement-casing interface. To minimize the beam-hardening effect, the samples should be scanned vertically (see Figure 6-5b). However, in this case, only a section of the sample can be scanned with 2.81 μm resolution. If we want to scan the entire sample, the resolution of the CT scan decreases down to 4.59 μm, as shown in Figure 6-5c. Micro-CT images analyzed in the main part of this paper were all scanned in a way shown in Figure 6-5c.

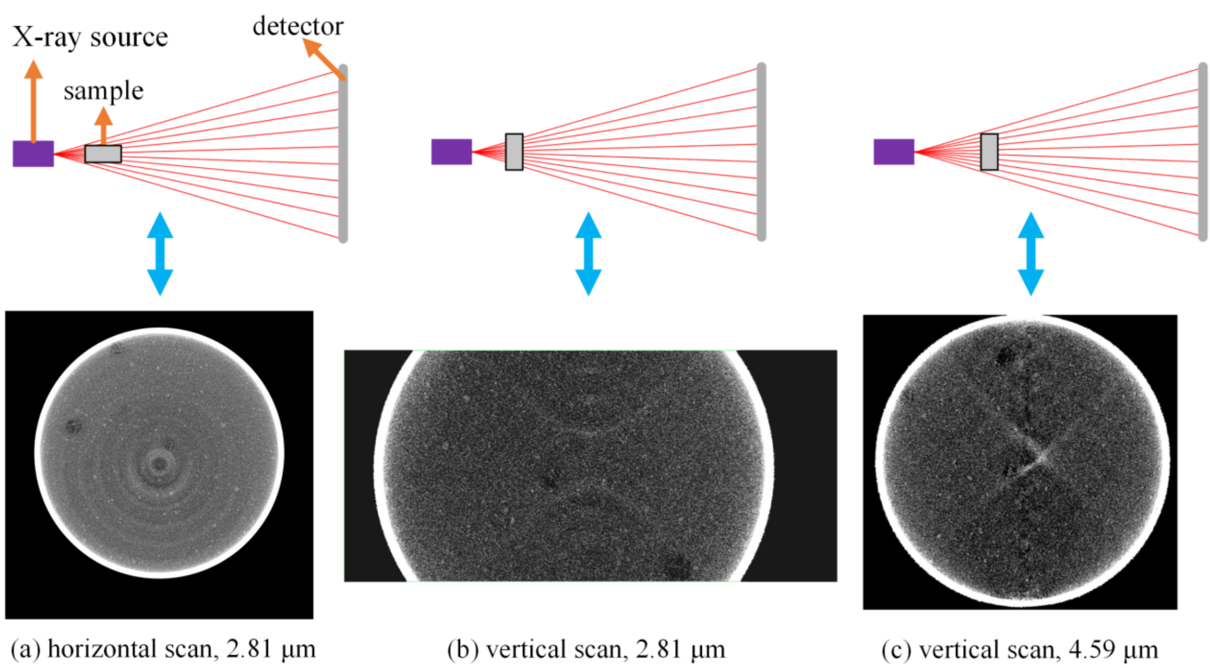

Figure 6-5 Comparison of the CT images obtained from horizontal and vertical scan.

Each CT scan will create about 1000 greyscale projection images. These images were further converted into about 2000 cross-section images, which are in 4000 × 4000 pixel format. The cross-section CT images were then imported into ScanIP, the commercial 3D visualization and analysis software to reconstruct the realistic 3D structures of the cement-casing interface samples. Readers can refer to Yang et al. (2019) for more detailed information regarding the cement CT scan and 3D reconstruction.

6.3.5 Gap size measurement using SEM/ESEM images

The resolution of the CT images varied depending on the sample size. As we scan the samples vertically to minimize the beam-hardening artifacts, the maximum resolution that CT scan can reach was 4.59 μm. Compared to previous research using 100-200 μm resolution when characterizing the microannuli (Vrålstad and Skorpa, 2020), the resolution we achieved in the current study (as low as 4.59 μm) allowed more accurate evaluation of the integrity of cement-casing samples. Besides, although the smaller gaps may have limited impact on the short-term permeability, they may function as the starting point of chemical attack and thus jeopardize the long-term wellbore integrity. In order to capture these small gaps and have a closer look at the cement-casing interface, a higher resolution characterization tool is thus needed. As a surface characterization equipment, SEM can be used to characterize the cement features beyond the resolution of the micro-CT. A Zeiss Sigma Field Emission SEM located in the Department of Earth and Atmospheric Science, University of Alberta was used to characterize the cement-casing interface samples. Its resolution can reach 0.01 μm. Since the cement is a non-conductive material, the cement-casing interface samples were coated by carbon to make them conductive. The carbon may affect the CT scan result and, therefore, the CT scan measurements should be performed before conducting any SEM scan.

Cement chemical shrinkage and drying shrinkage are important factors that influence the bonding quality (Goboncan and Dillenbeck, 2003; Reddy et al., 2009). Previous research (Bisschop and van Mier, 2002; Neubauer et al., 1997) has indicated that the traditional SEM coating and characterization can cause cement drying shrinkage because both processes take place in a high vacuum chamber whose RH is pretty low. To minimize the cement drying shrinkage, an environmental scanning electron microscope (ESEM) would probably be a more appropriate technique to use as the ESEM is able to image the hydrated cement interface samples at the controlled RH conditions (Kjellsen and Jennings, 1996; Neubauer et al., 1997). In this study, Zeiss EVO Environmental SEM located in the Department of Earth and Atmospheric Science, University of Alberta was selected to capture images of cement-casing interface at RH ranges varying from 15% to 95%. The ESEM chamber temperature was maintained at 10 °C. The target

RH can be achieved by adjusting the chamber pressure. Images were captured after the RH stabilized for at least 5 minutes.

As shown in Figure 6-6a, images (SEM or ESEM) were captured at 16 different locations under 2000×magnification. On each image, five green overlays were drawn to estimate the mean gap (debonding) size (Figure 6-6b).

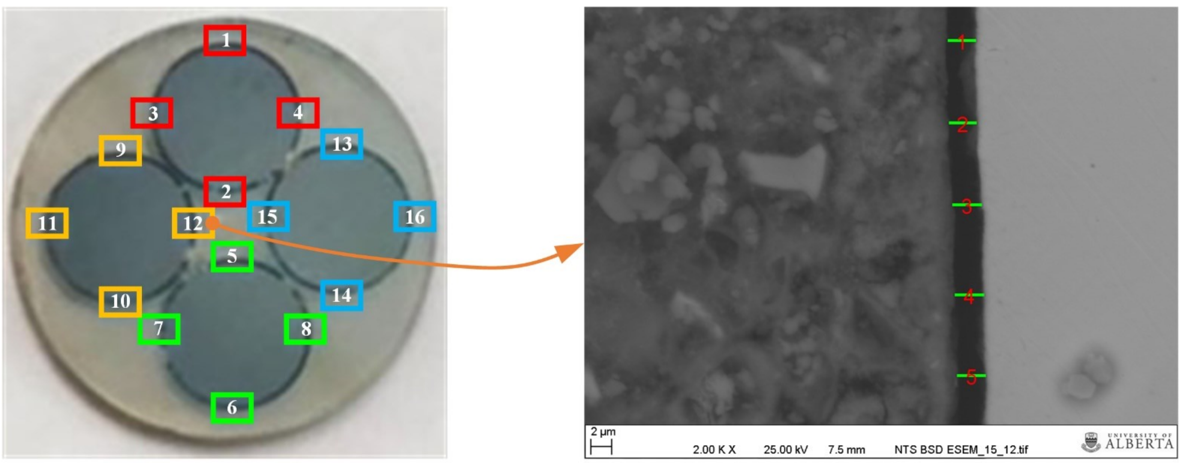

(a) (b)

Figure 6-6 Illustration of where and how gap size was measured.

6.4 Results and discussion

6.4.1 Effect of polishing

In this section, the effect of polishing was discussed based on the SEM images of individual cement-casing interface samples (not composite samples). All the samples mentioned in this section were stored under the water seal condition for one week.

Using polish-free samples probably is the best way to avoid any polishing effect on the cement interface characterization. Images shown in Figure 6-7 were obtained from the two polish-free samples, Sample G_PF1 and Sample G_PF2. Fortunately, we found some clean (i.e. uncovered by cement) cement-casing interface sections that clearly showed the gap between cement and casing.

From the polish-free samples, we could confirm that the gap was not caused by the polishing. To have a better understanding of the gap size distribution and also to improve the analysis efficiency, it was still necessary to polish the samples.

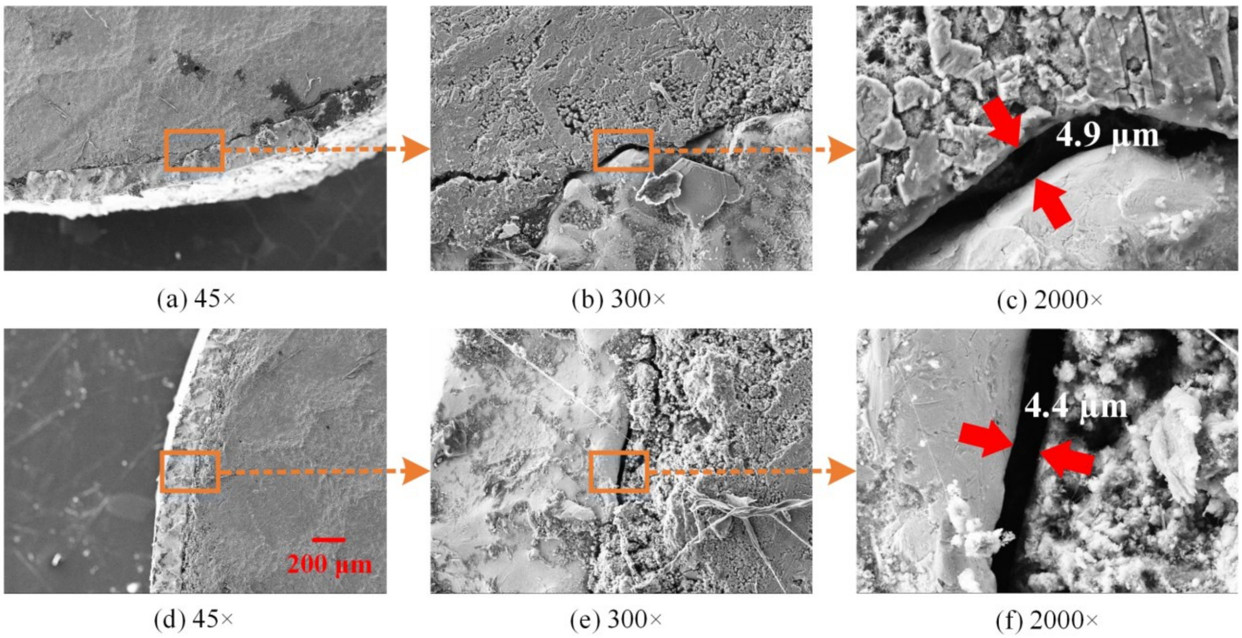

Figure 6-7 SEM images of two uncovered spots in the polish-free samples.

(a), (b) and (c) are SEM images of Sample G_PF1, whereas (d), (e) and (f) are SEM images of Sample G_PF2.

Figure 6-8 summarized the SEM images of the cement-casing interface samples polished by Ultra-fine (2000 grit) sandpapers. Schematic sample diagrams show the positions of the captured SEM images. The most interesting images were those captured at the positions where the direction of polishing scratches was almost perpendicular to the cement-casing interface. As shown in Figure 6-8, depending on the positions, the images were divided into two groups: front images and rear images. In the front images, there were almost no gaps at the cement-casing interface, whereas in rear images, cracks and fragmented surfaces were observed. A possible explanation for this difference might be that the sandpaper polishing caused the decentralization of the hardened cement paste (or just the surface). Due to the sandpaper polishing, the interface at the front side was squeezed, while the interface at the rear side was stretched. Another important finding was that the sandpaper severely reshaped the casing surfaces and edges. We found that there were small cracks, which were all perpendicular to the polishing direction, distributed in the near wall zone. These cracks were likely to be created by the tensile stress due to the polishing.

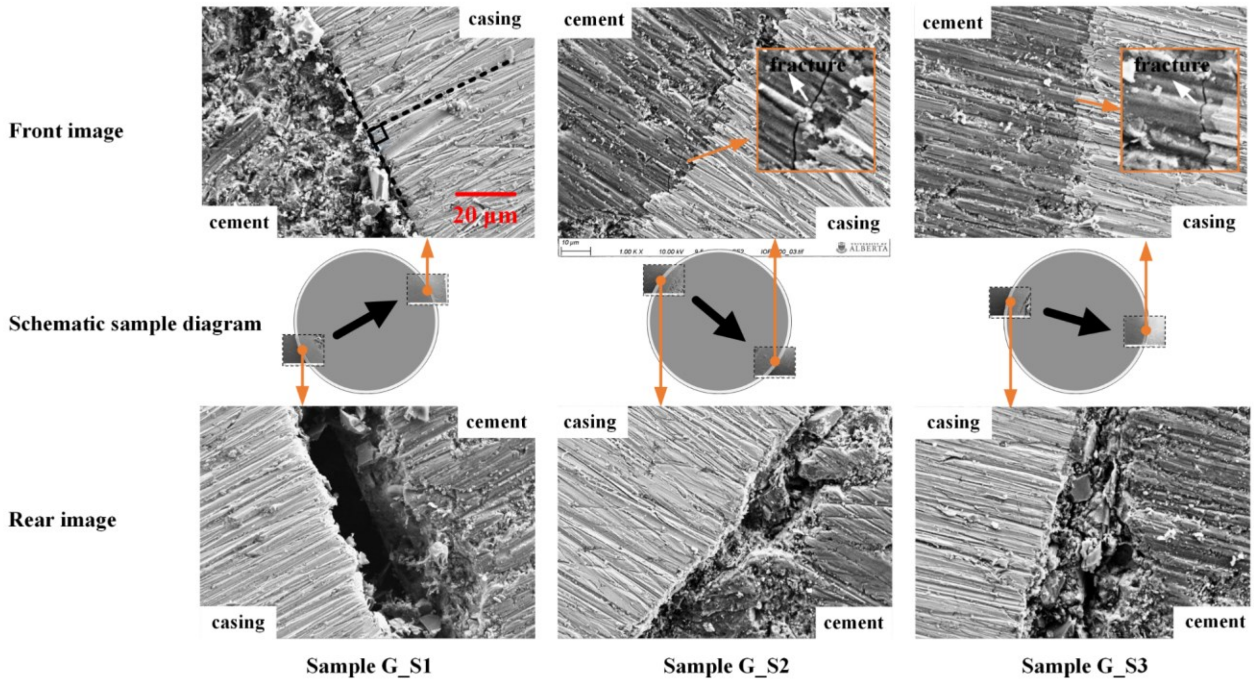

Figure 6-8 SEM images of three samples which were manually polished by the sandpapers.

Above analyses suggested that the sandpaper polishing might have decentralized the hardened cement paste. A basic assumption behind this suggestion was that some gaps must have been already present at the cement-casing interface before the polishing. To prove this assumption, a new polishing method was needed. As stated in the Section 6.3.2, another method, which impregnated the epoxy into the cement interface sample before conducting any polishing work was utilized. Figure 6-9 shows the SEM images of the cement interface samples polished by this new method.

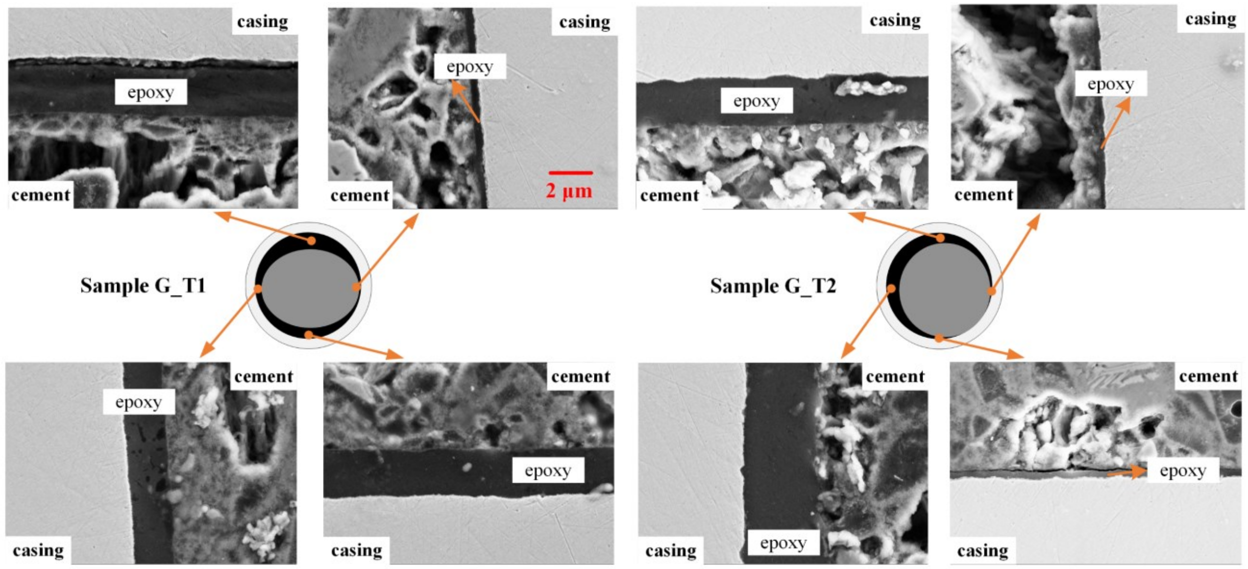

Figure 6-9 SEM images of the two samples located in a composite thin section.

As we can see from Figure 6-9, use of finer diamond paste (down to 0.25 µm) reduced the size of the polishing scratches significantly. Consequently, the cement and casing boundaries were well preserved. Use of solid epoxy technique proved that some gaps between the cement and the casing boundaries already existed before the polishing. Moreover, based on the SEM images, we have observed that the gap size varied with the positions along the cement-casing interface. This finding suggests that the hardened cement paste or at least the cement surface, was not a perfect cylinder. Then the question arises how the gaps were formed?

6.4.2 Effect of cement drying shrinkage

Several mechanisms have been suggested to be responsible for the generation of the gaps between the cement and the casing. Using SEM scanning technique, Torsæter et al. (2015) suggested that these gaps were likely to be caused by the cement shrinkage. This part mainly discusses the effect of drying shrinkage on the microstructure of cement-casing interface.

Considering the drying shrinkage is highly sensitive to RH gradients, the gaps shown in SEM images might have been induced not only by the polishing process but also sample storage conditions or SEM characterization technique. To clarify the contribution of drying shrinkage to the creation of the gaps, environmental SEM (ESEM) was used to control the RH while observing the cement interface samples.

Figure 6-10 shows the images of the gap size change with the RH at four different locations in Sample G_E. At each location, initially we planned to set a reference region under 95% RH and capture the images of this region under different RH to see how the interface will change with the RH. However, image quality was substantially decreased at 95% RH because of the skirting effect (Mathieu, 1999; Podor et al., 2019). In this case, we used the images at 75% RH as the reference and therefore in Figure 6-10, the images captured at 95% RH were not included.

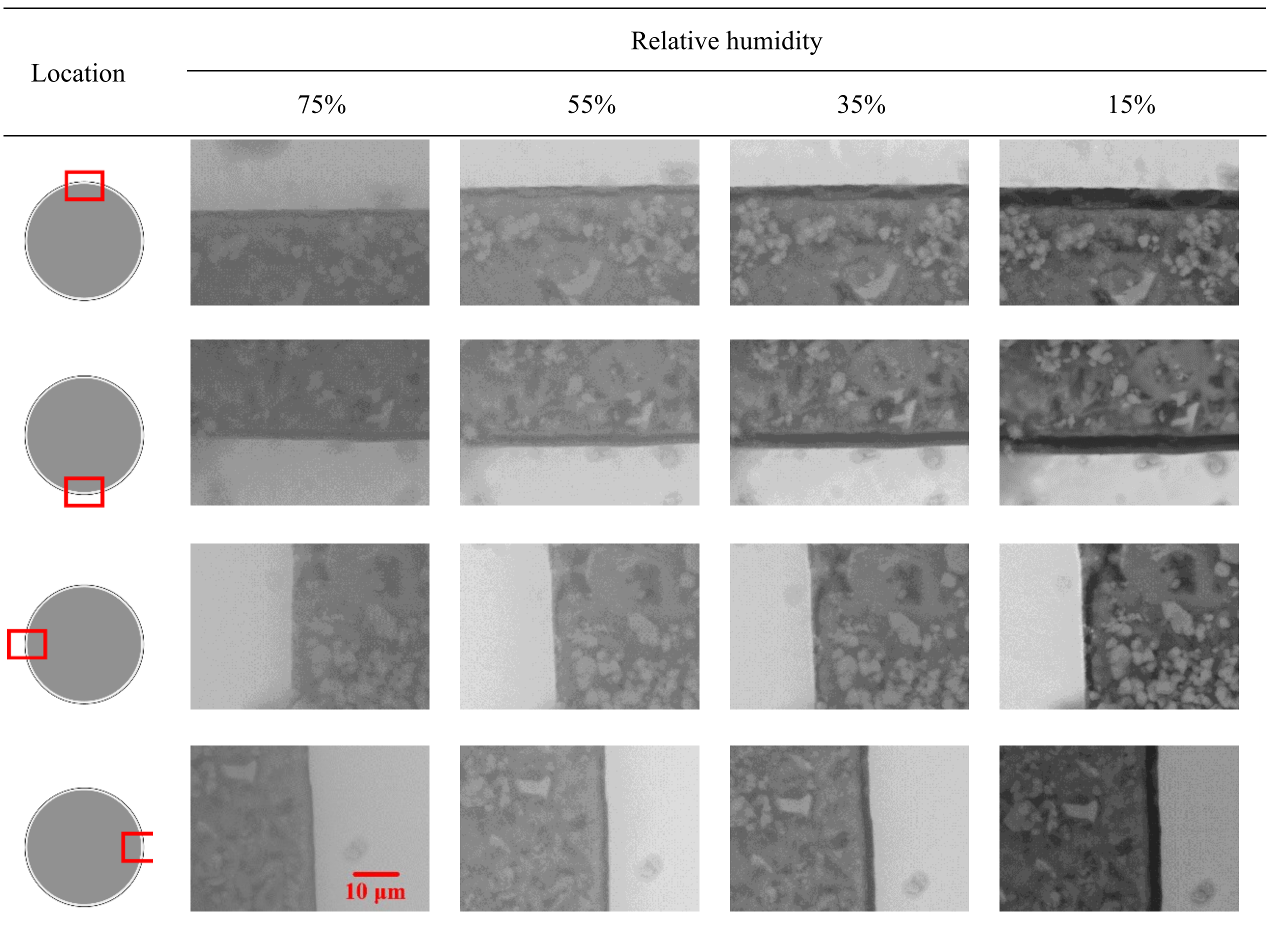

Figure 6-10 Gap size evolution at four different locations with the relative humidity change.

Gap size versus relative humidity measurements shown in Figure 6-11 revealed that the gap size has a non-linear relationship with the RH. When RH is greater than 75%, the gap size increases gradually with the decreasing RH, while the RH is lower than 75%, however, significant increment of the gap size was observed with the decreasing RH. Figure 6-11 also shows the gap size has a non-uniform distribution. This result may partly be explained by the temperature and humidity gradient in the ESEM chamber because uniform temperature and humidity fields in the chamber are hard to achieve. It took about 4 hours to finish all the ESEM scans. During this short time period, the gap size changed significantly under ESEM. The average gap size increased by 2.72 μm in 4 hours. This means that the cement sample shrunk 0.6% (in 2D) when RH decreased by 80% in a 4-hour time period.

The average gap size of the samples characterized under different RH conditions are summarized in Table 6-1. From the results shown in Figures 6-10 and 11 and the Table 6-1, it is apparent that (average) gap size increased with the decreasing RH. Similar results, indicating the shrinkage of the cement paste is inversely proportional to the RH, have also been reported by previous studies (Bissonnette et al., 1999; Neubauer et al., 1997). Standard deviation of the gap size was also calculated. When RH higher than 50%, the standard deviation is very close to the average gap size, which further confirms the gap size has a non-uniform distribution.

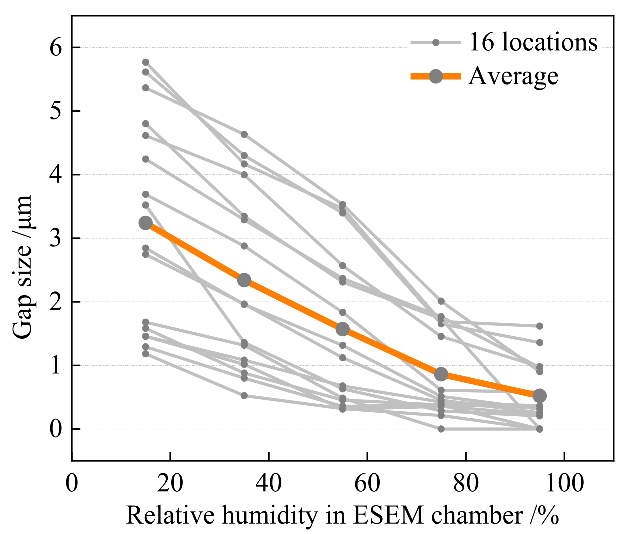

Figure 6-11 Gap size versus relative humidity at different locations.

Table 6-1 Average gap size of samples characterized in different RH conditions.

Sample ID	Storage condition	Storage RH	Scan method	Relative humidity	Average gap size /µm	Standard deviation /µm
Sample G_E	water seal	99%	Environmental SEM	95%	0.52	0.50
				75%	0.86	0.68
				55%	1.57	1.17
				35%	2.34	1.39
				15%	3.24	1.62

6.4.3 Effect of storage condition

Figure 6-12 shows the RH of different storage conditions measured as a function of time. Unsealed condition has the lowest RH as it is recorded under the room condition, which is influenced by the fluctuating local weather condition. The cement samples stored under sealed conditions all have an approximate RH at the beginning around 73% RH. The RH of the cement sample kept under water seal condition stabilized at 100% whereas for the samples stored under humid seal condition, the RH reached to 90% at the end of the test. Ambient seal condition kept RH of the cement sample at around 75% with a slight decrease in time.

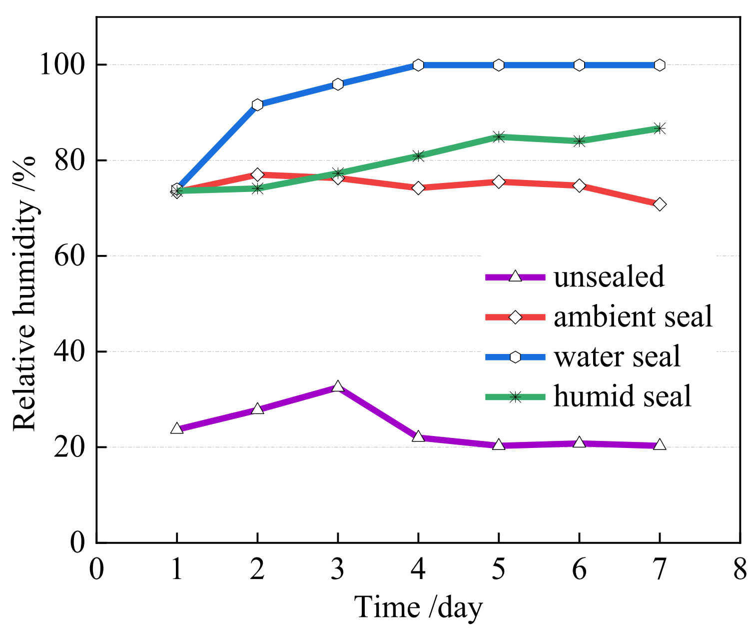

Figure 6-12 Relative humidity of different storage conditions.

We also measured the gap size of the cement samples stored under different conditions and the results are summarized in Table 6-2. In order to maintain a high RH level and obtain high quality image at the same time, 75% RH was used while characterizing the samples with ESEM. Based on the average gap sizes measured from the ESEM images, we found that the gap sizes were also following the same trend as the ones we discussed in the previous section confirming that the gap size was inversely proportional to the RH. Standard deviation data also indicates the gap size has a non-uniform distribution regardless of storage condition or scan method.

Table 6-2 Average gap size of samples stored in different conditions.

Sample ID	Storage condition	Storage RH	Scan method	Characterization RH	Average gap size /μm	Standard deviation /μm
Sample G_A	unsealed	20%	Environmental SEM	75%	1.58	1.59
Sample G_B	ambient seal	71%		75%	0.99	0.62
Sample G_C	water sealed	99%		75%	0.76	0.29
Sample G_D	humid sealed	86%		75%	0.82	0.84
Sample G_A	unsealed	20%	Normal SEM	0%	2.36	3.28
Sample G_B	ambient seal	71%		0%	2.82	0.96
Sample G_C	water seal	99%		0%	4.38	2.50
Sample G_D	humid seal	86%		0%	4.24	2.64

After the ESEM scan, the samples were directly scanned by the normal SEM again. Contrary to the ESEM measurements, the gap size measured from the SEM images increased with the increasing RH. When we characterize the samples using normal SEM, the SEM vacuum chamber makes the RH dramatically decrease to almost 0%. Compared to the Sample G_C, the Sample G_A was stored in a less humid environment and, therefore, the Sample G_A did not undergo as much RH change as the Sample G_C during SEM scan. Consequently, the Sample G_A showed a smaller average gap size than Sample G_B. These results indicate that the gap size was strongly affected by the change in the RH between the storage and the test conditions. The harsh RH change has also been claimed as a cause for the collapse of calcium silicate hydrate (C-S-H) (Z. Zhang et al., 2018).

6.4.4 Effect of expansion agent on the size of the gap at the cement-casing interface

Given that the shrinkage would create the gap between the cement and casing , a solution to minimize the gap is to engineer the cement blend to minimize shrinkage or to add expansion agent to the cement blend (Baumgarte et al., 1999; Goboncan and Dillenbeck, 2003). As we have developed an analytical technique for characterizing the cement-casing interface, we then wanted to apply the same technique to determine the effect of some commercially used expansion additives on the cement-casing interface integrity.

To investigate the influence of the expansion agent on the cement-casing bonding, we have prepared four types of cement-casing samples using Class G cement with (Sample G_W) and without expansion agent (Sample G_WO), and two abandonment-based blends. One system was a novel abandonment blend with engineered chemistry to minimize permeability, improve chemical resistance and show no chemical shrinkage (Sample A_W) and the other one a more traditional abandonment blend which was not engineered to give enhanced performance and will likely show chemical shrinkage (Sample A_WO).). All samples were cured at the same condition (50 °C and 1500 psi for 7 days) as described in Section 6.3.1. The expansion agent used in both cement is less than 2% BWOC. For each type of cement-casing samples, one set of composite samples (shown in Figure 6-3e) was prepared and analyzed using the preferred method described in Section 6.4.3. The measured average gap sizes are summarized in Table 6-3. Examples of the ESEM images captured from the cement samples are shown in Figure 6-13.

Table 6-3 Average gap size of samples prepared using different blends w/wo expansion agents.

Sample ID	Storage condition	Storage RH	Scan method	Characterization RH	Average gap size /µm	Standard deviation /µm
Sample G_WO	ambient seal	71%	Environmental SEM	75%	1.64	1.29
Sample G_W	ambient seal	71%		75%	1.48	0.81
Sample A_WO	ambient seal	71%		75%	8.07	3.38
Sample A_W	ambient seal	71%		75%	1.34	1.58

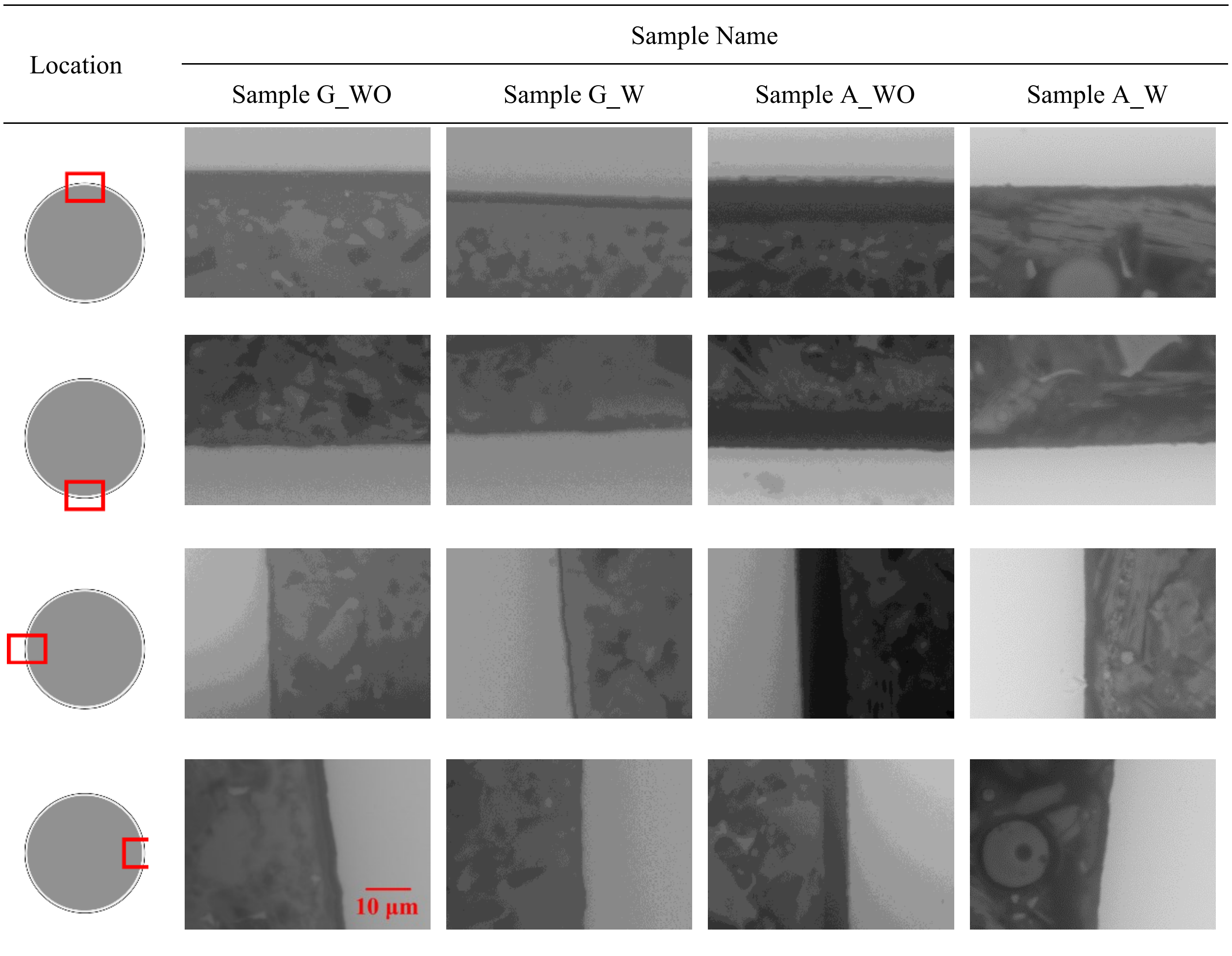

Figure 6-13 Examples of ESEM images captured at four different locations of cement samples.

According to the standard deviation data, gap size is nonuniformly distributed in all kinds of samples. A note of caution is due here as the samples prepared using traditional abandonment blend (Sample A_WO) exhibits bigger gap than both Class G blends. The traditional abandonment blend contains chloride-based accelerators which are known to cause shrinkage while the Class G and Class G with expansion agent (Sample G_WO) blend does not. The accelerators are needed for the cement to gain strength as the two Class G blends would have delayed strength development, which would sub-optimal in a field application.

Table 6-3 also illustrates with the expansion agent, the gap size in the abandonment sample (Sample A_W) was reduced. For Class G blends, the effect of expansion agent is not significant.

In fact, without sufficient additives, the Class G blends have some inherent flaws. For example, for Class G samples (Sample G_W, G_WO), we have observed some signs of particle settling with lower density cement on top. Porosity of the Class G samples is also higher than the abandonment samples, which means the permeability of Class G samples is most likely higher than the abandonment samples and the high permeability is not good for the long-term well integrity. These observations demonstrate the importance of using engineered cement blends with optimized slurry properties in experiments such as these to reduce the impact of free water or particle segregation giving misleading results.

6.4.5 Discussion and implication for field practice

Overall, the aforementioned discussions indicate that the gap size at the cement-casing interface was significantly affected by the cement drying shrinkage as a result of RH change. Gap size results also varied depending on the storage condition and SEM/ESEM characterization method. The cement interface samples are always somewhat subject to cement drying shrinkage unless characterize them at high RH using ESEM. However, the image quality obtained in high RH will be substantially decreased. Compromise has been made by characterizing the samples under 75% RH. In addition, to avoid the rapid RH change, it is better to keep a consistent RH from storage to characterization. Ambient seal storage condition maintains a RH around 75% and it is also a convenient way to store samples. Taken together, these results suggest that storing samples in an ambient seal condition and characterizing them using ESEM at 75% RH should be a preferred method.

As for the implications of these results from practical field applications point of view, we may conclude that as long as the RH condition is uniform, the gap size at the cement-casing interface would be minimal. Once the cement is pumped downhole and set behind the casing, it would be safe to assume that the cement column would be cured under relatively constant (downhole) RH conditions. Based on our lab-scale observations, we can say that these relatively constant RH conditions would help to minimize the possible cement drying shrinkage (and the size of the resultant gap between the cement-casing interface) and, hence, have a favorable impact on the quality of the cement-casing bond.

SEM/ESEM measurements are limited to the cement-casing interface at the polished surface of the cement column. In other words, SEM/ESEM measurements do not tell anything about if the gap seen at the cement polished surface is in fact extended below the cement surface (i.e. connectivity of the gap along the cement/casing interface). This is why we need to conduct 3-D characterization of the cement-casing interface using Micro CT scanning tests.

6.5 Connectivity of the gaps at the cement-casing interface

The inner diameter of the casing pipe is 8600 μm. According to the average gap size values shown in Tables 1 and 2, the highest shrinkage (2D shrinkage) is about 0.1%. This value is consistent with the previous experimental measurement results (Garci Juenger and Jennings, 2002). In a typical wellbore geometry, say for a cement column placed in the annulus between 8.625 inch (ID) and 7.0 inch (OD) casings, assuming no size effect on the drying shrinkage and the shrinkage is uniform throughout the sample, 0.1% shrinkage would result in a gap size of around 15 μm. This value is very small (close to an average cement particle size, (Taylor, 1997)). More importantly, does the gap have any continuity along the axial direction of the wellbore?

Analyses of micro-CT images showed that the gap only occurs at the surface and the depth (i.e. continuity along the wellbore axis) of the gap is very limited. Figures 6-14a and 14b show a group of cropped cross-sectional CT images of Sample A_WO (abandonment blend without expansion agent), which yields the largest average gap size as shown in Table 6-3. Fig Figure 6-14a was captured at a position near the surface. We can clearly see that there is a gap between the cement and casing interface. Figure 6-14b shows the CT image of the same sample at a deeper location (0.12 mm below the surface), which indicates that the gap vanished as there were no clear gaps seen at this location.

Similar groups of cropped cross-sectional CT images of Sample A_W (Figures 6-14c and 14d), Sample G_WO (Figures 6-14e and 14f) and Sample G_W (Figures 6-14g and 14h) were also captured. Figures 6-14c, 14e and 14g were captured at the positions near the surface and there were no significant gaps observed in these images. Figures 6-14d, 14f and 14h were captured at the positions 0.12 mm below the surface and we did not observe any gap in Figures 6-14d, 14f and 14h either.

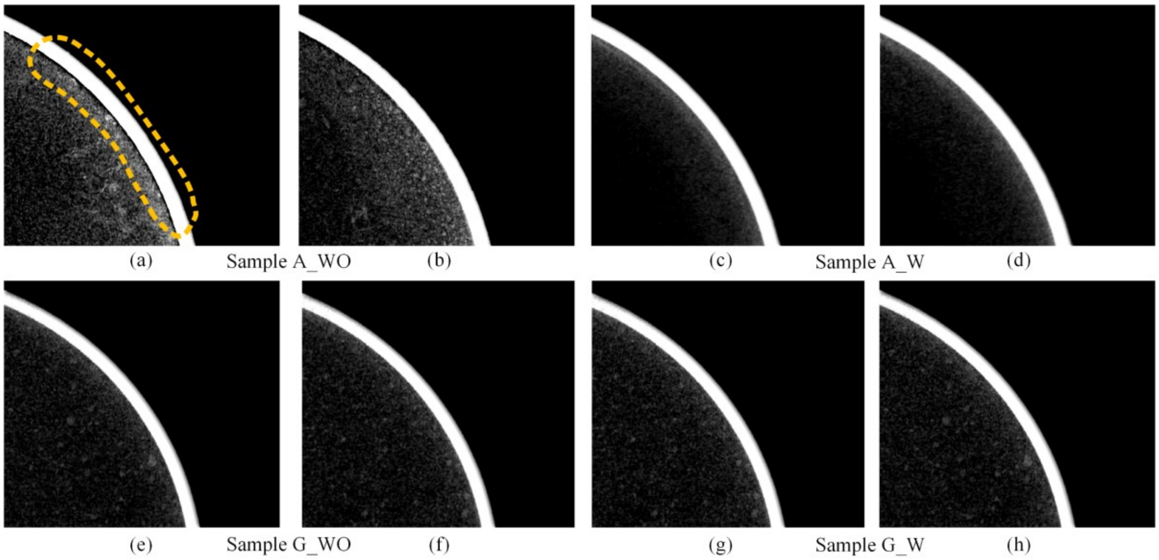

Figure 6-14 Comparison of gap in CT images at different horizontal levels (Resolution 4.59 µm).

Figs a, c, e and g were captured at the near surface. Figs b, d, f and h were captured at a deeper location (0.12 mm below the surface).

Figure 6-15 shows the visualized 3D gaps reconstructed from the micro-CT images of the Sample A_WO. In Figure 6-15, we can see how the discontinuity of the gap progresses from the cement surface to down below the surface (along the pipe axis). In Figure 6-15a, the 3D gaps in Sample A_WO were marked in blue color. An enlarged view of the 3D gap with dimensions is displayed in Figure 6-15b. The arc length of the gap along the circumference of the cement-casing interface was about 3.00 mm. The width of the gap was not constant along the circumference. The largest gap size (i.e. gap width) measured at the surface was about 13.31 µm. We have also measured the change of the gap width along the axial direction and the results are shown in Figure 6-16. In general, the gap became smaller at the deeper positions and eventually vanished at a depth of around 0.12 mm. Nevertheless, the gap didn't break through the sample in the axial direction. Thus, the gap was discontinuous in the axial direction and locally distributed along the circumference of the cross-sectional plane.

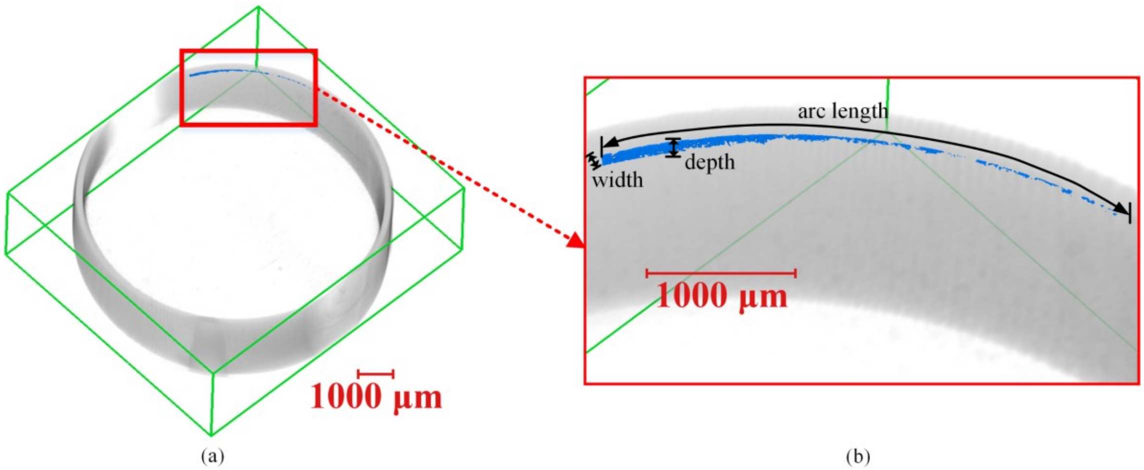

Figure 6-15 Illustration of the 3D gap reconstructed from the micro-CT images of Sample A_WO.

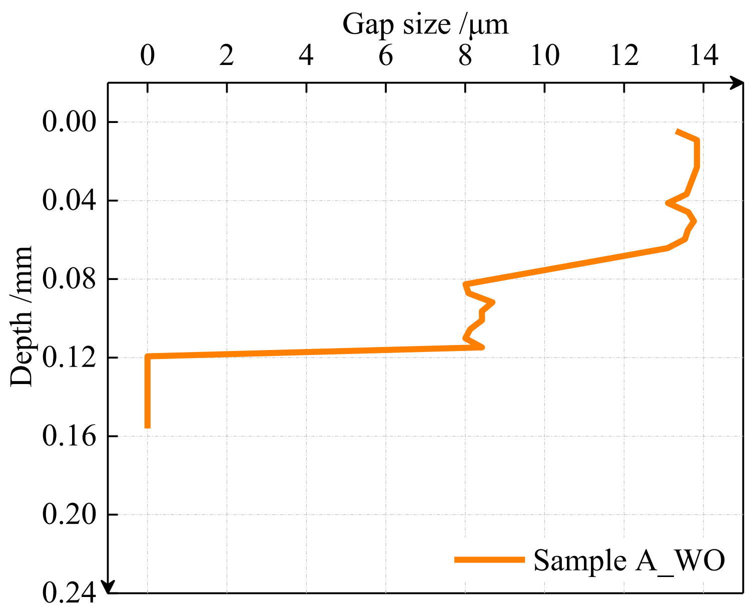

Figure 6-16 Change in the size of the gap width between cement and casing versus depth (0 mm depth level represents the sample surface).

Curves in Figure 6-16 are not very smooth. They look more like piecewise curves. This is due to the resolution of the micro-CT. The resolution of CT images shown in Figure 6-14 is 4.59 µm, therefore, the gap size should be a multiple of 4.59 µm. This explains why most of the data in Figure 6-14 concentrate around 4.59 µm, 9.18 µm and 13.77 µm.

6.6 Discussion of the results and the limitations of the study

It is worthwhile to note that the application of micro-CT in characterizing cement interface study is somewhat limited by the resolution of the technique. For the samples we prepared, the highest CT resolution we could achieve was 4.59 μm. However, as shown in Tables 6-2 and 3, the average gap size measured by using SEM/ESEM techniques varied from 0.52-4.38 μm. Therefore, only some of the gaps could be identified by using the micro-CT technique. For example, Figure 6-17 provides the detailed gap size distribution data of the cement samples listed in Table 6-3. Most of the measured gap size was below the CT resolution. At location 16, Although both Sample A_W and Sample G_WO have gap sizes larger than CT resolution, they are still close to the CT resolution and therefore cannot be clearly captured. On the contrary, most of the gap in Sample A_WO exceeds the CT resolution. That is why we only discussed Sample A_WO in Figures 6-14 and 15. We should be very cautious about making broad conclusions based on the result obtained from the micro-CT because of the presence of a large number of small gaps, which were beyond the CT resolution and might have been already filtered. Data shown in Figure 6-17 also indicate that the gap size varies significantly.

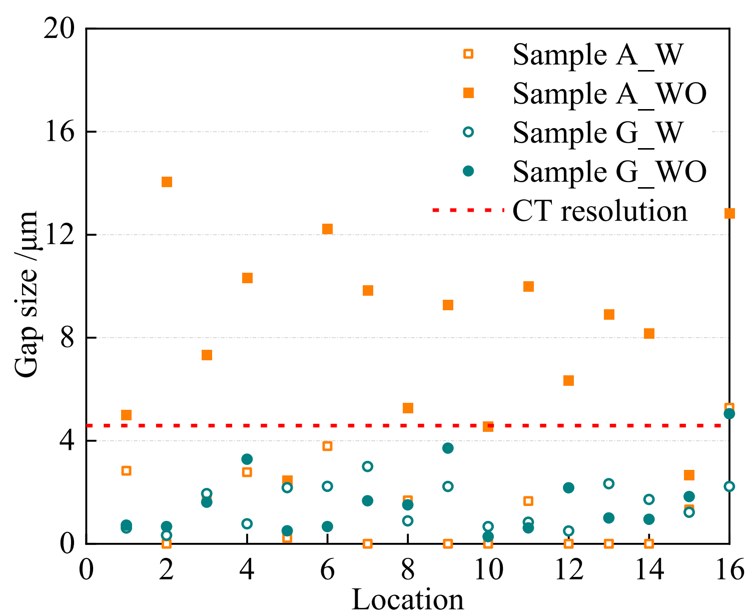

Figure 6-17 Detailed gap size data of cement samples listed in Table 6-3 (SEM/ESEM data).

Since the presented lab results were obtained at the micron scale, special attention should be paid when comparing the lab results with the field data. The shrinkage value is a dimensionless parameter and, therefore, is independent of sample dimensions. However, size effect exists in the hardened cement paste (Ba et al., 2013; Wee et al., 1987). The study is limited by the lack of information regarding the size effect on the gap between the cement and casing. In addition, drilling fluid and its associated residues (e.g. mud cake, drilled cuttings, etc.) on the wellbore and/or casing wall should be displaced before the cementing but in reality, ideal displacement is hard to achieve. This study was also limited by the absence of drilling fluid (i.e., mud cake) at the interface.

High cement shrinkage and interfacial debonding were known as the major reasons that lead to gas migration (Bonett and Pafitis, 1996; Parcevaux and Sault, 1984). (Torsæter et al., 2015b) pointed out that even for a 10 μm gap with a circumferential length of 1 m and depth of 1 km, the leakage rate caused by the gap is on the order of 0.63 m^3 per year. This is a rather small flow rate. More importantly, most cracks show rather limited connectivity, it is probably safe to say that the 3D gaps are not likely to induce significant leakage pathways. However, further studies are needed for more confirmation of these conclusions, in particular, to see what happens to the integrity of the cement/casing interface under in-situ stress conditions.

6.7 Conclusions

Effects of the environmental conditions (i.e. relative humidity of the storage and testing conditions), cement drying shrinkage and the expansion agent on the integrity of the bonding at the cement-casing interface at micron scale have been investigated by using environmental scanning electron microscopy (ESEM) and micro-CT (μ-CT) scanning techniques. Based on the experimental observations following conclusions can be offered:

- Any drastic change in the relative humidity (RH) of the environment during the cement preparation, curing and testing process significantly affects the degree of the de-bonding at the cement-casing interface.

- The 2D non-uniform gap size between the cement and the casing is inversely proportional to the change in the relative humidity (RH) of the environment.
- Storing cement samples in an ambient seal condition (~71% RH) and characterizing them using ESEM at 75% RH seems to be the most suitable method to obtain high resolution images of the cement-casing interface as well as minimize the cement drying shrinkage.
- Characterizing the cement-casing interface under high resolution allows us to capture the smaller gaps. Although these smaller gaps may have limited impact on the short-term permeability, they may function as the starting point of chemical attack and thus jeopardize the long-term wellbore integrity.
- The gap between the cement and the casing mostly occurs at the cement surface and the debonding does not show any significant connectivity below the cement surface.
- Cement slurries set and cured under downhole conditions with relatively constant RH may not undergo significant shrinkage and yield only minimal debonding effect.
- As long as the RH of the environment does not change significantly, the cement is expected to undergo a limited shrinkage and the debonding between the cement and the casing may not induce any significant leakage pathway as the debonding is only locally distributed at the cement surface without showing any connectivity along the wellbore axis.
- Optimizing the chemistry of the cement system enhances the cement casing bond integrity by reducing the gap size at the cement-casing interface. Wellbore cement which was designed to provide zonal isolation should be optimized to have no shrinkage, as it is the best insurance policy against degradation in integrity during the entire life of the well.

We will conduct further studies to investigate integrity of the cemented wellbores under more realistic wellbore geometry conditions such as samples simulating the casing-cement-casing and rock-cement-casing interfaces. The effect of rewetting and drilling fluid on the gap size change remains to be elucidated. Experimentally testing the permeability of the cement-casing samples is also vital to evaluate the leakage potential. Such efforts are expected to result in better understanding of the factors controlling cemented wellbore integrity and help design enhanced cementing jobs with minimal gas leakage potential from oil and gas wells.

Chapter 7 Characterization of the Microstructure of the Cement-rock Interface Using ESEM and Micro CT Scan Techniques*

7.1 Summary

Cement-rock interface is a major component of the wellbore barrier system. Leakage may result from the poor bonding between cement and rock interface. This paper investigates possible factors, which may affect the cement-rock interface bonding. More specifically, integrity of the cement-rock interface was characterized using micro-CT (μ-CT) and environmental scanning electron microscopy (ESEM).

Hollow cylinder rock samples were prepared by using rock samples (e.g. Banff-Dolostone, Pekisko-Limestone, Doig-Sandstone, Notikewin-Siltstone, Montney-Siltstone, Wilrich-Siltstone) collected from different Alberta wells at various depths. Two abandonment cement blends were injected into the rock open hole. After curing the cement-rock samples in water at ambient temperature (~21 °C) and 1500 psi for 7 days, the samples were then processed into thin sections. By using Environmental SEM (0.05 μm resolution) and micro-CT (11.92 μm resolution) techniques, the 2D and 3D models of cement-rock interface were developed. Using the CT images, CFD models were built to simulate fluid flow through the cement-rock samples.

For both cement and rock, there is a non-uniform porosity distribution in radial and axial direction. For most of the cement-rock samples, highest porosity region in the cement column was found at the cement-rock interface. According to CT analysis, average porosity of rocks is higher than that of cement. Traditional abandonment cement not only has a higher average porosity, but also has more fluctuations in the axial porosity distribution. Optimizing the chemistry of the cement system enhances the cement-rock interface bond by effectively reducing the gap between cement and rock observed in ESEM images. The gap reduction rate (traditional versus optimized abandonment

---

* This chapter was submitted to SPE Journal as "Yang, X., Kuru, E., Gingras, M., Iremonger, S., Biddle, S., & Lin, Z. Characterization of the Microstructure of the Cement-Rock Interface Using ESEM and Micro CT Scan Techniques.".

cement formulation) varied depending on the rock properties such as rock density and porosity. The gap reduction rate decreased with the increasing rock density. CT-based CFD simulation on the cement-rock samples showed that the location of the main flow depends on the permeability variance among cement, rock and interface. The cement-rock interface has more chance to act as the main flow pathway when intact (low permeability) caprock exists.

The sample preparation, image analysis and simulation methods used in this study can be also applied to other cement interface studies (e.g. cement-casing, casing-cement-rock). All these efforts are likely to result in a better understanding of the factors influencing the gas leakage from oil and gas wells, which will be useful for reducing the greenhouse gas emissions from oil and gas wells.

7.2 Introduction

Wellbore cement is the most important barrier elements as it provides zonal isolation to prevent uncontrolled flow of formation fluid to surface as well as cross flow among various underground formations. A good wellbore cementing practice is expected to provide zonal isolation throughout the life of a well, which expands from a well construction, through hydrocarbon production, to post-abandonment. However, even when cement is properly placed in the well, zonal isolation can be lost over time. Loss of zonal isolation not just harms the work safety but also brings long-term risks to the environment (after the abandonment of a well), such as emission of greenhouse gases and/or contamination of water aquifers (Bachu 2017; Dusseault e al., 2000).

Previous research (Bonett and Pafitis 1996; Celia et al., 2005; Viswanathan et al., 2008) summarized that possible causes of the zonal isolation loss. The most common cases are due to the failure of the cement interfaces in the well, either cement-casing interface, or the cement-formation interface (Baumgarte et al., 1999; Bourgoyne et al., 2000). In this study, we focused on the integrity of the cement-rock interface. Rock properties at the cement-rock interface vary a lot as a well is normally drilled through several different formations. Therefore, as far as the interface properties are considered, the cement-rock interface seems more prone to have leakage than the cement-casing interface. A notable example has been observed in a well after 30 years of CO_2-flooding operation, where textural studies on the cores revealed that the cement-rock interface degraded much more than the cement-casing interface and there was a high porosity zone at the cement-rock interface (Carey et al. 2007).

Many previous cement-rock interface studies have been related to the Carbon Capture and Storage (CCS) wells, where the main focus was to understand the influence of chemical reaction at the cement-rock interface (Carey et al., 2007; Agbasimalo and Radonjic 2012; Jung et al., 2013; Newell and Carey, 2013; Jung et al., 2014; Labus and Wertz, 2017). It was noteworthy that the geometry of cement-rock interface of the samples used in these studies had either a flat surface or some other irregular shape but did not have a realistic circular shape.

Researchers from SINTEF have investigated the effect of mud properties (Opedal et al., 2014; Opedal, et al., 2014), cement defect (Kjøller et al., 2016), interface geometry (Torsæter et al., 2015) and cement stiffness (Lavrov, 2018) on cement-rock interface integrity. In the majority of these studies, micro-CT scanning technique was used to non-destructively characterize the cement-rock interface. Due to the large sample sizes used in these studies, the resolution of micro-CT was limited to 24-200 µm. Considering the multiscale nature of the cement, in order to have a closer look at the interface microstructure, scanning electron microscope was used together with micro-CT as SEM can characterize the cement microstructure at nanoscale. However, traditional SEM characterization can cause cement shrinkage and thus degrade the quality of characterization results.

So far, however, very little attention has been paid to the role of formation rock properties on the cement-rock interface integrity. One good recent work by Opedal, et al. (2014) had a short discussion of rock types on cement-rock interface integrity where they qualitatively concluded that the different rock formations exhibited different interactions with the cement. But they did not offer much discussion about what actual mechanisms were behind their conclusion. To answer this question, more in-depth quantitative studies are needed. The cement used in their study was neat

Portland cement which has been commonly employed in previous cement-rock studies such as Agbasimalo and Radonjic (2012); Opedal et al. (2014); Labus and Wertz (2017). However, the neat Portland cement without additives suffers from significant density segregation and free fluid, and if fluid loss additives are not present then dehydration of the slurry is possible if pressure is applied to the slurry while adjacent to a permeable formation. A cement blend that is used in real wellbores should be considered in the cement-rock interface study as it is more relevant to the industrial practice.

The aim of this study is to explore the effect of formation rock types on the cement-rock integrity, and how to improve the cement-rock integrity by applying suitable cement blends. Unlike the using of outcrop rocks (Opedal et al., 2014), we used the formation rocks collected from wells drilled in Alberta. The resolution of micro-CT characterization was also improved to 11.92 μm by optimizing the sample preparation. A novel method was also proposed allowing to characterize the cement-rock interface at around 0.05 μm resolution with minimal cement shrinkage by using Environmental SEM. Moreover, we quantitatively characterized and analyzed the cement-rock interface at micron scale. Potential leakage pathways in the cement-rock samples was also discussed via CT-based flow simulations.

7.3 Materials and methods

7.3.1 Materials and sample preparation

Rock core samples collected from the Core Research Center depository in Calgary were sampled from multiple wells located in Western Canadian Sedimentary Basin, as shown in Figure 7-1a. These rock cores covered a wide range of rock types as they were obtained from six formations at various depth (Figure 7-1b). One sample from each formation was made into petrographic thin sections to confirm the rock lithology (Figure 7-1c). Petrographic thin sections were examined using a Nikon Eclipse E600 POL microscope, with photomicrographs taken using an Infinity1 Lumenera camera. Analysis results are summarized in Table 7-1.

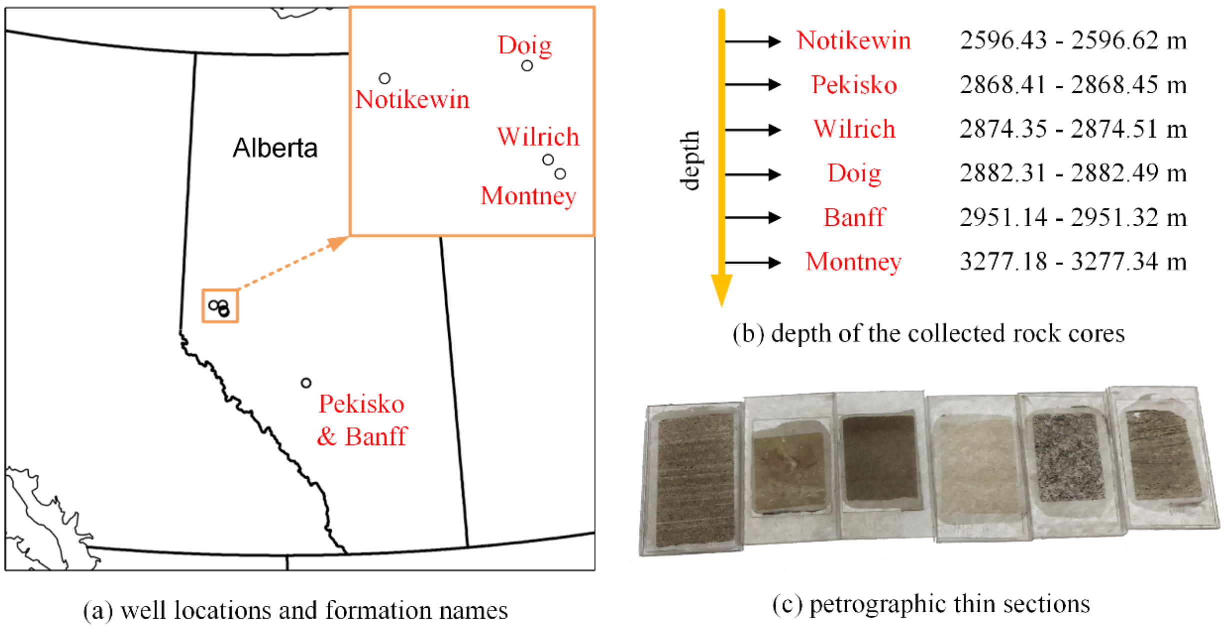

Figure 7-1 Locations and depths of the collected rock cores.

Table 7-1 Rock lithology of the collected formation samples.

Formation	Lithology from Alberta Table of Formations (Alberta Geological Survey 2019)	Actual lithology
Banff	limestone or dolostone	Dolostone
Pekisko	limestone or dolostone	Fossiliferous limestone
Doig	sandstone or siltstone	Quartzose very-fine-grained sandstone
Notikewin	sandstone or siltstone	Quartzose sandy siltstone
Montney	sandstone or siltstone	Quartzose coarse-grained siltstone
Wilrich	shale or mudstone	Quartzose coarse-grained siltstone

After drilling, cutting and polishing, the rock cores were processed into hollow cylinders (Figure 7-2a). The height of the samples in Figure 7-2b is about 9-11 mm. The diameter and hole size of the rocks in Figure 7-2b is about 21 mm and 8 mm, respectively. Rock density was calculated by measuring the volume and weight of the rock hollow cylinders.

Two cement blends were used in this study: One was a novel abandonment blend with engineered chemistry to minimize permeability, improve chemical resistance and show no chemical shrinkage (REM) and the other one a more traditional abandonment blend which was not engineered to give enhanced performance and will likely show chemical shrinkage (GAB). Throughout this paper, the term ‘REM’ and ‘GAB’ are used to refer to the two cement blends. Both blends have been used in the field applications.

The cement slurry was mixed according to API standard 10A and the slurry was then injected into the rock open hole. A small tamping rod was used to remove the bubbles from the slurry. Both ends of the rock were sealed by the electrical tape. The samples were conditioned at ambient temperature (~21 °C) and cured in a steel pressure cell filled with tap water at ambient temperature (~21 °C) and 1500 psi for 7 days. Figure 7-2b shows examples of cement-rock samples after curing. These are the samples prepared by using REM cement. Once the samples were taken out of the high pressure cell, they were stored in a small sealed plastic bags to prevent the water loss and isolate the cement interface samples from contacting the air.

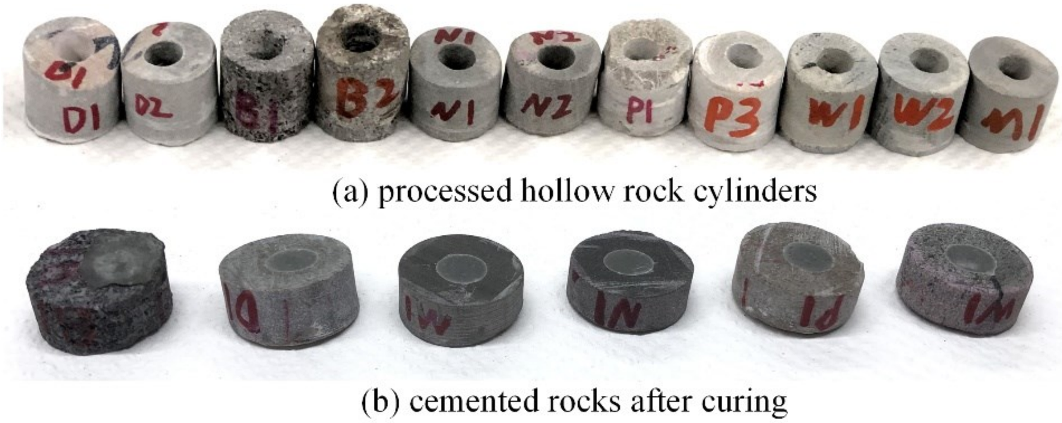

(a) processed hollow rock cylinders

(b) cemented rocks after curing

Figure 7-2 Preparation of the cement-rock samples.

Rock diameter is 21 mm and the hole size is 8 mm. Height of cement-rock samples is around 11 mm.

The prepared cement-rock samples were first characterized by using micro-CT. Then, they were processed into specialized thin sections so they can be characterized using environmental scanning electron microscope. Figure 7-3 shows how the cement-rock thin sections were prepared. Steps shown in Figure 7-3a to Figure 7-3c, describe a standard process, which is commonly called as epoxy impregnation.

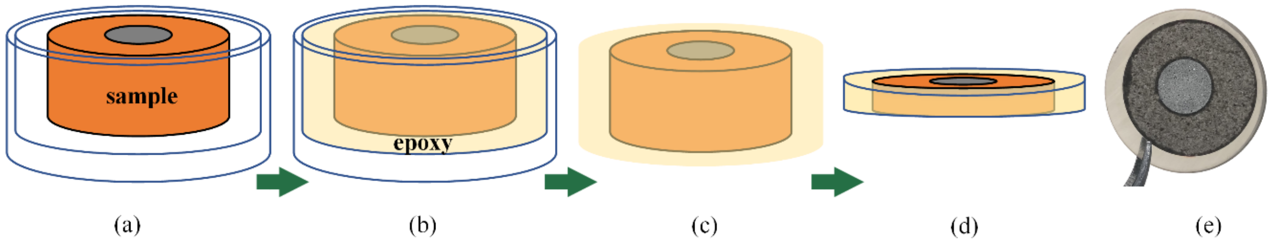

Figure 7-3 Procedure for the preparation and polishing of the composite thin sections.

(a) place the individual samples in a container. (b) vacuum the container and then inject epoxy. (c) remove the container once the epoxy solidified. (d) polish the composite thin section to certain thickness. (e) is the final sample.

7.3.2 3D characterization using micro-CT scan technique

After curing, all prepared cement-rock samples were characterized by a SkyScan 1172 micro-CT scanner (Bruker 2013) located at the Department of Earth and Atmospheric Science, University of Alberta. Computed tomography is currently the only mature method, which can non-destructively investigate 3D microstructure of the materials (Withjack et al., 2003; Cnudde and Boone 2013). Considering the high densities of both cement and the rock, high-energy X-rays are needed for the scan. So copper plus aluminum filter (Cu + Al) was selected to improve the contrast of CT images and to reduce the beam-hardening artifact. Flat-field correction and alignment tests were performed before the CT scan to ensure that the CT images have high contrast with less noise.

During the CT scan, the cement-rock samples were wrapped with plastic film to prevent the dehydration of cement. It is also important to note that CT images are created based on the materials density profile. Some rocks may have similar density with cement (because rocks are the raw materials to make cement (Stutzman, 2012)) and brings difficulties to differentiate the cement-rock interface in CT images. Prior to injection of cement slurry, an additional CT scan of the rock hollow cylinder can be used to solve this problem. The CT images of rock then can be utilized as the reference to differentiate the cement-rock interface.

Entire cement-rock sample was scanned at a resolution of 11.92 μm. Each CT scan will create about 1000 greyscale projection images. These images were further converted into about 1000 cross-section images, which are in 2000 × 2000 pixel format. The cross-section CT images were then imported into ScanIP, the commercial 3D visualization and analysis software (Synopsis, Mountain View, California, USA) to reconstruct the realistic 3D structures of the cement-rock interface samples. Readers can refer to Yang et al. (2019) for more detailed information regarding the cement CT scan and 3D reconstruction.

Based on the CT images of cement-rock samples, porosity distribution in radial and axial direction were determined. As shown in Figure 7-4a, 10 zones which have the same volume were identified. Zone 1-4 are the cement zones while 6-10 are the rock zones. The cement-rock interface is in Zone 5. Porosity distribution in radial direction, hence, can be determined based on the porosity of these 10 zones (Figure 7-4b). As for porosity distribution in axial direction, we simply calculated the cement porosity from each cross-section CT images (Figure 7-4c). Rock porosity data at the same depth (or close depth) of the same formation, were also collected from the public database AccuMap (IHS Markit 2019).

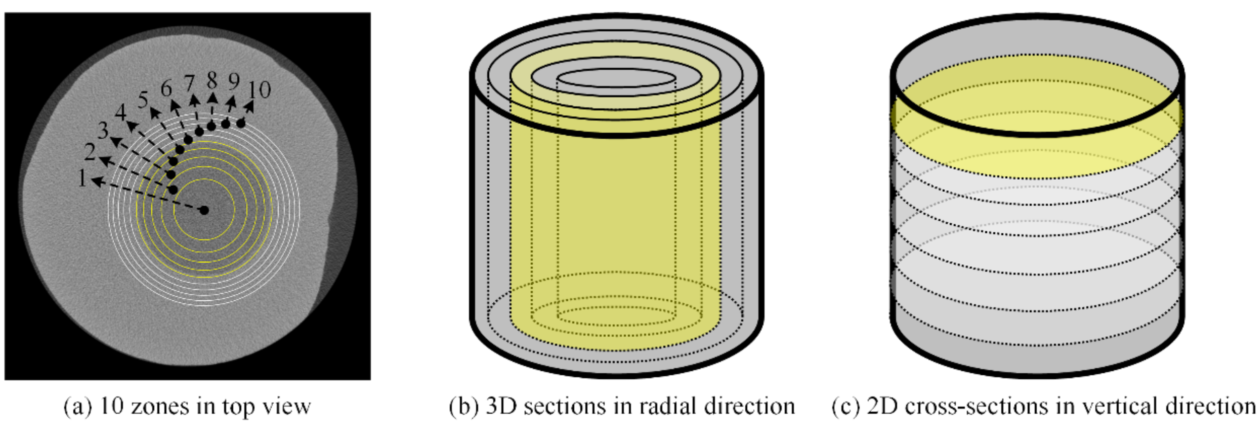

Figure 7-4 Schematic diagram of porosity distribution calculation.

7.3.3 2D characterization using ESEM

The highest resolution of our CT scan depends on how small the sample size we can prepare. The aforementioned 11.92 um is the highest resolution we can achieve. Higher resolution characterization tool is needed to capture more details regarding the cement-rock interface.

Scanning electron microscope (SEM) is a surface characterization equipment and can be used to characterize the cement features beyond the resolution of the micro-CT (Ramandi et al., 2017; Yang et al. 2020). Traditional SEM characterizes the samples under a high vacuum and low relative humidity (RH) condition (Neubauer et al., 1997; Bisschop and van Mier, 2002). This condition can cause significant cement shrinkage and affects the observation of cement-rock interface. To minimize the cement shrinkage, an environmental scanning electron microscope (ESEM) would probably be a more appropriate technique to use as the ESEM is able to image the hydrated cement interface samples at the controlled RH conditions.

In this study, Zeiss EVO ESEM located in in Department of Earth and Atmospheric Science, University of Alberta was used to capture images of the cement-rock interface. High RH can limit the cement shrinkage but also substantially decrease the image quality due to the skirting effect (Mathieu, 1999; Podor et al., 2019). To balance the image quality and cement shrinkage, a RH of 75% was selected. The ESEM chamber temperature was maintained at 10 °C. The 75% RH can be achieved by adjusting the chamber pressure. Images were captured after the RH stabilized at 75% for at least 5 minutes.

As shown in Figure 7-5a, ESEM images were captured at four different locations under 200× magnification. On each image, five yellow overlays were drawn to estimate the mean gap size (Figure 7-5b) by using the ImageJ software (Schneider et al., 2012).

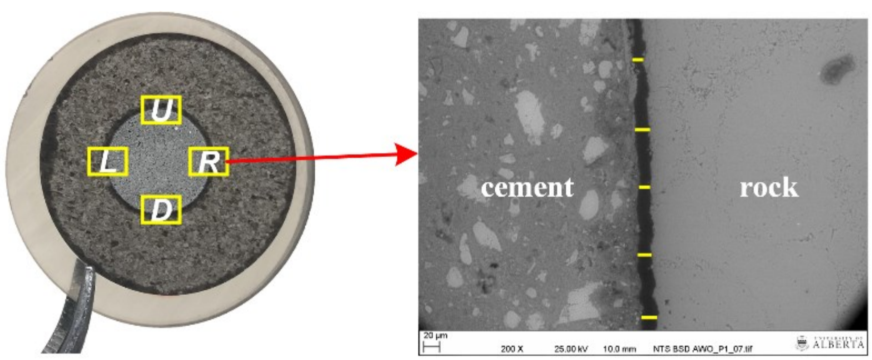

(a) cement-rock thin section (b) ESEM image of the cement-rock thin section

Figure 7-5 Illustration of where and how the gap size was measured.

7.3.4 CT-CFD integrated flow simulation

The 3D models reconstructed from cement CT images are called as digital cement models (Yang et al., 2019; Yang et al., 2020; Vrålstad and Skorpa, 2020). These 3D models can be directly used as the physical models in the CFD simulation. CT-CFD integrated simulation techniques have recently been used to investigate the mechanical and transport properties of cement paste or rock (Kjøller et al., 2016; Kabilan et al., 2016; Yang et al., 2019; Vrålstad and Skorpa, 2020). However, for the cement-rock interface study, the permeability of cement-rock composite is more important than the sole cement or rock permeability. In this study, multi CT-based flow simulations were performed to investigate the flow transport through the cement-rock samples.

Due to limit of the CT resolution, the connected pores or fractures from the tight or low-permeable section may not be captured. As a result, these sections were normally assumed as impermeable section. However, this does not fully represent the actual condition as the permeability values can be tested through experimental measurement. To overcome this problem, in this study we employed the dual-domain model (Yang et al., 2020) in the flow simulation. The dual-domain model treats the tight or low-permeable section as the porous domain, which is conveniently used to model the features that can not be practically resolved or discretized. For the detailed application of CT-based 3D simulation and the implementation of the dual-domain model, the readers may refer to Yang et al. (2019, 2020).

Figure 7-6 shows the physical geometries and boundary settings of the simulation. In reality, a well normally penetrates through various formations, including an impermeable caprock. The caprock plays an important role as it significantly limits the reservoir fluid flow due to its relatively impermeable characteristic. Therefore, considering realistic well condition, we build the 3D geometries of cement-rock samples with a caprock layer at the top. As can be seen in Figure 7-6a, a single formation layer model can be represented by the prepared cement-rock samples. To avoid any confusion, we call the formation rock as reservoir rock to differentiate it from the caprock. In Figure 7-6a, the cement part corresponds to the Zones 1-4 shown in Figure 7-4a, while the reservoir rock part is Zone 6-10 shown in Figure 7-4a. Zone 5 indicates the interface part.

Cement, interface, reservoir rock and caprock sections in Figure 7-6a are set as porous domains and their porosity and permeability need to be configured before running the simulation. The cement used in both cases is REM cement. According to our CT analysis and permeability measurement, the cement porosity and permeability can be obtained. The caprock porosity and permeability were collected from the published shale data. The interface porosity can be inferred from the CT analysis results. The only unknown is the interface permeability. Since our previous analysis shows that the interface zone has a higher porosity than cement, so in the simulation we assumed that the interface has a higher permeability (0.5 mD) than the bulk of the cement. Depending on the rock type, the rock permeability may be lower or higher than the interface permeability. To cover all the possible cases, we selected the Banff and Notikewin rocks. Banff rock has a permeability of 1.72 mD which is higher than the assumed interface permeability. In contrast, Notikewin rock has a permeability of 0.07 mD, lower than the interface zone. Detailed porosity and permeability settings in the simulation are summarized in Table 7-2.

Table 7-2 Porosity and permeability settings in the simulation.

Section	Banff case		Notikewin case	
	Porosity	Permeability	Porosity	Permeability
cement	1.10%	0.001 mD	1.10%	0.001 mD
interface	1.30%	0.5 mD	1.40%	0.5 mD
reservoir rock	7.20%	1.72 mD	4.00%	0.07 mD
caprock	3.00%	0.0001 mD	3.00%	0.0001 mD

The observed rock fractures from the CT images were also considered in the simulation as the largest rock fracture was included in the 3D physical geometries. The rock fracture was set as fluid domain. Figure 7-6b shows the boundary settings. The inlet boundary is the lateral surface of the rock and the outlet is the top surface of the 3D model. The pressure gradient used in the simulation is about 610 psi/ft and the fluid in the simulation was set as water.

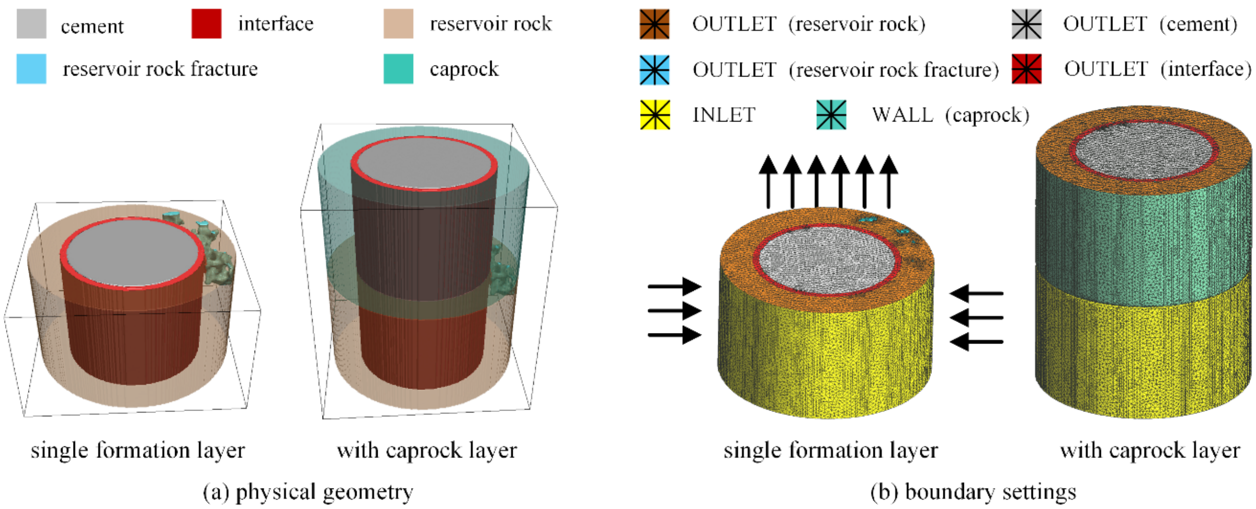

Figure 7-6 3D physical geometry and boundary settings for the flow simulation.

7.4 Results and discussion

7.4.1 3D porosity distribution in cement-rock samples

Figure 7-7 shows the porosity distribution of rock and cement in radial direction. X-axis is the Zone ID which is labeled in Figure 7-4a. Considering the resolution of CT image is 11.92 µm, some small pores and fractures may not be captured, which would lead to the relatively low porosity values.

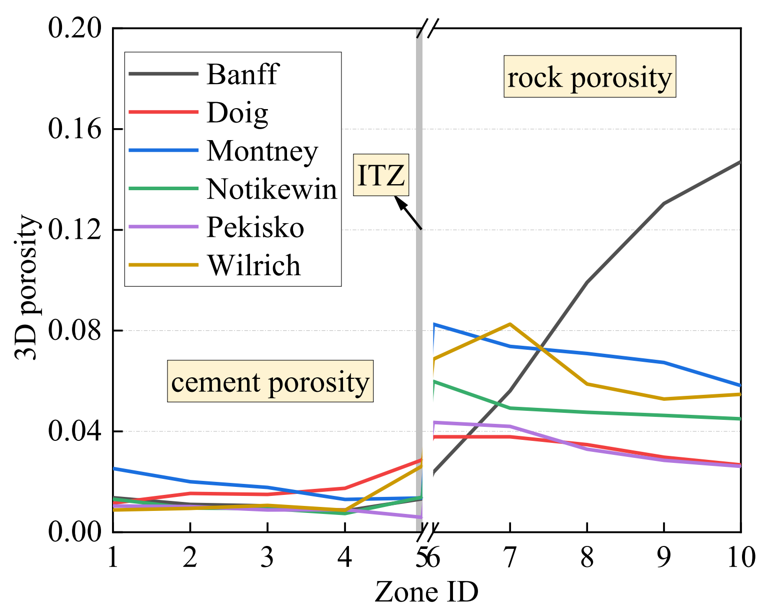

(a) Samples with REM cement

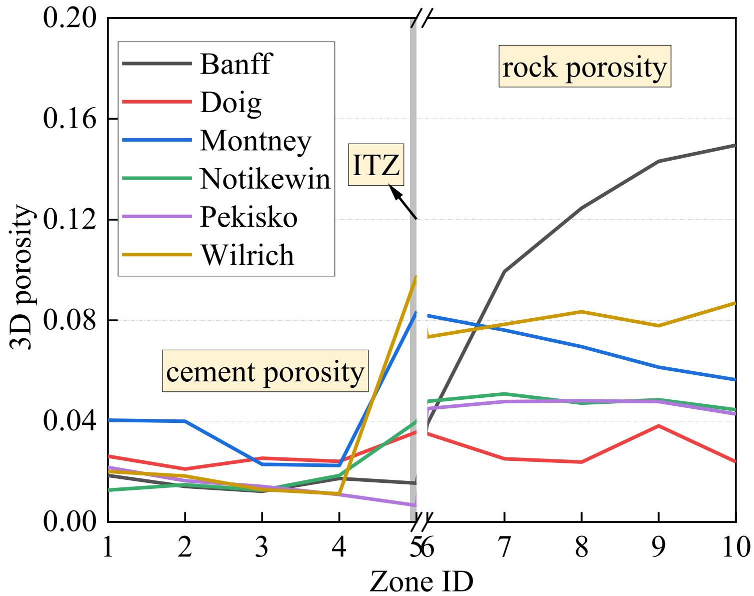

(b) Samples with GAB cement

Figure 7-7 Radial porosity distribution in cement-rock samples.

As can be seen from the Figure 7-7, for both cement and rock, there is a non-uniform porosity distribution in radial direction. In general, the porosities of rocks are higher than that of the cement. Even though we were using the same cement slurry formulation, the cement porosity distribution varied depending on the rock type. This means that the rock properties may affect the cement porosity distribution. For example, the rock permeability and wettability affects the cement-rock interface bonding (Nelson, 1990; Szewczyk and Opedal, 2019). The varied rock permeability and wettability may lead to slight dewatering of the cement slurry and results in varied cement porosity distribution. Nevertheless, caution must be applied when interpret the results based on the limited samples.

There seem to be a mutual interaction process at the cement-rock interface as the cement slurry filtrate invasion also affects the rock porosity distribution. One example of such cement filtration invasion into the porous rock can be seen in Banff rock. The Banff rock has a lower porosity at the zone close to cement because the cement slurry may have filled the voids of Banff rocks and caused the decrease of the rock porosity.

One important finding was that in some samples with GAB cement, Zone 5 which entails the cement-rock interface, had shown significantly higher porosity than its neighboring zones. Since Zone 5 had contribution from both cement and rock (i.e. interface), the porosity increase in this zone might have been because it contained some high porosity rocks. However, we didn't observe such significant porosity increase in Zone 5 of the samples with REM cement. Therefore, we infer the porosity increase in Zone 5 might have been mostly related to the characteristics of the cement microstructure at the interface.

Scrivener, Crumbie, and Laugesen (2004) proposed the interfacial transition zone (ITZ) theory for concrete material and claimed that the ITZ leads to a local increase in porosity. Torsæter, Todorovic, and Lavrov (2015) extended the ITZ theory to cement material. They indicated that a high-porosity zone of fine-grained material builds up at the interface because it is not possible to pack large particles in the near-wall region as densely as they are packed in the bulk cement. The REM cement has a wider range of particle sizes than the GAB cement. The finer particles in the REM cement is likely allow improved packing at the ITZ and this might explain why the Zone 5 in REM cement has lower porosity than the Zone 5 in GAB cement.

Rock samples collected from the cemented wellbore sections also showed the existence of high porosity region at the cement-rock interface (Carey et al., 2007). Assuming that the permeability of any porous media generally correlates well with porosity of the same, we may expect that the permeability of the cement-rock interface zone can be higher than the bulk cement permeability.

Figure 7-8 shows the cement porosity distribution in the axial direction. As the length of the cement-rock samples are different, dimensionless parameter "percentage of the cement length" was employed in the X-axis. Similar to the cement porosity distribution in radial direction, the porosity distribution in axial direction is also non-uniform. For both cement blends, higher porosity values were observed in the upper half of the sample (> 50% length), which also showed large porosity fluctuations. This result may be explained by the movement of the air bubbles as air bubbles rose to the cement top surface and caused the upper half of the cement sample to have lower density. The constant porosity increase in GAB cement may be related to the particle settling. For the lower half of the cement plug, porosity distribution in samples with GAB cement also shows some fluctuations. This difference might have been contributed by the difference in the solids fraction of the two cement blends since the REM cement had a higher solid fraction.

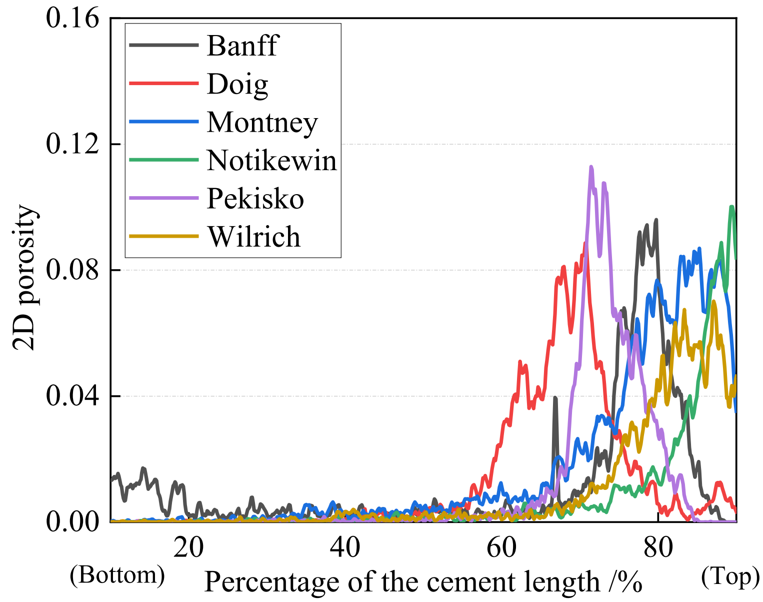

(a) Samples with REM cement

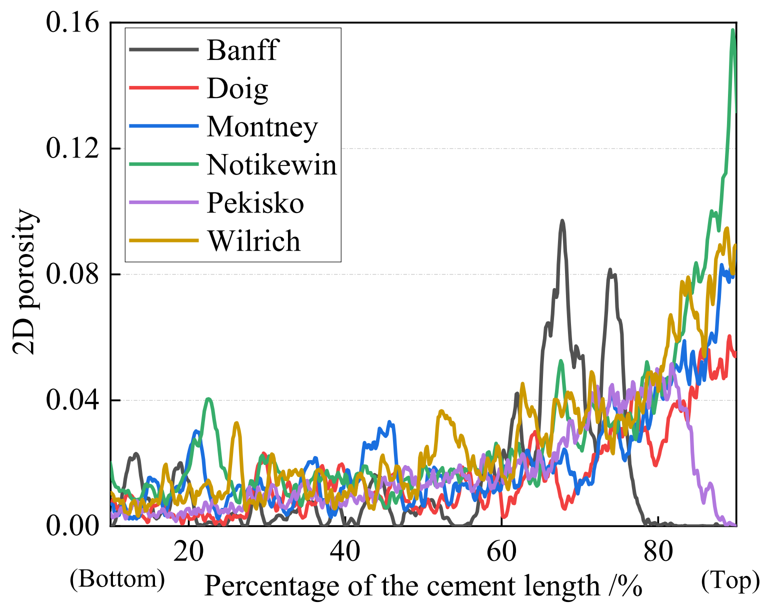

(b) Samples with GAB cement

Figure 7-8 Vertical cement porosity distribution in cement-rock samples.

Cement porosity is inversely correlated with the increasing cement density and solids fraction. However, the cement porosity variation in the axial direction might also have been affected by the gap observed at the cement-rock interface.

7.4.2 Gaps at cement-rock interface

Figure 7-9 presents several example images captured by using Environmental SEM. Since the resolution of the ESEM images is 0.55 μm, the boundaries of both cement and rock can be clearly identified. Gaps between cement and rock were observed in almost every ESEM images. Samples prepared using the cement blend with GAB cement seem to have larger gaps (Figure 7-9). To confirm this quantitatively, we measured the gap size using the ESEM images and plotted the results in Figure 7-10.

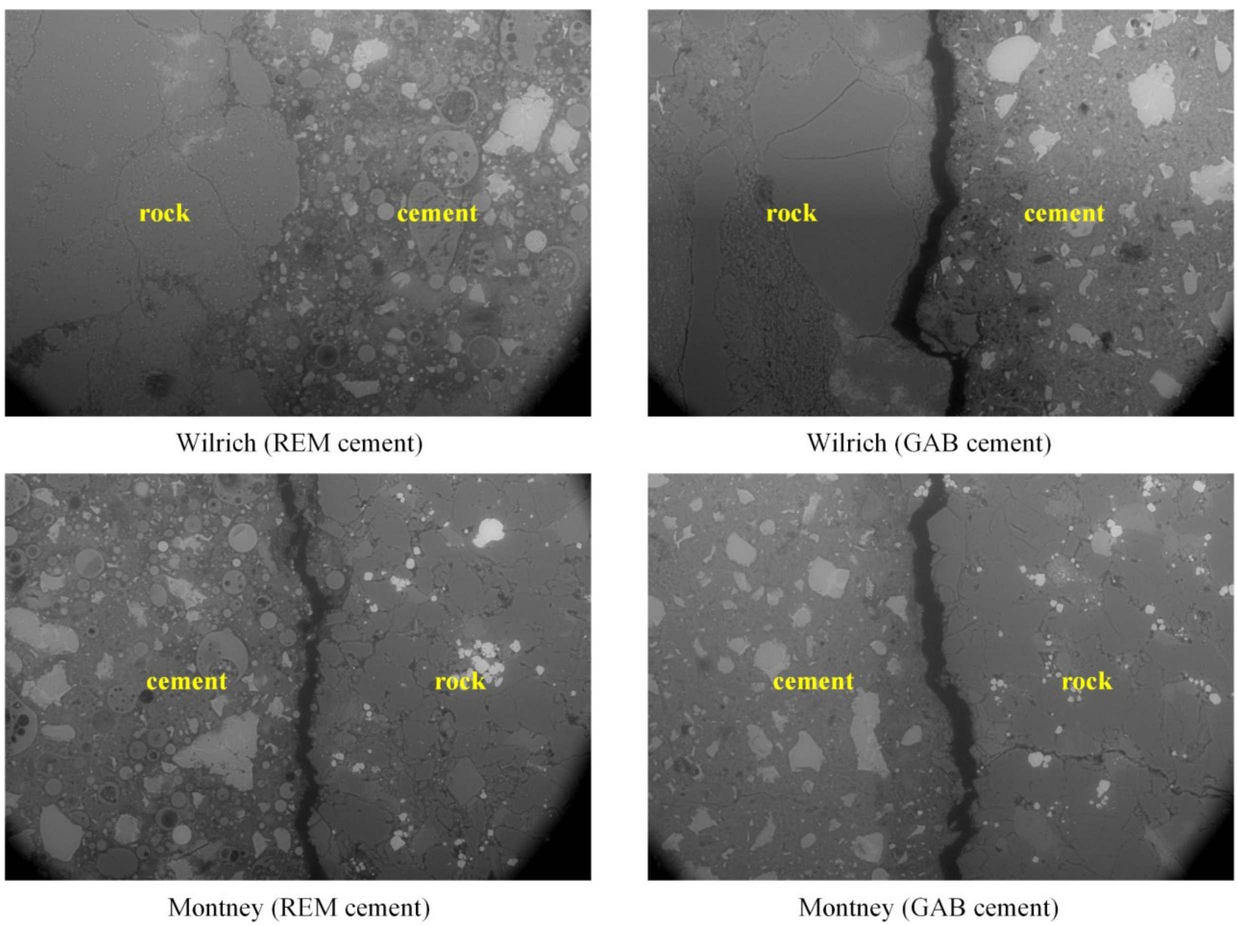

Figure 7-9 Examples of ESEM images of the cement-rock samples.

As shown in Figure 7-10 the gap sizes in cement-rock samples are distributed non-uniformly. The red dash line in Figure 7-10 is the limiting resolution of the micro-CT. Most of the gaps in samples with REM cement were beyond the detection capability (resolution) of micro-CT. On the contrary, the majority of gaps in samples with GAB cement could be captured using micro-CT.

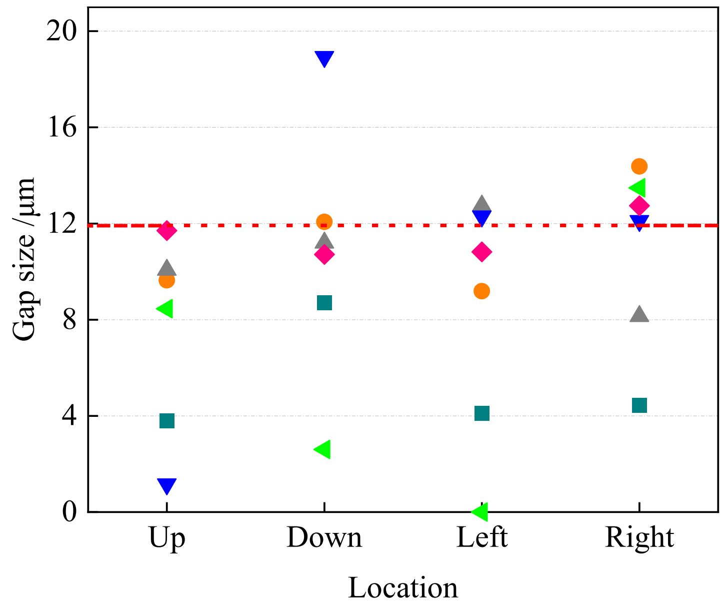

(a) Samples with REM cement

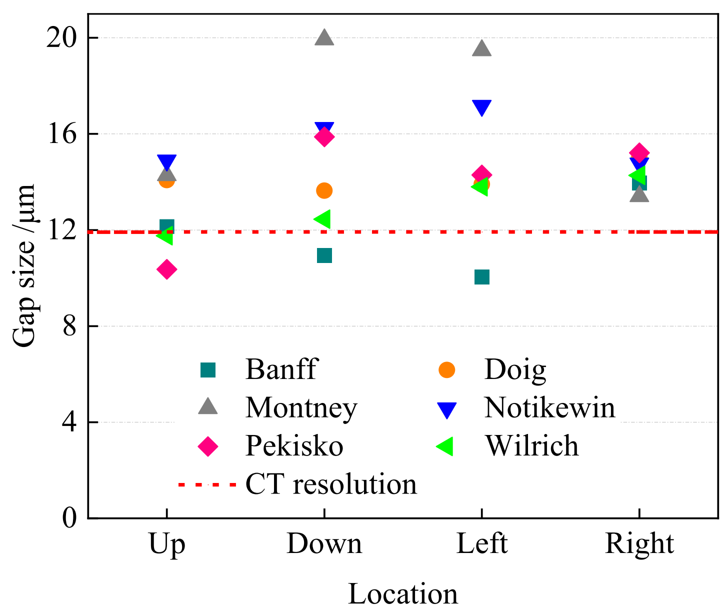

(b) Samples with GAB cement

Figure 7-10 Measured gap size from the ESEM images of cement-rock samples.

Although some gaps in ESEM images fall in the detectable range of micro-CT, it does not mean these gaps can be fully captured in CT images. One possible reason is that the cement samples were slightly dehydrated during the ESEM scan as the relative humidity is lower than 100%. So the observed gaps in ESEM images could be different with the gaps in the CT images because the cement samples were sealed to avoid dehydration during the CT scan.

Another reason for the observation difference might have been the small density difference between cement and rock leading to the low contrast of the CT images. One example is shown in Figure 7-11. In Figure 7-11a, the density of the cement and rock were 1.9 and 2.67 g/cc, respectively. The sample shown in Figure 7-11b used the same cement blend as in Figure 7-11a but the rock density was 2.89 g/cc. Obviously, the interface in Figure 7-11b is much clearer than in Figure 7-11a. The other possible reason for missing the gaps in CT images might have been the partial volume effect (Kato et al., 2013) induced by inherent resolution limitations of X-ray micro-CT. Due to the partial volume effect, the boundaries of cement and rock were blurred, which would make it very difficult to detect the gap.

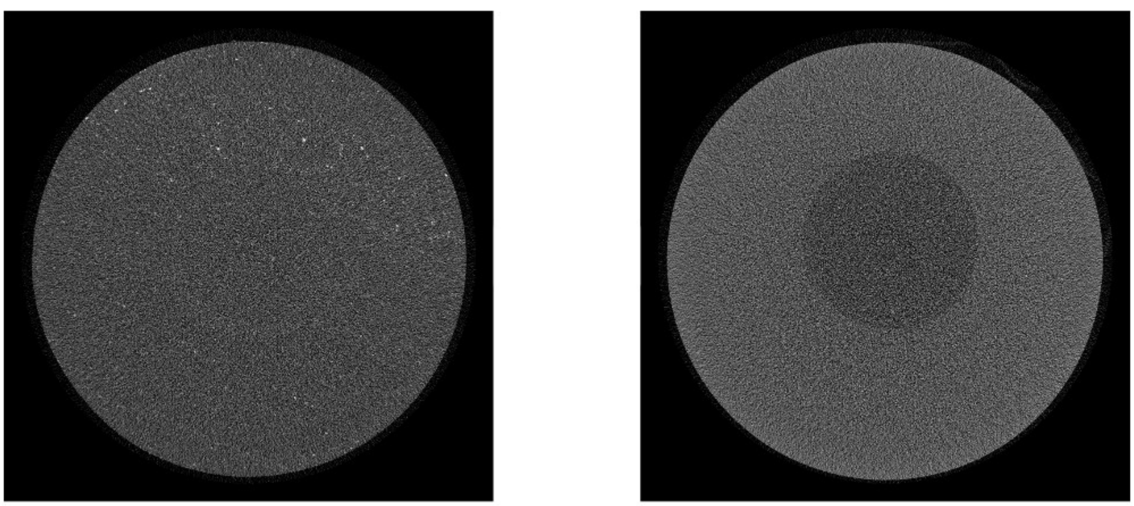

(a) Montney (GAB cement)　　(b) Pekisko (REM cement)

Figure 7-11 Contrast of CT images depends on the density difference between cement and rock.

Although we did not find any circumferential gap from CT images, we did observe several spots with gaps (voids) from the CT images, as shown in Figure 7-12. The gaps are all located at the near surface positions. The gap size changed along the axial direction and more importantly, the length of gap in the axial direction is very limited. For the gaps marked in Figure 7-12, we measured the change of their size along the axial direction and the results are shown in Figure 7-13.

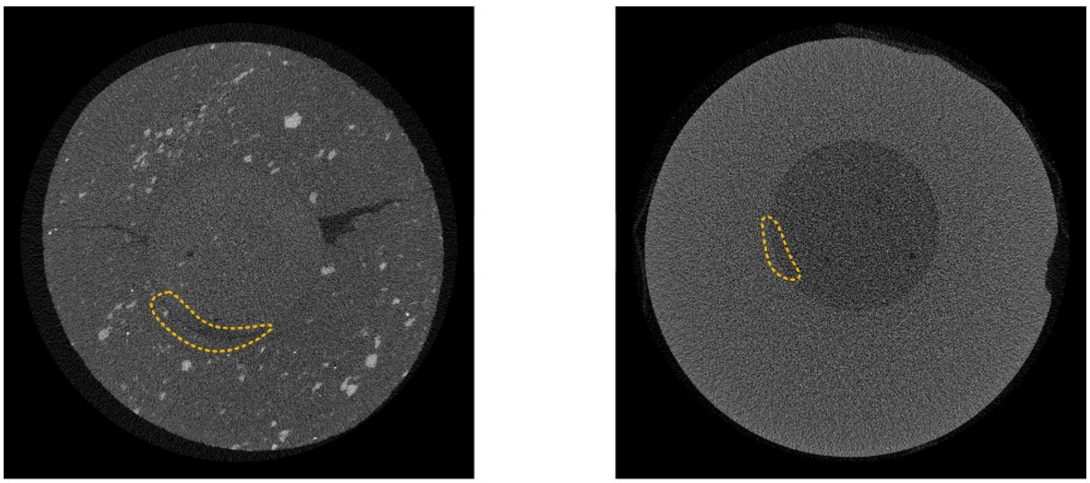

(a) Wilrich (GAB cement) (b) Pekisko (GAB cement)

Figure 7-12 Observed gaps in CT images of cement-rock samples.

Figure 7-13 shows the gaps observed in CT images are much bigger than the gaps observed in the ESEM images (Figure 7-10). There is a significant gap size change from the near surface level to a deeper level and at about 0.2 mm distance from the surface, the gap was completely vanished. The significant gap size change might have been caused by the uneven surface of the rock inner wall surface. Bachu and Bennion (2009) indicated that the presence of a through-going annular gap and/or cracks in the order of 10–300 μm in aperture leads to a significant increase in effective permeability in the range of 0.1–1 mD. However, the gaps shown in Figure 7-13 have poor connectivity as they didn't break through the sample in the axial direction. Therefore, these gaps are not likely to induce significant leakage. Although these locally distributed gaps may have limited impact on the short-term permeability, they may function as the starting point of chemical attack and thus jeopardize the long-term wellbore integrity.

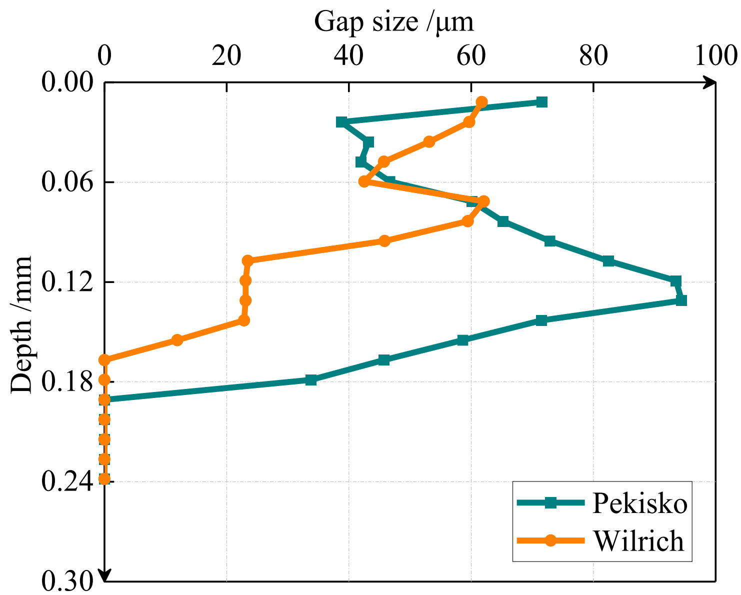

Figure 7-13 Change in the size of the gap width between cement and rock versus depth. 0 mm depth level represents the sample surface.

Table 7-3 summarized the average gap size calculated using the data shown in Figure 7-10. What stands out in the table is the gap size was significantly reduced in the samples using REM cement. The data in the last column was defined as the gap reduction rate (GRR). Closer inspection of the table shows the gap reduction rate also seems to be related to rock properties.

Table 7-3 Average gap size of samples prepared using abandonment blends w/wo expansion agents.

Rock	Samples with GAB cement (L_{GAB}) /µm	Samples with REM cement (L_{REM}) /µm	$L_{GAB} - L_{REM}$ /µm	$\frac{L_{GAB}-L_{REM}}{L_{GAB}}$ /µm
Banff	11.78	5.26	6.52	55%
Doig	14.16	11.32	2.84	20%
Montney	16.78	10.54	6.24	37%
Notikewin	15.77	11.13	4.64	29%
Pekisko	13.94	11.49	2.45	18%
Wilrich	13.07	6.14	6.93	53%

7.4.3 Rock properties versus gap reduction rate.

Figure 7-14 are the photomicrographs of the formation rocks. The details of the rock lithology were summarized in Table 7-1. From the Alberta Formation Map (Alberta Geological Survey 2019), the lithology of Wilrich Formation is identified as 'shale or mudstone'. However, according to our photomicrographs, the rock core samples at the elevation we collected from the Wilrich Formation are siltstone. These formations vary in lithologic properties throughout their depth, and therefore, for cement-rock interface study, confirmation of the rock lithology throughout the formations should be a mandatory step.

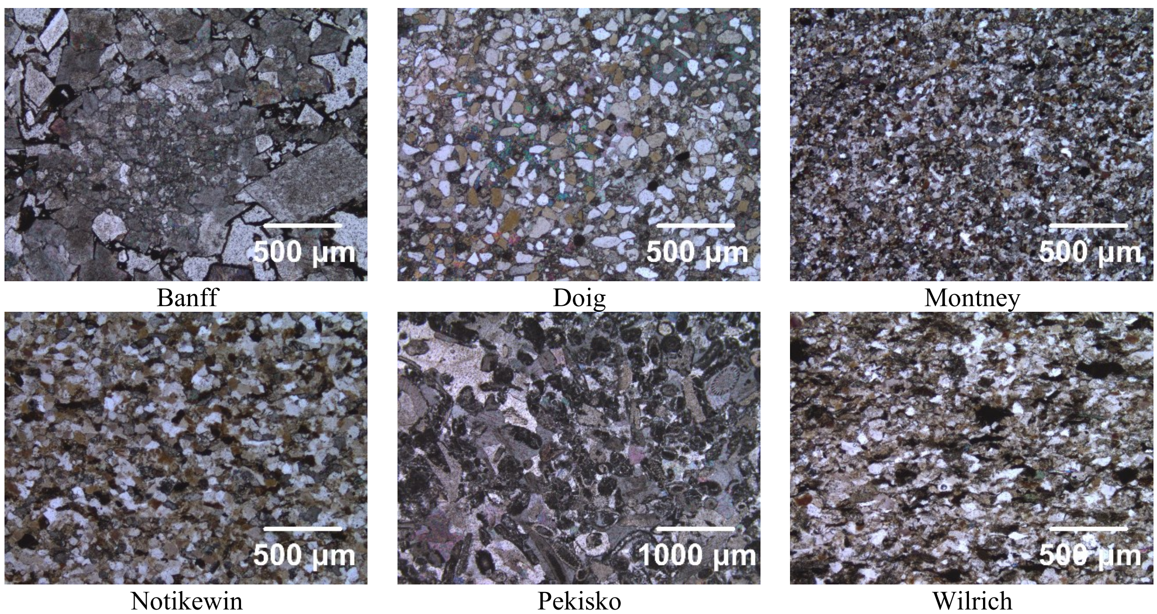

Figure 7-14 Photomicrographs of formation rock thin sections.

Table 7-4 summarized the rock properties and the gap reduction rate extracted from Table 7-3. Results shown in previous sections point out the gap reduction rate may be related to rock properties. In Table 7-4, we have three columns of the quantified rock properties: bulk density, porosity from AccuMap and porosity from CT images. Here comes a question: Does rock density or porosity affect the gap increase? To answer this question, we have made three plots shown in Figure 7-15.

In Figure 7-15, linear curve fittings were performed and the R-squared of each plot was calculated. R-squared of correlation between gap reduction rate and rock density is higher than the other two (i.e. porosity from field measurement and CT analyses). This implies that the gap size reduction due to optimization of the cement blend becomes more effective with the low rock density. Baumgarte et al. (1999) pointed out that the rock stiffness affects the cement-rock interface integrity. We didn't measure the rock stiffness in our study, however, the rock Young's modulus, which controls the rock stiffness was proven to have direct correlation with the increasing rock density (Ashby and Cebon, 1993). Overall, these findings suggest that there is a strong link between the rock properties and the integrity of cement-rock interface.

Table 7-4 Formation rock properties with gap reduction rate.

Sample	Lithology	Bulk density g/cc	Porosity from AccuMap	Porosity from CT	Gap reduction rate (GRR)
Banff	dolostone	2.15	7.20%	10.10%	55%
Doig	sandstone	2.89	1.10%	3.10%	20%
Montney	siltstone	2.67	4.20%	6.90%	37%
Notikewin	siltstone	2.43	4.00%	4.80%	29%
Pekisko	limestone	2.82	0.90%	4.00%	18%
Wilrich	siltstone	2.66	3.50%	7.10%	53%

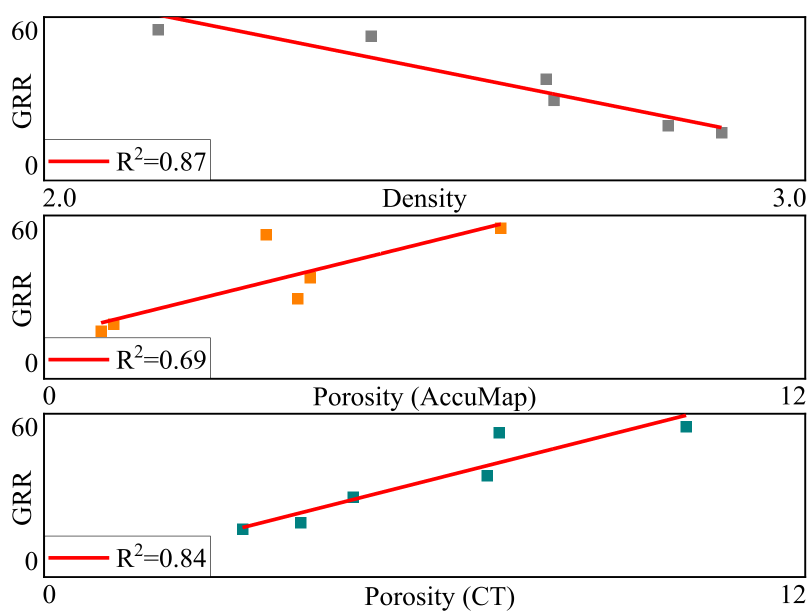

Figure 7-15 Correlations between gap reduction rate and rock properties (porosity and density).

7.4.4 CFD simulation results of water flow through cement-rock samples

Figure 7-16 shows the simulation streamlines of the water flow through the cement-rock samples. The color of the streamlines represents the velocity. Flow rate across different sections of the cement-rock samples was calculated and listed in Table 7-5. For the Banff single layer case (Figure 7-16a), the reservoir rock fracture connected the inlet and outlet, and therefore the velocity in the reservoir rock fracture and reservoir rock matrix varied several orders of magnitude. Under this circumstance, most of the flow occurs through the reservoir rock fracture. For the flow through the other sections, the flow rate depends on many parameters and can be explained by the Darcy's law:

$$Q = -\frac{Ak}{\mu}\frac{\Delta P}{\Delta x} \qquad \text{Eq. (7-1)}$$

where ΔP is pressure difference between inlet and outlet, Δx is the distance between inlet and outlet, μ is the viscosity, k is the permeability and A is the cross-sectional area of the flow channel. Longer flow path (higher Δx) leads to lower pressure gradient and results in lower flow rate Q. For example, cement part is at the center and the distance between inlet and outlet is the longest, when other parameters are constant, flow rate through cement part is lowest. Besides, cement permeability is lower than the permeability of reservoir rock and interface. This explains why flow rate of cement, shown in Table 7-5, is lowest in this case.

Table 7-5 Flow rate across different sections of the cemented rock sections of the wellbore. (unit: m^3/year)

Section name	Banff case		Notikewin case	
	single layer	with caprock	single layer	with caprock
cement	3.17×10^{-5}	1.56×10^{-5}	2.75×10^{-5}	1.88×10^{-5}
interface	4.69×10^{-3}	1.65×10^{-3}	4.29×10^{-3}	2.31×10^{-3}
reservoir rock	0.30	-	1.22×10^{-2}	-
reservoir rock fracture	90.56	-	-	-
caprock	-	2.01×10^{-6}	-	2.42×10^{-6}

For the Banff rock with caprock case (Figure 7-16b), the existence of the low permeable caprock changed the distribution of the streamlines. Although the reservoir rock has a larger permeability than cement, the low permeable caprock forced the flow through the relatively high-permeable interface zone. So the majority of the streamlines are distributed through the interface in this case. Table 7-5 also shows that most of the flow is through the interface.

For the Notikewin rock single layer case (Figure 7-16c), the reservoir rock fracture does not connect to the outlet, and it actually functions as an isolated fracture. Under this circumstance, the shortest flow path between the inlet and outlet is through the reservoir rock matrix. So even though the rock in this case has lower permeability than the interface zone, the main flow is through reservoir rock. Since the interface has the higher permeability, the slopes of the streamlines increase when they get through the interface.

Figure 7-16d shows the results of the Notikewin with caprock layer case. The influence of the caprock on the streamline distribution is the same as what we have seen in the Banff case: highest flow occurs through the interface. From these two case studies, we found that the rock fracture propagating to the surface generates the highest leakage. An intact caprock could limit the flow through rock itself. In this case the interface will be the relatively high permeable zone and also provides the shortest flow path for the fluid leakage. So when an intact caprock exists, the cement-rock interface is more prone to leakage regardless of the permeability of the reservoir rock.

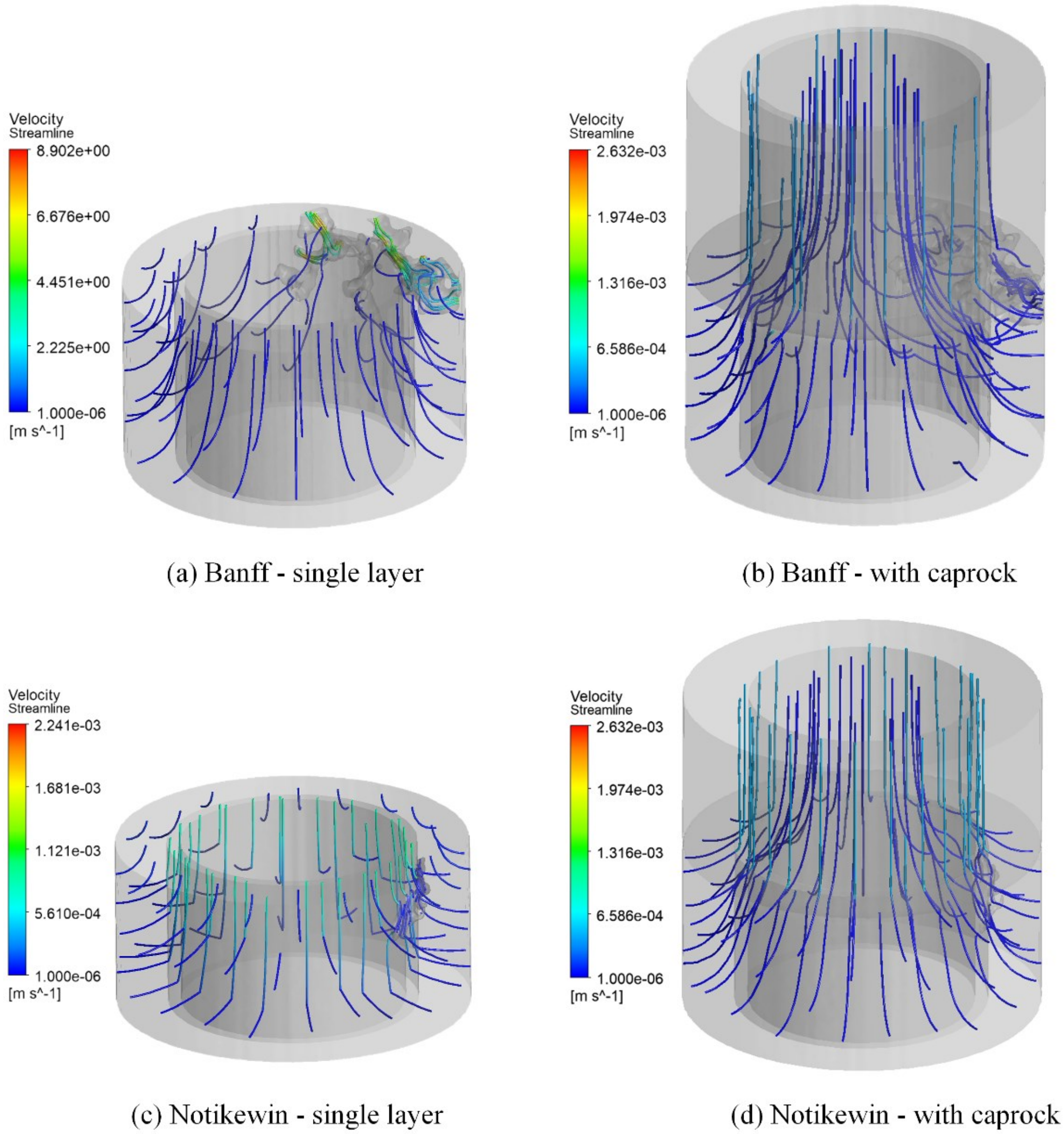

Figure 7-16 Streamlines of the Banff and Notikewin samples with expansion agent.

7.5 Conclusions

In this study we have characterized the microstructure of cement-rock samples at microscale by using microscope, micro-CT and ESEM.

Based on the analyses of the CT images, we have determined the radial porosity distribution in the cemented rock samples, which revealed that the interface zone had higher porosity than its neighboring zones. CT-based flow simulation study implies the cement-rock interface is more likely to provide the leakage pathway when intact caprock exists.

Gaps were observed at the cement-rock interface through ESEM images. The gap size was significantly reduced by optimizing the cement chemistry. The size of the gap between cement and rock varied depending on the rock properties such as rock density and porosity. The gap size reduction rate decreased with the increasing rock density.

Further studies will focus on to experimentally measure the permeability of cement-rock samples. More realistic sample geometries including the casing-cement-rock interfaces will also be investigated.

7.6 Appendix A-CT images of rocks with and without cement

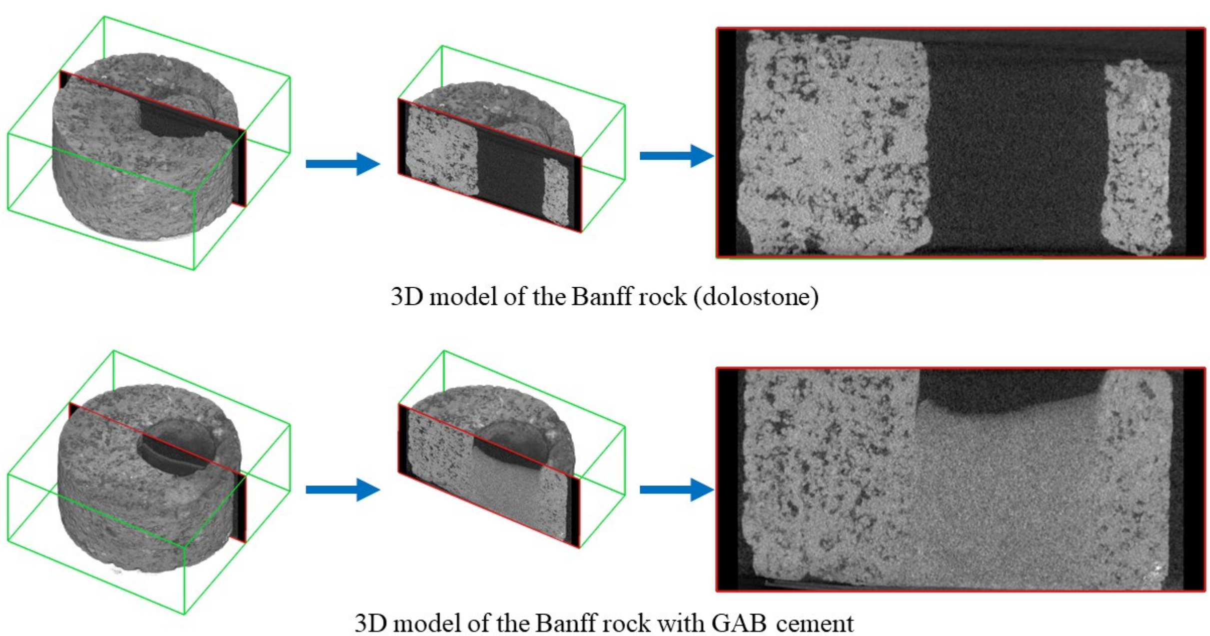

Figure 5A-1 CT images of Banff rock with and without cement.

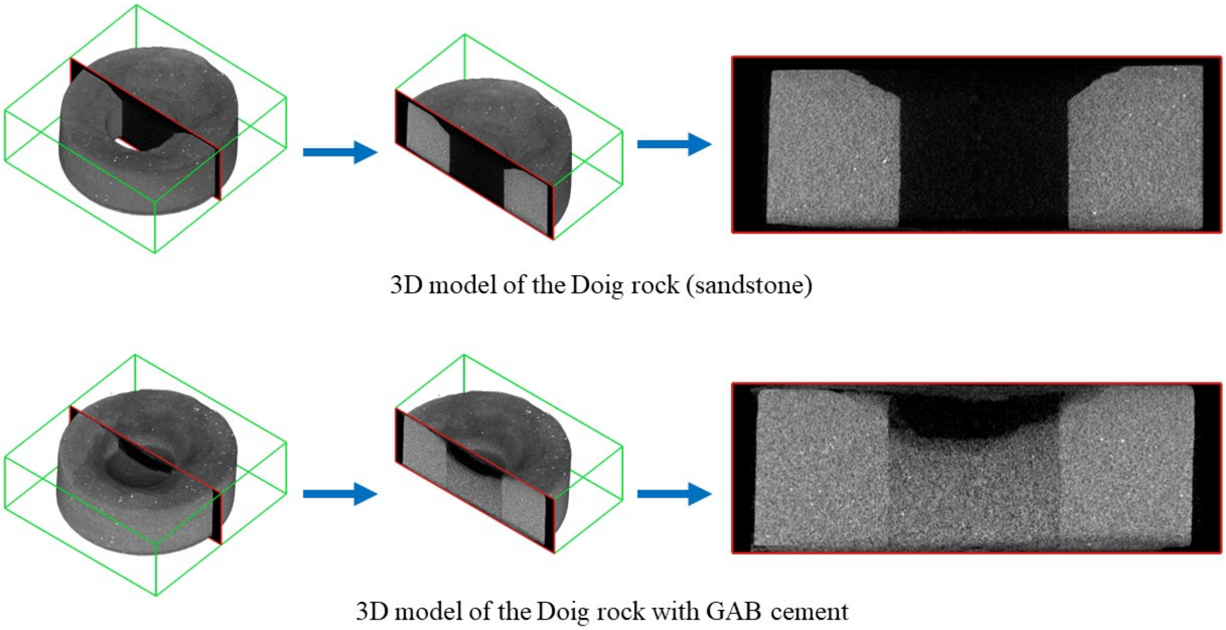

Figure 5A-2 CT images of Doig rock with and without cement.

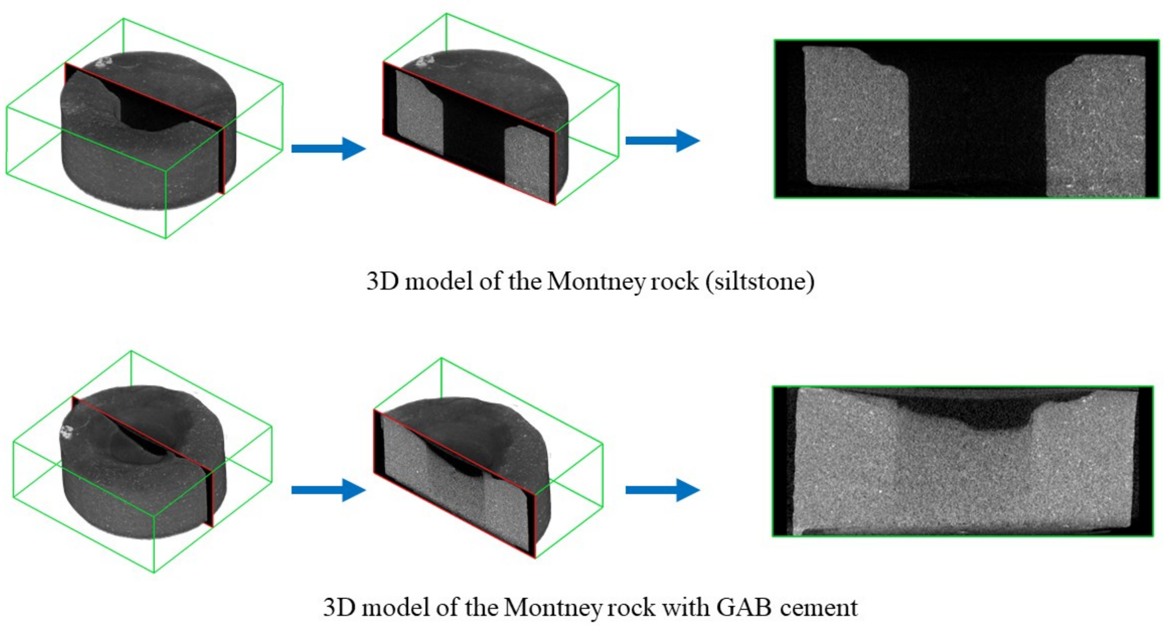

Figure 5A-3 CT images of Montney rock with and without cement.

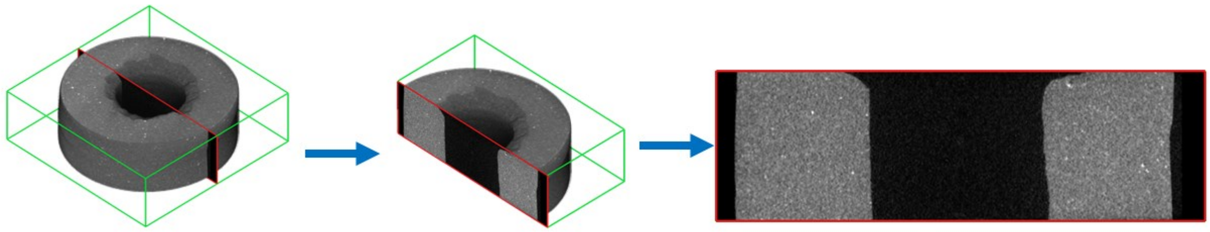

3D model of the Notikewin rock (siltstone)

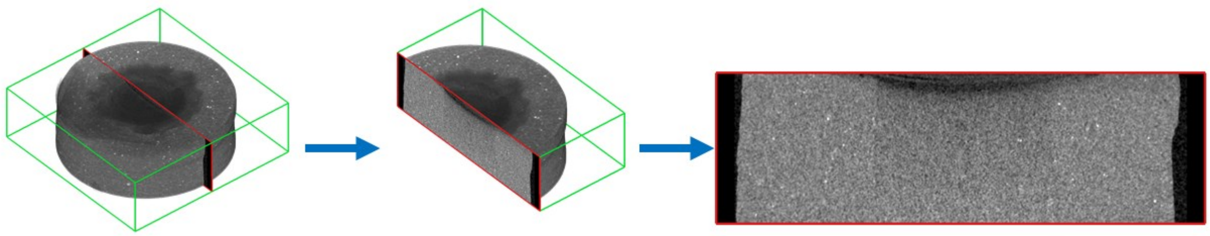

3D model of the Notikewin rock with GAB cement

Figure 5A-4 CT images of Notikewin rock with and without cement.

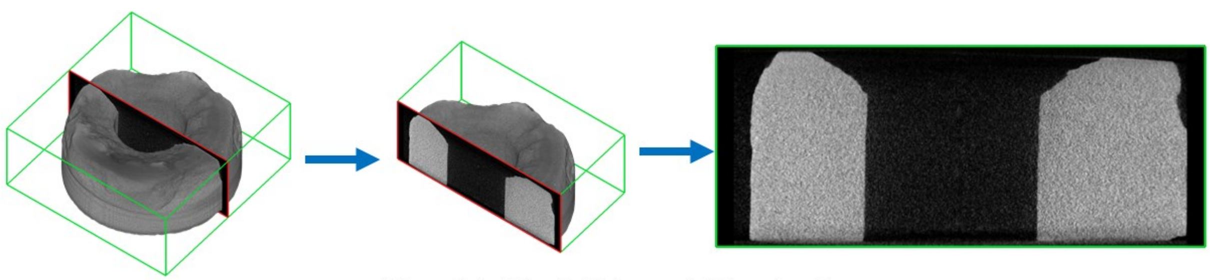

3D model of the Pekisko rock (limestone)

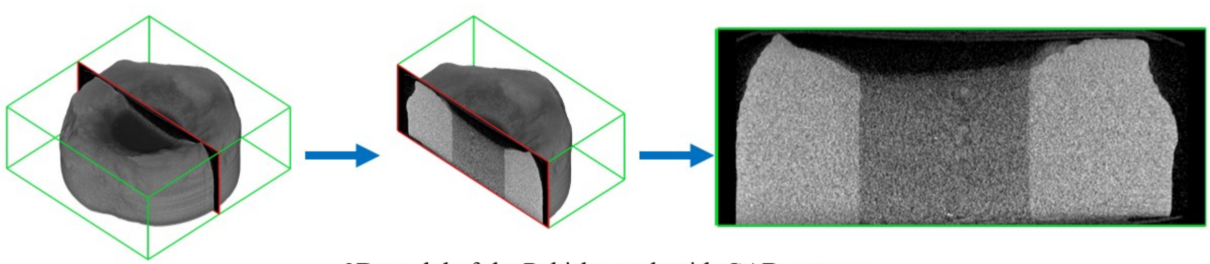

3D model of the Pekisko rock with GAB cement

Figure 5A-5 CT images of Pekisko rock with and without cement.

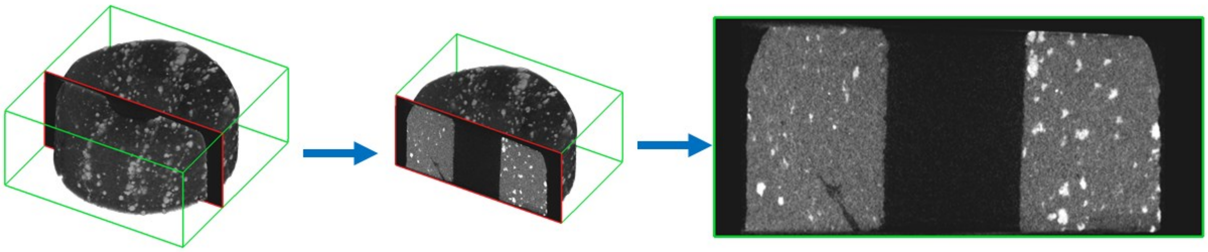

3D model of the Wilrich rock (siltstone)

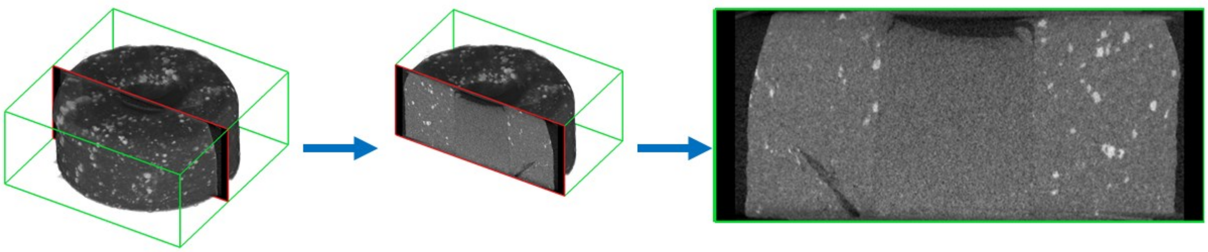

3D model of the Wilrich rock with GAB cement

Figure 5A-6 CT images of Wilrich rock with and without cement.

Chapter 8 Characterization of the Microstructure of the Casing-cement-casing Samples Using Micro CT Scan Technique

8.1 Introduction

Cement sheaths between the production casing and surface casing is an important component of the wellbore barrier system and essential for overall well integrity. Failure of the cement sheaths in between the casings can cause the surface casing vent flow (SCVF). Characterization of the microstructure of the cement sheath in between casings can help with better design of the cement job and thus help avoiding cement sheath failure in this case.

Microannulus formation is one of the cement sheath failures. The cement sheath located in between two casings has two interface geometry: the concave cement surface (cement-inner casing interface) and the convex cement surface (cement-outer casing interface). Torsæter et al. (2015) indicated that the microstructure at the two cement-casing interfaces are different. Most of the studies only focus on one interface, either the cement-inner casing interface or the cement-outer casing interface. The characterization of the microstructure of the convex cement-casing interface has been discussed in Chapter 6. Bachu and Bennion (2009) studied the leakage potential through convex cement-casing interface. Nath et al. (2018) investigated the cement-casing bonding using digital image correlation.

To date, there are few studies that have investigated the microstructure of the two cement-casing interfaces of a cement sheath. Based on the laboratory testing and field operations, Rusch et al. (2004) studied the performance of the pressure-activated sealant on sealing the microannulus channels in the cement sheath. Li et al. (2020) presented experimental and numerical investigations of the emergence and development of the cement sheath microannulus generated by the cumulative plastic strain.

In order to have good understanding of the microstructure of the cement-casing interfaces under more realistic conditions, it is better to work with one sample allowing to investigate the microstructure of the both cement-casing interfaces simultaneously. This is the main objective of this study.

8.2 Materials and methods

8.2.1 Preparation of the casing-cement-casing samples

As shown in Figure 8-1, two 304 stainless steel pipes in different sizes were used to simulate the casings. The inner pipe (OD: 9mm, Wall thickness: 0.2 mm) is the same one used for cement-casing sample preparation. The outer pipe (OD: 11.4 mm, Wall thickness: 0.3 mm) is a slightly thicker pipe. Both pipe were cut into short sections of 4 mm length. Cement will be injected at the annulus between two pipes. It is noteworthy to mention that field practice calls for the cement sheath OD/cement sheath ID to be around 1.26. In this work, the ratio is about 1.27, which is close to the expected value.

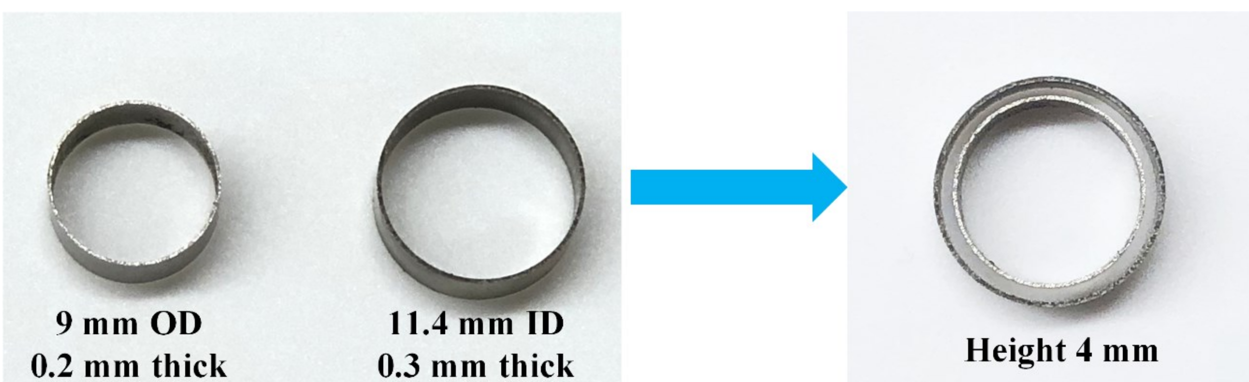

Figure 8-1 Dimensions of the casing pipes.

Two cement blends were investigated in this study. One blend is the Class G cement with an expansion agent (GEX). The expansion agent used in the cement is less than 2% BWOC. The other one is a novel abandonment blend (REM) with engineered chemistry to minimize permeability, improve chemical resistance and show no chemical shrinkage.

The cement slurry was mixed according to API standard 10A and the slurry was then injected into the pipe annulus. Figure 8-2 shows the slurry injection process. As the annulus ring size is about 1.2 mm, a special tool should be used to perform the injection. A syringe was used in this study to inject the cement slurry. A small needle was also utilized to tap the slurry to minimize the air voids in the annulus.

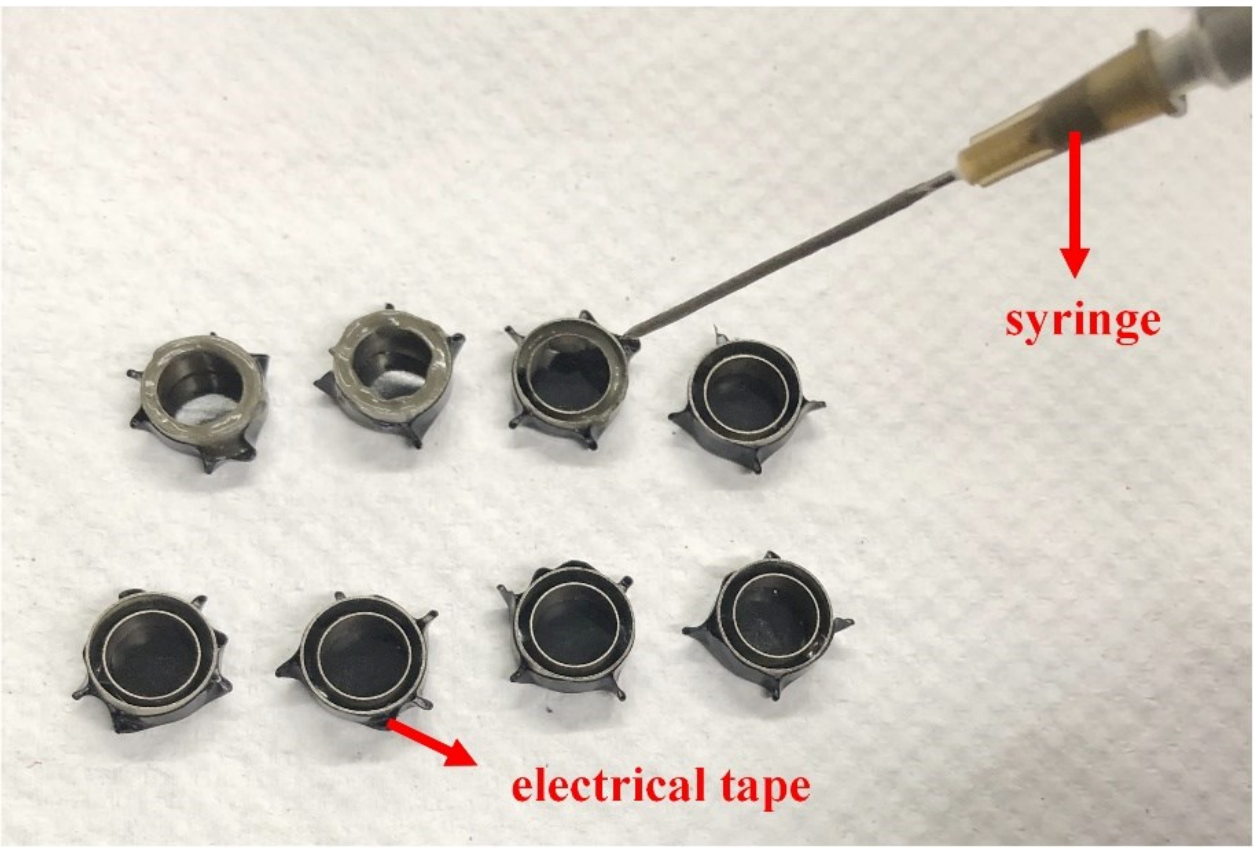

Figure 8-2 Injection of cement slurry into the annulus between casing pipes.

Electrical tape were used to seal both the top and bottom surface of prepared samples. The electrical tape has a good bond to the stainless-steel pipe, and this bond can be also used to centralize the inner pipe.

The casing-cement-casing samples were conditioned at ambient temperature (~21 °C) and cured in water under 50 °C and 1500 psi for 7 days. After curing, the samples were wrapped with plastic film to minimize dehydration. Considering the smaller annular ring size (1.2 mm), any polishing process, such as the thin section process, will damage the samples with no doubt. Therefore, these casing-cement-casing samples were only characterized by using the micro-CT technique, which is non-destructive to the samples.

8.2.2 Characterize the samples using micro-CT

The casing-cement-casing samples were scanned vertically using micro-CT, as the vertical CT scan can reduce the beam-hardening artifacts. The highest resolution of the CT image depends on the size of the outer casing. In this study, all samples were scanned at a resolution of 5.96 μm. One example of the cross-sectional CT image is shown in Figure 8-3a. Compared to the CT images of cement-casing samples shown in Figure 8-3b, two light white lines exist both at the top and the bottom parts of the samples. This is an unexpected result. The light white lines are probably artifacts rather than the real structure. To confirm our speculation, we conducted two CT scans (as shown in Figure 8-4).

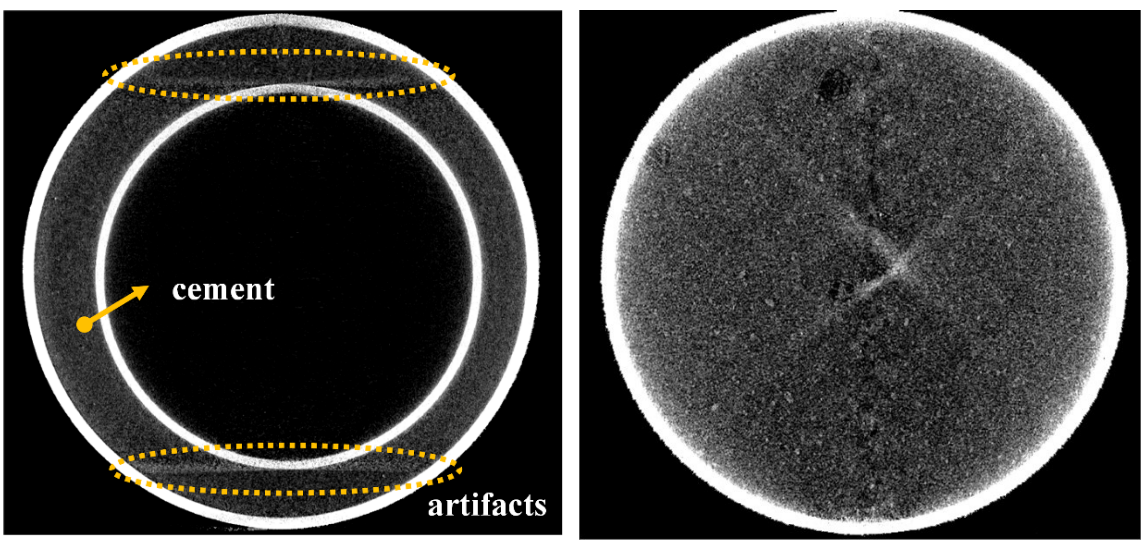

(a) casing-cement-casing sample (b) cement-casing sample

Figure 8-3 CT image of casing-cement-casing sample.

For the first CT scan, the sample was scanned vertically as usual. The top position was labeled using a marker. For the second CT scan, everything is the same except the sample is rotated 90° clockwise. CT images were reconstructed after the CT scan and two examples are shown in Figure 8-4. It is apparent that both CT images have similar characteristic: two light white lines exist in both top and bottom surface, and the remaining parts of CT images don't have the light white lines. This result verifies that the light white lines are artifacts rather than the real structure.

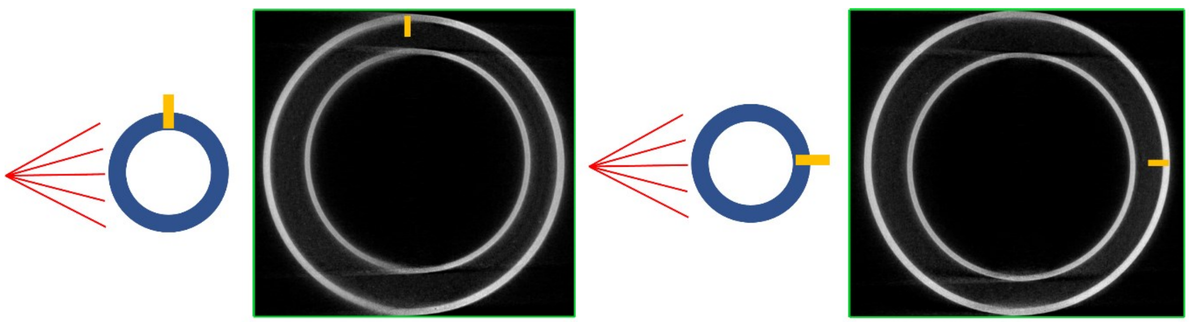

(a) CT image, first scan (b) Rotate 90° clockwise, scan again

Figure 8-4 Two CT scans on the same casing-cement-casing sample.

Another observed artifact exists in the cement annulus. As can be seen from the Figure 8-5a, there is a dark ring in the middle part of the cement annulus. The dark ring is the artifact because the horizontal CT scan (Figure 8-5b) on the sample didn't exhibit the same feature. Further observation also shows that only a few CT images have the dark ring. The dark ring would affect the cement porosity distribution calculation. Therefore, the CT images with dark rings should be excluded from the calculation.

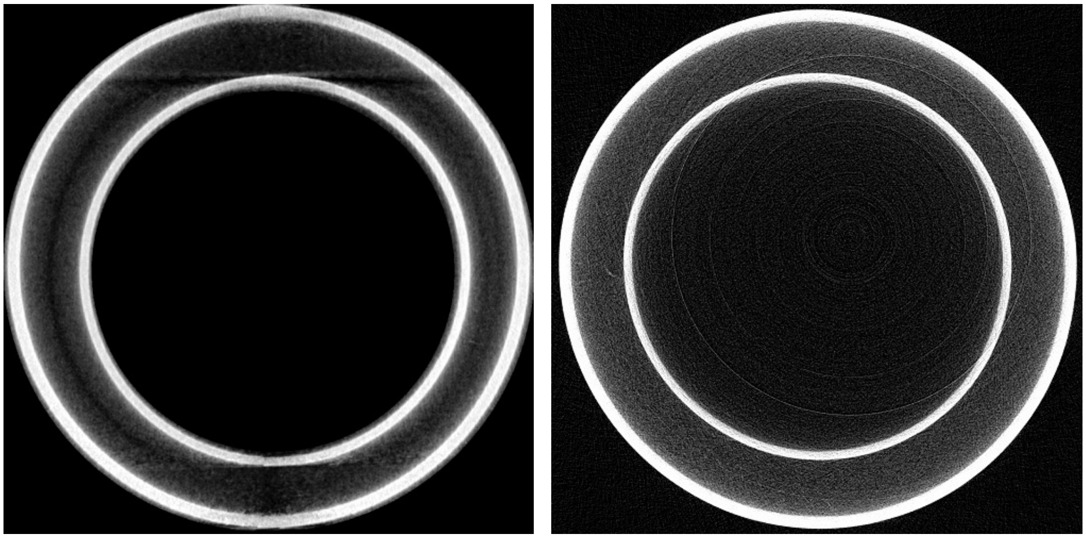

(a) vertical CT scan (b) horizontal CT scan

Figure 8-5 Vertical and horizontal CT scan on the sample.

8.2.3 Calculation of the porosity distribution in radial and axial direction

The porosity of the cement matrix can be calculated by using the CT images. The cross-sectional CT images were optimized before the porosity calculation. Basically, the casing pipes and white line artifacts were removed from the CT images, so there is only cement matrix in the processed CT images. One example of the processed CT image is shown in Figure 8-6.

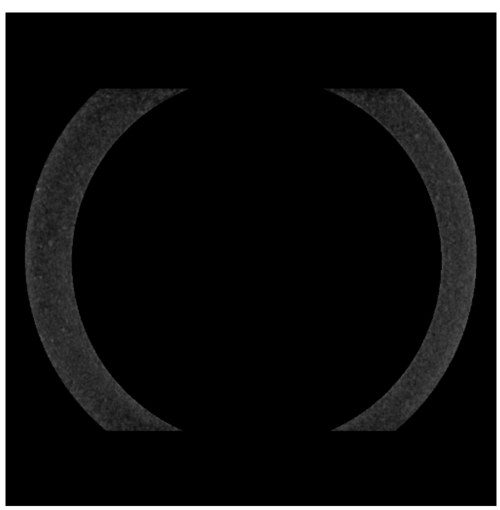

Figure 8-6 Processed CT image after removing casings and white line artifacts.

The cross-sectional CT images can be directly used to calculate the porosity distribution in an axial direction (along the casing length). The porosity calculated in an axial direction is, therefore, 2D porosity, as it is calculated from the 2D image.

For radial porosity distribution, the ideal process is to divide the cement sheath into annular subsections and calculate the porosity of subsections. However, due to the artifacts, both the top and bottom parts of the cement sheath were removed and the current cement sheath was separated into two parts. Besides, the divided subsections should have the same volume, and this is hard to achieve when the cement sheath does not have a regular shape.

In this study, we have employed a method of cement radial porosity calculation proposed by Lavrov et al. (2018). As shown in Figure 8-7, an inscribed rectangular area was labeled in the cement sheath and it was divided into five subsections, which has the same volume. As the annular ring size of cement sheath may vary from sample to sample, the width of rectangular area is also changed. The width of the subsection is between 178-208 μm. The length is fixed at 1895 μm. Porosity calculated from each zone is 3D porosity.

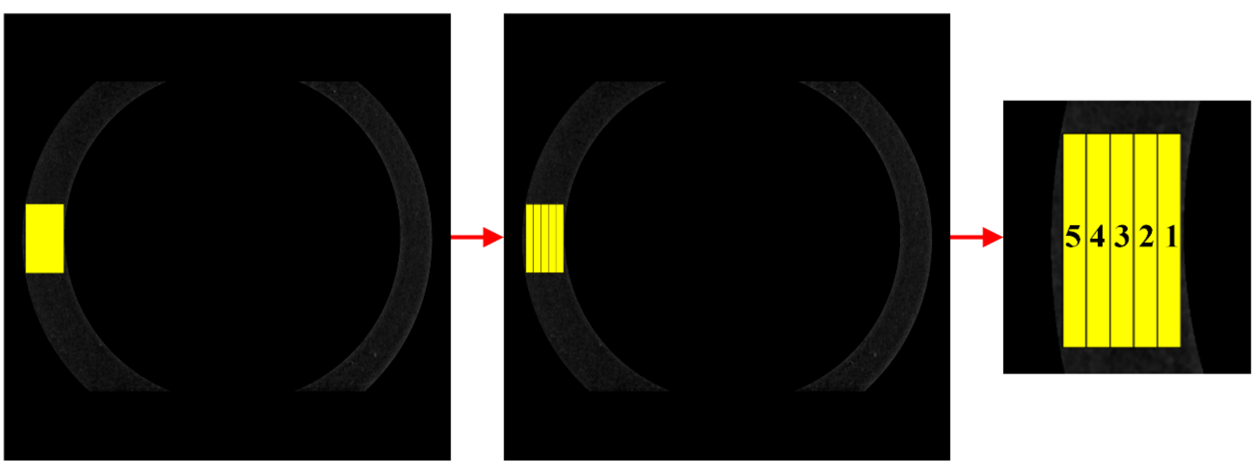

Figure 8-7 Calculation of the porosity of bins distributed in radial direction.

8.3 Results and discussions

8.3.1 Porosity distribution in the axial direction

The results of porosity distribution in the axial direction are shown in Figure 8-8. Two samples of each cement blend were analyzed. Although the casings all have a length of 4 mm, the length of the cement sheath column is varied. Therefore, for the x-axis in Figure 8-8, the dimensionless length parameter 'percentage of the cement length' was used.

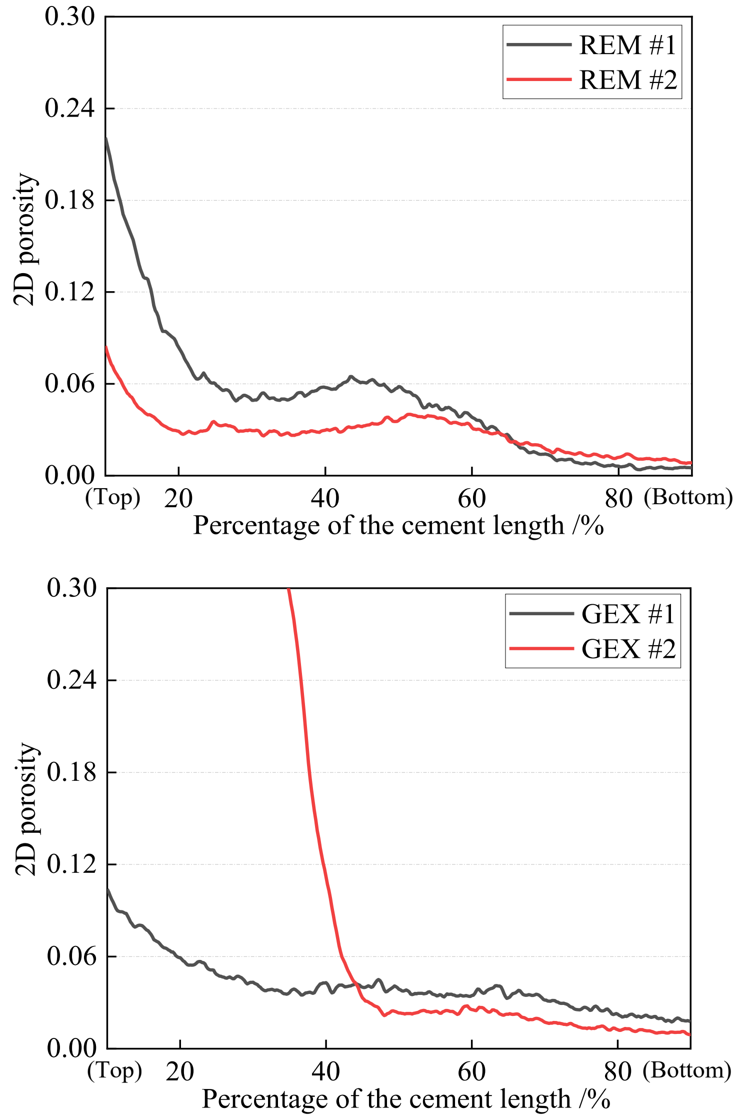

Figure 8-8 Axial porosity distribution of casing-cement-casing samples prepared using cement blends REM and GEX.

For samples prepared using REM cement, the porosity distribution in the axial direction is not uniform. The 2D porosity decreases from top to bottom surface of the cement sheath column. This trend is most likely caused by the density gradient observed in the side view cross section CT images. As can be seen from Figure 8-9, the left picture shows a side view of the cross-sectional CT image of the REM#1 sample, and the right picture is the enlarged view of the area marked in red. The enlarged view shows that the color of the cement is changing in the vertical direction, as cement at a lower level has a brighter color than the cement at the upper level. In the CT image, color represents the density, brighter color means higher density. So we can see that there is a density gradient in the vertical direction and the low density cement is located at the top part. Therefore, the porosity should be higher at the top. The density gradient may be explained by the particle settling (due to gravity) in the cement slurry causing the upper half of the cement sample to have lower density.

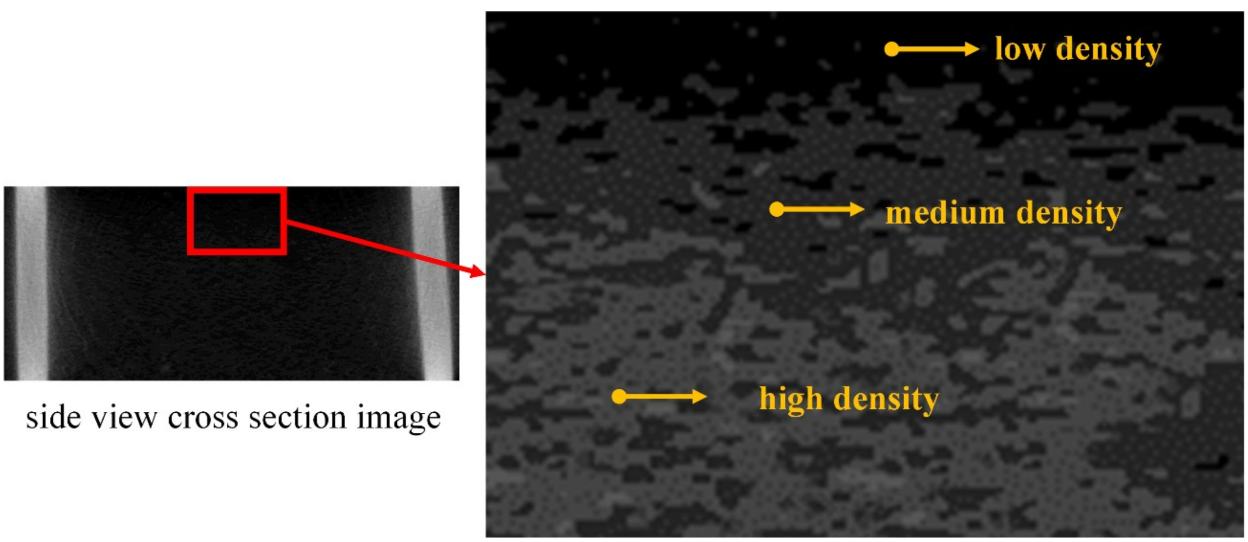

Figure 8-9 Density gradient in axial direction.

For a sample prepared using GEX blend, there is a rapid porosity increase in sample #2. The rapid porosity increase is caused by the uneven top surface of the cement sheath. The existence of the uneven top surface indicates that the volume of the injected cement slurry is smaller than the expected. Some air bubbles (see Figure 8-10) might have been entrapped in the cement slurry and the high pressure in the curing cell might have compacted the cement slurry and squeezed the air bubbles out of the sheath, and lead to the uneven cement top surface.

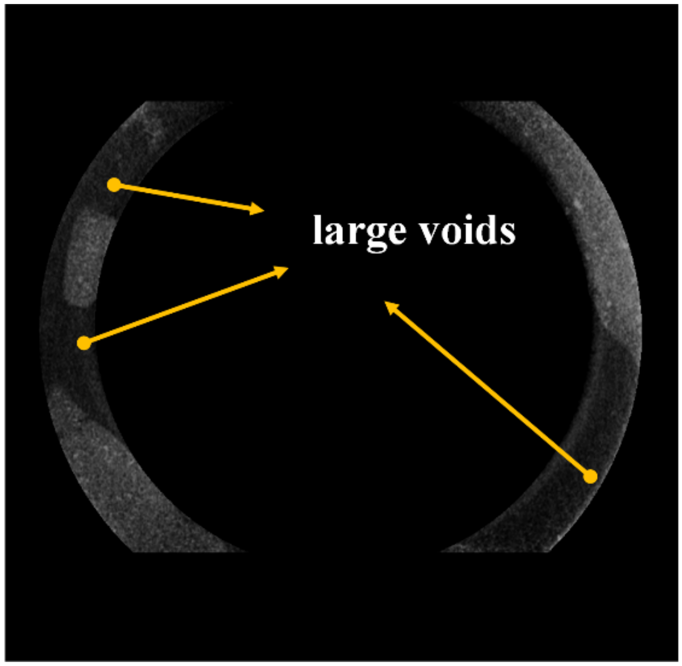

Figure 8-10 Large voids in the cement sheath.

8.3.2 Porosity distribution in radial direction

Figure 8-11 presents the results of the radial porosity calculations. Large fluctuations of the porosity in radial direction were observed. As shown in Figure 8-6, Zone 1 is close to the inner casing and the Zone 5 is close to the outer casing. For all four samples, regardless of the cement type, the highest porosity was found in Zone 2 or Zone 3, which indicates that the high porosity region is not located in the near-wall zone.

However, it is apparent for all four samples, the porosity of the Zone 1 is always lower than the porosity of the Zone 5. This implies that the outer casing near-wall zone has a higher porosity than the inner casing near-wall zone. This porosity difference might have been caused by the gap that existed at the cement-outer casing interface. More details of the annular gap (i.e. micro channel) characteristics will be discussed in the next section.

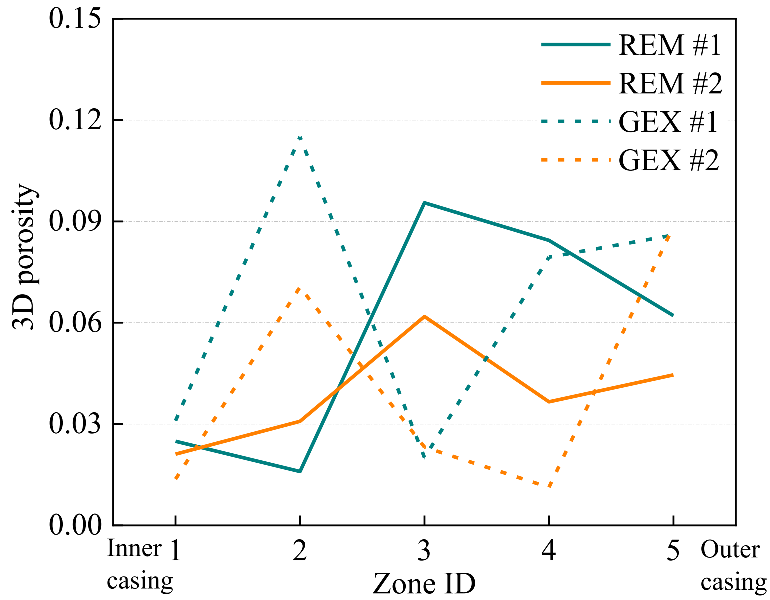

Figure 8-11 Cement porosity distribution in the radial direction.

8.3.3 Cement-Casing annular gap size change in the axial direction

Bonding between the cement and casing affects the integrity of the interface. Annular gaps were observed at the cement-casing interface in all samples. Examples of annular gaps were presented in Figure 8-12. All samples show a number of common key features.

Firstly, the location of the gaps were close to the bottom surface. There are about 671 cross section CT images in the sample's axial direction. Images shown in Figure 8-12 are two examples of the 671 CT images and they their locations were near the bottom surface.

Secondly, the gaps were mostly located at the interface between the cement and the outer casing. No gaps were observed at the interface between cement and the inner casing. This finding is consistent with previous research (Torsæter et al., 2015a), which indicated that the cement shrunk toward the inner casing and thus the inner case interface showed better bonding.

The last similarity is that all gaps have limited connectivity in the axial (vertical) direction. This finding was obtained from the analysis shown in Figure 8-13.

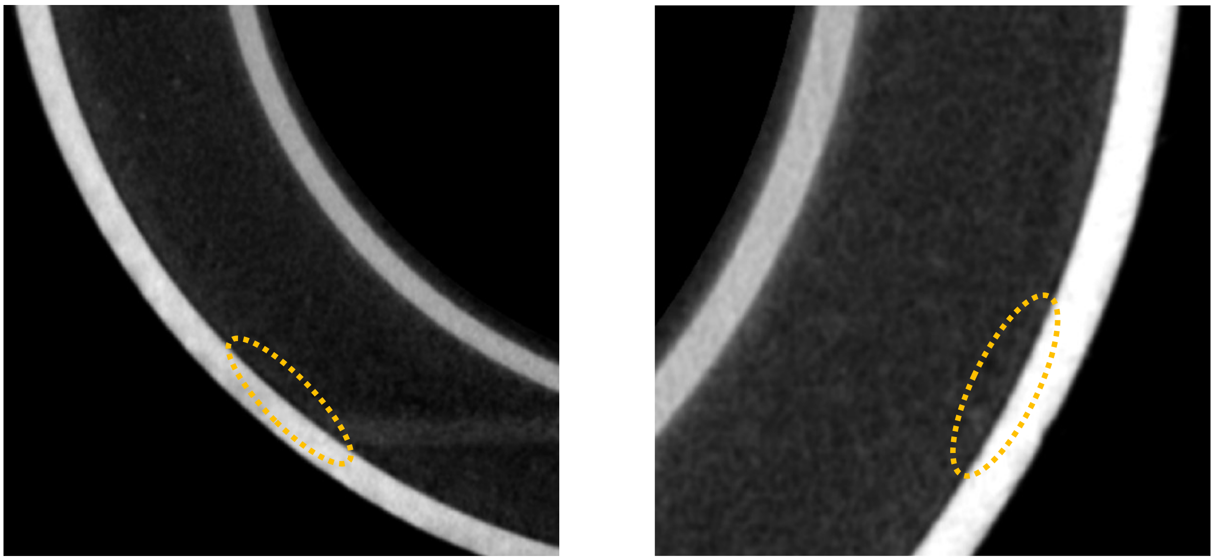

(a) REM #1 (b) GEX #1

Figure 8-12 Gaps at the cement-casing interface (outer casing).

Figure 8-13 shows how the gap size change in the axial direction. 4 mm depth means the bottom surface of the casing-cement-casing sample. From Figure 8-13, we can see that the width of the gap varied from sample to sample. The maximum gap size was observed in the REM #1 sample, which is larger than 80 μm. The gap in REM #1 vanished at a depth of around 3.88 mm. Although the GEX #1 sample has a smaller maximum gap size, contrary to REM#1, the gap developed bigger at the deeper depth from the top surface of the sample.

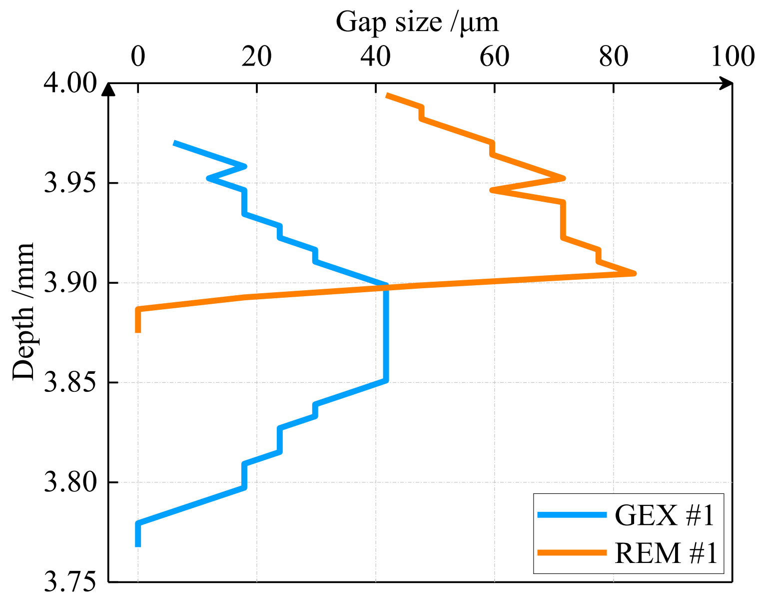

Figure 8-13 Gap size versus depth (along the axial direction).

8.4 Conclusions

Compared to the cement-rock sample or cement-casing sample, casing-cement-casing sample has a more complex structure. The small annular ring size makes the cement column fragile and therefore, cannot be further processed into thin sections. Moreover, for casing-cement-casing samples, artifacts have more influence over the characterization work. Special treatment should be applied to analyze the porosity distribution in the radial direction.

The density gradient caused the non-uniform porosity distribution in the vertical direction, and caused the cement has an increasing trend of porosity from the bottom surface to the top surface. Sample preparation has a significant impact on the microstructure of the samples. The uneven top surface and entrapped air bubbles in the cement sheath can cause rapid porosity increase in vertical direction.

Although radial porosity distribution has large fluctuations, all analyzed samples shown that the outer casing near-wall zone has a higher porosity than the inner casing near-wall zone. Gap observation also show that the inner cement-casing interface have a better bonding than the outer cement-casing interface. The better bonding at the inner casing might be caused by the cement shrinkage because cement shrunk toward the inner casing and therefore, improved, the bonding quality of inner cement-casing interface.

Chapter 9 Characterization of the Microstructure of the Rock-cement-casing Samples Using Micro CT Scan Technique

9.1 Introduction

Microstructure of the cement-rock and cement-casing interfaces involved in the most complex rock-cement-casing system has been investigated using micro CT scan technique and the results are presented in this chapter.

Several numerical and theoretical studies have been conducted to investigate the rock-cement-casing systems. Lavrov (2018) developed a finite-element model and investigated the effect of cement and rock stiffness on the well integrity under thermal loading and under changing far-field in-situ stress conditions. Gheibi et al. (2019) used a modified discrete element method to model the formation of radial fractures under pressure testing of rock-cement-casing system. The modified discrete element method was calibrated by using the experimental results. Effect of the confinement and rock tensile strength on the radial fracture development were investigated. Based on the classical Mohr-Coulomb yield criterion, Chu et al. (2015) built a theoretical model, which considered the interaction amongst the casing, the cement sheath and the formation. They were able to estimate the size of the micro-annulus using this model. Zhang et al. (2017) established an analytical model, which simulated the casing, the cement sheath and surrounding rocks as multi-layer cylinders and used thermoelastic, elastoplastic and poroelastic theory to analyze each section, respectively. This model considered the interaction of the casing, cement sheath and surrounding rocks under the effects of the inner casing pressure and the outer radial far-field in-situ stress and the resultant debonding of the cement-rock, cement-casing interfaces. This model also considered the change of casing pressure, temperature and pore pressure due to cyclic injection and production operations.

However, only a few studies have experimentally investigated the microstructure of the composite rock-cement-casing samples. Mito et al. (2015) prepared composite wellbore samples using J-55 steel casing, Class A cement and Tago Sandstone to model a well at a CO_2 geological storage site. De Andrade et al. (2016) built a laboratory setup to study the cement-sheath-failure mechanisms during thermal cycling with downscaled samples of rock, cement, and pipe. Their setup allowed for conducting tests with different combinations of rock casing and cement. More importantly, they were able to visually inspect the cement-casing, cement-rock interfaces by using three-dimensional X-ray CT measurements. However, resolution of their measurements were limited by the dimensions of their experimental apparatus. The resolution of the CT characterization varied between 100 μm to 200 μm in this case. However, in order to have a closer look at the interfaces involved in rock-cement-casing systems, higher resolution characterization is needed. In this study, we have prepared small scale rock-cement-casing samples (RCC samples) allowing us microstructure characterization by using CT at a resolution of 11.92 μm.

9.2 Materials and methods

9.2.1 Preparation of the rock-cement-casing samples

Rock samples were collected from five different Alberta formations: Banff, Doig, Notikewin, Pekisko and Wilrich. The collected rock cores were processed into hollow cylinders. Some processed hollow rock cylinders are shown in Figure 9-1. Rock lithology information is summarized in Table 9-1. It can be seen from the data in Table 9-1 that the collected rock samples cover a wide range of rock types.

Figure 9-1 Hollow formation rock cylinders.

Table 9-1 Rock lithology of the collected formation samples.

Formation	Lithology from Alberta Table of Formations (Alberta Geological Survey 2019)	Actual lithology
Banff	limestone or dolostone	Dolostone
Pekisko	limestone or dolostone	Fossiliferous limestone
Doig	sandstone or siltstone	Quartzose very-fine-grained sandstone
Notikewin	sandstone or siltstone	Quartzose sandy siltstone
Wilrich	shale or mudstone	Quartzose coarse-grained siltstone

A 316 stainless steel tubing was used to prepare the downscaled casing pipe. From the field practice, the ratio between cement sheath OD and ID should be around 1.26. Hole diameter in the rock samples were more or less constant, which dictated the OD of the casing as well. The 316 stainless steel pipe was the most suitable pipe readily available in this case. Considering the hollow rock cylindrical samples were slightly different in length, the 316 pipes were cut into short sections with different length (Figure 9-2).

Figure 9-2 Short casing sections machined from 316 stainless steel tubing pipes.

The OD of the casing was 6.35 mm (1/4 inch) and the rock hole size was 7.93 mm (5/16 inch). This combination resulted in a do/di ratio of 1.25. Two cement blends were investigated in this study. One blend is the Class G cement with an expansion agent (GEX). The expansion agent used in the cement is less than 2% BWOC. The other one is a novel abandonment blend (REM) with engineered chemistry to minimize permeability, improve chemical resistance and show no chemical shrinkage.

The cement slurry was mixed according to API standard 10A. The bottom surface of the rock hollow cylinder was sealed by the electrical tape. To centralize the casing, the pipe was stuck to the electrical tape sealing the bottom end of the rock. The cement slurry was then injected into the annulus between the pipe and rock. As the annulus ring size is about 0.79 mm, a syringe was used to inject the cement slurry. A small needle was also utilized to tap the slurry to minimize the air voids in the annulus. Figure 9-3 shows the cemented samples.

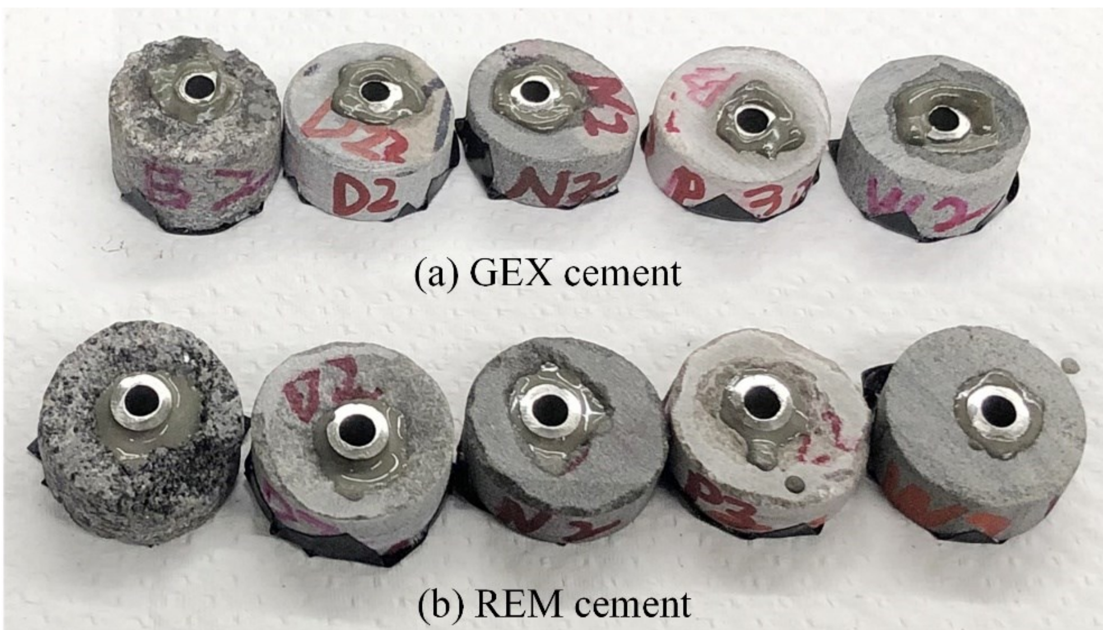

Figure 9-3 Preparation of the rock-cement-casing samples.

It was also observed that the rheology of the cement slurry also affects uniformity of the sample preparation. Attention should be paid when injecting cement slurry into the annulus, as the slurry may not completely fill the annulus.

The rock-cement-casing samples were cured in water under ambient temperature (~21 °C) and 1500 psi for 7 days. After curing, the samples were wrapped with plastic film to minimize dehydration. Considering the smaller annular ring size (0.79 mm), any polishing process for taking SEM pictures will damage the samples. Therefore, these rock-cement-casing samples were only characterized by using the micro-CT technique, which is non-destructive to the samples.

9.2.2 Characterization of the rock-cement-casing (RCC) samples using micro-CT

After curing, the prepared RCC samples were characterized by using the micro-CT. The resolution of the CT images was 11.92 μm. RCC samples have a complex structure. This is not only because these samples consist of three different materials (i.e. cement, rock and metal pipe), but also. the 316 stainless-steel pipe has a relatively thicker wall than the 304 pipe (which was used for cement-casing sample preparation). Therefore, special attention had to be paid when scanning the RCC samples. High energy X-ray should be used by adjusting scan filters.

CT images are created based on the material's density profile. When the cement and rock have significant density difference, the interface between them can be easily identified. For example, Figures 9-4 a and b show the CT images of Pekisko rock. Pekisko rock has a density of around 2.82 g/cc, whereas the density of REM and GEX cement are 1.75 g/cc and 1.90 g/cc, respectively. As the density difference between Pekisko rock and REM cement (Figure 9-4a) is higher than that of Pekisko rock and GEX cement (Figure 9-4b), the cement-rock interface in Figure 9-4a can be seen much more clearly than the cement-rock interface in Figure 9-4b.

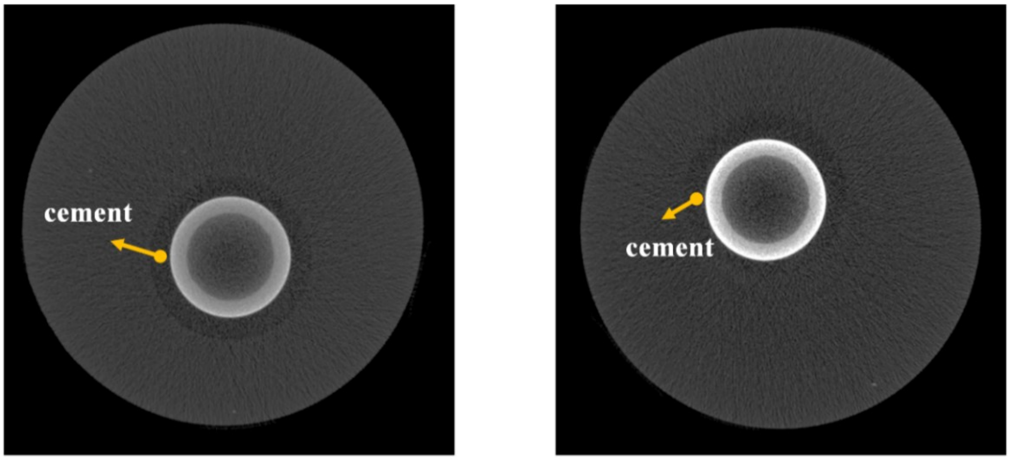

(a) Pekisko rock with REM cement (b) Pekisko rock with GEX cement

Figure 9-4 CT images Pekisko rock samples cemented by different cement blends.

9.2.3 Calculation of the porosity distribution in radial and axial direction

Radial and axial porosity distributions were calculated based on the CT images. For radial porosity distribution, we have employed a method of cement radial porosity calculation proposed by Lavrov et al. (2018). As shown in Figure 9-5, five rectangular area were marked in the cement sheath. The width and length of the rectangles are 143 μm and 715 μm, respectively. The 2D rectangles were then converted into cuboids and the porosity of each cuboid was calculated. Thus the calculated radial porosity is the 3D porosity.

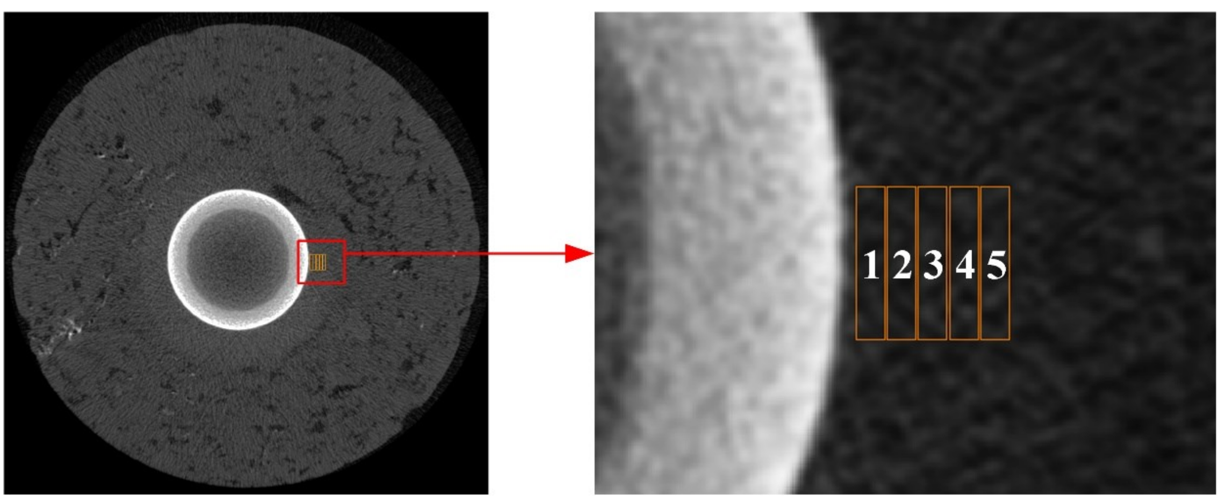

Figure 9-5 Calculation of the radial porosity distribution in the cement sheath.

Porosity distribution in the axial direction was also calculated. A yellow square was drawn in Figure 9-6a, the porosity of the yellow square in each cross-sectional CT image was calculated. Appendix A presents the 3D reconstruction results of the prepared samples. From Appendix A we can see that the length of the cement sheath column varied from one sample to other. One example is shown in Figure 9-6b, because of the existence of air voids, the length of the cement sheath is smaller than the length of the hollow rock cylinders. Under this condition, the axial porosity distribution was calculated only at the fully cemented section of the sample (marked between the two yellow arrows).

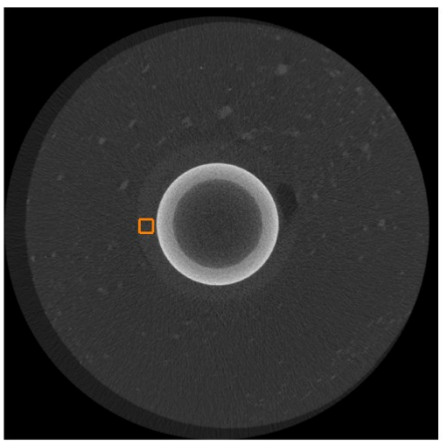

(a)

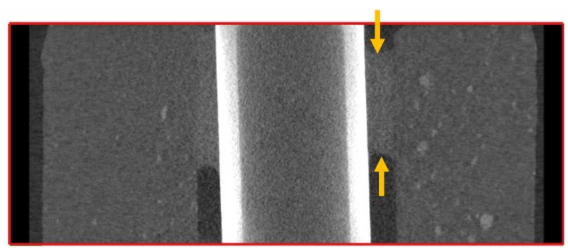

(b)

Figure 9-6 Calculation of the axial porosity distribution of the cement sheath.

9.3 Results and discussion

9.3.1 Radial porosity distribution

Figure 9-7 shows the porosity distribution in the radial direction. In general, porosity in radial direction has an increasing trend from the cement-casing interface to cement-rock interface. For all samples, porosity close to the cement-rock interface is higher than the porosity close to the cement-casing interface. Also, it seems that the porosity of the samples prepared using GEX cement is higher than the porosity of the REM samples.

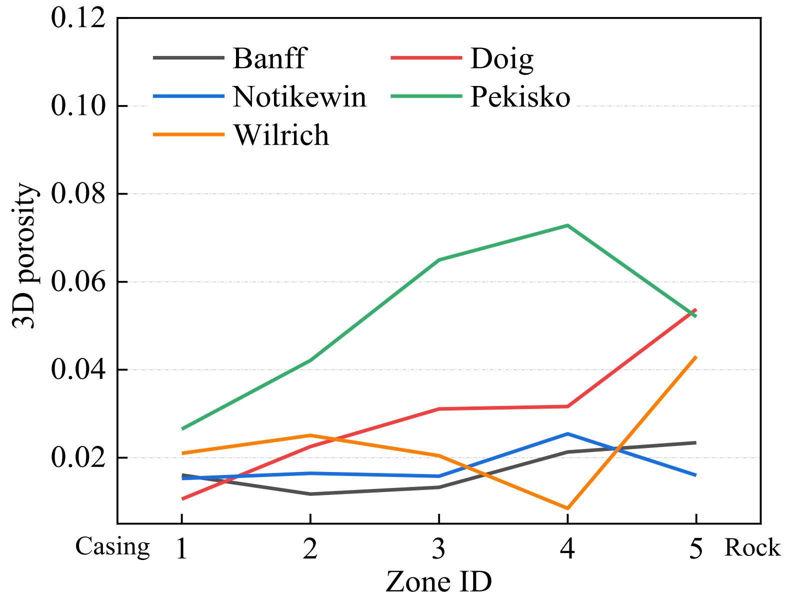

(a) REM

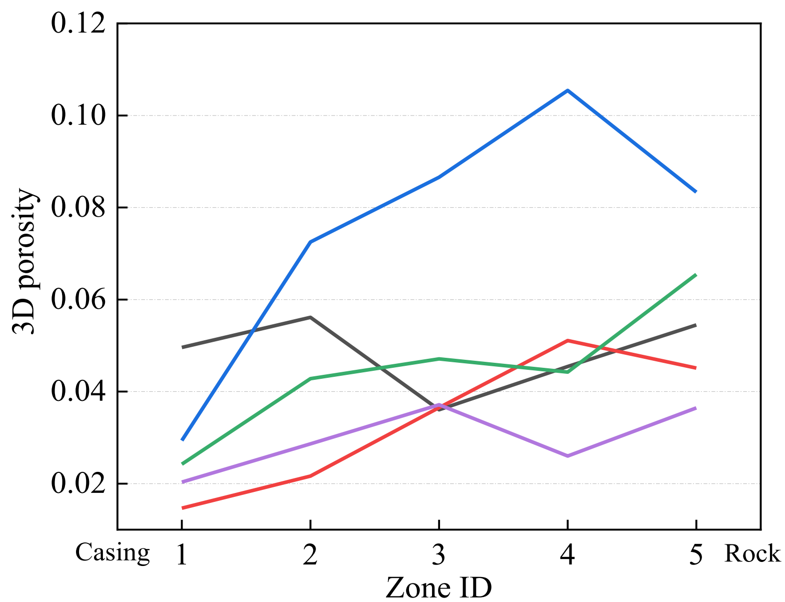

(b) GEX

Figure 9-7 Porosity distribution in the radial direction.

9.3.2 Axial porosity distribution

The porosity distribution in the axial direction significantly fluctuated (Figure 9-8). The upper half of the samples have more significant porosity fluctuations than the lower half, especially for samples prepared using GEX cement. When compare the porosity distribution in GEX and REM samples, it is apparent that the average cement porosity of GEX samples is higher than the porosity of the REM samples. These results are also in line with the results obtained from the radial porosity distribution analyses.

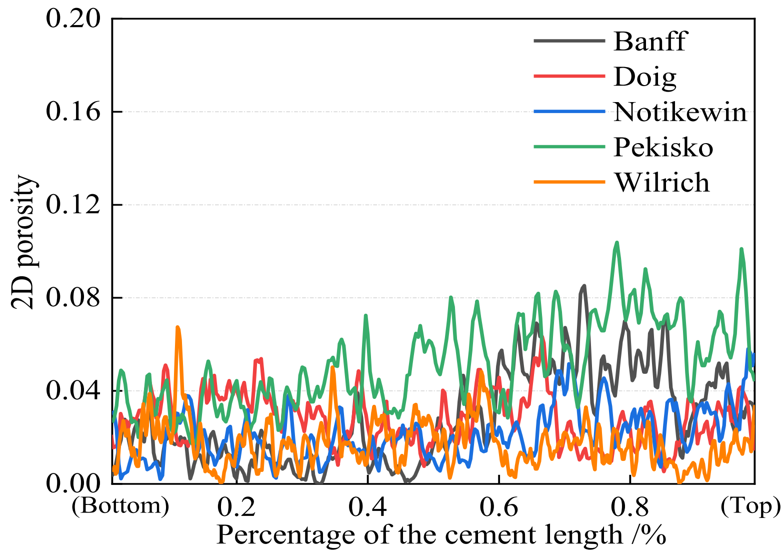

(a) REM

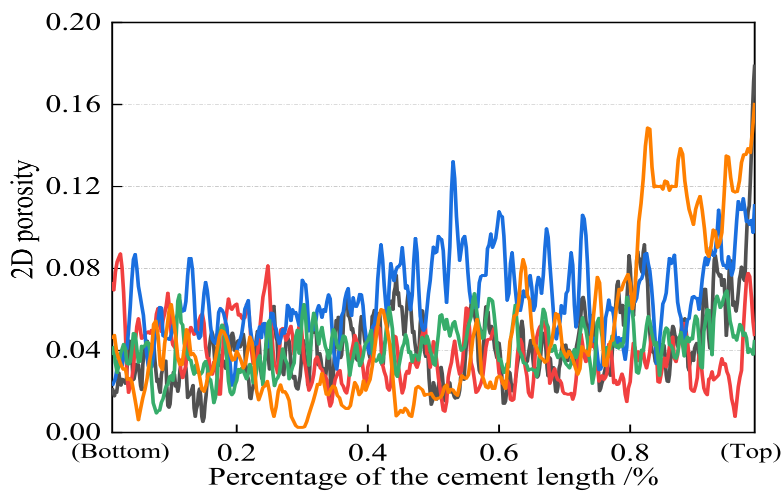

(b) GEX

Figure 9-8 Porosity distribution in axial direction.

9.3.3 Annular gap size change in the axial direction

Examples of annular gaps observed in CT images are presented in Figure 9-9. Side view CT images provide a good way to observe the annular gap at the interface. Surprisingly, all the observed gaps are located at the cement-rock interface. More importantly, annular gaps were observed only in GEX samples. Unlike the annular gaps at the bottom surface of the cement-casing samples, for RCC samples, the annular gaps were found in many different locations: the top surface, the bottom surface and even in the middle section of the sample. For instance, gap #1 was located at the bottom surface but gaps #2 and 3# were located at the top surface and middle section, respectively.

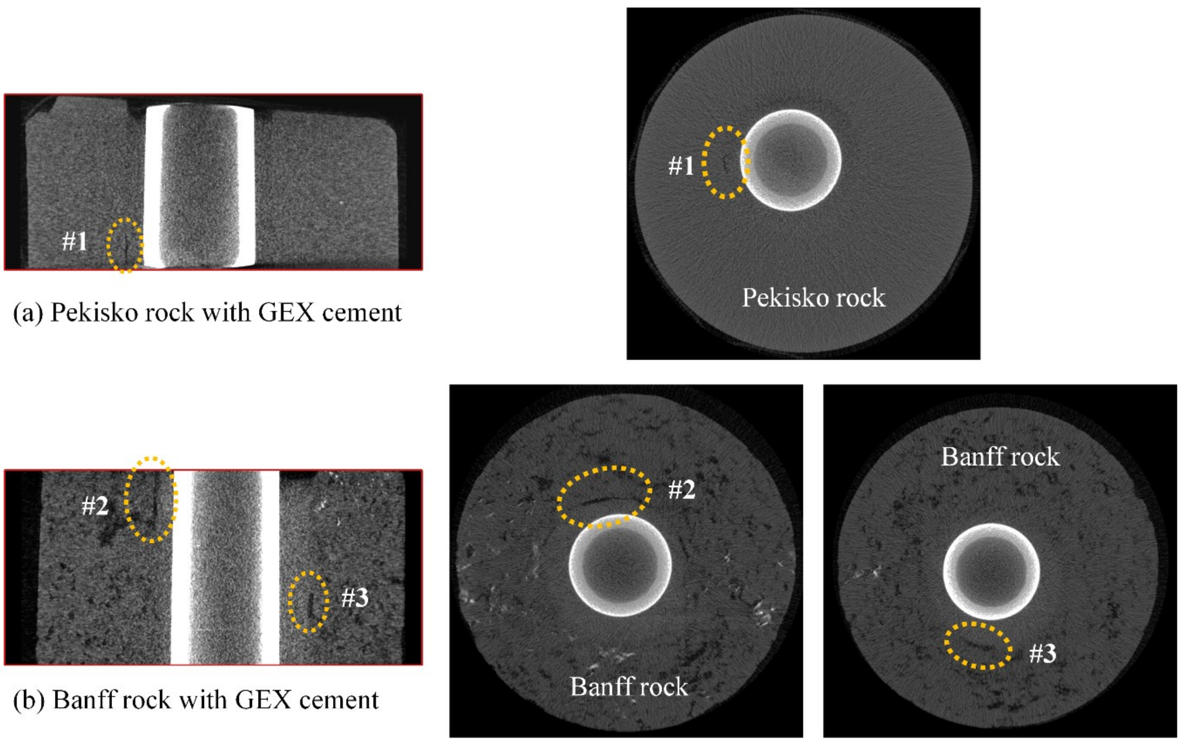

(a) Pekisko rock with GEX cement

(b) Banff rock with GEX cement

Figure 9-9 Annular gaps at the casing-cement-rock interfaces.

Annular gap size change along the axial direction was also measured and summarized in Figure 9-10. In this figure zero depth means the top surface. For the gaps observed at the bottom surface, the gap extension was very short in the axial direction and the size of the gap was very small compared to the gap observed in the other positions. The maximum gap size was observed in gap

#2, which was around 520 μm in the radial direction. This is the largest gap size we have ever observed in all kinds of samples investigated.

There were two similarities amongst these three gaps. On the one hand, before reaching the maximum gap size, the gap size was gradually increasing with increasing depth along the axial direction. However, once it reached to the maximum size, the gap rapidly decreased to a smaller size and then eventually vanished. The extension of the gap is limited which means these gaps are only local micro channels. On the other hand, even in the smallest size gap (#1), the maximum gap size, was still higher than the maximum size of the gaps observed in the cement-casing samples.

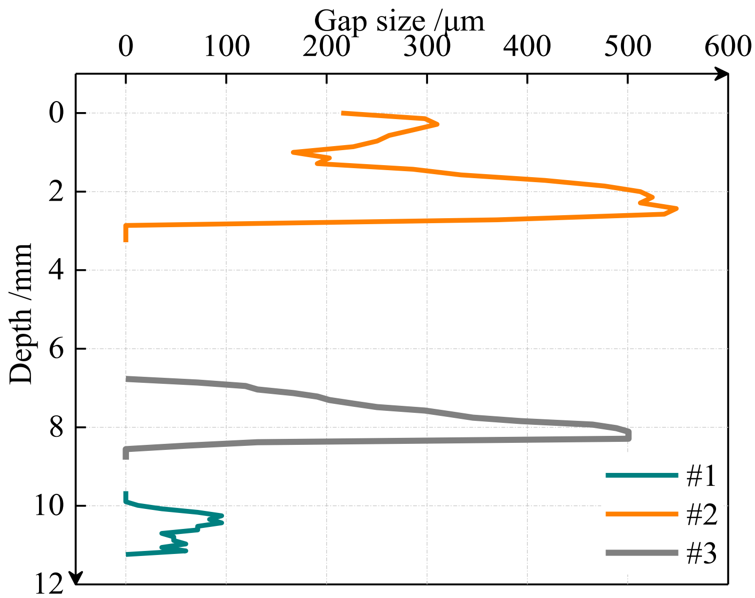

Figure 9-10 Gap size change along the axial direction of Banff and Pekisko samples. Gap #1 is in Pekisko rock. Gap #2 and Gap #3 are in Banff rock.

9.4 Conclusions

One of the most significant findings in the rock-cement-casing samples is the porosity at the cement-casing near zone is higher than the porosity at the cement-rock near zone. This result is valid independent of rock type. The gaps observed at the cement-rock interface also supports this finding.

The annular gap size observed at the cement-rock interface is significantly larger than that of the gaps observed at the cement-casing interface. Two similarities were found among the gaps at the cement rock interface. i) The extension of the gap is limited which means these gaps are only local micro channels. ii) the gaps observed at the cement-rock interface is larger than the gaps at the cement-casing interface.

9.5 Appendix A-3D reconstruction results of rock-cement-casing samples

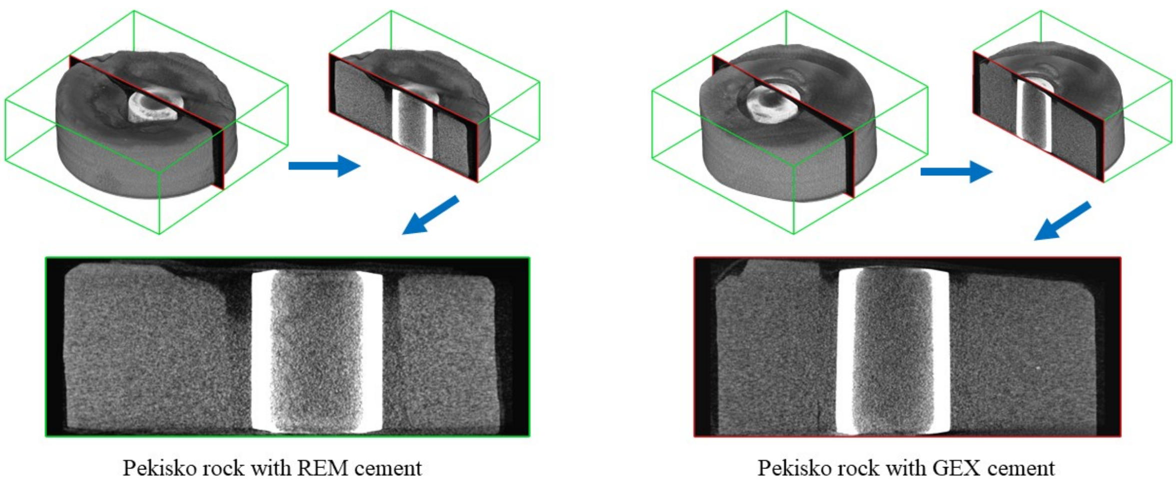

Figure 9A-1 3D models of Pekisko rock with REM and GEX cement.

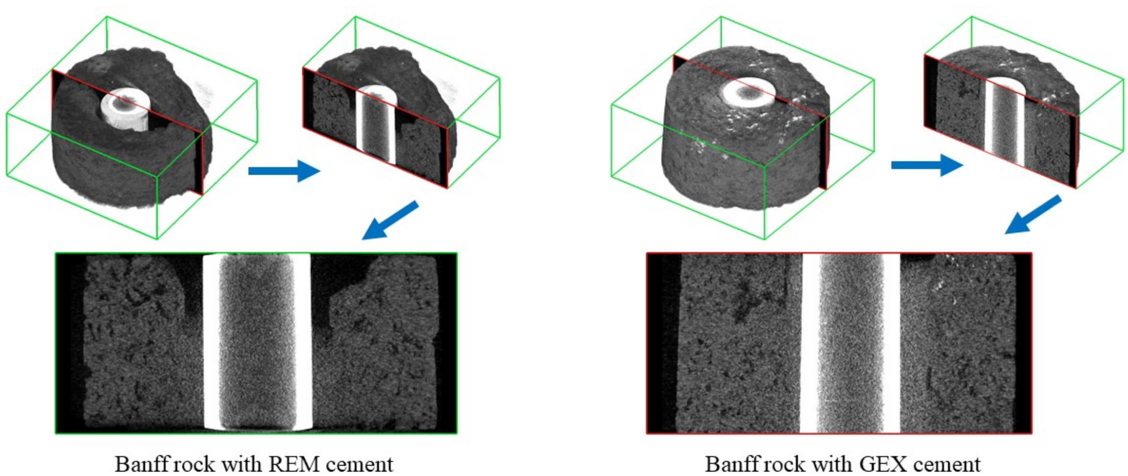

Figure 9A-2 3D models of Banff rock with REM and GEX cement.

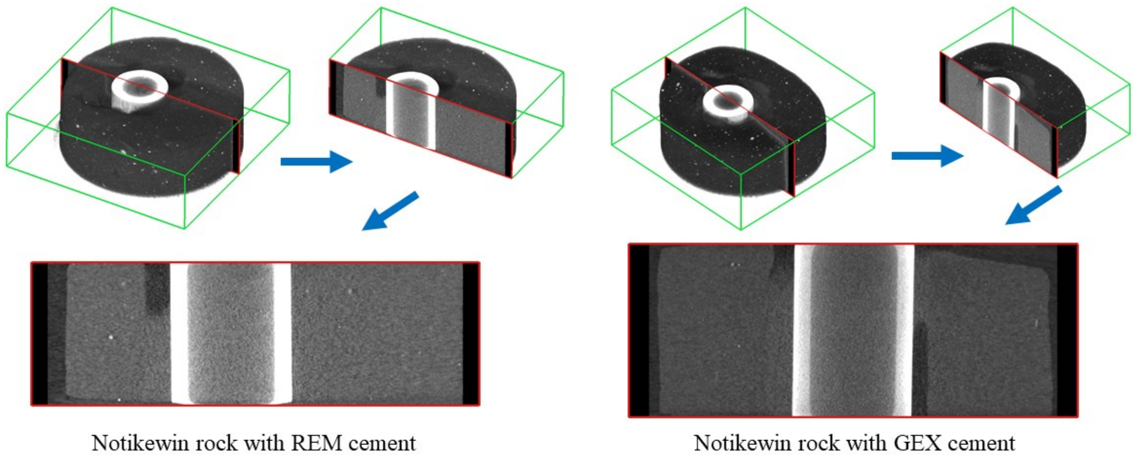

Figure 9A-3 3D models of Notikewin rock with REM and GEX cement.

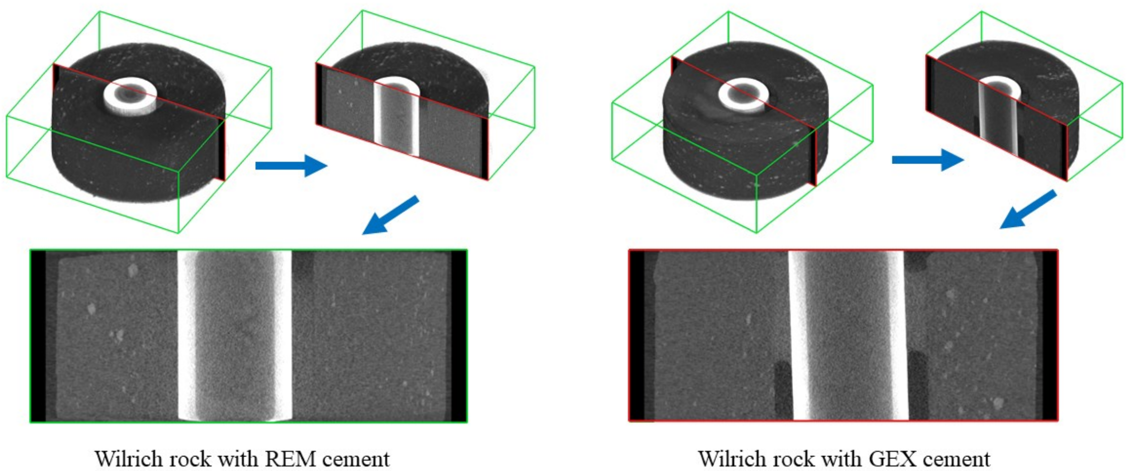

Figure 9A-4 3D models of Wilrich rock with REM and GEX cement.

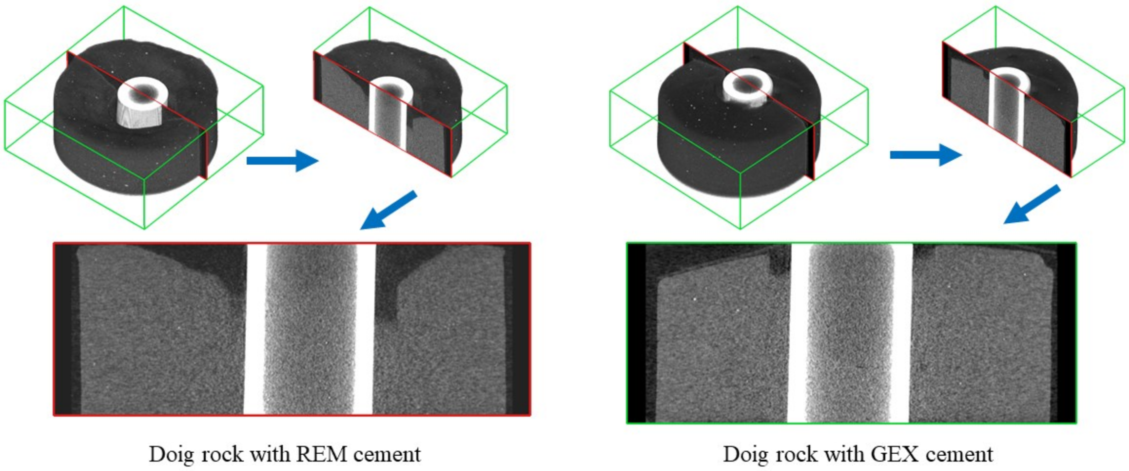

Figure 9A-5 3D models of Doig rock with REM and GEX cement.

Chapter 10 Conclusions and Recommendations

10.1 Conclusions

The main conclusions and findings of the presented work were summarized in this chapter. In previous chapters, all concluding remarks were already discussed. Therefore, the aim of this chapter is to provide a concise review of the results and discussions that have been extensively discussed in previous sections.

10.1.1 Executive summary

A comprehensive experimental and numerical study was performed to investigate the microstructure of varied types of potential leakage pathways of a well. Based on the analysis results, following conclusions can be offered:

- At the micron scale (2-34 μm), non-uniform porosity distribution in the cement sample was observed, which caused the permeability disparities at different locations. The minimum size of the representative volume element (REV) should be determined on a case-by-case basis. For early age well cement, there is a linear correlation between the cement permeability and the effective porosity.
- Average effective porosity values calculated from the REV can be introduced into a generalized porosity and permeability correlation curve to determine the permeability of the cement sample.
- The permeability of neat early-age cement is close to the permeability of tight sandstone formations. The linear relationship between porosity and permeability of neat early-age well cement samples in semi-log plot indicates its permeability behavior will approach to that of shale if the hydration process of cement is continued.
- After uniaxial compressive loading, pre-peak cement samples shows that 90% of the 2D fractures have length and width smaller than 100 μm and 5 μm, respectively. Although higher compressive stress reshaped the 3D fractures and increased the fracture length and width, no well-propagated fractures were observed.

- After uniaxial compressive loading, post-peak cement samples exhibit distinctly visible (> 0.1 mm) well-propagated fractures were generated but failed to penetrate the entire sample, therefore, the effect of stress-induced fractures (up to 1.0% strain) on cement sample's permeability is limited.
- CT-based 3D visualization and simulation both show that the inclusion of a correctly engineered fiber additive is able to blunt the fracture propagation in cement samples.
- Cement fractures created by the monotonic compressive stress (up to the limit of uniaxial compressive strength, UCS), are not likely to form continuous leakage pathways. This is because the 2D fractures in cement matrix as shown by SEM images are in limited dimensions while the 3D fractures in cement matrix observed from CT-based 3D models have poor connectivity, generally indicating that leakage pathways of significant permeability would not form as a result of compressing the cement samples up to their UCS limit.
- Any significant change in the relative humidity (RH) of the environment during the cement preparation, curing and testing process significantly affects the size of the gap at the cement -casing interface in test samples.
- Analyses of the ESEM images have shown that the 2D non-uniform gap size between the cement and the casing is inversely proportional to the change in the RH of the environment.
- Cement sample inside the casing shrunk 0.6% when RH decreased by 80% over a 4-hour time period.
- Cement slurries set and cured under downhole conditions with relatively constant RH may not undergo significant shrinkage and yield only a minimal debonding effect.
- Storing cement samples at an ambient seal condition (~71% RH) and characterizing them using ESEM at 75% RH seems to be the most suitable method to obtain high resolution images of the cement-casing interface as well as minimize the cement drying shrinkage.
- The 3D gap model reconstructed from the micro-CT images confirmed that the gap between cement and casing mostly occurred at the polished cement surface and the gap

didn’t show any significant connectivity below the polished cement surface indicating that common sample preparation methods can significantly impact the near surface interface.

- Cement blends prepared with expansion additives have shown smaller gap size. The use of expansion additives enhances the cement-casing interface integrity by effectively reducing the gap size at the cement-casing interface.
- As long as the RH of the environment does not change significantly, the cement is expected to undergo a limited shrinkage and the gap between the cement and the casing may not induce any significant leakage pathway as the gap is only locally distributed at the polished cement surface without showing any significant connectivity along the wellbore axis.
- For cement-rock samples, non-uniform porosity distributions in the radial and axial direction were observed in both cement and rock. For most of the cement-rock samples, the highest porosity region in the cement column was found at the cement-rock interface.
- Cement without an expansion agent not only has a higher average porosity but also has more fluctuations in the axial porosity distribution. The size of the non-uniform gaps observed at the cement-rock interface can be significantly reduced by using an expansion agent in the cement blend.
- For cement-rock samples, permeability variance between cement, rock and interface will change the flow direction. CT-based simulation indicated that regardless of reservoir rock permeability, the cement-rock interface has more chance to form the leakage pathway when intact caprock exists.
- For a cement sheath between two casing pipes, CT images support that the outer casing interface is prone to have gaps at the interface.
- For a cement sheath between rock and casing pipe, a radial porosity distribution shows a higher porosity was observed at the cement-rock interface.

10.1.2 Main conclusions

The most important contribution of the current work is the comprehensive experimental study of the various potential leakage pathways along the cemented wellbore at the micron scale.

For the microstructure study, the most suitable methods regarding sample preparation, characterization and analysis were established based on the detailed analyses. These types of the microstructure data obtained from the micro-CT and SEM/ESEM analyses in this work rarely exist in the petroleum literature. Various cement blends, including the widely used blend in the field, have been studied and specific cement additives and their impact on the well integrity were also investigated. Such efforts are likely to result in a better understanding of the factors influencing the gas leakage from oil and gas wells. The main contributions from the work presented in Chapters 4 to 9 are summarized below.

- In Chapter 4, a CT-CFD integrated approach is proposed to investigate the permeability of neat early-age well cement sample. This approach provides a quantitative means to estimate the porosity and permeability of representative volume elements selected from the cement sample. The characteristic effective porosity versus permeability correlation curve was generated to calculate the permeability of the cement sample. Comparative study on the porosity and permeability of early-age well cement and formation rocks reveals that the cement poroperm data are mainly comparable to tight sandstone. Comparisons also show that the early-age well cement has a narrower permeability range than formation rocks. The trend of cement linear fitting curve suggests that if the hydration process of neat early-age well cement sample continues, poroperm characteristics will approach those of shale.

- Chapter 5 investigated the impact of stress-induced cement fractures on the wellbore cement integrity. Results demonstrate that the monotonic compressive stress (up to 1.0% strain) is unlikely to create significant leakage pathways in wellbore cement. Under pre-peak stress loading conditions, most of the observed 2D fractures are smaller than 5 μm. The fractures generated by the pre-peak stress do not increase the permeability of the cement and thus, is not a contributing factor to the formation of leakage pathways. Once the compressive stress exceeds the uniaxial compressive strength, the higher strain will lead to considerable fracture propagation. However, these larger well-propagated fractures observed in the post-peak cements failed to penetrate the entire sample and therefore, still have poor overall connectivity. The addition of a fiber additive to post-peak stress cements was found to mitigate the number and size of the stress-induced fractures, giving a more robust structure through blunting of fracture propagation under these conditions.

- The microstructure of the cement-casing interface was characterized and analyzed in Chapter 6. Storing cement samples in an ambient seal condition (~71% RH) and characterizing them using ESEM at 75% RH seems to be the most suitable method to obtain high resolution images of the cement-casing interface as well as minimize the cement drying shrinkage. Although the smaller gaps observed in ESEM images may have a limited impact on the short-term permeability, they may function as the starting point of chemical attack and thus jeopardize the long-term wellbore integrity. As long as the RH of the environment does not change significantly, the cement is expected to undergo a limited shrinkage and the debonding between the cement and the casing may not induce any significant leakage pathway as the debonding is only locally distributed at the cement surface without showing any connectivity along the wellbore axis. Optimizing the chemistry of the cement system enhances the cement casing bond integrity by effectively reducing the gap size at the cement-casing interface. Wellbore cement designed to provide zonal isolation should be optimized to have no shrinkage, as this is the best insurance policy against degradation in integrity during the entire life of the well.
- In Chapter 7, the microstructure of the cement-rock samples were characterized at microscale using microscope, micro-CT and ESEM. Based on the analyses of the CT images, we have determined the radial porosity distribution in the cemented rock samples, which revealed that the interface zone had higher porosity than its neighboring zones. CT-based flow simulation study implies that the cement-rock interface is more likely to provide the leakage pathway when intact caprock exists. The size of the gaps observed at the cement-rock interface through ESEM images was significantly reduced by using the expansion agent in the cement slurry. The effect of the expansion agent on gap size change, however, varied depending on the rock properties such as rock density and porosity. The reduction rate of the gap size due to the addition of the expansion agent was found to be improved with the increasing rock density.
- Chapter 8 focused on the microstructure of casing-cement-casing samples. The casing-cement-casing samples have a more complex structure than the cement-casing sample or cement-rock sample. For the casing-cement-casing samples, the small annular ring size makes it fragile and, therefore, cannot be further processed into thin sections. Moreover,

for casing-cement-casing samples, artifacts have more influence over the characterization work. Special treatment should be applied to analyze the porosity distribution in the radial direction. Porosity and gap size analyses show that the interface between inner casing and cement have a better bonding than the interface between outer casing and cement. The density gradient caused the non-uniform porosity distribution in the vertical direction. Sample preparation has a significant impact on the microstructure of the samples.

- Chapter 9 investigated the rock-cement-casing samples. The most significant finding in rock-cement-casing samples is the porosity at the cement-casing near zone is higher than the porosity at the cement-rock near zone. And this result is independent of the rock type. The gaps observed at the cement-rock interface also supports this finding. Besides, the gap size observed at the cement-rock interface is significantly larger than the gaps observed at the cement-casing interface. We also found that the rheology of the cement slurry also affects the sample preparation. Attention should be paid when injecting cement slurry into the annulus, as the slurry may not completely fill the annulus.

10.2 Recommendation for future work

This thesis contributes to the knowledge of the microstructure of wellbore cement. The most suitable methods regarding sample preparation, characterization and analysis were established and the type of the cement microstructure data we presented in this work rarely exist in the petroleum literature. Based on the findings of this study, the following suggestions can be made for future research:

- Effect of cyclic stress on fracture development and cement permeability change needs to be further investigated. In chapter 5, the impact of monotonic uniaxial stress on cement microstructure was investigated. Future study may focus on the effect of cyclic stress as this research has significant implications for the understanding of how multi-stage hydraulic fracturing operations affect the wellbore cement integrity.
- A further study could also assess the influence of various stress types on wellbore cement integrity. This thesis investigated how uniaxial compressive stress affects cement microstructure; however, modern wells subjected to complex stress conditions. In the

future, shear stress, tensile stress, thermal stress and triaxial stress and their impact on the cement fracture propagation and interface bonding can be studied.

- Further studies regarding the influencing factors on interface bonding would be worthwhile. Mud cake is not considered when studying the cement-casing interface or cement-rock interface. The role of drilling fluid on the interface bonding needs to be investigated. This thesis studied the effect of rock type on cement-rock interface bonding. Dolostone, limestone, sandstone and siltstone were studied. In future work, more rock types such as shale and mudstone can also be considered. For cement-casing interface study, further research should be undertaken to explore the effect of roughness of the casing on cement-casing interface bonding.
- Further numerical simulations are needed to fully understand the implications of the change of cement microstructure and cement interface on the permeability of the wellbore cement system. CT-based fluid flow simulation based on the casing-cement-casing samples (Chapter 8) and rock-cement-casing samples (Chapter 9) should be performed. A natural progression of the simulation work is considering the stress condition in the simulation. A stress-fluid coupled numerical model would make a contribution to a better understanding of the mechanisms of leakage in the wellbore cement.

References

Abbas, G., Irawan, S., Kumar, S., Khan, M. N., & Memon, S. (2013). Gas Migration Prevention Using Hydroxypropylmethylcellulose as a Multifunctional Additive in Oil Well Cement Slurry. *SPE/PAPG Annual Technical Conference*. https://doi.org/10.2118/169643-MS

Abdoulghafour, H., Luquot, L., & Gouze, P. (2013). Characterization of the mechanisms controlling the permeability changes of fractured cements flowed through by CO2-rich brine. *Environmental Science and Technology*, *47*(18), 10332–10338. https://doi.org/10.1021/es401317c

Abo-El-Enein, S. A., El-Hosiny, F. I., El-Gamal, S. M. A., Amin, M. S., & Ramadan, M. (2018). Gamma radiation shielding, fire resistance and physicochemical characteristics of Portland cement pastes modified with synthesized Fe 2 O 3 and ZnO nanoparticles. *Construction and Building Materials*, *173*, 687–706. https://doi.org/10.1016/j.conbuildmat.2018.04.071

ACI Committee 224. (2001). Control of Cracking in Concrete Structures. In *American Concrete Institute*. https://doi.org/0097-8515

Aguilera, R. (2014). Flow Units: From Conventional to Tight-Gas to Shale-Gas to Tight-Oil to Shale-Oil Reservoirs. *SPE Reservoir Evaluation & Engineering*, *17*(02), 190–208. https://doi.org/10.2118/165360-PA

Alberta Energy Regulator. (2019). *Upstream Petroleum Industry Flaring and Venting Report: Industry Performance for Year Ending December 31, 2018*. https://www.aer.ca/documents/sts/ST60B-2019.pdf

Alford, N. M. N., & Rahman, A. A. (1981). An assesment of porosity and pore sizes in hardened cement pastes. *Journal of Materials Science*, *16*(11), 3105–3114. https://doi.org/10.1007/BF00540319

American Petroleum Institute. (2002). *API Recommended Practice 10A: Specification for cements and materials for well cementing* (Vol. 44).

Ammouche, A., Breysse, D., Hornain, H., Didry, O., & Marchand, J. (2000). A new image analysis technique for the quantitative assessment of microcracks in cement-based materials. *Cement and Concrete Research*, *30*(1), 25–35.

https://doi.org/http://dx.doi.org/10.1016/S0008-8846(99)00212-4

Anderson, S. H., Wang, H., Peyton, R. L., & Gantzer, C. J. (2003). Estimation of porosity and hydraulic conductivity from X-ray CT-measured solute breakthrough. *Geological Society, London, Special Publications*, *215*(1), 135–149. https://doi.org/10.1144/GSL.SP.2003.215.01.13

ASTM, C. (2003). *Standard Practice for Making and Curing Concrete Test Specimens in the Field*. C31/C31M-12.

ASTM D4525-13e1. (n.d.). *Standard Test Method for Permeability of Rocks by Flowing Air, ASTM International, West Conshohocken, PA, 2013, www.astm.org*. https://doi.org/10.1520/D4525

Attiogbe, E., & Darwin, D. (1987). Submicrocracking in cement paste and mortar. *Materials Journal*, *84*(6), 491–500. https://www.concrete.org/publications/internationalconcreteabstractsportal/m/details/id/2448

Atzeni, C., Pia, G., & Sanna, U. (2010). A geometrical fractal model for the porosity and permeability of hydraulic cement pastes. *Construction and Building Materials*, *24*(10), 1843–1847. https://doi.org/10.1016/j.conbuildmat.2010.04.020

Bachu, S. (2017). Analysis of gas leakage occurrence along wells in Alberta, Canada, from a GHG perspective – Gas migration outside well casing. *International Journal of Greenhouse Gas Control*, *61*(April), 146–154. https://doi.org/10.1016/j.ijggc.2017.04.003

Bachu, S., & Bennion, D. B. (2009). Experimental assessment of brine and/or CO2 leakage through well cements at reservoir conditions. *International Journal of Greenhouse Gas Control*, *3*(4), 494–501. https://doi.org/10.1016/j.ijggc.2008.11.002

Bágel', L., & Živica, V. (1997). Relationship between pore structure and permeability of hardened cement mortars: On the choice of effective pore structure parameter. *Cement and Concrete Research*, *27*(8), 1225–1235. https://doi.org/10.1016/S0008-8846(97)00111-7

Banthia, N., & Mindess, S. (1989). Water permeability of cement paste. *Cement and Concrete Research*, *19*(c), 727–736. https://doi.org/10.1016/0008-8846(89)90043-4

Barnes, P., & Bensted, J. (2002). Structure and Performance of Cements, 2nd edition. In *Spon Press,Taylor & Francis Group*.

Baroghel-Bouny, V., Nguyen, T. Q., & Dangla, P. (2009). Assessment and prediction of RC structure service life by means of durability indicators and physical/chemical models. *Cement and Concrete Composites*, *31*(8), 522–534. https://doi.org/10.1016/j.cemconcomp.2009.01.009

Basheer, L., Kropp, J., & Cleland, D. J. (2001). Assessment of the durability of concrete from its permeation properties: A review. *Construction and Building Materials*, *15*(2–3), 93–103. https://doi.org/10.1016/S0950-0618(00)00058-1

Baumgarte, C., Thiercelin, M., & Klaus, D. (1999, April 4). Case Studies of Expanding Cement To Prevent Microannular Formation. *SPE Annual Technical Conference and Exhibition*. https://doi.org/10.2118/56535-MS

Beaudoin, J. J. (1979). Porosity measurement of some hydrated cementitious systems by high pressure mercury intrusion-microstructural limitations. *Cement and Concrete Research*, *9*(6), 771–781. https://doi.org/10.1016/0008-8846(79)90073-5

Bentz, D. P. (2006). Quantitative comparison of real and CEMHYD3D model microstructures using correlation functions. *Cement and Concrete Research*, *36*(2), 259–263. https://doi.org/10.1016/j.cemconres.2005.07.003

Bentz, D. P., Garboczi, E. J., Haecker, C. J., & Jensen, O. M. (1999). Effects of cement particle size distribution on performance properties of Portland cement-based materials. *Cement and Concrete Research*, *29*(10), 1663–1671. https://doi.org/10.1016/S0008-8846(99)00163-5

Bisschop, J., & van Mier, J. G. . (2002). How to study drying shrinkage microcracking in cement-based materials using optical and scanning electron microscopy? *Cement and Concrete Research*, *32*(2), 279–287. https://doi.org/10.1016/S0008-8846(01)00671-8

Bissonnette, B., Pierre, P., & Pigeon, M. (1999). Influence of key parameters on drying shrinkage of cementitious materials. *Cement and Concrete Research*, *29*(10), 1655–1662. https://doi.org/10.1016/S0008-8846(99)00156-8

Bloch, S., Lander, R. H., & Bonnell, L. (2002). Anomalously high porosity and permeability in deeply buried sandstone reservoirs: Origin and predictability. *AAPG Bulletin*, *86*(2), 301–

328. https://doi.org/10.1306/61EEDABC-173E-11D7-8645000102C1865D

Bol, G., Grant, H., Keller, S., Marcassa, F., & de Rozieres, J. (1991). Putting a Stop to Gas Channeling. *Oilfield Review*, *3*(2), 35–43.

Bonett, A., & Pafitis, D. (1996). Getting to the Root of Gas Migration. *Oilfield Review*, *8*(1), 36–49.

Bossa, N., Chaurand, P., Vicente, J., Borschneck, D., Levard, C., Aguerre-Chariol, O., & Rose, J. (2015). Micro- and nano-X-ray computed-tomography: A step forward in the characterization of the pore network of a leached cement paste. *Cement and Concrete Research*, *67*, 138–147. https://doi.org/10.1016/j.cemconres.2014.08.007

Bourgoyne, A. T., Scott, S. L., & Manowski, W. (2000). A Review of Sustained Casing Pressure Occurring on the OCS. In *LSU Final Report submitted to the Mineral Management Services*. https://www.bsee.gov/sites/bsee.gov/files/tap-technical-assessment-program//008de.pdf

Brace, W. F. (1980). Permeability of crystalline and argillaceous rocks. *International Journal of Rock Mechanics and Mining Sciences and Geomechanics*, *17*(5), 241–251. https://doi.org/10.1016/0148-9062(80)90807-4

Brisard, S., Davy, C. A., Michot, L., Troadec, D., & Levitz, P. (2018). Mesoscale pore structure of a high-performance concrete by coupling focused ion beam/scanning electron microscopy and small angle X-ray scattering. *Journal of the American Ceramic Society*, *August*, jace.16059. https://doi.org/10.1111/jace.16059

Bruker. (2008). *Method Notes, Skyscan 1172 micro-CT*. papers2://publication/uuid/5B90158C-47FC-47C6-A6C2-DB6FE975BA31

Bruker. (2013). *Compact X-ray micro-CT SkyScan 1172 User Manual*.

Cai, C., He, W., Jiang, L., Li, K., Xiang, L., & Jia, L. (2014). Petrological and geochemical constraints on porosity difference between Lower Triassic sour- and sweet-gas carbonate reservoirs inthe Sichuan Basin. *Marine and Petroleum Geology*, *56*, 34–50. https://doi.org/10.1016/j.marpetgeo.2014.04.003

Carey, J. W, Svec, R., Grigg, R., Zhang, J., & Crow, W. (2010). Experimental investigation of wellbore integrity and CO2-brine flow along the casing-cement microannulus. *International Journal of Greenhouse Gas Control*, *4*(2), 272–282. https://doi.org/10.1016/j.ijggc.2009.09.018

Carey, J. William, Mori, H., Brown, D., & Pawar, R. (2014). Geomechanical behavior of caprock and cement: Plasticity in hydrodynamic seals. *Energy Procedia*, *63*, 5671–5679. https://doi.org/10.1016/j.egypro.2014.11.600

Carey, J William, & Lichtner, P. C. (2011). *Computational Studies of Two-Phase Cement / CO 2 / Brine Interaction in Wellbore Environments*. *February 2010*, 2–4.

Carroll, S. A., Iyer, J., & Walsh, S. D. C. (2017). Influence of Chemical, Mechanical, and Transport Processes on Wellbore Leakage from Geologic CO2 Storage Reservoirs. *Accounts of Chemical Research*, *50*(8), 1829–1837. https://doi.org/10.1021/acs.accounts.7b00094

Celia, M., S, B., JM, N., S, G., & HK, D. (2005). Quantitative estimation of CO2 leakage from geological storage: Analysical models, numerical models, and data needs. *Greenhouse Gas Control Technologies*, *7*(1), 663–671. https://doi.org/10.1016/B978-008044704-9/50067-7

Chavez Panduro, E. A., Torsæter, M., Gawel, K., Bjørge, R., Gibaud, A., Yang, Y., Bruns, S., Zheng, Y., Sørensen, H. O., & Breiby, D. W. (2017). In-Situ X-ray Tomography Study of Cement Exposed to CO2Saturated Brine. *Environmental Science and Technology*, *51*(16), 9344–9351. https://doi.org/10.1021/acs.est.6b06534

Cheung, P. R., & Myrick, B. D. (1983, April 4). Field Evaluation of an impermeable Cement System for Controlling Gas Migration. *SPE Annual Technical Conference and Exhibition*. https://doi.org/10.2118/11983-MS

Christensen, B. J., Mason, T. O., & Jennings, H. M. (1996). Comparison of measured and calculated permeabilities for hardened cement pastes. *Cement and Concrete Research*, *26*(9), 1325–1334. https://doi.org/10.1016/0008-8846(96)00130-5

Chu, W., Shen, J., Yang, Y., Li, Y., & Gao, D. (2015). Calculation of micro-annulus size in casing-cement sheath-formation system under continuous internal casing pressure change. *Petroleum Exploration and Development*, *42*(3), 414–421. https://doi.org/10.1016/S1876-3804(15)30033-1

Coker, O. D., Harris, K. L., & Williams, T. A. (1992). Preventing Shallow Gas Migration in Offshore Wells: The Performance of Lead Cements. *European Petroleum Conference*, *1*. https://doi.org/10.2118/24978-MS

Cowan, K. M., & Eoff, L. (1993). Surfactants: Additives To Improve the Performance Properties of Cements. *SPE International Symposium on Oilfield Chemistry*, *1*, 317–327. https://doi.org/10.2118/25181-MS

Cui, L., & Cahyadi, J. H. (2001). Permeability and pore structure of OPC paste. *Cement and Concrete Research*, *31*(2), 277–282. https://doi.org/10.1016/S0008-8846(00)00474-9

Das, S., Maroli, A., & Neithalath, N. (2016). Finite element-based micromechanical modeling of the influence of phase properties on the elastic response of cementitious mortars. *Construction and Building Materials*, *127*, 153–166. https://doi.org/10.1016/j.conbuildmat.2016.09.153

Datta, S. S. (2013). *Getting Out Of A Tight Spot : Physics Of Flow Through Porous Materials*. *September*.

De Andrade, J., Sangesland, S., Todorovic, J., & Vrålstad, T. (2015, April 22). Cement Sheath Integrity During Thermal Cycling: A Novel Approach for Experimental Tests of Cement Systems. *SPE Bergen One Day Seminar*. https://doi.org/10.2118/173871-MS

De Andrade, J., Torsaeter, M., Todorovic, J., Opedal, N., Stroisz, A., & Vralstad, T. (2014). Influence of Casing Centralization on Cement Sheath Integrity During Thermal Cycling. *IADC/SPE Drilling Conference and Exhibition*, *2*(1992), 870–879. https://doi.org/10.2118/168012-MS

De Andrade, Jesus, Sangesland, S., Skorpa, R., Todorovic, J., & Vrålstad, T. (2016). Experimental Laboratory Setup for Visualization and Quantification of Cement-Sheath Integrity. *SPE Drilling & Completion*, *31*(04), 317–326. https://doi.org/10.2118/173871-PA

Devarrewaere, W., Foqué, D., Heimbach, U., Cantre, D., Nicolai, B., Nuyttens, D., & Verboven, P. (2015). Quantitative 3D Shape Description of Dust Particles from Treated Seeds by Means of X-ray Micro-CT. *Environmental Science & Technology*, *49*(12), 7310–7318. https://doi.org/10.1021/acs.est.5b02250

Diamond, S., & Leeman, M. E. (1994). Pore Size Distributions in Hardened Cement Paste by

Sem Image Analysis. *MRS Proceedings*, *370*, 217. https://doi.org/10.1557/PROC-370-217

Dixit, T., & Ghosh, I. (2018). Simulation intricacies of open-cell metal foam fin subjected to convective flow. *Applied Thermal Engineering*, *137*(April), 532–544. https://doi.org/10.1016/j.applthermaleng.2018.04.011

Dong, T., Harris, N. B., Ayranci, K., Twemlow, C. E., & Nassichuk, B. R. (2017). The impact of composition on pore throat size and permeability in high maturity shales: Middle and Upper Devonian Horn River Group, northeastern British Columbia, Canada. *Marine and Petroleum Geology*, *81*, 220–236. https://doi.org/10.1016/j.marpetgeo.2017.01.011

Ehrenberg, S. N., Eberli, G. P., Keramati, M., & Moallemi, S. A. (2006). Porosity-permeability relationships in interlayered limestone-dolostone reservoirs. *AAPG Bulletin*, *90*(1), 91–114. https://doi.org/10.1306/08100505087

Ehrenberg, Stephen N., Eberli, G. P., & Baechle, G. (2006). Porosity-permeability relationships in Miocene carbonate platforms and slopes seaward of the Great Barrier Reef, Australia (ODP Leg 194, Marion Plateau). *Sedimentology*, *53*(6), 1289–1318. https://doi.org/10.1111/j.1365-3091.2006.00817.x

El-Dieb, A. S., & Hooton, R. D. (1994). Evaluation of the Katz-Thompson model for estimating the water permeability of cement-based materials from mercury intrusion porosimetry data. *Cement and Concrete Research*, *24*(3), 443–455. https://doi.org/10.1016/0008-8846(94)90131-7

El-Gamal, S. M. A., Abo-El-Enein, S. A., El-Hosiny, F. I., Amin, M. S., & Ramadan, M. (2018). Thermal resistance, microstructure and mechanical properties of type I Portland cement pastes containing low-cost nanoparticles. *Journal of Thermal Analysis and Calorimetry*, *131*(2), 949–968. https://doi.org/10.1007/s10973-017-6629-1

Ergun, S. (1952). Fluid flow through packed columns. *Chemical Engineering Progress*, *2*(48), 82–94. papers3://publication/uuid/25D57E8A-5839-47CD-A106-AB71472B0737

Esrafili-Dizaji, B., & Rahimpour-Bonab, H. (2009). Effects of depositional and diagenetic characteristics on carbonate reservoir quality: a case study from the South Pars gas field in the Persian Gulf. *Petroleum Geoscience*, *15*(4), 325–344. https://doi.org/10.1144/1354-079309-817

Faiz, M. (2014). *Comparison of porous media permeability: experimental, analytical and numerical methods*.

Ferziger, J. H., & Perić, M. (2002). Computational Methods for Fluid Dynamics. In *Computers & Mathematics with Applications* (Vol. 46, Issues 2–3). Springer Berlin Heidelberg. https://doi.org/10.1007/978-3-642-56026-2

Fjaer, E., Folstad, J. S., & Li, L. (2016). How creeping shale may form a sealing barrier around a well. *50th US Rock Mechanics / Geomechanics Symposium*.

Fjar, E., Holt, R.M., Raaen, A.M., Risnes, R. and Horsrud, P. (2008). Petroleum related rock mechanics. In *Elsevier*. https://doi.org/10.1016/0148-9062(93)92632-Z

Fossen, H. (2010). Structural Geology. In *Cambridge University Press*. Cambridge University Press. https://doi.org/10.1017/CBO9780511777806

Gajewicz, A. M., Gartner, E., Kang, K., McDonald, P. J., & Yermakou, V. (2016a). A 1H NMR relaxometry investigation of gel-pore drying shrinkage in cement pastes. *Cement and Concrete Research*, *86*, 12–19. https://doi.org/10.1016/j.cemconres.2016.04.013

Gajewicz, A. M., Gartner, E., Kang, K., McDonald, P. J., & Yermakou, V. (2016b). A 1 H NMR relaxometry investigation of gel-pore drying shrinkage in cement pastes. *Cement and Concrete Research*, *86*, 12–19. https://doi.org/10.1016/j.cemconres.2016.04.013

Gallé, C. (2001). Effect of drying on cement-based materials pore structure as identified by mercury intrusion porosimetry - A comparative study between oven-, vacuum-, and freeze-drying. *Cement and Concrete Research*, *31*(10), 1467–1477. https://doi.org/10.1016/S0008-8846(01)00594-4

Gallucci, E., Scrivener, K., Groso, A., Stampanoni, M., & Margaritondo, G. (2007). 3D experimental investigation of the microstructure of cement pastes using synchrotron X-ray microtomography (μCT). *Cement and Concrete Research*, *37*(3), 360–368. https://doi.org/10.1016/j.cemconres.2006.10.012

Garboczi, E. J., & Bullard, J. W. (2004). Shape analysis of a reference cement. *Cement and Concrete Research*, *34*(10), 1933–1937. https://doi.org/10.1016/j.cemconres.2004.01.006

Garboczi, Edward J. (1990). Permeability, diffusivity, and microstructural parameters: A critical review. *Cement and Concrete Research*, *20*(4), 591–601. https://doi.org/10.1016/0008-8846(90)90101-3

Garci Juenger, M. C., & Jennings, H. M. (2002). Examining the relationship between the microstructure of calcium silicate hydrate and drying shrinkage of cement pastes. *Cement and Concrete Research*, *32*(2), 289–296. https://doi.org/10.1016/S0008-8846(01)00673-1

Garnier, A., Laudet, J.-B., Neuville, N., Le Guen, Y., Fourmaintraux, D. M., Rafai, N., Burlion, N., & Shao, J. F. (2010). CO2-Induced Changes in Oilwell Cements Under Downhole Conditions: First Experimental Results. *SPE Annual Technical Conference and Exhibition*, *2*, 1–15. https://doi.org/10.2118/134473-MS

Gheibi, S., Sangesland, S., & Vrålstad, T. (2019). Numerical Modeling of Radial Fracturing of Cement Sheath Caused by Pressure Tests. *Volume 8: Polar and Arctic Sciences and Technology; Petroleum Technology*, *8*, 1–7. https://doi.org/10.1115/OMAE2019-96319

Gitman, I. M., Askes, H., & Sluys, L. J. (2007). Representative volume: Existence and size determination. *Engineering Fracture Mechanics*, *74*(16), 2518–2534. https://doi.org/10.1016/j.engfracmech.2006.12.021

Givens, N. B., Survey, K. G., Nissen, S. E., Ave, C., Wells, C., & Fields, S. C. (1990). *Fracture and Karst Features Affecting Reservoir Performance in a Mississippian Reservoir , Cheyenne County , Colorado ~*. Kansas Geological Survey Open-File Report. http://www.kgs.ku.edu/PRS/publication/2006/2006-14/index.html

Goboncan, V. C., & Dillenbeck, R. L. (2003). Real-Time Cement Expansion/Shrinkage Testing Under Downhole Conditions For Enhanced Annular Isolation. *SPE/IADC Drilling Conference*, *l*. https://doi.org/10.2118/79911-MS

Government of Canada. (2018). *Modelling of greenhouse gas projections*. https://www.canada.ca/en/services/environment/weather/climatechange/climate-action/modelling-ghg-projections.html

Government of Canada. (2019). *Canada's methane regulations for the upstream oil and gas sector*. https://www.canada.ca/en/environment-climate-change/services/canadian-environmental-protection-act-registry/proposed-methane-regulations-additional-information.html

Grassl, P., Wong, H. S., & Buenfeld, N. R. (2010). Influence of aggregate size and volume fraction on shrinkage induced micro-cracking of concrete and mortar. *Cement and Concrete Research*, *40*(1), 85–93. https://doi.org/10.1016/j.cemconres.2009.09.012

Haecker, C. J., Garboczi, E. J., Bullard, J. W., Bohn, R. B., Sun, Z., Shah, S. P., & Voigt, T. (2005). Modeling the linear elastic properties of Portland cement paste. *Cement and Concrete Research*, *35*(10), 1948–1960. https://doi.org/10.1016/j.cemconres.2005.05.001

Hearn, N., Hooton, R., & Mills, R. (1994). Pore Structure and Permeability. In *Significance of Tests and Properties of Concrete and Concrete-Making Mate rials: Vol. d* (pp. 240-240–23). ASTM International. https://doi.org/10.1520/STP36424S

Helfen, L., Dehn, F., Mikulík, P., & Baumbach, T. (2005). Three-dimensional imaging of cement microstructure evolution during hydration. *Advances in Cement Research*, *17*(3), 103–111. https://doi.org/10.1680/adcr.2005.17.3.103

Hlobil, M., Šmilauer, V., & Chanvillard, G. (2016). Micromechanical multiscale fracture model for compressive strength of blended cement pastes. *Cement and Concrete Research*, *83*, 188–202. https://doi.org/10.1016/j.cemconres.2015.12.003

Holly, J., Hampton, D., & Thomas, M. D. A. (1993). Modelling relationships between permeability and cement paste pore microstructures. *Cement and Concrete Research*, *23*(6), 1317–1330. https://doi.org/10.1016/0008-8846(93)90069-L

Hoseini, M., Bindiganavile, V., & Banthia, N. (2009). The effect of mechanical stress on permeability of concrete: A review. *Cement and Concrete Composites*, *31*(4), 213–220. https://doi.org/10.1016/j.cemconcomp.2009.02.003

Hughes, D. C. (1985). Pore structure and permeability of hardened cement paste. *Magazine of Concrete Research*, *37*(133), 227–233. https://doi.org/10.1680/macr.1985.37.133.227

Iassonov, P., Gebrenegus, T., & Tuller, M. (2009). Segmentation of X-ray computed tomography images of porous materials: A crucial step for characterization and quantitative analysis of pore structures. *Water Resources Research*, *45*(9), 1–12. https://doi.org/10.1029/2009WR008087

Iremonger, S. S., Bolt, M., & Lawrence, S. C. (2015). Enhanced Thermal Well Integrity Through The Use Of A New Cement Tensile Strength-enhancing Fiber. *SPE Canada Heavy Oil*

Technical Conference, 1–12. https://doi.org/10.2118/174483-MS

Iremonger, S. S., Cheung, B., & Carey, J. (2017, November 28). Direct Strain Mapping of a Cement Sheath; A New Tool for Understanding and Preventing Cement Failure in Thermal Wells. *SPE Thermal Well Integrity and Design Symposium*. https://doi.org/10.2118/188151-MS

Jankovic, D., & van Mier, J. G. M. (2002). Preliminary investigation of drying shrinkage cement paste specimens. *International Conference on New Challenges in Mesomechanics*, 265–271.

Jikich, S. A., McIntyre, D., Bromhal, G. S., & Crandall, D. (2010). Mechanical properties, flow properties, and heterogeneous CO<inf>2</inf>sorption in confined powder river coal cores. *44th US Rock Mechanics Symposium - 5th US/Canada Rock Mechanics Symposium*, 2–7.

Jules, R., Ye, J., & Cao, Q. (2016). Geological Conditions and Hydrocarbon Accumulation Processes in the Sahul Platform, Northern Bonaparte Basin, Australia. *International Journal of Geosciences*, *07*(06), 792–827. https://doi.org/10.4236/ijg.2016.76061

Jung, H. B., Jansik, D., & Um, W. (2013). Imaging wellbore cement degradation by carbon dioxide under geologic sequestration conditions using X-ray computed microtomography. *Environmental Science and Technology*, *47*(1), 283–289. https://doi.org/10.1021/es3012707

Jung, H. B., Kabilan, S., Carson, J. P., Kuprat, A. P., Um, W., Martin, P., Dahl, M., Kafentzis, T., Varga, T., Stephens, S., Arey, B., Carroll, K. C., Bonneville, A., & Fernandez, C. A. (2014). Wellbore cement fracture evolution at the cement-basalt caprock interface during geologic carbon sequestration. *Applied Geochemistry*, *47*, 1–16. https://doi.org/10.1016/j.apgeochem.2014.04.010

Justo-Reinoso, I., Srubar, W. V., Caicedo-Ramirez, A., & Hernandez, M. T. (2018). Fine aggregate substitution by granular activated carbon can improve physical and mechanical properties of cement mortars. *Construction and Building Materials*, *164*, 750–759. https://doi.org/10.1016/j.conbuildmat.2017.12.181

Kabilan, S., Jung, H. B., Kuprat, A. P., Beck, A. N., Varga, T., Fernandez, C. A., & Um, W. (2016). Numerical Simulation of Permeability Change in Wellbore Cement Fractures after Geomechanical Stress and Geochemical Reactions Using X-ray Computed Tomography

Imaging. *Environmental Science & Technology*, *50*(12), 6180–6188. https://doi.org/10.1021/acs.est.6b00159

Kaiser, Â. (2006). *Non-linear flow in fractured rock*.

Katz, A. J., & Thompson, A. H. (1986). Quantitative prediction of permeability in porous rock. *Physical Review B*, *34*(11), 8179–8181. https://doi.org/10.1103/PhysRevB.34.8179

Kawashima, S., & Shah, S. P. (2011). Early-age autogenous and drying shrinkage behavior of cellulose fiber-reinforced cementitious materials. *Cement and Concrete Composites*, *33*(2), 201–208. https://doi.org/10.1016/j.cemconcomp.2010.10.018

Kendall, K., Howard, A. J., Birchall, J. D., Pratt, P. L., Proctor, B. A., & Jefferis, S. A. (1983). The Relation between Porosity, Microstructure and Strength, and the Approach to Advanced Cement-Based Materials [and Discussion]. *Philosophical Transactions of the Royal Society A: Mathematical, Physical and Engineering Sciences*, *310*(1511), 139–153. https://doi.org/10.1098/rsta.1983.0073

Kibodeaux, K. R. (2014, October 27). Evolution of Porosity, Permeability, and Fluid Saturations During Thermal Conversion of Oil Shale. *SPE Annual Technical Conference and Exhibition*. https://doi.org/10.2118/170733-MS

Kjellsen, K. O., & Jennings, H. M. (1996). Observations of microcracking in cement paste upon drying and rewetting by environmental scanning electron microscopy. *Advanced Cement Based Materials*, *3*(1), 14–19. https://doi.org/10.1016/S1065-7355(96)90065-6

Kjøller, C., Sigalas, L., Frykman, P., Bjørge, R., & Torsæter, M. (2016). Cement Self-Healing as a Result of CO2 Leakage. *Energy Procedia*, *86*, 342–351. https://doi.org/10.1016/j.egypro.2016.01.035

Kjøller, C., Torsæter, M., Lavrov, A., & Frykman, P. (2016). Novel experimental/numerical approach to evaluate the permeability of cement-caprock systems. *International Journal of Greenhouse Gas Control*, *45*, 86–93. https://doi.org/10.1016/j.ijggc.2015.12.017

Klaver, J., Hemes, S., Houben, M., Desbois, G., Radi, Z., & Urai, J. L. (2015). The connectivity of pore space in mudstones: insights from high-pressure Wood's metal injection, BIB-SEM imaging, and mercury intrusion porosimetry. *Geofluids*, *15*(4), 577–591. https://doi.org/10.1111/gfl.12128

Kutchko, B. G., Strazisar, B. R., Huerta, N., Lowry, G. V., Dzombak, D. A., & Thaulow, N. (2009). CO2 reaction with hydrated class H well cement under geologic sequestration conditions: Effects of flyash admixtures. *Environmental Science and Technology*, *43*(10), 3947–3952. https://doi.org/10.1021/es803007e

L. Martin, J., Darwin, D., & Terry, R. E. (1991). *Cement Paste, Mortar and Concrete Under Monotonic, Sustained and Cyclic Loading* (Issue October). https://doi.org/10.1.1.689.2509

Lake, L. W. (1989). Enhanced Oil Recovery. In *Enhanced Oil Recovery*. Prentice Hall.

Lake, L. W. (2006). *Petroleum Engineering Handbook, Volume I: General Engineering*. Society of Petroleum Engineers.

Lavrov, A, & Cerasi, P. (2013). Numerical modeling of tensile thermal stresses in rock around a cased well caused by injection of a cold fluid. *47th US Rock Mechanics/Geomechanics Symposium*.

Lavrov, Alexandre. (2018). Stiff cement, soft cement: Nonlinearity, arching effect, hysteresis, and irreversibility in CO2-well integrity and near-well geomechanics. *International Journal of Greenhouse Gas Control*, *70*(June 2017), 236–242. https://doi.org/10.1016/j.ijggc.2017.11.012

Lavrov, Alexandre, Anabela Chavez Panduro, E., Gawel, K., & Torsæter, M. (2018). Electrophoresis-induced structural changes at cement-steel interface. *AIMS Materials Science*, *5*(3), 414–421. https://doi.org/10.3934/matersci.2018.3.414

Lavrov, Alexandre, Panduro, E. A. C., & Torsæter, M. (2017). Synchrotron Study of Cement Hydration: Towards Computed Tomography Analysis of Interfacial Transition Zone. *Energy Procedia*, *114*(1876), 5109–5117. https://doi.org/10.1016/j.egypro.2017.03.1666

Lavrov, Alexandre, Todorovic, J., & Torsæter, M. (2016). Impact of voids on mechanical stability of well cement. *Energy Procedia*, *86*(1876), 401–410. https://doi.org/10.1016/j.egypro.2016.01.041

Lavrov, Alexandre, & Torsæter, M. (2016). *Physics and Mechanics of Primary Well Cementing*. Springer. https://doi.org/10.1007/978-3-319-43165-9

Lawn, B. R., & Evans, A. G. (1977). A model for crack initiation in elastic/plastic indentation fields. *Journal of Materials Science*, *12*(11), 2195–2199. https://doi.org/10.1007/BF00552240

Le-Minous, J. C., Mutti, D., Bouvet, A., Unanue-Rodriguez, I., Chang, A., Massie, I., Xiao, E., & Schnell, E. (2017, March 14). Permeability Study of API Class G and B Cements Considering Seawater and WBM Contamination. *SPE/IADC Drilling Conference and Exhibition*. https://doi.org/10.2118/184613-MS

Li, J., Xi, Y., Tao, Q., Li, Y., & Qu, G. (2020). Experimental investigation and numerical simulation of the emergence and development of micro-annulus in shale gas wells subjected to multistage fracturing. *Journal of Natural Gas Science and Engineering*, *78*(July 2019), 103314. https://doi.org/10.1016/j.jngse.2020.103314

Li, K., Stroeven, M., Stroeven, P., & Sluys, L. J. (2016a). Investigation of liquid water and gas permeability of partially saturated cement paste by DEM approach. *Cement and Concrete Research*, *83*, 104–113. https://doi.org/10.1016/j.cemconres.2016.02.002

Li, K., Stroeven, P., Stroeven, M., & Sluys, L. J. (2016b). Estimating permeability of cement paste using pore characteristics obtained from DEM-based modelling. *Construction and Building Materials*, *126*, 740–746. https://doi.org/10.1016/j.conbuildmat.2016.09.096

Lim, C. C., Gowripalan, N., & Sirivivatnanon, V. (2000). Microcracking and chloride permeability of concrete under uniaxial compression. *Cement and Concrete Composites*, *22*(5), 353–360. https://doi.org/10.1016/S0958-9465(00)00029-9

Liu, Z., & Winslow, D. (1995). Sub-distributions of pore size: A new approach to correlate pore structure with permeability. *Cement and Concrete Research*, *25*(4), 769–778. https://doi.org/10.1016/0008-8846(95)00067-M

Loizzo, M., Lecampion, B., & Mogilevskaya, S. (2017). The Role of Geological Barriers in Achieving Robust Well Integrity. *Energy Procedia*, *114*(November 2016), 5193–5205. https://doi.org/10.1016/j.egypro.2017.03.1673

Luping, T., & Nilsson, L. O. (1992). A study of the quantitative relationship between permeability and pore size distribution of hardened cement pastes. *Cement and Concrete Research*, *22*(4), 541–550. https://doi.org/10.1016/0008-8846(92)90004-F

Marcondes, F., Santos, L. O. S., Varavei, A., & Sepehrnoori, K. (2013a). A 3D hybrid element-based finite-volume method for heterogeneous and anisotropic compositional reservoir simulation. *Journal of Petroleum Science and Engineering*, *108*(1–2), 342–351. https://doi.org/10.1016/j.petrol.2013.04.024

Marcondes, F., Santos, L. O. S., Varavei, A., & Sepehrnoori, K. (2013b). A 3D hybrid element-based finite-volume method for heterogeneous and anisotropic compositional reservoir simulation. *Journal of Petroleum Science and Engineering*, *108*(1–2), 342–351. https://doi.org/10.1016/j.petrol.2013.04.024

Mathieu, C. (1999). The Beam-Gas and Signal-Gas Interactions in the Variable Pressure Scanning Electron Microscope. *Scanning Microscopy*, *13*(1), 23–41.

Mbia, E. N., Fabricius, I. L., Krogsboll, A., Frykman, P., & Dalhoff, F. (2014). Permeability, compressibility and porosity of Jurassic shale from the Norwegian-Danish Basin. *Petroleum Geoscience*, *20*(3), 257–281. https://doi.org/10.1144/petgeo2013-035

Mito, S., Xue, Z., & Satoh, H. (2015). Experimental assessment of well integrity for CO 2 geological storage: Batch experimental results on geochemical interactions between a CO 2 –brine mixture and a sandstone–cement–steel sample. *International Journal of Greenhouse Gas Control*, *39*, 420–431. https://doi.org/10.1016/j.ijggc.2015.06.007

Morton-Thompson, D., & Woods, A. M. A. (1993a). *Development Geology Reference Manual: AAPG Methods in Exploration Series, No. 10*. AAPG. https://books.google.com/books?id=4NoVAgAAQBAJ&pgis=1

Morton-Thompson, D., & Woods, A. M. A. (1993b). *Development Geology Reference Manual: AAPG Methods in Exploration Series, No. 10*. AAPG.

Muljadi, B. P., Blunt, M. J., Raeini, A. Q., & Bijeljic, B. (2016). The impact of porous media heterogeneity on non-Darcy flow behaviour from pore-scale simulation. *Advances in Water Resources*, *95*, 329–340. https://doi.org/10.1016/j.advwatres.2015.05.019

Murtaza, M., Rahman, M. K., Al-Majed, A. A., & Samad, A. (2013). Mechanical, Rheological and Microstructural Properties of Saudi Type G Cement Slurry with Silica Flour Used in Saudi Oil Field under HTHP Conditions. *SPE Saudi Arabia Section Technical Symposium and Exhibition*, *Nelson 1990*. https://doi.org/10.2118/168101-MS

Nagatomo, A., & Archer, S. (2015). Termination geometries and reservoir properties of the

Forties Sandstone pinch-out, East Central Graben, UK North Sea. *Geological Society, London, Special Publications*, *403*, 133–155. https://doi.org/10.1144/SP403.14

Nath, F., Kimanzi, R. J., Mokhtari, M., & Salehi, S. (2018). A novel method to investigate cement-casing bonding using digital image correlation. *Journal of Petroleum Science and Engineering*, *166*(February), 482–489. https://doi.org/10.1016/j.petrol.2018.03.068

Nelson, E. B. (1990). Well Cementing. In *World* (Issue February 2004). Elsevier B.V.

Nemati, K. M., Monteiro, P. J. M., & Scrivener, K. L. (1998). Analysis of compressive stress-induced cracks in concrete. *ACI Materials Journal*, *95*(5), 617–630.

Němeček, J., Šmilauer, V., & Kopecký, L. (2011). Nanoindentation characteristics of alkali-activated aluminosilicate materials. *Cement and Concrete Composites*, *33*(2), 163–170. https://doi.org/10.1016/j.cemconcomp.2010.10.005

Neubauer, C. M., Bergstrom, T. B., Sujata, K., Xi, Y., Garboczi, E. J., & Jennings, H. M. (1997). Drying shrinkage of cement paste as measured in an environmental scanning electron microscope and comparison with microstructural models. *Journal of Materials Science*, *32*(24), 6415–6427. https://doi.org/10.1023/A:1018682404655

Nitka, M., & Tejchman, J. (2018). A three-dimensional meso-scale approach to concrete fracture based on combined DEM with X-ray μCT images. *Cement and Concrete Research*, *107*(May 2017), 11–29. https://doi.org/10.1016/j.cemconres.2018.02.006

Opedal, N., Torsæter, M., Vrålstad, T., & Cerasi, P. (2014). Potential Leakage Paths along Cement-formation Interfaces in Wellbores; Implications for CO2 Storage. *Energy Procedia*, *51*, 56–64. https://doi.org/10.1016/j.egypro.2014.07.007

Ozyurtkan, M. H., Altun, G., Mihcakan, I. M., & Serpen, U. (2013). An experimental study on mitigation of oil well cement gas permeability. *International Petroleum Technology Conference*, *March*, 26–28. https://doi.org/10.2523/IPTC-16577-MS

Pang, X. (2011). *Effects of Curing Temperature and Pressure on the Chemical, Physical, and Mechanical Properties of Portland Cement* [Columbia University]. https://doi.org/10.7916/D8RF620F

Pang, X., Maxson, J. K., Cuello Jimenez, W., Singh, J. P., & Morgan, R. G. (2017). Microscale

Characterization of Field and Laboratory Foamed Cement by Use of X-Ray Microcomputed Tomography. *SPE Journal*, *22*(05), 1690–1703. https://doi.org/10.2118/180278-PA

Parcevaux, P. A., & Sault, P. H. (1984, September). Cement Shrinkage and Elasticity: A New Approach for a Good Zonal Isolation. *Proceedings of SPE Annual Technical Conference and Exhibition*. https://doi.org/10.2523/13176-MS

Pelissou, C., Baccou, J., Monerie, Y., & Perales, F. (2009). Determination of the size of the representative volume element for random quasi-brittle composites. *International Journal of Solids and Structures*, *46*(14–15), 2842–2855. https://doi.org/10.1016/j.ijsolstr.2009.03.015

Phung, Q. T., Maes, N., De Schutter, G., Jacques, D., & Ye, G. (2013). Determination of water permeability of cementitious materials using a controlled constant flow method. *Construction and Building Materials*, *47*, 1488–1496. https://doi.org/10.1016/j.conbuildmat.2013.06.074

Podor, R., Bouala, G. I. N., Ravaux, J., Lautru, J., & Clavier, N. (2019). Working with the ESEM at high temperature. *Materials Characterization*, *151*(February), 15–26. https://doi.org/10.1016/j.matchar.2019.02.036

Powers, T. C. (1954). Permeability of portland cement paste. *Journal of American Concrete Institute*, *26*(3), 285–298. https://archive.org/details/PermeabilityOfPortlandCementPasteByT.c.Powers...etAl.

Promentilla, M. A. B., Sugiyama, T., Hitomi, T., & Takeda, N. (2009). Quantification of tortuosity in hardened cement pastes using synchrotron-based X-ray computed microtomography. *Cement and Concrete Research*, *39*(6), 548–557. https://doi.org/10.1016/j.cemconres.2009.03.005

Ramandi, H. L., Mostaghimi, P., & Armstrong, R. T. (2017). Digital rock analysis for accurate prediction of fractured media permeability. *Journal of Hydrology*, *554*, 817–826. https://doi.org/10.1016/j.jhydrol.2016.08.029

Ramandi, H. L., Mostaghimi, P., Armstrong, R. T., Saadatfar, M., & Pinczewski, W. V. (2016). Porosity and permeability characterization of coal: a micro-computed tomography study. *International Journal of Coal Geology*, *154–155*, 57–68. https://doi.org/10.1016/j.coal.2015.10.001

Reddy, B. R., Xu, Y., Ravi, K., Gray, D. W., & Pattillo, P. (2009). Cement Shrinkage Measurement in Oilwell Cementing--A Comparative Study of Laboratory Methods and Procedures. *SPE Drilling & Completion*, *24*(01), 104–114. https://doi.org/10.2118/103610-PA

Rimmelé, G., Barlet-Gouédard, V., Porcherie, O., Goffé, B., & Brunet, F. (2008). Heterogeneous porosity distribution in Portland cement exposed to CO2-rich fluids. *Cement and Concrete Research*, *38*(8–9), 1038–1048. https://doi.org/10.1016/j.cemconres.2008.03.022

Rusch, D., Fred, S., & John, A. (2004). Microannulus Leaks Repaired with Pressure-Activated Sealant. *Proceedings of SPE Eastern Regional Meeting*, 83–90. https://doi.org/10.2523/91399-MS

Ruzyla, K. (1986). Characterization of Pore Space by Quantitative Image Analysis. *SPE Formation Evaluation*, *1*(04), 389–398. https://doi.org/10.2118/13133-PA

Saasen, A., Wold, S., Ribesen, B. T., Tran, T. N., Huse, A., Rygg, V., Grannes, I., & Svindland, A. (2011). Permanent Abandonment of a North Sea Well Using Unconsolidated Well-Plugging Material. *SPE Drilling & Completion*, *26*(03), 371–375. https://doi.org/10.2118/133446-PA

Saito, M., & Ishimori, H. (1995). Chloride permeability of concrete under static and repeated compressive loading. *Cement and Concrete Research*, *25*(4), 803–808. https://doi.org/10.1016/0008-8846(95)00070-S

Sakai, Y., Nakatani, M., Takeuchi, A., Omorai, Y., & Kishii, T. (2016). Mechanical Behavior of Cement Paste and Alterations of Hydrates under High-Pressure Triaxial Testing. *Journal of Advanced Concrete Technology*, *14*(1), 1–12. https://doi.org/10.3151/jact.14.1

Sammartino, S., Siitari-Kauppi, M., Meunier, A., Sardini, P., Bouchet, A., & Tevissen, E. (2002). An Imaging Method for the Porosity of Sedimentary Rocks: Adjustment of the PMMA Method--Example of a Characterization of a Calcareous Shale. *Journal of Sedimentary Research*, *72*(6), 937–943. https://doi.org/10.1306/053002720937

Schneider, C. A., Rasband, W. S., & Eliceiri, K. W. (2012). NIH Image to ImageJ: 25 years of image analysis. *Nature Methods*, *9*(7), 671–675. https://doi.org/10.1038/nmeth.2089

Scrivener, K. L., Crumbie, A. K., & Laugesen, P. (2004). The interfacial transition zone (ITZ) between cement paste and aggregate in concrete. *Interface Science*, *12*(4), 411–421. https://doi.org/10.1023/B:INTS.0000042339.92990.4c

SEM Lab. (2020). *Scanning Electron Microscope Laboratory*. https://www.eas.ualberta.ca/sem/

Shadravan, A., Schubert, J., Amani, M., & Teodoriu, C. (2015). Using Fatigue-Failure Envelope for Cement-Sheath-Integrity Evaluation. *SPE Drilling & Completion*, *30*(01), 68–75. https://doi.org/10.2118/168321-PA

Skorpa, R., & Vrålstad, T. (2018). Visualization of Fluid Flow Through Cracks and Microannuli in Cement Sheaths. *SPE Journal*, *23*(04), 1067–1074. https://doi.org/10.2118/180019-PA

Skyscan NV. (2011). *NRecon User Manual*.

Song, R., Liu, J., & Cui, M. (2017). A new method to reconstruct structured mesh model from micro-computed tomography images of porous media and its application. *International Journal of Heat and Mass Transfer*, *109*, 705–715. https://doi.org/10.1016/j.ijheatmasstransfer.2017.02.053

Spooner, D. C., Pomeroy, C. D., & Dougill, J. W. (1976). Damage and Energy-Dissipation in Cement Pastes in Compression. *Mag Concrete Res*, *28*(94), 21–29.

Stutzman, P. E. (2012). Microscopy of Clinker and Hydraulic Cements. *Reviews in Mineralogy and Geochemistry*, *74*(1), 101–146. https://doi.org/10.2138/rmg.2012.74.3

Su, J., Ye, J., Fang, Z., & Zhao, M. (2015). Size effect on cubic and prismatic compressive strength of cement paste. *Journal of Central South University*, *22*(10), 4090–4096. https://doi.org/10.1007/s11771-015-2954-3

Tang, J., Wu, K., Zuo, L., Xiao, L., Sun, S., & Ehlig-Economides, C. (2019). Investigation of Rupture and Slip Mechanisms of Hydraulic Fractures in Multiple-Layered Formations. *SPE Journal*, *24*(05), 2292–2307. https://doi.org/10.2118/197054-PA

Tang, S. W., Li, Z. J., Zhu, H. G., Shao, H. Y., & Chen, E. (2014). Permeability interpretation for young cement paste based on impedance measurement. *Construction and Building Materials*, *59*, 120–128. https://doi.org/10.1016/j.conbuildmat.2014.02.054

Taud, H., Martinez-Angeles, R., Parrot, J. F., & Hernandez-Escobedo, L. (2005). Porosity estimation method by X-ray computed tomography. *Journal of Petroleum Science and*

Engineering, *47*(3–4), 209–217. https://doi.org/10.1016/j.petrol.2005.03.009

Taylor, H. F. W. (1997). *Cement Chemistry. 2nd*. Thomas Telford.

Tiab, D., & Donaldson, E. C. (2015). *Petrophysics: theory and practice of measuring reservoir rock and fluid transport properties*. Gulf professional publishing.

Torsæter, M., Todorovic, J., & Lavrov, A. (2015a). Structure and debonding at cement-steel and cement-rock interfaces: Effect of geometry and materials. *Construction and Building Materials*, *96*, 164–171. https://doi.org/10.1016/j.conbuildmat.2015.08.005

Torsæter, M., Todorovic, J., & Lavrov, A. (2015b). Structure and debonding at cement–steel and cement–rock interfaces: Effect of geometry and materials. *Construction and Building Materials*, *96*, 164–171. https://doi.org/10.1016/j.conbuildmat.2015.08.005

Ueda, T., Oki, T., & Koyanaka, S. (2018). Experimental analysis of mineral liberation and stereological bias based on X-ray computed tomography and artificial binary particles. *Advanced Powder Technology*, *29*(3), 462–470. https://doi.org/10.1016/j.apt.2017.11.004

Valenza, J. J., & Thomas, J. J. (2012). Permeability and elastic modulus of cement paste as a function of curing temperature. *Cement and Concrete Research*, *42*(2), 440–446. https://doi.org/10.1016/j.cemconres.2011.11.012

Vandamme, M., & Ulm, F.-J. (2009). Nanogranular origin of concrete creep. *Proceedings of the National Academy of Sciences*, *106*(26), 10552–10557. https://doi.org/10.1073/pnas.0901033106

Viejo, I., Esteves, L. P., Laspalas, M., & Bielsa, J. M. (2016). Numerical modelling of porous cement-based materials by superabsorbent polymers. *Cement and Concrete Research*, *90*, 184–193. https://doi.org/10.1016/j.cemconres.2016.07.018

Visschedijk, A. J. H., Denier van der Gon, H. A. C., Doornenbal, H. C., & Cremonese, L. (2018). Methane and ethane emission scenarios for potential shale gas production in Europe. *Advances in Geosciences*, *45*, 125–131. https://doi.org/10.5194/adgeo-45-125-2018

Viswanathan, H. S., Pawar, R. J., Stauffer, P. H., Kaszuba, J. P., Carey, J. W., Olsen, S. C., Keating, G. N., Kavetski, D., & Guthrie, G. D. (2008a). Development of a hybrid process and system model for the assessment of wellbore leakage at a geologic CO2sequestration site. *Environmental Science and Technology*, *42*(19), 7280–7286. https://doi.org/10.1021/es800417x

Viswanathan, H. S., Pawar, R. J., Stauffer, P. H., Kaszuba, J. P., Carey, J. W., Olsen, S. C., Keating, G. N., Kavetski, D., & Guthrie, G. D. (2008b). Development of a Hybrid Process and System Model for the Assessment of Wellbore Leakage at a Geologic CO 2 Sequestration Site. *Environmental Science & Technology*, *42*(19), 7280–7286. https://doi.org/10.1021/es800417x

Vrålstad, T., & Skorpa, R. (2020). Digital Cement Integrity: A Methodology for 3D Visualization of Cracks and Microannuli in Well Cement. *Sustainability*, *12*(10), 4128. https://doi.org/10.3390/su12104128

Vrålstad, T., Todorovic, J., Saasen, A., & Godøy, R. (2016, April 20). Long-Term Integrity of Well Cements at Downhole Conditions. *SPE Bergen One Day Seminar*. https://doi.org/10.2118/180058-MS

Wang, C., Chen, X., & Wang, R. (2017). Do chlorides qualify as accelerators for the cement of deepwater oil wells at low temperature? *Construction and Building Materials*, *133*, 482–494. https://doi.org/10.1016/j.conbuildmat.2016.12.089

Wang, G., Chu, X., & Yang, X. (2016). Numerical simulation of gas flow in artificial fracture coal by three-dimensional reconstruction based on computed tomography. *Journal of Natural Gas Science and Engineering*, *34*, 823–831. https://doi.org/10.1016/j.jngse.2016.07.039

Wang, J. S. Y., & Narasimhan, T. N. (1985). Hydrologic Mechanisms Governing Fluid Flow in a Partially Saturated, Fractured, Porous Medium. *Water Resources Research*, *21*(12), 1861–1874. https://doi.org/10.1029/WR021i012p01861

Wang, Y. S., & Dai, J. G. (2017). X-ray computed tomography for pore-related characterization and simulation of cement mortar matrix. *NDT and E International*, *86*(April 2016), 28–35. https://doi.org/10.1016/j.ndteint.2016.11.005

Williams, S. M., Carlsen, T., Constable, K. C., & Guldahl, A. C. (2009). Identification and Qualification of Shale Annular Barriers Using Wireline Logs During Plug and Abandonment Operations. *SPE/IADC Drilling Conference and Exhibition*, 1–15.

https://doi.org/10.2118/119321-MS

Wong, H. S., Zimmerman, R. W., & Buenfeld, N. R. (2012). Estimating the permeability of cement pastes and mortars using image analysis and effective medium theory. *Cement and Concrete Research*, *42*(2), 476–483. https://doi.org/10.1016/j.cemconres.2011.11.018

Xie, S. Y., Shao, J. F., & Burlion, N. (2008). Experimental study of mechanical behaviour of cement paste under compressive stress and chemical degradation. *Cement and Concrete Research*, *38*(12), 1416–1423. https://doi.org/10.1016/j.cemconres.2008.06.011

Yalcinkaya, T., Radonjic, M., Hughes, R. G., Willson, C., & Ham, K. (2011). The Effect of CO2-Saturated Brine on the Conductivity of Wellbore-Cement Fractures. *SPE Drilling & Completion*, *26*(03), 332–340. https://doi.org/10.2118/139713-PA

Yang, X., Kuru, E., Gingras, M., & Iremonger, S. (2019). CT-CFD integrated investigation into porosity and permeability of neat early-age well cement at downhole condition. *Construction and Building Materials*, *205*, 73–86. https://doi.org/10.1016/j.conbuildmat.2019.02.004

Yang, X., Kuru, E., Gingras, M., Iremonger, S., Taylor, J., Lin, Z., & Chase, P. (2020). Quantifying the Impact of 2D and 3D Fractures on Permeability in Wellbore Cement after Uniaxial Compressive Loading. *SPE Journal*, *2000*(February), 19–21. https://doi.org/10.2118/198683-PA

Ye, G. (2005). Percolation of capillary pores in hardening cement pastes. *Cement and Concrete Research*, *35*(1), 167–176. https://doi.org/10.1016/j.cemconres.2004.07.033

Yio, M. H. N., Wong, H. S., & Buenfeld, N. R. (2017). Representative elementary volume (REV) of cementitious materials from three-dimensional pore structure analysis. *Cement and Concrete Research*, *102*(May), 187–202. https://doi.org/10.1016/j.cemconres.2017.09.012

Zajac, M., Skocek, J., Müller, A., & Ben Haha, M. (2018). Effect of sulfate content on the porosity distribution and resulting performance of composite cements. *Construction and Building Materials*, *186*, 912–919. https://doi.org/10.1016/j.conbuildmat.2018.07.247

Zalzale, M., & McDonald, P. J. (2012). Lattice Boltzmann simulations of the permeability and capillary adsorption of cement model microstructures. *Cement and Concrete Research*, *42*(12), 1601–1610. https://doi.org/10.1016/j.cemconres.2012.09.003

Zalzale, M., McDonald, P. J., & Scrivener, K. L. (2013). A 3D lattice Boltzmann effective media study: Understanding the role of C-S-H and water saturation on the permeability of cement paste. *Modelling and Simulation in Materials Science and Engineering*, *21*(8). https://doi.org/10.1088/0965-0393/21/8/085016

Zeng, J., Sun, F., Li, P., Liu, A., & Gao, Y. (2012). Study of Salt-tolerable Latex Cement Slurries. *The Twenty-Second International Offshore and Polar Engineering Conference, 17-22 June, Rhodes, Greece*, *4*, 1037–1040. https://www.onepetro.org/conference-paper/ISOPE-I-12-075?sort=&start=0&q=Study+of+Salt-tolerable+Latex+Cement+Slurries&from_year=&peer_reviewed=&published_between=&fromSearchResults=true&to_year=&rows=25#

Zeng, Z., & Grigg, R. (2006). A Criterion for Non-Darcy Flow in Porous Media. *Transport in Porous Media*, 57–69. https://doi.org/10.1007/s11242-005-2720-3

Zhang, F., Damjanac, B., & Maxwell, S. (2019). Investigating Hydraulic Fracturing Complexity in Naturally Fractured Rock Masses Using Fully Coupled Multiscale Numerical Modeling. *Rock Mechanics and Rock Engineering*, *52*(12), 5137–5160. https://doi.org/10.1007/s00603-019-01851-3

Zhang, Hong, Shen, R., Yuan, G., Ba, Z., & Hu, Y. (2017). Cement sheath integrity analysis of underground gas storage well based on elastoplastic theory. *Journal of Petroleum Science and Engineering*, *159*(September), 818–829. https://doi.org/10.1016/j.petrol.2017.10.012

Zhang, Hongzhi, Šavija, B., Figueiredo, S. C., & Schlangen, E. (2017). Experimentally validated multi-scale modelling scheme of deformation and fracture of cement paste. *Cement and Concrete Research*, *102*(September), 175–186. https://doi.org/10.1016/j.cemconres.2017.09.011

Zhang, J., Ma, G., Ming, R., Cui, X., Li, L., & Xu, H. (2018). *Numerical study on seepage flow in pervious concrete based on 3D CT imaging*. *161*, 468–478. https://doi.org/10.1016/j.conbuildmat.2017.11.149

Zhang, Z., Scherer, G. W., & Bauer, A. (2018). Morphology of cementitious material during early hydration. *Cement and Concrete Research*, *107*(September 2017), 85–100.

https://doi.org/10.1016/j.cemconres.2018.02.004

Zhao, H., & Darwin, D. (1992). Quantitative backscattered electron analysis of cement paste. *Cement and Concrete Research*, *22*(4), 695–706. https://doi.org/10.1016/0008-8846(92)90022-N

Zhao, Y., Zhu, G., Zhang, C., Liu, S., Elsworth, D., & Zhang, T. (2018). Pore-Scale Reconstruction and Simulation of Non-Darcy Flow in Synthetic Porous Rocks. *Journal of Geophysical Research: Solid Earth*, *2013*, 2770–2786. https://doi.org/10.1002/2017JB015296

Zhou, C., Ren, F., Wang, Z., Chen, W., & Wang, W. (2017). Why permeability to water is anomalously lower than that to many other fluids for cement-based material? *Cement and Concrete Research*, *100*(June), 373–384. https://doi.org/10.1016/j.cemconres.2017.08.002